School of Earth and Planetary Science

Department of Applied Geology

Understanding Fluid–Rock Interactions and Lixiviant/Oxidant Behaviour for the In-situ Recovery of Metals from Deep Ore Bodies

Tania Marcela Hidalgo Rosero

This thesis is presented for the degree of Doctor of Philosophy

of

Curtin University

February 2020

Declaration

To the best of my knowledge and belief, I declare that this work of thesis contains no material published by any other person, except where due acknowledgements have been made. This thesis contains no material which has been accepted for the award of any other degree or diploma in any university.

Tania Marcela Hidalgo Rosero Date: 28/01/2020

Abstract

In-situ recovery (ISR) processing has been recognised as a possible alternative to open-pit mining, especially for low-grade resources. In ISR, the fluid–rock interaction between the target ore and the lixiviant results in valuable- (and gangue-) metal dissolution. This interaction is achieved by the injection and recovery of fluid by means of strategically positioned wells. Although the application of ISR has become more common (ISR remains the preferential processing technique for uranium and has been applied in pilot programs for treating oxide zones in copper deposits), its application to hard-rock refractory and low-grade copper-sulfide deposits is still under development. This research is focused on the possible application of ISR to primary copper sulfides usually found as deep ores.

Lixiviant/oxidant selection is an important aspect to consider during planning and operation in the ISR of copper-sulfide ores. Oxidant addition is required to break down the refractory copper-sulfide structure. During the course of the reaction, the fluid stability, mineral selectivity and accessibility (from precipitation or side reactions) may be affected, which in turn limits the application of ISR. Extensive research has been conducted on lixiviant kinetics under heap-leaching conditions, especially for common oxidants (Fe^{3+} and O_2) in acid solutions for fine-grained powder, pure-mineral and concentrate samples and from ambient temperature to 90°C. However, few studies have investigated different reagents for ISR application and with a focus on coarse materials.

This study focuses on the changes in the chemical composition of both the solutions and the mineral samples after their reaction with different lixiviant/oxidant solutions under conditions that may simulate an ISR application. Copper-sulfide samples used included natural chalcopyrite, bornite, chalcocite and covellite with different percent contents of gangue (e.g., pyrite, carbonates and silicates) and sample types that varied from powder (–38 μm to –160 μm) to cuboids (~4 mm on each side).

To identify potential alternative lixiviant/oxidant solutions for ISR environments, a comparative analysis of chalcopyrite dissolution was performed. The tests were performed on cuboids with eleven leach solutions ($FeCl_3$, $CuCl_2$ and $K_2Cr_2O_7$ in HCl;

$Fe_2(SO_4)_3$, $CuSO_4$, $NaNO_3$ and H_2O_2 in H_2SO_4; O_2 and H_2O_2 in glycine; $(NH_4)_2SO_4$ in ammonium hydroxide and ferric methanesulfonate) at 110°C (below the sulfur melting point) and 170°C (above the sulfur melting point), and under anoxic conditions. Copper dissolution tended to increase with an increase in temperature, but some solutions, such as potassium dichromate and hydrogen peroxide, were affected negatively by elevated temperature. Mineralogical characterisation of the reacted solids showed the formation of different surface layers, which depended on the fluid chemistry. Some of the product phases that replaced chalcopyrite had a porous texture and the initial fracture size increased as the reaction proceeded. Ferric chloride in hydrochloric acid was found to be the most efficient leach solution.

Once the preferred leach solution had been selected, kinetic analyses were performed to identify energy requirements for pure (chalcopyrite) and composite (chalcopyrite/bornite) samples when leached with ferric-chloride solution. Activation energies were determined by using the shrinking-core model and the 'time-to-a-given-fraction' method. The latter method proved more appropriate when mineral dissolution occurred as a result of a combination of mechanisms. The kinetics of the composite samples were driven by the major phase present, and the activation energy increased because of the presence of chalcopyrite. The experimental data could not be fitted accurately to the equations in the shrinking-core model and led to incorrect estimates of the activation energies. This result suggests that, for ISR targets (composite with gangue), the best approach for kinetic analysis is to use model-independent equations that allow for the calculation of activation energies throughout the reaction. The calculation of partial activation energies helps to understand the propensity for subsurface solid transformation and the dissolution rates.

Experiments were conducted under replicate ISR conditions to identify copper-sulfide transformations and mineralogical changes in acidic solutions with depleted oxidant. Even at low temperatures, bornite and chalcocite/digenite transformed to covellite. The replacements showed characteristic features of an interface-coupled dissolution–reprecipitation (ICDR) mechanism, such as sharp chemical interfaces and porosity development in newly formed phases. Bornite transformations indicated the coexistence of an ICDR mechanism with solid-state diffusion processes by the formation of fluid-mediated exsolution of copper-deficient lamellas.

Finally, multistage fluid–rock interactions were studied using natural low-grade samples with a high concentration of gangue to replicate fluid movement through subsurface ore. Acid consumption and changes in pH resulted in the precipitation of jarosite, akaganeite and gypsum because of cation and anion build up in solution. Sulfate solutions showed higher precipitation rates compared with chlorides, but NaCl addition increased gypsum precipitation. The precipitates act as passivation layers and could produce blockages that present a risk for subsurface ISR operations.

This research presents a geometallurgical approach to ISR processing by understanding the fluid–rock interactions through solid–fluid analysis after reaction. The results provide valuable information for fluid selection in an ISR process, which, when coupled with other research efforts currently underway to progress understanding towards ISR, may unlock the reality of hard-rock copper ISR processing.

Acknowledgement

I would like to thank all my supervisors for their support given during this PhD. Thank you for believing in me and for providing me with this opportunity. All my gratitude to Dr Laura Kuhar for all the time spent working with me, I could not have completed this work without having an outstanding mentor such as you. Special thanks to Prof. Andrew Putnis; it has been an honour to work with someone as experienced as you, and I have learned a lot from you during this research. I would like to thank Dr Andreas Beinlich for all the help with the research and for taking the time to help me familiarize myself with new techniques in the laboratory. To Dr Robbie McDonald, I consider you as one my supervisors, thank you for all the draft revisions, training and helping me to understand my results.

I want to thank to my sponsors, the Minerals Research Institute of Western Australia (MRIWA), BASF and the former Parker Centre from which grants were obtained for MRIWA project M488, which allowed me to conduct all experiments and analysis required to finalize this research. I am very grateful to Drs Dave Robinson, Denis Shiers, Jian Li and Richard Macoun for all the good ideas and useful comments on the experiments and manuscripts. I am incredibly grateful for having had the opportunity to work at CSIRO Mineral Resources; as an engineer and scientist I think that CSIRO serves as a great bridge between scientific research and industry requirements. Thank you to all the people that helped me with analysis, experiments, planning and training. Special acknowledgements to Michael Verrall, Peter Austin, Karl Bunney, Tuyen Pham, Nicky Chapman, Rebecca Meakin, Dr Belinda Godel, Dr Martijn Woltering and Milan Chovancek.

Many thanks to all the people I met in Australia. Thanks for the encouragement and good times to Cameron, Michelle, Tobi, Sophia, Aja, Evelien, Franzi and Lars.

To my family, you are the reason of all my efforts, thank you for always believing in me and for being there even though we are on different sides of the globe. This work would not exist without your support and love.

Table of Contents

Declaration **2**

Abstract **3**

Acknowledgement **6**

List of Tables **11**

List of Figures **14**

Nomenclature **28**

Chapter 1. Introduction **29**

1.1. In-situ recovery of copper sulfides 29

1.1.1. Gaps in current knowledge 31

1.2. Research objectives 33

1.3. Significance 34

1.4. Thesis outline and publications 35

References 37

Chapter 2. Comparative analysis of copper dissolution and mineral transformations in coarse chalcopyrite for different lixiviant/oxidant systems at elevated temperature (110°C to 170°C) **42**

2.1. Introduction 42

2.2. Materials and methods 48

2.2.1. Samples 48

2.2.2. Analytical techniques 48

2.2.3. Leaching tests 50

2.3. Results and discussion 53

2.3.1. Initial sample characterisation 53

2.3.2. Fluid analysis 54

2.3.3. Solids analysis 55

2.3.4. Morphological changes 67

2.3.5. Implications for ISR 71

2.4. Recommendations for fluid selection 73

2.5. Conclusions 76

Acknowledgments 78

References 78

Chapter 3. Kinetic study of chalcopyrite dissolution with iron(III) chloride in methanesulfonic acid **91**

3.1. Introduction 91

3.2. Experimental 97
3.2.1. Materials 97
3.2.2. Methods 97
3.3. Results and discussion 98
3.3.1. Effect of initial acid concentration 99
3.3.2. Effect of initial iron(III) concentration 100
3.3.3. Effect of particle size 101
3.3.4. Effect of temperature 101
3.3.5. Kinetic analysis by shrinking-core models 102
3.3.6. Residue characterisation 109
3.4. Concluding remarks 111
Acknowledgments 112
Nomenclature 112
References 113

Chapter 4. Kinetics and mineralogical analysis of copper dissolution from a bornite/chalcopyrite composite sample in ferric-chloride and methanesulfonic-acid solutions 119

4.1. Introduction 119
4.2. Experimental 126
4.2.1. Materials and methods 126
4.3. Results and discussion 129
4.3.1. Kinetic results 129
4.3.2. Kinetic analysis 131
4.3.3. Mineralogical analysis 141
4.4. Conclusions 151
Acknowledgments 152
Nomenclature 153
References 153

Chapter 5. Replacement reactions of copper sulfides at moderate temperature in acidic solutions 162

5.1. Introduction 162
5.2. Materials and methods 165
5.2.1. Experimental procedure 165
5.2.2. Analytical methods 166
5.2.3. Starting material 167
5.3. Results 168
5.3.1. Copper and iron dissolution rates 168
5.3.2. Solid transformations 169

5.4. Discussion 180
5.4.1. Replacement mechanism 180
5.4.2. Preservation of fluid pathways 183
5.5. Implications for *in-situ* leaching operations 184
Acknowledgments 185
References 185
Chapter 6. Effect of multistage solution–mineral contact for low-grade natural copper samples: extraction, acid consumption, gangue-mineral changes and precipitation 193
6.1. Introduction 193
6.2. Experimental 195
6.2.1. Materials and characterisation 195
6.2.2. Contact test methods 196
6.3. Results and discussion 197
6.3.1. Initial sample characterisation 197
6.3.2. Fluid analysis 200
6.3.3. Residue analysis 204
6.4. Conclusions and implications for ISR 212
Acknowledgments 214
References 214
Chapter 7. Conclusions and recommendations for ISR application 219
References 224
Appendix A. Comparative analysis of lixiviant/oxidant systems for chalcopyrite leaching from coarse samples at elevated temperature 226
A.1. Introduction 226
A.2. Experimental conditions 228
A.3. Results 229
A.4. Discussion 235
A.5. Conclusions 238
Acknowledgments 239
References 239
Appendix B. Staged leaching of bornite with acidic solutions at moderate temperature in an in-situ recovery environment 243
B.1. Introduction 244
B.2. Results 248
B.3. Discussion 255
B.4. Conclusions 259
Acknowledgments 260

References 260
Appendix C. Complementary data chapter 2 265
Appendix D. Complementary data chapter 5 270
Statements of Authorship 272

List of Tables

Table 1-1. Comparative dissolution rates in laboratory-scale tests using acidic sulfide systems for different copper-bearing minerals in heaps and dumps of low-grade ores (modified from Watling, 2013). 31

Table 2-1. Summary of previous experimental studies using known oxidants for copper-sulfide ores. 45

Table 2-2. Summary of system starting conditions used for experiments at 110°C . 51

Table 2-3. Summary of initial system conditions used in experiments at 170°C 52

Table 2-4. Chemical composition of initial mineral sample 53

Table 2-5. Summary of solid product layers after 4 days of reaction in different solutions at 110°C and 170°C (characterised by XRD, SEM-EDS,QEMSCAN and TIMA analyses). 63

Table 2-6. Advantages and disadvantages of different systems tested 77

Table 3-1. Review of literature on chalcopyrite dissolution with ferric-ion oxidant. 94

Table 3-2. Baseline experimental conditions. 98

Table 3-3. Chemical composition of the initial chalcopyrite sample. 99

Table 3-4. Determination coefficients (R^2) for six kinetic experimental equations for selected 104

Table 3-5. Kinetics rate constants for chalcopyrite dissolution as a function of temperature for the Arrhenius and 'time-to-a-given-fraction' methods 109

Table 4-1. Review of literature on bornite kinetics and reported activation energies and leaching mechanisms. 122

Table 4-2. Review of literature on kinetic studies using MSA. 125

Table 4-3. Chemical composition of the initial bulk mineral sample. 127

Table 4-4. Baseline experimental conditions. 128

Table 4-5. Correlation coefficients (R^2) for six kinetic experimental equations applied to the copper leaching of a bornite/chalcopyrite composite sample at variable temperature for the shrinking-core model. 133

Table 4-6. Activation parameters calculated for pure chalcopyrite, pure bornite and bornite/chalcopyrite dissolution as a function of temperature for Arrhenius and time-to-a-given-fraction methods. 141

Table 4-7. Powder-diffraction data for the copper-deficient intermediate phase formed by leaching after 30 min (-106+75 μm), and reference patterns of idaite, chalcopyrite and bornite. 143

Table 4-8. SEM-EDS chemical compositions of reacted residues of –106+75 μm bornite particles for 0.5 h, 1 h, 2 h, 4 h, 6 h and 8 h with a $FeCl_3$ (3 mol L^{-1}) and MSA (0.5 mol L^{-1}) solution at 90°C (stdv < 2). 147

Table 4-9. Normalised modal mineralogies (% area) for copper and iron and phases of the –106+75 μm sample before leaching and after 0.5 h leaching with $FeCl_3$ (3 mol L^{-1}) and MSA (0.5 mol L^{-1}). The quartz percentage was assumed to be constant and was used as a reference to determine changes in copper-containing minerals after leaching. 151

Table 5-1. Chemical compositions and formulae of phases identified after reaction in acidic solutions at 90°C..... 170

Table 6-1. Summary of systems and conditions used in the leaching tests..... 195

Table 6-2. Chemical and mineralogical composition of the initial bulk mineral sample by ICP-OES and QEMSCAN analyses..... 198

Table 6-3. Normalised modal composition of solid residues (in % mass) after stages 1 and 4..... 205

Table A-1. Summary of systems and conditions used in the leaching tests..... 229

Table C-1. Summary of pH after one and four days of reaction with different lixiviant systems for 110°C and 170°C showing the changes between initial and final pH.. 267

Table C-2. Summary of categorised physical, health and environmental hazards for different reagents used in experiments..... 267

Table C-3. Summary of initial reagent cost for different lixiviant systems used in experiments..... 268

Table C-4. Summary of comparative of changes in fracture-porosity areas calculated by ImageJ 1.x on cross-sections of solids after leaching with different reagents for 4 days at 110°C..... 269

List of Figures

Fig. 1-1. Idealised diagram of an ISR system for an intact material (modified from Sinclair and Thompson, 2015). Red and blue arrows represent the continuous flow between the ore and the wells, red arrows represent injected lixiviant solution and blue arrows pregnant solution recovered for processing. 29

Fig. 2-1 Schematic of experimental instruments used, **a.** 300 mL model 5521 Parr® titanium reactor: (1) gas injection line with internal and external gas release valves, (2) thermocouple, (3) autoclave cooling water outlet to drain, (4) magnetic drive overarm, (5) pressure gauge, (6) autoclave cooling water inlet, (7) fluid sampling line with needle valve, (8) impeller, (9) solid cuboid sample, (10) leach fluid, (11) heating jacket, (12) split ring closure with gauge block assembly, (13) 300 mL grade-3 titanium vessel, **b.** static stainless-steel batch reactor: (1) stainless-steel cap with setting spring, (2) stainless-steel reactor body, (3) internal Teflon liner, (4) leaching fluid, (5) solid cuboid sample. 52

Fig. 2-2. a. X-ray diffractogram of pre-leached sample, showing chalcopyrite as the predominant phase and pyrite as a minor phase, **b.** SEM images of cuboid samples before leaching showing initial sample surface texture, **c.** SEM-BSE image of cuboid samples before leaching with pyrite gangue distributed within the sample, and no rims or major fractures. 53

Fig. 2-3. TIMA-X integrated mineral analysis map of unreacted chalcopyrite cuboid showing major phases. 54

Fig. 2-4 Comparison of copper extraction from chalcopyrite for different leaching systems showing different dissolution patterns for selected solutions at higher temperatures, **a.** 110°C plots showing the best copper dissolution for the $K_2Cr_2O_7$+HCl solutions and the lowest dissolution for $Fe_2(SO_4)_3$+H_2SO_4, **b.** 170°C plots showing the best recovery for $FeCl_3$+HCl with the lowest dissolution occurring for H_2O_2+glycine. 55

Fig. 2-5 SEM-BSE surface images of cuboids after four days of reaction in different solutions at 110˚C, which lead to sulfur-layer formation, **a.** sulfur layer formed after reaction in $FeCl_3$+HCl solution showing globular sulfur adjacent to pyrite particles, b. sulfur layer formed after reaction in $Fe_2(SO_4)_3$+H_2SO_4 solution showing dense texture, **c.** chalcopyrite being replaced by sulfur after reaction in $CuCl_2$+HCl solution showing mesh texture adjacent to unreacted pyrite particles, **d.** chalcopyrite fissured surface after reaction in $Fe(MSA)_3$ solution, **e.** chalcopyrite replacement by globular sulfur as isolated surface zones after reaction with $NaNO_3$+H_2SO_4 solution, **f.** chalcopyrite transformation to sulfur in H_2O_2+H_2SO_4 acid solution, sulfur replaced chalcopyrite by what appear to be cleavage planes and exhibits a fractured surface texture. 57

Fig. 2-6 SEM elemental maps of chalcopyrite cuboid samples after leaching with different systems. The red areas represent a high copper concentration without iron in the product, green areas represent a high iron concentration and blue areas represent a high sulfur concentration. **a.** Reacted chalcopyrite leached with $CuSO_4$+H_2SO_4 at 110°C for 4 days showing a digenite rim, **b.** reacted chalcopyrite after three weeks of leaching with $CuSO_4$+H_2SO_4 at 170°C showing a digenite rim on the outer surfaces and along fractures, **c.** reacted chalcopyrite perimeter leached with $K_2Cr_2O_7$+HCl at 170°C for three weeks; three resultant layers include chromium(III) oxide (deep purple), hematite (lime green) and covellite (pink), **d.** chalcopyrite after reaction with $(NH_4)_2SO_4$+NH_4OH+$Na_2S_2O_8$ showing a bornite (pink) and loose layer of hematite (deep green) layer that occurs mainly in the internal fractures. 59

Fig. 2-7 X-ray diffraction pattern and SEM-BSE image for chalcopyrite after reaction, **a.** X-ray diffraction pattern of sample after 4 days in O_2+glycine solutions at 60°C, **b.** SEM-BSE solid phase of hematite formed at the surface showing gaps between chalcopyrite zones and near surface. 61

Fig. 2-8 X-ray diffraction pattern and SEM-BSE image for chalcopyrite after reaction, a. X-ray diffraction pattern of sample after 4 days in $K_2Cr_2O_7$+HCl solutions at 170°C, b. SEM-BSE solid phase of Cr_2O_3, hematite and covellite formed at the surface showing fracture filling with mixed precipitations and outer-perimeter rim. 62

Fig. 2-9 Pourbaix diagram showing Cr speciation as a function of pH and Eh at **a.** 25°C and **b.** 110°C **c.** 170°C. Diagrams were calculated by using Geochemists WorkBench© v10.0.05..... 62

Fig. 2-10 SEM-BSE images of chalcopyrite cuboid samples after leaching with different systems showing characteristic features of ICDR pseudomorphic replacements, **a.** chalcopyrite sample after reaction in $CuSO_4$+H_2SO_4 solutions after 4 days at 110°C, chalcopyrite-digenite sharp chemical interface with porous texture, **b.** chalcopyrite sample after reaction in O_2+glycine solution after 4 days at 60°C, chalcopyrite-hematite showing gaps between phases due to volume changes during the replacement, **c.** chalcopyrite sample after reaction in $(NH_4)_2SO_4$+NH_4OH+$Na_2S_2O_8$ solution after 4 days at 110°C, chalcopyrite-bornite and bornite-hematite interfaces. 66

Fig. 2-11 Optical microscopy images of post-leached samples, **a.** general view of chalcopyrite–pyrite sample partially replaced by sulfur after four days of reaction in $FeCl_3$+HCl solution at 110°C showing that pyrite is oxidised to sulfur, **b.** overview of chalcopyrite–pyrite sample that was replaced by sulfur after one day of leaching in $K_2Cr_2O_7$+HCl solutions at 110°C..... 67

Fig. 2-12 QEMSCAN and SEM images of chalcopyrite cuboids after leaching with $CuCl_2$+HCl at 170°C for 4 days **a**. QEMSCAN phase identification **b**. SEM-BSE image showing major cracks around chalcopyrite replaced by digenite..... 68

Fig. 2-13 Computed tomography images of cuboid sample pre- and post-leaching with $CuCl_2$+HCl solution at 110˚C for 4 days, **a. and b.** SEM-BSE images of unreacted and reacted sample showing a pitted perimeter and sulfur formation on the upper face of the cuboid, **c. and d.** 3D Reconstruction of external sample morphology before and after leaching showing major changes in the appearance of the solid and a decrease in volume, **e. and f.** 3D Images of top face showing sulfur morphology, pieces of undissolved pyrite and changes in cuboid perimeter. 70

Fig. 2-14 Optimal temperature and pH conditions for 11 fluid solutions tested. Showing the optimal working windows to obtain maximum copper recovery without thermal instability or major precipitations. Acid solutions show an optimal pH range between 0 and 3, and alkaline solutions between 8 and 12..... 74

Fig. 3-1. X-ray diffractogram of the initial sample, showing the presence of chalcopyrite, quartz and sphalerite..... 99

Fig. 3-2. Effect of experimental parameters on copper extraction from chalcopyrite: **a.** MSA concentration, **b.** ferric-ion concentration, **c.** particle size, **d.** temperature.... 102

Fig. 3-3. Plot of fitted temperature data by using the chemical-reaction-control model $1-(1-x)^{1/3}$ 105

Fig. 3-4. Activation parameter determination. **a.** Arrhenius plot for chalcopyrite dissolution using data from the experimental kinetic equation for a chemical-reaction-controlled model, **b.** Eyring plot for chalcopyrite leaching. 106

Fig. 3-5. Temperature data plotted as time-to-50% and -20% chalcopyrite leaching (x = 0.5 and x = 0.2) versus 1/T using the 'time-to-a-given-fraction' method for activation-energy determination..... 109

Fig. 3-6. X-ray diffractogram showing changes in peak intensity for six reaction times (0.5 h, 1 h, 2 h, 4 h, 6 h and 8 h) and for the –106+75-µm fraction at 90°C: **a**. Main chalcopyrite peak at 34.24° **b.** Main elemental sulfur peak at 26.87°. 110

Fig. 3-7. Scanning electron photomicrographs of –106+75 µm chalcopyrite after 8 h leaching under baseline conditions **a**. Magnified chalcopyrite particle that is encased almost entirely with a sulfur layer of 'cap head' globular masses with interconnected spaces. Pores in the sulfur allow for flow between the sample and the bulk reactant. **b.** Covered chalcopyrite particles with internal spaces in the sulfur that allow for flow between the sample and the bulk reactant..... 111

Fig. 4-1. X-ray diffractogram of the pre-leached sample (–38 µm), showing bornite as the predominant sulfide-containing mineral with chalcopyrite and sphalerite phases. 127

Fig. 4-2. Effect of experimental parameters on copper extraction for composite bornite/chalcopyrite sample: **a.** MSA concentration, **b.** ferric-ion concentration, **c.** particle size, **d.** temperature (different time scale for longer sampling times), maximum error as determined in replicate tests was 3% (excluded from the figure for clarity). 131

Fig. 4-3. Plots of fitted temperature data for bornite/chalcopyrite composite sample by diffusion through a product-layer-control model (spherical particles). Graphic shows the linear fit to plateau stage including the points of rapid dissolution between 0 and 2 h. 133

Fig. 4-4. Activation-parameter determination. **a.** Arrhenius plot for composite-sample dissolution using data from the experimental kinetic equation for diffusion through a product layer, **b.** Eyring plot. 135

Fig. 4-5 Arrhenius plot for theoretical pure bornite dissolution using data from the kinetic equation for diffusion through a product layer. 137

Fig. 4-6. Experimental temperature data for composite sample plotted as time-to-different percentages of copper recovery from experimental data (x = 0.1 to x = 0.7) versus $1/T$ using the time-to-a-given-fraction method for activation-energy determination (the slopes were taken from the linearised equations next to each line). 139

Fig. 4-7. Plots of copper leaching versus $1/T$ using the time-to-a-given-fraction method for activation-energy determination. **a.** theoretical pure bornite activation-energy behaviour showing the change in reaction requirement between 30% and 50% copper dissolution, **b.** pure chalcopyrite activation-energy behaviour showing a constant slope without major changes in the energy requirement. 140

Fig. 4-8. Final X-ray diffractogram after 8 h of leaching and showing the final reaction products. 144

Fig. 4-9. Scanning-electron photomicrographs of –106+75 μm bornite particles mounted on stubs for 0.5 h, 1 h, 2 h, 4 h, 6 h and 8 h of leaching with a $FeCl_3$ (3 mol L^{-1}) and MSA (0.5 mol L^{-1}) solution at 90°C (from a to f, respectively). 145

Fig. 4-10. Scanning electron photomicrographs of –106+75 μm chalcopyrite and bornite particles mounted on stubs after 8 h of reaction with a $FeCl_3$ (3 mol L^{-1}) and MSA (0.5 mol L^{-1}) solution. **a.** Chalcopyrite particle coated with porous globular elemental sulfur, **b.** bornite particle coated with sulfur layer without evident porosity. 146

Fig. 4-11. Scanning electron photomicrographs of –106+75 μm bornite-particle cross-sections for 0.5 h, 1 h, 2 h, 4 h, 6 h and 8 h of reaction with a $FeCl_3$ (3 mol L^{-1}) and MSA (0.5 mol L^{-1}) solution at 90°C (from a to f, respectively). 147

Fig. 4-12. Scanning-electron photomicrographs of –106+75 μm bornite mounted in epoxy and polished **a.** Initial sample before leaching, points 33 and 32 indicate chalcopyrite and points 34 and 35 correspond to the original bornite composition in the bulk sample. **b.** Bornite and chalcopyrite mixed particle after 6 h leaching with a $FeCl_3$ (3 mol L^{-1}) and MSA (0.5 mol L^{-1}) solution at 90°C. The chalcopyrite particle is surrounded by fragments of a copper mineral after the partial dissolution of bornite, and by elemental sulfur. Points 119 and 122 showed a copper-deficient composition, and points 120 and 121 showed a chalcopyrite composition (without changes from the unreacted composition). 149

Fig. 4-13. QEMSCAN particle map for –106+75 μm sample at 0.5 h leaching with a $FeCl_3$ (3 mol L^{-1}) and MSA (0.5 mol L^{-1}) solution at 90°C. **a.** Initial map of copper minerals before leaching, **b.** post-leaching map of copper minerals..... 150

Fig. 5-1. X-ray diffractogram of the pre-leached sample, showing bornite, chalcocite and quartz as the dominant phases. 167

Fig. 5-2. BSE and optical images of the polished surface of bornite and chalcocite in an unreacted cuboid. **a.** SEM-BSE image indicating compositional homogeneity of the starting chalcocite. **b.** Reflected light photomicrograph showing a similar starting material sulfide assemblage as in Fig. 2a. without evident variations in colour. **c.** SEM-BSE image indicating compositional homogeneity of the starting bornite, absence of reaction rims or compositional changes around fracture zones. **d.** Reflected light photomicrograph showing a similar starting material sulfide assemblage as in Fig. 2c. 168

Fig. 5-3. Copper and iron extraction vs. time for composite sample in different acid solutions using the same acid concentration (0.5 mol L^{-1}) at 90°C. **a.** Copper dissolved in solution (%) for reduced reaction times (75 h). **b.** Iron dissolved in solution (%) for reduced reaction times (75 h). **c.** Molar Cu/Fe ratio in solution for reduced reaction times (75 h). **d.** Copper dissolved in solution (%) for extended times (720 h). **e.** Iron dissolved in solution (%) for extended reaction times (720 h). **f.** Molar Cu/Fe ratio in solution for extended reaction times (720 h). 169

Fig. 5-4. Cu–Fe–S ternary diagram showing the observed changes in Cu-sulfide compositions. Additional phases: Dg_2: Fe-rich digenite from bornite replacement, 5*a*Dgss: 5a digenite solid solution (Grguric and Putnis, 1999), Id: idaite (Cu_3FeS_4) (Ugarte and Burkin, 1975), X-Bn_1: exsolved lamellae of Cu-rich bornite, X-Bn_2: exsolved lamellae of Cu-deficient bornite, X-Bn_3: bulk average composition of exsolution texture in bornite. 170

Fig. 5-5. Reflected light photomicrographs showing the transformation of chalcocite to digenite and covellite at 90°C. **a.** Chalcocite reacted in MSA after 8 days. Laminar texture reflects the presence of digenite accompanied by a minor variation in the Cu concentration. Copper-enriched zones were found as rims in bornite adjacent to chalcocite and along fractures in the bornite. **b.** Chalcocite reacted in MSA after 1 month. The original chalcocite was replaced by digenite, which in turn, was replaced

by covellite. **c.** Partial chalcocite replacement by digenite in HCl after 8 days, showing strong laminar texture with copper-enriched digenite zones, covellite nucleation along fractures, and digenite rims along chalcocite-bornite grain boundaries. **d.** Covellite formation after one-month reaction in HCl showing abundant porosity and shrinkage features. 172

Fig. 5-6. Reflected light photomicrograph and BSE images of polished bornite sections after one month of reaction in MSA solutions at 90°C. **a.** Bornite sample after reaction. Internal cracks show continuous rims of digenite with additional covellite forming in the centre of the fractures. **b. and c.** SEM-BSE images showing details of sharp replacement fronts between dark-grey bornite and light-grey digenite without detectable phase-internal compositional and textural changes towards the interface. At this stage of reaction, bornite remains homogeneous and does not show exsolution textures. 174

Fig. 5-7. STEM-HAADF image of the bornite–digenite replacement interface and a STEM-EDS concentration profile across the interface. The replacement interface between bornite (dark grey) and digenite zones (light grey) coincides with a sharp concentration change in Fe and Cu. The arrow in the STEM-HAADF image depicts the trace of the EDS line scan. 175

Fig. 5-8. QEMSCAN images of a bornite sample after 8 days of reaction in HCl solutions at 90°C. **a.** Reacted sample showing digenite rim formation surrounding fractures with covellite points spread on top, bornite zones show transformation into Cu-deficient bornite exsolution. **b.** Magnification of reacted solid sample showing zones of exsolution indexed as ‘Cu-deficient bornite’ showing patches of original bornite. 176

Fig. 5-9. SEM image and element distribution map of the bornite exsolution texture and digenite rim after reaction in HCl at 90°C for two weeks. **a.** BSE of the exsolution texture. **b.** EDS Cu concentration map showing lamellae of Cu-deficient bornite and the Cu-enriched digenite rim. 177

Fig. 5-10. SEM-BSE image of bornite after reaction in HCl at 90°C for two weeks showing an exsolution texture in the centre of the cuboid. SEM-EDS indicates that the dark lamellae have lower Cu concentrations, whereas the dark-grey matrix is depleted in Fe relative to unreacted bornite. 177

Fig. 5-11. QEMSCAN images of bornite samples after one-month reaction in acid solutions at 90°C. **a.** Solid sample reacted in MSA solution showing a thin sharp rim of digenite along bornite-quartz grain boundaries. Bornite zones do not show compositional changes and covellite nucleated on fracture joints. **b.** Bornite sample reacted in HCl solutions showing substantial replacement by covellite, which coincides with grain boundaries and fractures. Bornite shows compositional variations due to the presence of Cu-deficient bornite exsolution lamellae. 178

Fig. 5-12. Reaction textures of bornite after reaction in HCl solutions at 90°C. **a.** Reflected light photomicrograph showing covellite formation after reaction in HCl for two weeks. Covellite formation proceeded by replacement of digenite that formed initially from the original bornite along fractures. **b.** Reflected light photomicrograph showing covellite formation after reaction in HCl for one month, indicating continued covellite formation with experiment duration. **c.** Photomicrograph showing details of covellite formation in the area outlined in Fig. 12a. **d.** Photomicrograph showing details of covellite formation in the area outlined in Fig. 12b. **e**. Close-up SEM BSE image of the bornite exsolution texture after two weeks of reaction. The digenite rim shows fractures aligned with the orientation of the Cu-deficient exsolution lamellae. **f.** Close-up SEM BSE image of the bornite exsolution texture after one month of reaction, showing covellite replacing bornite containing the exsolution texture. 179

Fig. 5-13. Reflected light photomicrographs showing the comparison between unreacted solids and samples reacted for 2 weeks in HCl/MSA solutions at 90°C. **a.** Unreacted chalcocite zones without compositional changes. **b.** Chalcocite transformation after reaction in MSA solutions showing laminar texture of digenite replacement of chalcocite. **c.** Unreacted bornite zones showing uniform composition without obvious textural transformation. **d.** Exsolution texture showing copper

deficient lamellae and covellite nucleation on fracture zones after reaction in HCl solutions 182

Fig. 6-1. Schematic of multistage fluid–rock interaction in an ISR scenario. 197

Fig. 6-2. X-ray diffractogram of the unreacted sample (P_{80} 68 µm), showing predominant phases of silicates and carbonates. 199

Fig. 6-3. SEM-EDS element distribution maps of the unreacted sample. **a.** unreacted solid, **b.** silica, **c.** copper**, d.** iron, **e.** sodium, **f.** calcium, **g.** magnesium, **h.** potassium, **i.** sulfur. 200

Fig. 6-4. a. Redox potential and **b.** pH change after five contact stages with fresh solid. 201

Fig. 6-5. a. Copper and **b**. iron extraction during the five experimental stages (72 h each stage) (no iron dissolution occurred after stage 2). 202

Fig. 6-6. Metal extraction at stages 2, 4 and 5, **a.** calcium, **b.** aluminium, **c.** magnesium, **d.** sodium, **e.** potassium, **f.** sulfur 203

Fig.6-7. Eh–pH diagrams for **a, b.** copper, **c, d.** iron and **e, f.** calcium stability prepared by using the $Fe_2(SO_4)_3/H_2SO_4$ solution concentrations after stages 2 (left) and 4 (right) at 90°C and at atmospheric pressure. 204

Fig. 6-8. Comparison of change in precipitate mass percentage (% mass) relative to the initial sample for gypsum, jarosite and akageneite **a.** sulfate solutions, **b.** chloride solutions 206

Fig. 6-9. X-ray diffractograms of **a.** unleached sample (P_{80} 68 µm) compared with **b.** stage 3 and **c.** stage 5 residues for $FeCl_3$/HCl solution. Akaganeite peaks appear after stage 3. 207

Fig. 6-10. SEM-BSE of precipitates in different solutions, **a.** spindle-shaped akaganeite particles attached to albite particles, **b.** K-jarosite particles, **c.** Na-jarosite crystals, **d.** gypsum needles. 209

Fig. 6-11. SEM-BSE photomicrographs of the solid residue after leaching in $Fe_2(SO_4)_3$/MSA /NaCl solution. a. agglomerated particles surrounded by gypsum, b. magnification of a particle showing a layer composed of intergrown Na- and K-jarosite 210

Fig. 6-12. X-ray diffractograms of **a.** unleached sample (P_{80} 68 µm) compared with **b.** stage 3 and **c.** stage 5 for $Fe_2(SO_4)_3$/MSA /NaCl. Jarosite and gypsum appear after stage 3. 210

Fig. 6-13. Scanning-electron elemental maps of sample after stage 5 in $Fe_2(SO_4)_3$/MSA /NaCl showing partial elemental distribution, **a.** Initial sample, **b.** silica, **c.** sulfur**, d.** iron, **e.** sodium, **f.** calcium Note that the copper content in the residues was too low for visualisation. 211

Fig. 6-14. Comparison of P_{80}, surface area (by BET) and rugosity (ratio of BET to SSA) for the unreacted sample and the residues after five stages. 212

Fig. A-1. SEM elemental maps showing copper, iron and sulfur distributions in initial cube samples before leaching. **a.** No cracks existed at the peripheries of the sample, **b.** pyrite gangue distributed in the sample. 230

Fig. A-2. Final comparative Cu extractions from chalcopyrite (~64 mm^3 cube samples) at 170°C after three weeks of leaching. 231

Fig. A-3. SEM elemental maps of chalcopyrite cube samples after leaching with different systems at 170°C for three weeks. The red areas represent a high copper concentration without iron in the product, green areas represent a high iron concentration and blue areas represent a high sulfur concentration. **a.** Cube leached with ferric sulfate and sulfuric acid showing sulfur precipitation in cavities;

chalcopyrite that surrounded the sulfur areas had a higher sulfur content than the initial sample, **b.** cube after three weeks' leaching with cupric sulfate and sulfuric acid showing a digenite rim on the outer surfaces and along fractures, **c.** perimeter of a coarse cubic sample leached with potassium dichromate and hydrochloric acid; the three resultant layers include chromium (III) oxide (deep purple), hematite (deep green) and covellite (red), **d.** cube after reaction with glycine and hydrogen peroxide showing a bornite (orange) and goethite (deep green) layer that enters the internal fractures. 232

Fig. A-4. SEM image of cube sample after leaching with higher concentration of cupric chloride and hydrochloric acid at 170°C after 5 days, showing mostly elemental sulfur and a small piece of digenite attached to the external part of the residue. 233

Fig. A-5. SEM images of cube samples after leaching with glycine and hydrogen peroxide after three weeks; lighter greys represent the bornite reaction rim around fractures and the iron-oxide product inside cracks. 235

Fig. B-1. Scanning electron photomicrographs (SEM-BSE) of initial coarse sample, **a.** initial surface texture without major cracks or layers that coat the sample, **b.** elemental maps showing copper, iron and sulfur distributions, yellow is the resulting bornite phase and red is the secondary sulfide digenite. 248

Fig. B-2. Scanning electron photomicrographs (SEM-BSE) of the sample surface after 0.1 M hydrochloric acid pre-treatment, **a.** surface texture after 7 days of treatment, **b.** surface texture after 20 days showing major cracks. 250

Fig. B-3. Scanning electron photomicrographs (SEM) composition map of the sample cross-section after 20 days of pre-treatment with 0.1 mol L^{-1} hydrochloric acid. Red zones represent covellite replacement, yellow zone copper-deficient bornite and blue zones sulfur formation..... 250

Fig. B-4. Replicates of comparative copper extractions for 1 mol L^{-1} ferric methanesulfonate leaching at 110°C of samples after pre-treatment versus untreated

samples. **a.** Untreated sample compared with samples that had been pre-leached for 7 days, **b.** averages for the untreated and treated sample replicates up to 24 h; the extraction after 48 h (single sample) is given to indicate that leaching has plateaued. 252

Fig. B-5. SEM cross-section elemental maps of bornite coarse samples after leaching with 1 mol L^{-1} ferric methanesulfonate solution at 110°C for two days. The red areas represent copper without iron in the product, yellow areas represent copper and iron and blue areas represent sulfur. **a.** untreated sample after 1 day of leaching showing fracturing and sulfur inclusions in fractures, no zones of copper enrichment, **b.** untreated sample after 2 days of leaching showing major replacement of bornite ($Cu_{5-x}FeS_4$) by sulfur with some isolated zones of covellite, **c.** sample pre-treated for 7 days after 1 day of leaching showing a thick sulfur rim with small areas of copper enrichment (covellite) next to copper-deficient bornite, **d.** sample pre-treated for 7 days after 2 days of leaching showing main phase of sulfur with pieces of bornite ($Cu_{5-x}FeS_4$) and covellite, some pieces of bornite showed a rim of covellite. 254

Fig. B-6. SEM cross-section elemental maps of 20 days acid pre-treated bornite coarse samples after leaching with 1 mol L^{-1} ferric methanesulfonate solution at 110°C for one day. Iron concentrations remained homogenous in the resulting solid residue, with sulfur filling the cracks between bornite pieces and covering the perimeter of the sample. Copper concentration occurred as covellite encased by sulfur at the outer rim. 255

Fig. B-7. Schematic of pre-treatment outcomes compared to untreated samples.... 256

Fig. C-1. TIMA maps images of chalcopyrite samples after reaction in different lixiviant systems at 110°C for 4 days. **a.** solid after leaching in $FeCl_3$ + HCl. **b.** solid after leaching in $CuCl_2$ + HCl. **c.** solid after leaching in $Fe_2(SO_4)_3$ + H_2SO_4. **d.** solid after leaching in $CuSO_4$+ H_2SO_4. **e.** solid after leaching in O_2 + Glycine. **f.** solid after leaching in $C_3H_9FeO_9S_3$. **g.** solid after leaching in $NaNO_3$+ H_2SO_4. **h.** solid after leaching in H_2O_2+ H_2SO_4. **i.** solid after leaching in $(NH_4)_2SO_4$ + NH_4OH + $Na_2S_2O_8$. 265

Fig. C-2. TIMA high resolution maps images of chalcopyrite samples after reaction in different lixiviant systems at 110°C for 4 days. **a.** solid after leaching in $FeCl_3$ + HCl showing the lack of enrichment phases next to fracture leached zones. **b.** solid after leaching in $CuSO_4$+ H_2SO_4 showing digenite rim. **c.** solid after leaching in $(NH_4)_2SO_4$ + NH_4OH + $Na_2S_2O_8$ showing zones of bornite and hematite. **d.** solid after leaching in O_2 + Glycine showing hematite in rim and fracture zones. 266

Fig. C-3. X-ray diffractogram of samples after leaching with selected lixiviant systems showing product phases after leaching. **a.** X-ray pattern after leaching in after 8 days at 170°C $CuSO_4$+ H_2SO_4 solution showing the presence of digenite and chalcopyrite. **b.** X-ray pattern after leaching in after 4 days at 110°C solution $(NH_4)_2SO_4$ + NH_4OH + $Na_2S_2O_8$ solution showing the presence of hematite, chalcopyrite and bornite. .. 267

Fig. D-1. X-ray diffractogram of the bornite-chalcocite sample after reaction with HCl solutions for one month at 90°C, the major phase found was covellite with minor peaks of magnetite, tennantite and bornite. 270

Fig. D-2. a. Point X-ray diffractogram (acquisition time 48 h) of the bornite-chalcocite sample after reaction with HCl solutions for one month at 90°C focused in exsolution texture. Only one peak from chalcopyrite was found. **b.** Point X-ray diffractogram (acquisition time 48 h) from 33 (2θ) to 45 (2θ) of the bornite-chalcocite sample after reaction with HCl solutions for one month at 90°C focused in exsolution texture. Showing the chalcopyrite peak found. 271

Fig. D-3. EBSD maps images of the bornite exsolution texture after reaction in HCl at 90°C for one month. **a.** Band contrast of the exsolution texture **b.** EDS Cu concentration map showing the lamellae of Cu-deficient bornite. **c.** Phase map showing the distribution of orthorhombic (blue) and cubic (fuchsia) bornite. **d.** Inverse pole figure (IPF) map showing the relative orientation of orthorhombic and cubic bornite (the orientation key is attached to the image). 271

Nomenclature

A	pre-exponential factor
b	stoichiometric coefficient
bd_{ss}	bornite-digenite solid solution
C_a	concentration in main solution
CO	oxidant concentration
D_e	effective diffusion coefficient of reactant in product layer
E_a	activation energy
FA	free acidity
ΔG^{++}	Gibbs energy of activation
h	Planck's constant ($h = 6.626 \times 10^{-34}$ J s)
ΔH^{++}	enthalpy of activation
ICDR	Interface-coupled dissolution–reprecipitation
k_B	Boltzmann's constant ($k_B = 1.381 \times 10^{-23}$ J K^{-1})
k_c	apparent reaction rate constant
r	radius of unreacted particle at time t
r_0	initial particle radius
PS	particle size
R	ideal gas constant
ΔS^{++}	entropy of activation
t	time
t_x	time to transform a given fraction
T	recorded temperature
τ	time to completely consume the particle
x	fraction reacted
ρ	density
P	pressure

Chapter 1. Introduction

1.1. In-situ recovery of copper sulfides

In-situ recovery (ISR) is a mining technology that refers to the extraction of valuable metals from within an orebody without the removal of physical rock (Bates, 1987). ISR is not a new technology; this technique has existed for more than 65 years, but has increased in popularity during the last 15 years (Seredkin et al., 2016). This increase in acceptance is related to an increase in demand for metals and more stringent environmental regulations paired with a depletion of deposit grades, and technical limitations for low-grade-ore extraction. ISR provides an opportunity for copper recovery from low-grade copper-bearing sulfides that could otherwise produce large volumes of waste rock by using conventional hydro- or pyrometallurgical processes (Williamson, 1998). The ISR methodology includes the injection of a lixiviant solution via injection wells, which, when in contact with ore, induces chemical reactions that result in mineral dissolution and valuable metal recovery into the pregnant solutions. The resultant solution moves to a recovery well and is pumped back to the surface for further processing. Figure 1-1 shows an idealised diagram of an ISR system in an unmined area.

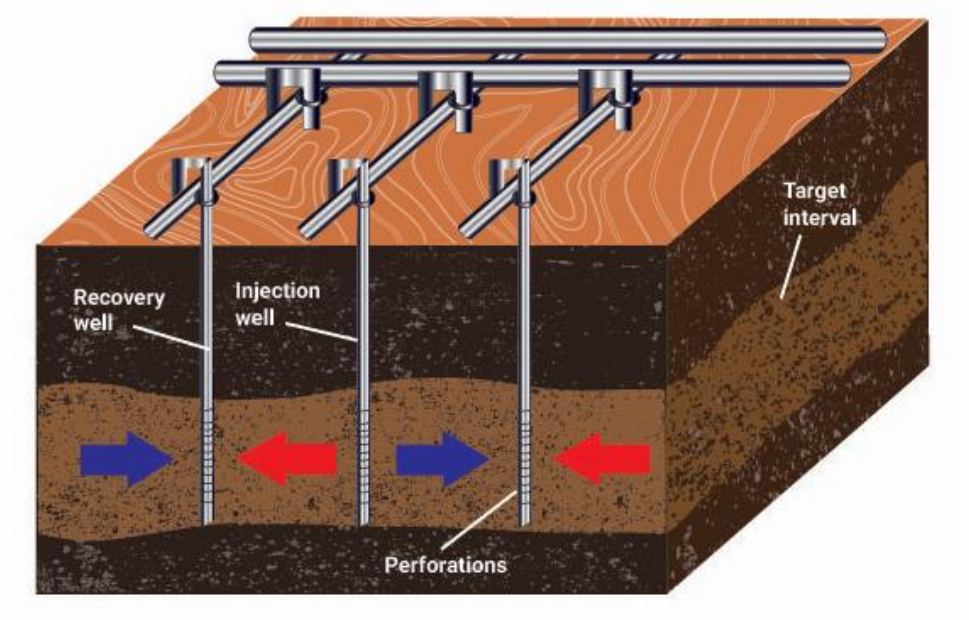

Fig. 1-1. Idealised diagram of an ISR system for an intact material (modified from Sinclair and Thompson, 2015). Red and blue arrows represent continuous flow between

the ore and the wells, red arrows represent injected lixiviant solution and blue arrows pregnant solution recovered for processing.

ISR is applied in uranium mining operations globally (e.g., USA, Kazakhstan) and accounts for more than 50% of global production. Copper deposits may also be promising candidates for ISR, especially for oxidised zones where sulfuric acid is the preferred lixiviant. Copper ISR has been applied to oxide zones in the USA and Russia (San Manuel, Silver Belt, Miami, Florence and Gumeshevskoye) (Seredkin and Savenya, 2019). In Australia, prior ISR operations have been relatively unsuccessful, such as at the Mutooroo deposit in South Australia in 1983 (Haque *et al*., 2014).

ISR presents several advantages compared with conventional mining techniques, including a low initial capital requirement and low development costs (Seredkin et al., 2016), a lower surface disturbance, accessibility to deep ore bodies, less dust and noise contamination and the option to process low-grade ores that would otherwise be considered uneconomical. Challenges in ISR copper operations include the prevention of groundwater contamination, ore accessibility enhancement and an understanding of the required lixiviant solutions (Djordjevic, 2016).

To be a suitable candidate for ISR exploitation, copper mineralisation should fulfil certain physico-chemical requirements. Copper mineralisation occurs in primary magmatic ores, secondary enrichment zones, and veins in igneous rocks and sediments (Habashi, 1978). Based on their source and characteristics, copper deposits can be classified as sediment-hosted or porphyry copper deposits (Williamson, 1998). Most copper minerals are present as copper sulfides (chalcopyrite, bornite, chalcocite and covellite) (Bulatovic, 2007) with primary copper-sulfide minerals (hypogene) being separated from the altered oxide zone (supergene) by a partially oxidised zone that is enriched in secondary copper-sulfide minerals. Hard-rock copper minerals, such as chalcopyrite, represent more than 70% of global copper (Li et al., 2013).

Refractory copper-sulfide (chalcopyrite, bornite, chalcocite, covellite) deposits may be candidates for ISR processing; such mineralisations may be low-grade (which makes them uneconomical to process by conventional means) and usually exist at medium depths (0.5 km) to depths that exceeded 2 km (Wallace, 1979), which implies that they are located deeper than ideal open pit and underground targets may be. The

implementation of copper ISR has been applied mainly to porous ores, and no low-accessibility hard-rock copper-sulfide ores have been processed by ISR. These mineral types are more difficult to leach than oxide ores, and an understanding of the rock changes that result from fluid interaction is a key point to unlock their successful exploitation. Unlike oxide minerals that are soluble in acid or alkaline lixiviants, in the hydrometallurgical processing of copper-sulfide minerals, an oxidant is necessary for sulfide oxidation to release copper into solution (Schlesinger *et al*., 2011). Furthermore, primary-sulfide dissolution from primary copper sulfides can show slow leach kinetics (see Table 1-1).

Table 1-1. Comparative dissolution rates in laboratory-scale tests using acidic sulfide systems for different copper-bearing minerals in heaps and dumps of low-grade ores (modified from Watling, 2013).

Time required	Type	Mineral	Ideal formula
Hours to days	Oxide Zone	Atacamite	$Cu_2Cl(OH)_3$
		Chrysocolla	$CuSiO_3.2H_2O$
		Neotocite	$(Cu,Mn)_2H_2Si_2O_5(OH)\ nH_2O$
		Tenorite	CuO
		Malachite	$Cu_2(CO_3)(OH)_2$
		Azurite	$Cu_3(CO_3)_2(OH)_2$
		Antlerite	$CuSO_4.2Cu(OH)_2$
		Brochantite	$CuSO_4.3Cu(OH)_2$
Days to months	Enrichment zone	Native copper	Cu
		Cuprite	Cu_2O
		Chalcocite	Cu_2S
		Covellite	CuS
		Bornite	Cu_5FeS_4
Months to years	Primary mineralisation	Enargite	Cu_3AsS_4
		Chalcopyrite	$CuFeS_2$

1.1.1. Gaps in current knowledge

1.1.1.1. Mineral dissolution and fluid stability

An understanding of lixiviant/oxidant responses beyond the commonly studied temperature (and pressure) regimes may be required for execution of ISR. Uncontrollable changes in temperature and solution concentrations in an ISR environment may affect the solution pH and Eh, which could yield undesirable reactions and result in precipitate formation. Therefore, an evaluation of the efficiency of lixiviant systems should be conducted under conditions that replicate the ISR environment.

As chalcopyrite is the most abundant copper sulfide, its successful hydrometallurgical processing would be advantageous. Chalcopyrite leaching studies have attracted significant interest over the years. The most common oxidant that has been investigated extensively because of its cost and availability is ferric sulfate paired with sulfuric acid. When iron(III) is used as an oxidant, ideally, the complete oxidation of sulfide to sulfate and copper and iron release into solution by chalcopyrite dissolution should result (Equation 1).

$$CuFeS_2 + 4Fe^{3+} + 3O_2 + 2H_2O \rightarrow Cu^{2+} + 5Fe^{2+} + 2H_2SO_4 \quad (1)$$

A variety of other oxidants, acids and bases have been tested in hydrometallurgical processing. Oxidants include Cu^{2+}, O_2, $Cr_2O_7^{2-}$, NO_3^-, H_2O_2 and O_3 in sulfuric acid, hydrochloric acid, hydrofluoric acid, nitric acid, ammonium hydroxide and glycine (Antonijević et al., 1994; Aydogan et al., 2006; Beckstead and Miller, 1977; Córdoba et al., 2008; Dutrizac and Macdonald, 1978; Dutrizac et al., 1970; Oraby and Eksteen, 2014; Ruiz et al., 2011; Shiers et al., 2016; Sokić et al., 2009; Velásquez-Yévenes et al., 2010). Solutions have been tested under different conditions to evaluate their ability to extract copper from ores or concentrates. Test temperatures have been studied from room temperature to 90°C, with only a few studies exceeding 100°C (McDonald and Muir, 2007). ISR processing may be conducted at elevated temperatures (> 90°C) with restricted oxygen availability. To the author's knowledge limited research exists on the behaviour of these fluids and their impact on mineral dissolution and fluid stability under simulated ISR conditions.

1.1.1.2. Reaction kinetics and mechanisms

Natural deposits are heterogeneous, and in an ISR operation, the targeting of value minerals only is difficult. Composite natural ores contain gangue and different copper minerals, which makes it difficult to extrapolate fundamental kinetic and mineralogical studies that are available in the literature. Possible interactions between phases in targeted minerals may affect energy requirements for dissolution and enhance precipitation rates as a result of re-equilibration. The kinetic analysis of copper-sulfide dissolution has been studied for pure concentrate samples (Ahn et al., 2018; Dreisinger and Abed, 2002; Dutrizac, 1981; Hirato et al., 1987). Because beneficiation is not

possible in an ISR environment, an understanding of the kinetics of dissolution of natural gangue-containing samples is necessary.

1.1.1.3. Compositional and morphological transformations

Compared with tank, vat and heap leaching operations, ISR operation is challenging in terms of the control of leaching conditions. ISR requires a continuous flow of lixiviant along flow paths. The continuous interaction of the fluid and the rock produces physical and chemical changes (Williamson, 1998). The enhancement or reduction of permeability and porosity from sulfide dissolution or precipitation, respectively, has not been studied extensively, and to the author's knowledge, only Yang et al. (2019) described an increase in porosity in a low-grade chalcopyrite after leaching with ferric chloride solutions at 80°C. Porosity and permeability at the microscale can be compromised by the formation of surface layers that reduce the dissolution rate and, in the worst scenario, cause the dissolution to cease. This phenomenon has been described as "passivation". It has also been suggested that sulfur formation is responsible for the reduction in copper dissolution (Córdoba et al., 2009; Dutrizac, 1990). Therefore, an analysis of the reacted solid is important to understand the reaction-driven solid change and to avoid the potential for pathway clogging or "short-circuiting".

1.1.1.4. Low-grade ore dissolution and the effect of gangue minerals

Low-grade ores include higher amounts of gangue minerals, which increases the possibility of side reactions, precipitation, acid consumption and an accumulation of cations and anions in solution (Sinclair and Thompson, 2015). Permeability may be affected as a result of gangue dissolution. The dissolution response of low-grade minerals under ISR conditions is not available in the literature.

1.2. Research objectives

The aim of this research is to fill existing knowledge gaps by analysing and understanding the fluid–rock interaction of copper-sulfide minerals with a variety of

lixiviant/oxidant systems under expected ISR conditions. The specific objectives include:

- To identify the extent and rates of mineral dissolution for common and non-standard lixiviant/oxidant solutions under ISR conditions, including an understanding of the dissolved species solubility and solution stability and its impact on copper recovery rates.
- To understand the interaction between the fluid and the rock (dissolution/precipitation behaviour) with a focus on the reaction mechanisms and kinetic behaviour for pure and composite ores.
- To understand the fluid-mediated compositional and morphological transformations of coarse pieces of copper sulfides by interaction with different solutions (with and without oxidant), including secondary mineral formation and reaction products (iron precipitates, compact crystalline or non-crystalline sulfur layers, silica gel formation or hydroxide precipitation) at elevated temperatures (90°C to 170°C).
- To identify the effect of gangue-related reactions on the rock morphology (precipitation) and its influence on solution access.

1.3. Significance

In-situ recovery offers a step-change approach to the extraction of sub-surface values, when executed efficiently and effectively. The application depends on an appropriate knowledge of the target mineral system and the interaction of the said mineral system with the selected lixiviant system. The findings of this work present new information to contribute to the design of optimal extraction/recovery approaches in future ISR projects, which may include the lixiviant/oxidant selection, well spacing and initial reagent concentrations.

1.4. Thesis outline and publications

This PhD thesis comprises seven chapters. **Chapter 1** includes a general background on ISR and copper leaching from sulfide minerals, the research objectives and the significance of the work. **Chapters 2** to **6** have been prepared as individual published, submitted or draft research papers. Additional information

- **Chapter 2** compares 11 lixiviant/oxidant solutions under similar conditions. Experiments were performed on coarse pieces of chalcopyrite at elevated temperatures and pressures. The copper-leaching behaviour with the different lixiviant systems has been described, and includes the product phases, fluid stability and copper-dissolution rate. As additional information a conference paper is presented in Appendix A with supplementary data for high temperature experiments.

- **Chapters 3** and **4** focus on understanding the kinetics of chalcopyrite and composite chalcopyrite/bornite sample leaching with an acidified ferric-chloride solution. In order to understand how the complexity of the samples affects the kinetical analysis and identify the best manner to approach composite samples (characteristic of ISR targets).

- **Chapters 5** and **6** focus on the effect on solids under ISR operations, including deviations from ideal conditions (such as oxidant and acid depletion) and the presence of gangue. In Chapter 5, the leaching behaviour of natural copper-sulfide samples (bornite/chalcocite) is studied in acidic solutions in the absence of oxidant; rock transformation to copper-enriched phases occurred and possible explanations of the transformation mechanism are presented. As supplementary data about the reactivity of product layers resulting from mineral replacements is presented in Appendix B. In Chapter 6, a simulation of depleted acid conditions (as may occur in a real ISR scenario when fluid travels from the injection to recovery wells) was presented.

- **Chapter 7** contains a summary of the research contributions from this thesis and recommendations for ISR implementation.

The manuscripts from this work are as follows:

- Hidalgo, T., McDonald, R., Kuhar, L., Beinlich, A. and Putnis, A., 2020. Comparative analysis of copper dissolution and mineral transformations in coarse chalcopyrite for different lixiviant/oxidant systems elevated temperature (110˚C to 170˚C). **(Chapter 2)** *Manuscript under revision.*

- Hidalgo, T., Kuhar, L., Beinlich, A. and Putnis, A., 2018. Kinetic study of chalcopyrite dissolution with iron(III) chloride in methanesulfonic acid. Minerals Engineering, 125: 66-74. https://doi.org/10.1016/j.mineng.2018.05.025. **(Chapter 3)**

- Hidalgo, T., Kuhar, L., Beinlich, A. and Putnis, A., 2019. Kinetics and mineralogical analysis of copper dissolution from a bornite/chalcopyrite composite sample in ferric-chloride and methanesulfonic-acid solutions. Hydrometallurgy, 188: 140-156. https://doi.org/10.1016/j.hydromet.2019.06.009. **(Chapter 4)**

- Hidalgo, T., Verrall, M., Beinlich, A., Kuhar, L., and Putnis, A., 2020. Replacement reactions of copper sulphides at moderate temperature in acidic solutions. Ore Geology Reviews, 123, 103569, 1–13. https://doi.org/10.1016/j.oregeorev.2020.103569 **(Chapter 5)** *(modified version).*

- Hidalgo, T., Kuhar, L., Beinlich, A., and Putnis, A., 2020. Effect of multistage solution–mineral contact in in-situ recovery for low-grade natural copper samples: Extraction, acid consumption, gangue-mineral changes and precipitation. Minerals Engineering 159:106616. https://doi.org/10.1016/j.mineng.2020.106616 **(Chapter 6)** *(modified version).*

Conference papers resulting from this work are attached as Appendices to this thesis:

- Hidalgo, T., McDonald, R., Kuhar, L., Beinlich, A. and Putnis, A., 2018. Comparative analysis of lixiviant/oxidant systems for chalcopyrite leaching from coarse samples at elevated temperature, ALTA Nickel-Cobalt-Copper Symposium 2018, ALTA, Perth, Western Australia.

- Hidalgo, T., McDonald, R., Kuhar, L., Beinlich, A. and Putnis, A., 2019. Staged leaching of bornite with acidic solutions at moderate temperature in an in-situ recovery environment, ALTA In Situ Recovery (ISR) Symposium 2019, ALTA, Perth, Western Australia.

Support information for tables in chapter 2 and supplementary data for chapter 5 are presented in Appendices C and D.

Other two papers have been published as a co-author presenting results of this work:

- McDonald, R., Shiers, D., Collinson, D., Hidalgo, T., Kuhar, L. 2019. The impacts of chloride upon the leaching of chalcopyrite, ALTA NCC Symposium 2019, Perth, Western Australia.

- Kuhar, L., Godel, B., Hidalgo, T., Evans, A., Verrall, M., Beinlich, A., Rogers, K., 2020. High-resolution X-ray computed tomography study of coarse leached particles for in-situ recovery applications. ALTA ISR Symposium 2020, Perth, Western Australia.

References

Ahn, J., Barton, I.F., Shin, D. and Lee, J., 2018. The study of copper leaching from conichalcite and chalcopyrite using alternative lixiviants ,Materials processing fundamentals 2018, Materials processing fundamentals 2018, Phoenix, Arizona, pp. 171–180.

Antonijević, M.M., Janković, Z. and Dimitrijević, M., 1994. Investigation of the kinetics of chalcopyrite oxidation by potassium dichromate. Hydrometallurgy, 35(2): 187–201.

Aydogan, S., Ucar, G. and Canbazoglu, M., 2006. Dissolution kinetics of chalcopyrite in acidic potassium dichromate solution. Hydrometallurgy, 81(1): 45–51.

Bates, R.L., Jackson, Julia A., 1987. Glossary of geology. R. Bates and A. Jackson, editors. Alexandria, Va./: American Geological Institute.

Beckstead, L.W. and Miller, J.D., 1977. Ammonia, oxidation leaching of chalcopyrite -reaction kinetics. Metallurgical Transactions B, 8(1): 19–29.

Bulatovic, S.M., 2007. Handbook of flotation reagents - chemistry, Theory and practice, Volume 1 - Flotation of sulfide ores. Elsevier, pp. 235–239.

Córdoba, E.M., Muñoz, J.A., Blázquez, M.L., González, F. and Ballester, A., 2008. Leaching of chalcopyrite with ferric ion. Part I: General aspects. Hydrometallurgy, 93(3): 81–87.

Córdoba, E.M., Muñoz, J.A., Blázquez, M.L., González, F. and Ballester, A., 2009. Passivation of chalcopyrite during its chemical leaching with ferric ion at 68 °C. Minerals Engineering, 22(3): 229–235.

Dreisinger, D. and Abed, N., 2002. A fundamental study of the reductive leaching of chalcopyrite using metallic iron part I: kinetic analysis. Hydrometallurgy, 66(1): 37–57.

Djordjevic, N., 2016. In-situ recovery of metals - SMI next mine, The University of Queensland, [Power point slides]. Retrieved from; https://es.slideshare.net/NenadDjordjevic6/in-situ-recovery-smi-seminarfinal1.

Dutrizac, J., 1990. Elemental sulfur formation during the ferric-chloride leaching of chalcopyrite. Hydrometallurgy, 23(2-3): 153–176.

Dutrizac, J.E., Macdonald, R.J.C. and Ingraham, T.R., 1970. The kinetics of dissolution of bornite in acidified ferric sulfate solutions. Metallurgical Transactions, 1(1): 225–231.

Dutrizac, J.E. and Macdonald, R.J.C., 1978. The dissolution of sphalerite in ferric chloride solutions. Metallurgical Transactions B, 9(4): 543–551.

Dutrizac, J.E., 1981. The dissolution of chalcopyrite in ferric sulfate and ferric chloride media. Metallurgical Transactions B, 12(2): 371–378.

Habashi, F., 1978. Chalcopyrite: Its chemistry and metallurgy 1. McGraw-Hill, Quebec, Canada.

Haque, N., Norgate, Terry, 2014. The greenhouse gas footprint of in-situ leaching of uranium, gold and copper in Australia. Journal of Cleaner Production, 84: 382–390.

Hirato, T., Majima, H. and Awakura, Y., 1987. The leaching of chalcopyrite with ferric sulfate. Metallurgical transactions B, 18(3): 489–496.

Hitzman, S.D., Bull S., 2010. Formation of Sedimentary Rock-Hosted Stratiform Copper Deposits through Earth History. Economic Geology, 105: 627–639.

Li, Y., Kawashima, N., Li, J., Chandra, A.P. and Gerson, A.R., 2013. A review of the structure, and fundamental mechanisms and kinetics of the leaching of chalcopyrite. Advances in Colloid and Interface Science, 197–198: 1–32.

McDonald, M., Muir, D.M.,2007. Pressure oxidation leaching of chalcopyrite. Part I. Comparison of high and low temperature reaction kinetics and products. Hydrometallurgy, 86: 191–205.

Oraby, E.A. and Eksteen, J.J., 2014. The selective leaching of copper from a gold–copper concentrate in glycine solutions. Hydrometallurgy, 150: 14–19.

Ruiz, M.C., Montes, K.S. and Padilla, R., 2011. Chalcopyrite leaching in sulfate–chloride media at ambient pressure. Hydrometallurgy, 109(1-2): 37–42.

Schlesinger, M., King, M., Sole, K., Davenport, Wi., 2011. Extractive Metallurgy of Copper 5th edition. Elsevier: Oxford: England.

Seredkin, M. and Savenya, M., 2019. In-situ recovery for non-uranium metals ALTA 2019 Nickel- Cobalt - Copper, ALTA, Perth, Australia, pp. 208.

Seredkin, M., Zabolotsky, A., Jeffress, G., 2016. In situ recovery, an alternative to conventional methods of mining: Exploration, resource estimation, environmental issues, project evaluation and economics. Ore Geology Reviews, 79: 500–514.

Shiers, D.W., Collinson, D.M., Kelly, N.J. and Watling, H.R., 2016. Copper extraction from chalcopyrite: Comparison of three non-sulfate oxidants, hypochlorous acid, sodium chlorate and potassium nitrate, with ferric sulfate. Minerals Engineering, 85: 55–65.

Sinclair, T., Thompson, J., 2015. In situ leaching of copper: Challenges and future prospects. Hydrometallurgy, 157: 306–324.

Sokić, M.D., Marković, B. and Živković, D., 2009. Kinetics of chalcopyrite leaching by sodium nitrate in sulphuric acid. Hydrometallurgy, 95(3–4): 273–279.

Velásquez-Yévenes, L., Nicol, M. and Miki, H., 2010. The dissolution of chalcopyrite in chloride solutions: Part 1. The effect of solution potential. Hydrometallurgy, 103(1): 108–113.

Wallace, A.B., 1979. Possible signatures of porphyry-copper deposits in middle to late tertiary volcanic rocks of Western Nevada, Papers on mineral deposits of western north America: The International Association on the Genesis of Ore Deposits Fifth Quadrennial Symposium Proceedings. Nevada Bureau of Mines and Geology University of Nevada, Reno, pp. 69–76.

Watling, 2013. Chalcopyrite hydrometallurgy at atmospheric pressure. Review of acidic sulfate, sulfate-chloride and sulfate-nitrate process options. Hydrometallurgy, 140: 163–180.

Williamson, C., 1998. Hydrologic mechanisms and optimisation of in-situ copper leaching. case study: BHP Copper, PhD dissertation, San Manuel, Arizona, University of Arizona.

Yang, Y., Yang, Y., Gao, X., Petersen, J. and Chen, M., 2019. Microstructure evolution of low-grade chalcopyrite ores in chloride leaching - A synchrotron-based X-ray CT approach combined with a data-constrained modelling (DCM). Hydrometallurgy, 188: 1–13.

Chapter 2. Comparative analysis of copper dissolution and mineral transformations in coarse chalcopyrite for different lixiviant/oxidant systems at elevated temperature (110°C to 170°C)

Chalcopyrite ($CuFeS_2$) is the most common copper-bearing mineral and represents more than half of global copper mineral reserves. Copper sulfides, such as chalcopyrite, require oxidant addition for dissolution. Although numerous lixiviants have been evaluated in previous studies for conventional mining, limited information is available regarding their behaviour during the leaching of coarse chalcopyrite samples at high temperature, including their stabilities and secondary product formation. We compared the thermal stability of eleven lixiviant/oxidant systems (sulfuric acid, methanesulfonic acid, ammonium hydroxide, hydrochloric acid and glycine, and oxidants, including iron (III), copper (II), dichromate, sodium nitrate, ammonium sulfate and hydrogen peroxide) and their ability to leach copper from chalcopyrite at 110°C (below the sulfur melting point) and 170°C (above the sulfur melting point) under similar conditions. Tests were conducted for up to 576 h using solid cuboids (4-mm sides) to simulate in-situ recovery conditions. Sealed batch and Parr reactors were used to simulate an anaerobic environment that may be experienced in a subterranean application. This paper presents the findings from this study and compares the leaching systems at 110°C and 170°C based on copper release into solution, product identification, passivation phenomena and an analysis of superficial textures. The potential for use of the systems in deep-ore copper in-situ recovery processing is discussed based on the laboratory performance of the chosen systems.

2.1. Introduction

Chalcopyrite leaching studies have attracted significant interest because of the abundance of this mineral globally and its dissolution is challenging under mild conditions. During the hydrometallurgical processing of copper-sulfide minerals (chalcopyrite, bornite, chalcocite and covellite), an oxidant such as Fe^{3+} is used to

release copper into solution (Schlesinger et al., 2011). During this reaction, copper and iron from chalcopyrite dissolve and product layers may form as a result of reaction. The selection of a suitable lixiviant system can enhance the recovery rate and result in an increase in revenue. A variety of commercially available oxidants paired with lixiviants (acid or base), including ferric ions and oxygen, cupric ions, dichromate, nitrate, hydrogen peroxide and ammonia persulfate, have been tested in the laboratory under a range of conditions to assess their efficacy to extract copper from ores or concentrates. The most commonly investigated lixiviant system for chalcopyrite leaching is Fe^{3+} in sulfuric acid (Sinclair and Thompson, 2015).

Thermal environments in in-situ recovery (ISR) may pose limits to fluid stability and undesired reactions with gangue minerals that may compromise the operation. An understanding of the lixiviant/oxidant response beyond common experimental temperature (< 90°C) (and atmospheric pressure) regimes may be required in an ISR environment. For example, temperatures are reported to increase 25–30°C/km depending on the local geothermal gradient, and the increase in hydrostatic pressure with depth is approximately 10 MPa/km (Fridleifsson, 1996). For deep ore bodies (> 2 km) the minimum temperature is hypothesised to exceed 60°C at greater than 20 MPa. Although temperatures above 100°C may be uncommon for oxide zones, the existence of temperatures in this range is possible for primary sulfide ores. Unenriched porphyry deposits of chalcopyrite have been found at Red Mountain (Arizona) between 2–4 km below the surface. Although these deposits are currently only of academic interest (Wallace, 1979), they are potential targets for ISR in the future. Therefore, an understanding of the stability of solutions for use at a high temperature (> 100°C) is required. To the author's knowledge, only McDonald and Muir (2007) have compared commercially proposed concentrate processing systems up to 225°C, and concluded that a variation in experimental parameters, such as pulp density, free acidity and the addition of sodium chloride, impacts sulfide conversion, phases in the leach residue and copper recovery. Studies above 225°C have been performed for ferric ions, oxygen and ammonia sulfate/carbonate solutions (Padilla et al., 2008; Turan and Altundogan, 2013; Turan et al., 2015; Yu et al., 1973). No comparative analysis of different lixiviant/oxidant pairs under similar conditions is available in the literature for temperatures above 100°C. A summary of available information for different leaching systems is presented in Table 2-1.

Even though several kinetics studies have been performed using common lixiviant/oxidant pairs, and extensive research exists on the effect of different variables on the leaching behaviour of chalcopyrite, alternative systems, such as glycine (Eksteen et al., 2017; Oraby, 2014) or methanesulfonic acid (Ahn et al., 2018; Hidalgo et al., 2018), are still being investigated. Alkaline systems using glycine in alkaline media have been investigated for copper extraction at low temperatures. Hidalgo et al. (2018) reviewed the kinetic behaviour of chalcopyrite using MSA ferric solutions. However, limited information is available on the system leaching behaviour and product-layer formation for coarse grain sizes and leaches under pressure.

Table 2-1. Summary of previous experimental studies using known oxidants for copper-sulfide ores.

Oxidant	pH	Concentration (mol L^{-1})	Temp (°C)	Max recovery (%)	Particle size (µm)	Avg time (h)	Products from oxidant decomposition /precipitation	Mechanism	References
Cupric ions (Cu^{2+})	0.3 to 1.0	0.2 to 1	35 to 100	60 to 90	12 to 56	< 50	Copper hydroxides or chlorides in brine solutions, iron precipitates in the presence of oxygen	Surface chemical reaction and electrochemical control	Bonan et al. (1981); Velásquez-Yévenes et al. (2010); Hirato et al. (1987); Lundström et al. (2005); Skrobian et al. (2005)
Ferric ions (Fe^{3+})	0 to 2.5	0.2 to 3	35 to 100	50 to 100	10 to 106	< 50	Iron precipitates, sulfur	Surface reaction control by shrinking core model, diffusion through a product layer	Córdoba et al. (2008); Dutrizac (1981b); Hidalgo et al. (2018); Saxena and Mandre (1992); Shiers et al. (2016)
Oxygen (O_2)	-0.2 to 11.5	0.02 to 0.25	25 to 225	40 to 90	12 to 61	< 5	Iron precipitates, sulfur	Surface reaction by shrinking core model	Li et al., (2013); McDonald and Muir (2007); Ruiz et al. (2011);Tanda et al. (2019)
Dichromate ($Cr_2O_7^{2-}$)	0 to 0.7	0.01 to 0.4	30 to 90	70 to 90	4 to 270	< 10	Chromium hydroxides under >1 pH	Chemical reaction control and diffusion through a product layer	Aydogan et al. (2006); Antonijević et al. (1994); Murr and Hiskey (1981)

Nitrate (NO_3^-)	-0.3 to 0.5	0.15 to 0.60	40 to 90	70 to 100	37 to 75	< 5	Various NO_x gases	Mixed control model	Shiers et al. (2016); Sokić et al. (2009); Vracar et al. (2003); Watling (2013)
Hydrogen peroxide (H_2O_2)	-1.1 to 11	0.5 to 3	25 to 80	27 to 80	40 to 212	< 4	Oxygen (O_2), hydroxyl anion (OH^-) and hydroxyl radical ($HO^{\bullet}$).	Surface chemical reaction by shrinking core model	Eksteen et al. (2017); Mahajan et al. (2007); Olubambi and Potgieter (2009); Petrović et al. (2018); Solís-Marcíal and Lapidus (2014)
Ammonium sulfate/ carbonate or oxygen in ammonia (NH_3)	9 to 11.7	0.3 to 2.5	20 to 130	90 to 95	37 to 150	<4	Volatile NH_3	Diffusion through a product layer by shrinking core model	Baba et al. (2014); Turan et al. (2015); Bell et al. (1995); Beckstead and Miller (1977); Dutrizac (1981a); Liu et al. (2012)

In different leaching solutions, the initial solid undergoes several transformations that may result in the formation of product layers. The precipitation of surface layers that inhibit extraction is commonly termed "passivation" and has an important influence on the leaching rate. In some cases, product layers may restrict lixiviant access to the reaction interface. However, intermediate surface layer formation may be favourable for mineral dissolution if the resulting product phase is more porous than the original mineral. The nature of passivating layers is not understood fully. Dutrizac (1990) and Harmer et al. (2006) found that elemental sulfur production (S_0) could cause passivation. However, Munoz et al. (1979), Hackl et al. (1995) and Dutrizac (1981a) proposed that iron-oxide and -hydroxy compounds (e.g., hematite, jarosite) from ferric hydrolysis prevent lixiviant access to the mineral surface. Lázaro and Nicol (2003) suggested that selective iron dissolution results in the formation of a less reactive copper-enriched layer (CuS) that slowed down the solid-state diffusion of copper and iron. However, Nicol and Zhang (2017) proposed the formation of a copper polysulfide layer (CuS_2) that grows in thickness as the reaction continues and reduces the reaction rate. Other theories presented by Crundwell (2013) contradict the conception of polysulfides as responsible of passivation, arguing that no kinetical data has been presented to associate the rate reduction with the thickness of the layer. In a more detailed work Holmes and Crundwell (2013) concluded that polysulfide layer formed on pyrite surface did not passivate it, the thickness of the layer increased with potential along with the pyrite dissolution. Textural and morphological surface changes that can influence porosity and permeability resulting from chemical reactions with lixiviant systems have not been reviewed for large grains and in different stages of reaction.

Parameters and conditions that affect the leaching rate and the formation of reaction products in chalcopyrite as related to ISR conditions have not been discussed. A review of the relevant hydrometallurgical information of chalcopyrite leaching reveals numerous knowledge gaps on the analysis of leaching rates and reacted solid characterisation for coarse sample leaching, exposure to high temperatures and under pressure with low oxygen availability. As part of a global effort to unlock the possible application of ISR to copper sulfides, this study focuses on understanding fluid and solid transformations for the dissolution of coarse chalcopyrite samples by comparing various leaching systems under possible ISR conditions.

2.2. Materials and methods

2.2.1. Samples

Natural chalcopyrite rocks without a particular origin were cut in cuboid pieces of ~4 mm × 4 mm × 4 mm. The cuboids were polished to obtain flat surfaces and defined edges. Initial solids were characterised by the digestion of 8 g of milled cuboid pieces.

2.2.2. Analytical techniques

Unreacted and reacted solids were analysed by using various analytical techniques.

2.2.2.1. X-ray diffraction

X-ray diffraction (XRD) spectra were collected for cuboid samples in epoxy mounts, by using a PANalytical Empyrean X-ray diffractometer with a Bragg–Brentano HD incident monochromator equipped with cobalt X-ray tube operated at 40 kV and 40 mA. The system optics consisted of a diffracted beam pixel three dimensions (3D) array detector in scanning one dimension (1D) mode with 0.125° antiscatter slit and 0.02 rad soller slits. The scanning range was from 3° to 120° with a 2 h scanning time. Phase mineral identification was performed using PANalytical High Score Plus 3.0d.

2.2.2.2. Scanning electron and optical microscopy

Reacted solids were mounted on stubs and analysed by scanning electron microscopy-energy dispersive spectrometry (SEM-EDS). Cuboids were set in epoxy mounts and polished. Samples were carbon coated to avoid surface charging. Cross-sections were analysed by optical microscopy with a Nikon Eclipse EV100N POL light optical microscope. Scanning electron microscopy was performed using a JEOL-JSM-7001 instrument with 10 mm silicon drift detector, EDS detector and a resolution of 125 eV for chemical composition and elemental map distributions, at 20 kV with an 8 to 10 mm working distance.

2.2.2.3. Quantitative Evaluation of Minerals by Scanning Electron Microscopy

Mineralogical analysis was performed using a E430 Pro Quantitative Evaluation of Minerals by Scanning Electron Microscopy (QEMSCAN) instrument and an internal

CSIRO protocol for mineral identification (Meyer et al., 2013). The final data were processed with FEI Idiscover 5.2 software. Cross-sectional mineralogical maps were obtained using a Tescan Mira3 SEM instrument with EDAX X-ray detectors and TIMA Tescan software V1.6.65. The system was operated at 25 kV and 7.29 nA; and data were collected with a 4-µm step size across the sample and with a 0.5-µm step size on selected areas.

2.2.2.4. Solid porosity and permeability analysis

One cuboid pre- and post-leaching was submitted for X-ray computed tomography (CT) scanning to identify reaction-induced changes using a XRADIA Zeiss Versa XRM 520 3D-X ray microscope (160 kV, 9 W and voxel size of 3 µm). A total of 1601 projections were recorded for each scan over a 360° sample rotation and were used for volume reconstruction. An approximation of sample volume and porosity changes was achieved by using changes in sample volume and surface area (because the voxel size was kept constant for both scans).

The volumes were processed with Thermo scientific Avizo 2019-2 software and in-house workflows (Godel, 2013). To compare changes in fractures and void space between different samples, cross-sections (110°C) were analysed by using ImageJ 1.x (a public-domain image-processing software that allows for image area measurements (Schneider et al., 2012)). Measurements of void space were compared with unreacted samples to obtain a percentage change that occurred during reaction.

2.2.2.5. Fluid analysis

Fluids were analysed and elemental concentrations (Cu, Fe and S) were measured by inductively coupled plasma optical emission spectrometry. pH and Eh (Ag/AgCl) values were obtained with Ionode ORP and pH (IJ44A and IJ64) combination electrodes. Glycine solutions were analysed by Fourier-transform infrared spectroscopy (FTIR) using a Bruker Vertex 70 instrument to confirm total decomposition by using unreacted glycine solution as a standard and MilliQ water as a blank. The working parameters were a spectral region of 800–4000 cm^{-1} and a resolution of 4 cm^{-1}.

Mineral chemical compositions are expressed in mass percent unless stated otherwise. Mineral abbreviations in photomicrographs and electron images follow the recommendations by Whitney and Evans (2010).

2.2.3. Leaching tests

The release of copper from chalcopyrite dissolution (referred to as copper dissolution in the rest of the text) was compared at 110°C (below the sulfur melting point) and 170°C (above the sulfur melting point) for different acid or alkaline lixiviant systems with a known oxidant. Initial screening showed that glycine decomposition to ammonia started to occur above 60°C and, therefore, this temperature was used in subsequent experiments (O_2 and H_2O_2). Lower-temperature experiments (110°C) were performed in a 300 mL Parr® reactor, model 5521, with associated temperature controller (Fig. 2-1a), because of the possibility of gas release during the test, to allow oxygen injection as required and to enable fluid samples to be taken for kinetic plots. High-temperature experiments (170°C) were performed in closed stainless-steel reactors (batch reactors) with selected lixiviants only (i.e., those that would not generate gas). The experimental reaction times were extended for the 170°C tests to establish whether the solid composition changed more extensively and whether copper dissolution increased. Multiple reactors were used to acquire solid samples at different reaction times. Copper extraction was calculated based on the average mineralogy and initial copper concentration in the blank solids after QEMSCAN and ICP-OES analysis. Screening experiments showed a copper dissolution variation of ± 3.5% because of sample heterogeneity.

At 110°C, ten solutions were tested under “initial standard conditions” (Table 2-2). Concentrations were chosen based on a literature review of previous experiments on fine-grained samples and showed optimal conditions for each oxidant/lixiviant (see Table 2-1). Experiments were conducted in the Parr® reactor with constant agitation at 150 rpm by a magnetically driven impeller. The solid was placed in the vessel, covered with 150 mL of solution, closed, and residual oxygen was flushed with 1000 kPa of industrial-purity nitrogen three times at ambient conditions. Once the reactor had reached the desired temperature, solution samples (2–4 mL) were taken at 4 h and

over four days of the reaction. When sampling, the first fluid volume was discarded (to flush the sampling port) and the second fluid volume was retained for analysis. Leachates were filtered and diluted. Solid samples were taken at one and four days, rinsed with deionised water and dried at 30°C for further analysis.

Table 2-2. Summary of system starting conditions used for experiments at 110°C

Oxidant	Conc. (mol L^{-1})	Lixiviant	Conc. (mol L^{-1})	Additive	Conc. (mol L^{-1})	ρ (g/mL)	Initial pH	Initial Eh vs SHE (mV)	P (MPa)
$FeCl_3$	0.5	HCl	0 5	N. A	N. A	0.99	–0.07	695	0.2
$Fe_2(SO_4)_3$	0.5	H_2SO_4	0 5	N. A	N. A	1.07	–0.03	676	0.2
$CuCl_2$	0.5	HCl	0 5	N. A	N. A	0.96	–0.02	560	0.2
$CuSO_4$	0.5	H_2SO_4	0 5	N. A	N. A	0.99	0.23	492	0.2
$K_2Cr_2O_7$	0.2	HCl	0 5	N. A	N. A	1.00	0.16	843	0.2
O_2	0.2	Glycine[a]	0 2	NaOH[b]	0.3	0.94	10.5	164	0.4
Fe $(MSA)_3$[c]	0.2	MSA	0 2	N. A	N. A	0.99	–0.06	537	0.2
$NaNO_3$	0.5	H_2SO_4	0 5	N. A	N. A	0.95	0.11	651	0.6
H_2O_2	0.5	H_2SO_4	0 5	N. A	N. A	0.91	0.23	685	0.6
$Na_2S_2O_8$	0.5	$NH_4OH/(NH_4)_2SO_4$	0 5	N. A	N. A	0.96	10.6	375	0.6

[a] Experimental temperature 60°C

[b] To maintain pH

[c] Ferric methanesulfonate obtained by iron (III) in methanesulfonic acid (MSA) $\alpha FeOOH + 3CH_3SO_3H \rightarrow Fe(CH_3SO_3)_3 + 2H_2O$

At 170°C, six solutions were selected from the original group based on their performance, common use in the industry or uniqueness (alternative to common oxidants/lixiviants, such as potassium dichromate or glycine). Extended times and higher concentrations were chosen based on stoichiometric calculations from initial solid masses and assuming 100% chalcopyrite dissolution, with conditions provided in Table 2-3. Experiments were conducted with solid cuboids and 5 mL of fluid in 10-mL Teflon-lined closed stainless-steel reactors (Fig. 2-1b). Air was flushed from the vessels by using nitrogen before the reactor was closed and placed in a standard convection oven. Each batch reactor was used as a unique data point to obtain solid samples weekly over a three-week period.

Table 2-3. Summary of initial system conditions used in experiments at 170°C

Oxidant	Conc. (mol L^{-1})	Molar ratio oxidant/ ccp	Lixiviant	Conc. (mol L^{-1})	Addition	Conc. (mol L^{-1})	ρ (g/mL)	pH	Initial Eh vs SHE (mV)
$FeCl_3$	5	16	HCl	0.5	N. A	N. A	1.36	–1 .26	826
$Fe_2(SO_4)_3$	3.2	8	H_2SO_4	0.25	N. A	N. A	1.5	–0.18	765
$CuCl_2$	3.4	15	HCl	0.5	NaCl	3.4	1.39	–1.07	853
$CuSO_4$	1	2	H_2SO_4	0.34	N. A	N. A	1.05	-0.6	786
$K_2Cr_2O_7$	0.5	2.8	HCl	0.4	N. A	N. A	1.09	0.65	1062
H_2O_2	2.2	2	Glycine[a]	1	NaOH[b]	1 5	1.07	12.83	93

[a] Experimental temperature 60°C and 170°C
[b] To maintain pH
[c] Excess 200%

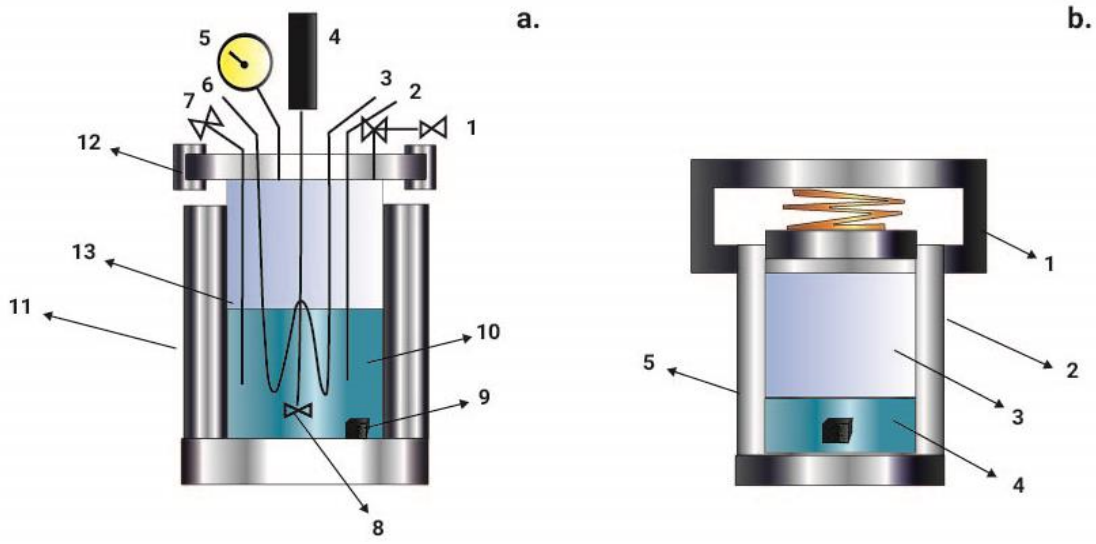

Fig. 2-1 Schematic of experimental instruments used, **a.** 300 mL model 5521 Parr® titanium reactor: (1) gas injection line with internal and external gas release valves, (2) thermocouple, (3) autoclave cooling water outlet to drain, (4) magnetic drive overarm, (5) pressure gauge, (6) autoclave cooling water inlet, (7) fluid sampling line with needle valve, (8) impeller, (9) solid cuboid sample, (10) leach fluid, (11) heating jacket, (12) split ring closure with gauge block assembly, (13) 300 mL grade-3 titanium vessel, **b.** static stainless-steel batch reactor: (1) stainless-steel cap with setting spring, (2) stainless-steel reactor body, (3) internal Teflon liner, (4) leaching fluid, (5) solid cuboid sample.

2.3. Results and discussion

2.3.1. Initial sample characterisation

The unreacted cuboid samples contained chalcopyrite ($CuFeS_2$) (85.8% ± 5%) and pyrite (FeS_2) (11.5% ± 4%) (Fig. 2-2a) with small dispersed zones of quartz (SiO_2) (1.6% ± 1.3%) and magnetite (Fe_3O_4) (0.1% ± 0.1%) (Fig. 2-3) (numbers based on QEMSCAN mass%). The solid surfaces were smooth with well-defined edges, no sulfur or oxidation products and small surface fractures (Fig. 2-2b). Sample cross-sections showed uniform compositions of chalcopyrite (close to the theoretical chalcopyrite composition ± 1% copper, Fig. 2-2c). Table 2-4 shows the average sample chemical composition that was obtained from a bulk sample of milled cuboids from the original bulk rock. The Cu, Fe and S contents between analysed samples differed by less than 2%.

Table 2-4. Chemical composition of initial mineral sample

Concentration (mass %)											
Al	**Ca**	**Cu**	**Fe**	**K**	**Mg**	**Na**	**Ni**	**Pb**	**S**	**Si**	**Zn**
0.053	0.029	35.9	31.0	< 0.005	0.0092	0.20	<0.005	< 0.005	31.8	0.088	< 0.005

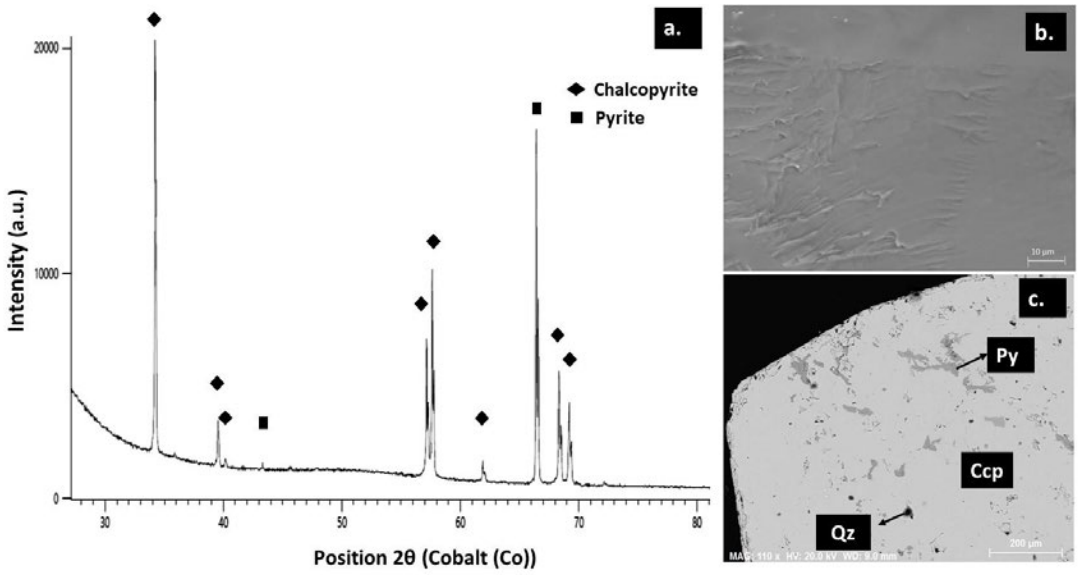

Fig. 2-2. a. X-ray diffractogram of pre-leached sample, showing chalcopyrite as the predominant phase and pyrite as a minor phase, **b.** SEM images of cuboid samples before

leaching showing initial sample surface texture, **c.** SEM-BSE image of cuboid samples before leaching with pyrite gangue distributed within the sample, and no rims or major fractures.

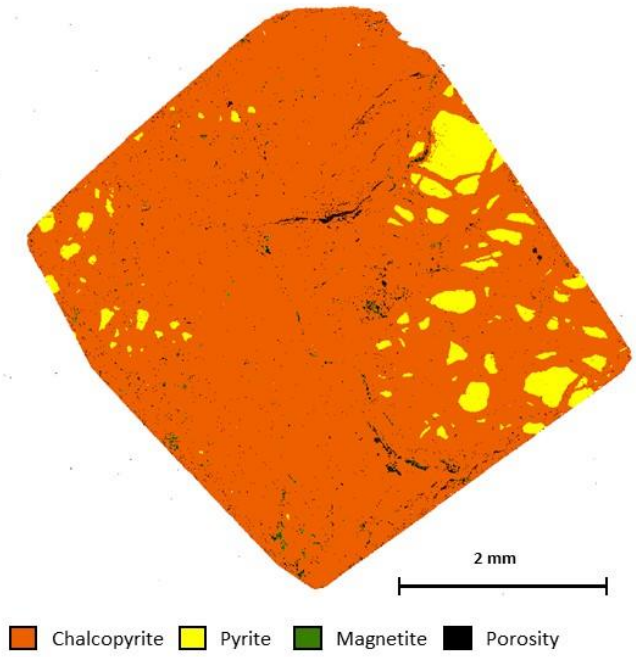

Fig. 2-3. TIMA-X integrated mineral analysis map of unreacted chalcopyrite cuboid showing major phases.

2.3.2. Fluid analysis

At 110°C, copper extractions for the $K_2Cr_2O_7$+HCl (100% copper extracted after 72 h), $FeCl_3$+HCl (86% copper extraction after 98 h), $CuCl_2$+HCl (63% copper extracted after 98 h) and $NaNO_3$+H_2SO_4 (40% copper extracted after 98 h) lixiviant systems were highest. Other systems reached lower maximum copper extractions, and all reached a plateau over the experimental time period. The lowest values were found for H_2O_2+H_2SO_4 (10% copper extracted after 98 h) and O_2+glycine (6% copper extracted after 98 h). The kinetic data are shown in Fig. 2-4a.

Alkaline solutions (H_2O_2+glycine) showed a maximum of 2% copper dissolution, which was 4% less than that with O_2 as oxidant (both solutions were tested at 60°C). Iron dissolved in all acid solutions (data not shown) but was relatively insoluble in the alkaline systems (< 0.5% iron dissolved).

At 170°, the copper dissolution (Fig. 2-4b) improved or decreased in different systems. The chloride-containing systems proved most effective; 100% and 80% copper dissolution was achieved by the $FeCl_3$+HCl and $CuCl_2$+HCl systems, respectively, after 560 h. The $CuSO_4$+H_2SO_4 and $Fe_2(SO_4)_3$+H_2SO_4 systems achieved a maximum of 50% copper dissolution after 360 h. The $K_2Cr_2O_7$+HCl system was sensitive to the high temperature and achieved only 5% copper dissolution after 120 h.

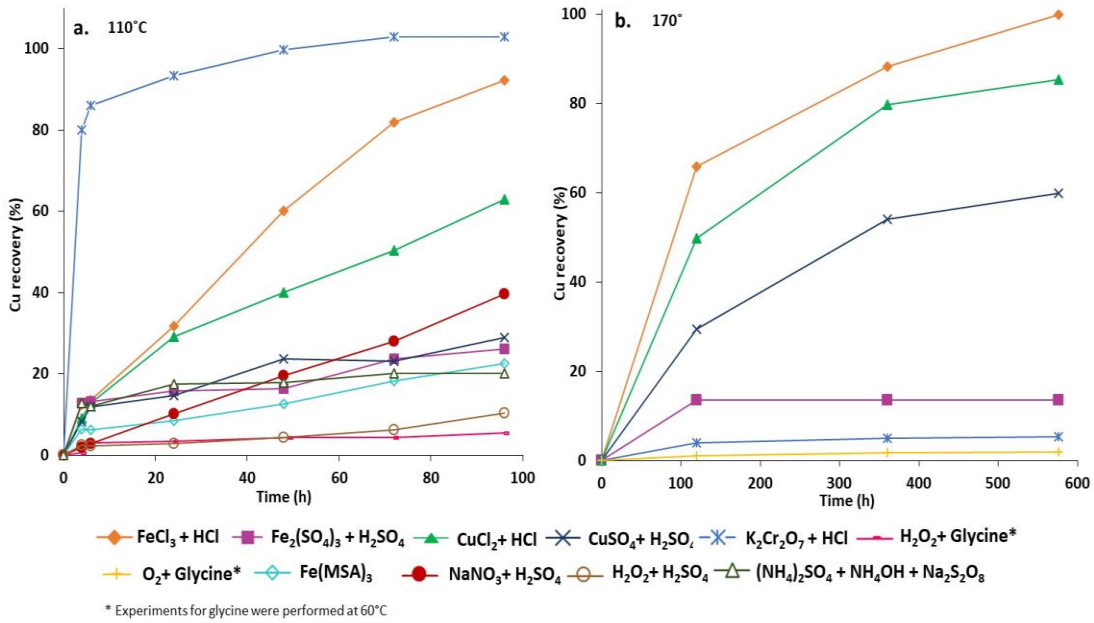

Fig. 2-4 Comparison of copper extraction from chalcopyrite for different leaching systems showing different dissolution patterns for selected solutions at higher temperatures, **a.** 110°C plots showing the best copper dissolution for the $K_2Cr_2O_7$+HCl solutions and the lowest dissolution for $Fe_2(SO_4)_3$+H_2SO_4, **b.** 170°C plots showing the best recovery for $FeCl_3$+HCl with the lowest dissolution occurring for H_2O_2+glycine.

2.3.3. Solids analysis

2.3.3.1. Product-layer formation

The reduction in copper dissolution that occurred in several of the solutions tested may be related to surface passivation. Important features related to product-layer formation were evidenced by solid characterisation. Presented phases were confirmed by chemical composition and crystal information (XRD, SEM-EDS, QEMSCAN, TIMA and optical microscopy).

2.3.3.1.1. Sulfur layers

Sulfur (S^0), as the most common phase in the acid systems at 110°C was the product of incomplete sulfide oxidation (Fig. 2-5). Dutrizac (1990) found that sulfur is present as 95% of the product composition compared with the 5% sulfate when chalcopyrite is dissolved in ferric-chloride solutions. Sulfur layers show different textures in the presence of chloride compared with sulfate-reacted solids. Sulfur formed in chloride solutions showed a porous texture with zones of chalcopyrite exposed for fluid interaction, as was presented by Hidalgo et al. (2018). A similar conclusion was made by Parker et al. (2008) who found by using Raman spectrometry that sulfur formed in sulfate solutions had longer sulfur–sulfur bonds and a tighter remnant lattice compared with chloride solutions. Our results indicate that changes in sulfur textures and morphologies result when solutions of different chemical composition are used under similar Eh–pH conditions. Sulfur textures and morphologies at 110°C for different solutions varied (Fig. 2-5). Chloride solutions ($FeCl_3$+HCl and $CuCl_2$+HCl), potassium dichromate ($K_2Cr_2O_7$+HCl) and sodium nitrate ($NaNO_3$+H_2SO_4) showed the most porous globular texture (Fig. 2-5a, c and e), which was matched with a higher total copper dissolution. Sulfur that formed in methanesulfonate, ferric-sulfate and hydrogen-peroxide solutions showed tighter sulfur layers with an amorphous appearance. Based on this observation, sulfur passivation may differ for different acidic solutions and be based on the chemistry of the fluid used. The sulfur morphology changed during different stages of reaction, which changed the dissolution kinetics, as was evidenced previously for bornite leaching (Hidalgo et al., 2019a).

The sulfur characteristics differed for the experiments at 170°C. Mobile molten sulfur allowed for an increased fracture penetration by the lixiviant and an enhanced dissolution rate resulted for the sulfate solutions. The sulfur became impermeable upon cooling.

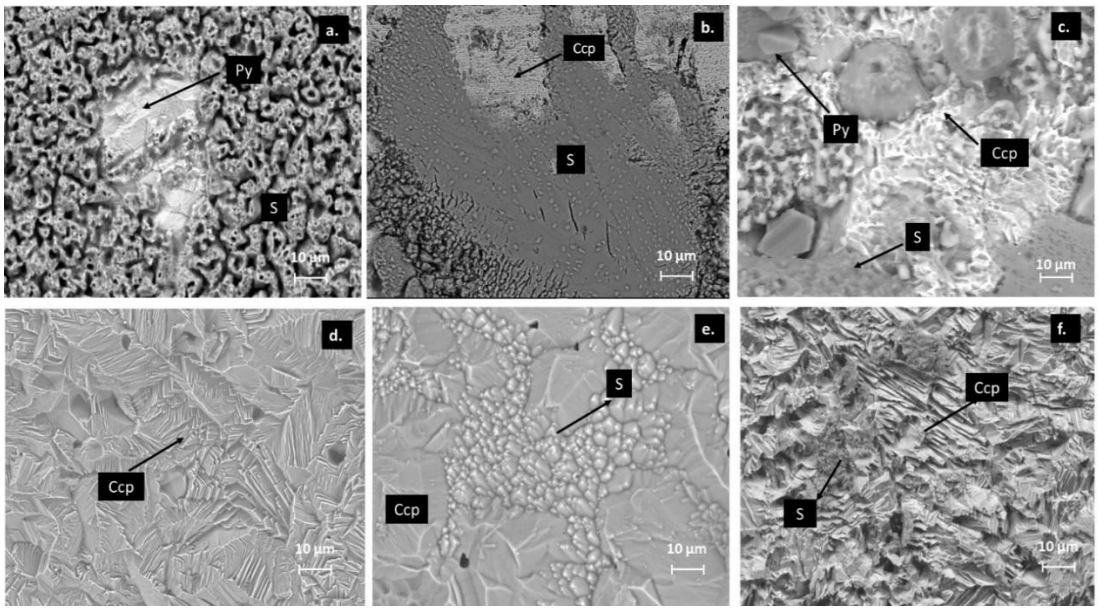

Fig. 2-5 SEM-BSE surface images of cuboids after four days of reaction in different solutions at 110˚C, which lead to sulfur-layer formation, **a.** sulfur layer formed after reaction in $FeCl_3$+HCl solution showing globular sulfur adjacent to pyrite particles, b. sulfur layer formed after reaction in $Fe_2(SO_4)_3$+H_2SO_4 solution showing dense texture, **c.** chalcopyrite being replaced by sulfur after reaction in $CuCl_2$+HCl solution showing mesh texture adjacent to unreacted pyrite particles, **d.** chalcopyrite fissured surface after reaction in $Fe(MSA)_3$ solution, **e.** chalcopyrite replacement by globular sulfur as isolated surface zones after reaction with $NaNO_3$+H_2SO_4 solution, **f.** chalcopyrite transformation to sulfur in H_2O_2+H_2SO_4 acid solution, sulfur replaced chalcopyrite by what appear to be cleavage planes and exhibits a fractured surface texture.

2.3.3.1.2. Copper-enrichment layers

Many systems showed sulfur as the sole product, but copper-enrichment layers were also present as product layers that coated the sample perimeter except when ferric ion was used as an oxidant. Of these product phases, digenite ($Cu_{1.8}S$), covellite (CuS) and bornite (Cu_5FeS_4) were most common (Fig. 2-6). Copper-enrichment layers resulted at different solution potentials (375 mV to 1062 mV vs SHE) and in alkaline to acid solutions. Solutions with high initial concentrations of cupric ions showed a preferential formation of digenite rims ($CuCl_2$+HCl and $CuSO_4$+H_2SO_4). The resulting phases showed extensive growth with an increase in temperature (Fig. 2-6a and b), but a modest increase resulted at 110°C. The product layers started forming in fractures

and zones with fluid access. More and deeper fractures were found when the replacement thickness was significant; the newly formed copper phase showed a more porous texture, as was also identified by Muszer et al. (2013) and Zhao et al. (2014) in copper layers formed after chalcopyrite and bornite replacements. Leaching of the copper-enriched phase (CuS) enhanced copper extraction and did not hinder further chalcopyrite dissolution as was also evidenced in our results and previous work (Hidalgo et al., 2019b). Some copper-enrichment layers were coated by other precipitates that may hinder lixiviant/oxidant access (Fig.2- 6c and d). In these cases, the phase showed slow growth after the total reaction extent.

The formation of copper-enrichment phases may be related to higher concentrations of Cu^{2+} and Fe^{2+} in solution from chalcopyrite oxidation and an associated reduction in Fe^{+3} concentration. Hiroyoshi et al. (2000) found that chalcocite phases formed when chalcopyrite leached in the presence of ferrous ions, and the resulting phase was more reactive than the original chalcopyrite. The reaction of chalcopyrite in the presence of copper sulfate resulted in the formation of digenite:

$$3CuFeS_2 + 6CuSO_4 + 4H_20 \rightarrow 5Cu_{1.8}S + 3FeSO_4 + 4H_2SO_4 \quad (1)$$

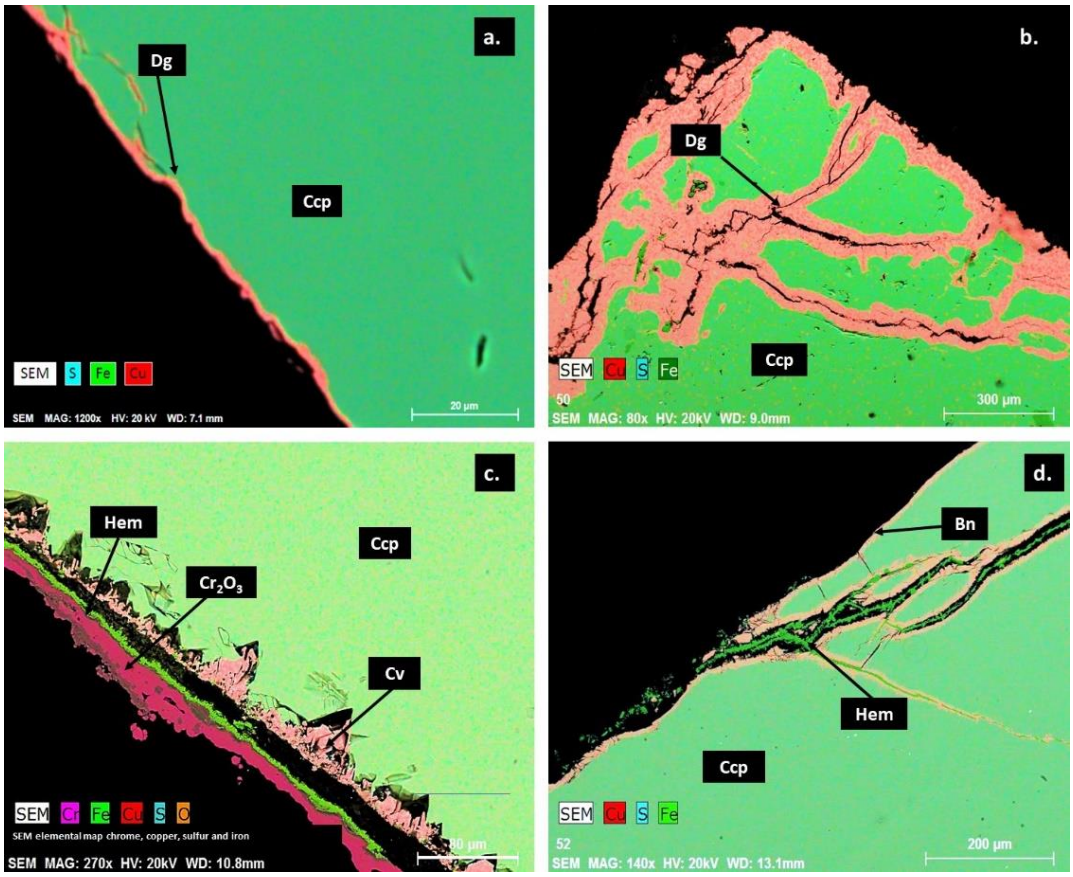

Fig. 2-6 SEM elemental maps of chalcopyrite cuboid samples after leaching with different systems. The red areas represent a high copper concentration without iron in the product, green areas represent a high iron concentration and blue areas represent a high sulfur concentration. **a.** Reacted chalcopyrite leached with $CuSO_4$+H_2SO_4 at 110°C for 4 days showing a digenite rim, **b.** reacted chalcopyrite after three weeks of leaching with $CuSO_4$+H_2SO_4 at 170°C showing a digenite rim on the outer surfaces and along fractures, **c.** reacted chalcopyrite perimeter leached with $K_2Cr_2O_7$+HCl at 170°C for three weeks; three resultant layers include chromium(III) oxide (deep purple), hematite (lime green) and covellite (pink), **d.** chalcopyrite after reaction with $(NH_4)_2SO_4$+NH_4OH+$Na_2S_2O_8$ showing a bornite (pink) and loose layer of hematite (deep green) layer that occurs mainly in the internal fractures.

2.3.3.1.3. Iron oxides

Alkaline solutions were the only systems that yielded iron-oxide product layers. $(NH_4)_2SO_4$+NH_4OH+$Na_2S_2O_8$ solutions produced a loose layer of iron precipitates (identified as hematite by XRD) (Equation 2) with an underlying thin rim of bornite (Fig. 2-6d). The bornite layer increased in thickness at higher temperatures or with time and showed a distinctive chemical border with original chalcopyrite. Similar

products were found by Warren and Wadsworth (1984) that evidenced a slowdown in copper dissolution and was attributed to $Cu_{1-x}FeS_2$ beneath the iron-oxide layers. Solids leached with O_2 or H_2O_2+glycine solutions formed similar iron-oxide layers (Fig. 2-7a) but no copper enrichment was found (Fig. 2-7b). Our results show different products for different systems when the same pH (10.5) was used ($(NH_4)_2SO_4$+NH_4OH+$Na_2S_2O_8$ and O_2+glycine), which indicates the influence of solution chemistry on solid products as was also seen in acid solution. Halpern et al. (1959) compared copper dissolution between ammonia and glycine solutions. Ammonia had a higher kinetic rate constant (84 mg cm^{-2} $h^{-1}(mol\ L^{-1})^{-1}$ for ammonia vs 49 mg cm^{-2} $h^{-1}(mol\ L^{-1})^{-1}$ for glycine). The stability of the Cu^{+2} complexes was higher in glycine compared with ammonia (4.3 $logK_1$ for ammonia vs 8.4 $logK_1$ for glycine) Therefore, copper appears to be more soluble in glycine solutions (Aksu and Doyle, 2001). The different solids may result from the solubility and stability differences between solutions that result in copper reprecipitation in the form of bornite.

$$CuFeS_2 + 4NH_3 + 4.25O_2 + 2OH^- \rightarrow Cu(NH_3)_4^{2+} + 0.5Fe_2O_3 + 2SO_4^{2-} + H_2O \quad (2)$$

The iron-oxide precipitates were loosely packed and fractures surrounded the precipitates with gaps between the iron and copper phases (chalcopyrite for glycine and a bornite surface layer for ammonia). Cracks increased in length only when pyrite was not present (the pyrite surface was oxidised with a thin layer of iron-oxide reprecipitation). Based on these results, no evidence exists for passivation because of iron precipitate formation (also proposed by (Moyo *et al.*, 2015). Therefore, the low copper dissolution may be related to oxidant availability (low solubility under temperature conditions).

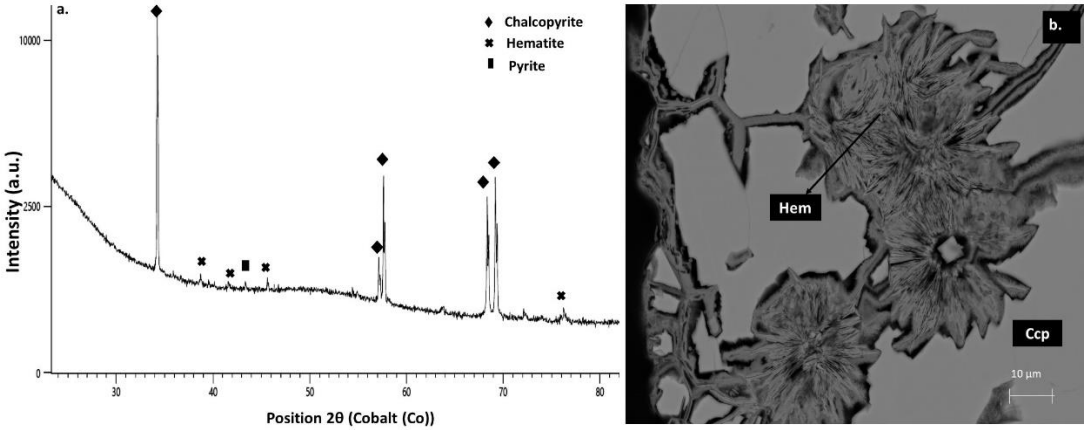

Fig. 2-7 X-ray diffraction pattern and SEM-BSE image for chalcopyrite after reaction, **a.** X-ray diffraction pattern of sample after 4 days in O_2+glycine solutions at 60°C, **b.** SEM-BSE solid phase of hematite formed at the surface showing gaps between chalcopyrite zones and near surface.

2.3.3.1.4. Other phases

The potassium dichromate ($K_2Cr_2O_7$+HCl) residue at 170°C showed copper enrichment (covellite (CuS)) and chromium- and iron-oxide precipitation as (Cr_2O_3) and hematite (Fe_2O_3), respectively (Fig. 2-6c). The products showed complex layering inside the cracks and around the surface perimeter (Fig. 2-8b). Copper dissolution was hindered by passivation at this temperature, and was 5% at 170°C compared with the 100% copper dissolution at 110°C. Similarly, a major reduction in copper dissolution was found by Murr and Hiskey (1981) in copper dissolution from chalcopyrite at 90°C with 0.05 mol L^{-1} potassium dichromate solutions, and was claimed to result from decreasing Cr(VI) absorption at the mineral surface. Our 110°C results are consistent with the solids reported by Murr and Hiskey (1981) and showed sulfur as the sole product. The formation of chromium-oxide (Cr_2O_3) at a higher pH (pH 3) when Cr(VI) is reduced to Cr(III) was evidenced by Cruz-Espinoza et al. (2012) with the absorption of Cr_2O_3 in activated carbon. Eskoliate (α-Cr_2O_3) was formed after calcination of the loaded carbon product at 1100°C. Our XRD results showed the formation of Cr_2O_3 (Fig. 2-8a) that could be assumed as a precursor phase to the formation of eskolaite.

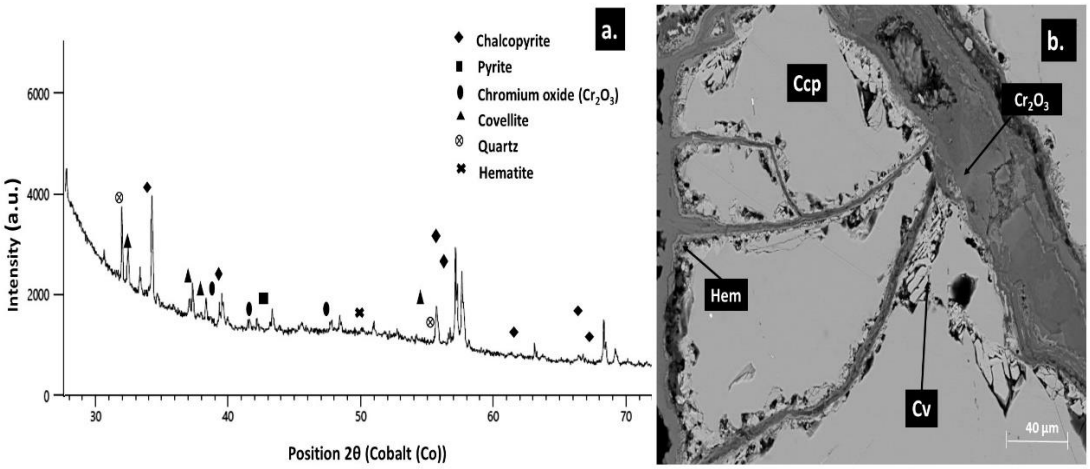

Fig. 2-8 X-ray diffraction pattern and SEM-BSE image for chalcopyrite after reaction, a. X-ray diffraction pattern of sample after 4 days in $K_2Cr_2O_7$+HCl solutions at 170°C, b. SEM-BSE solid phase of Cr_2O_3, hematite and covellite formed at the surface showing fracture filling with mixed precipitations and outer-perimeter rim.

Formation of chromium-oxide or eskolaite was suggested by the stability diagrams for potassium-dichromate solutions (modelled by using Geochemist's Workbench® at 25°C, 110°C and 170°C; Fig. 2-9). Eskoliate precipitation is proposed at room temperature for pH > 2 and Eh < 1 V. The stability region for the Cr^{3+} aqueous phase decreases with increasing temperature; at 170°C, precipitation occurs over the entire pH range as was evidenced by the solid analysis (our experimental pH was < 1).

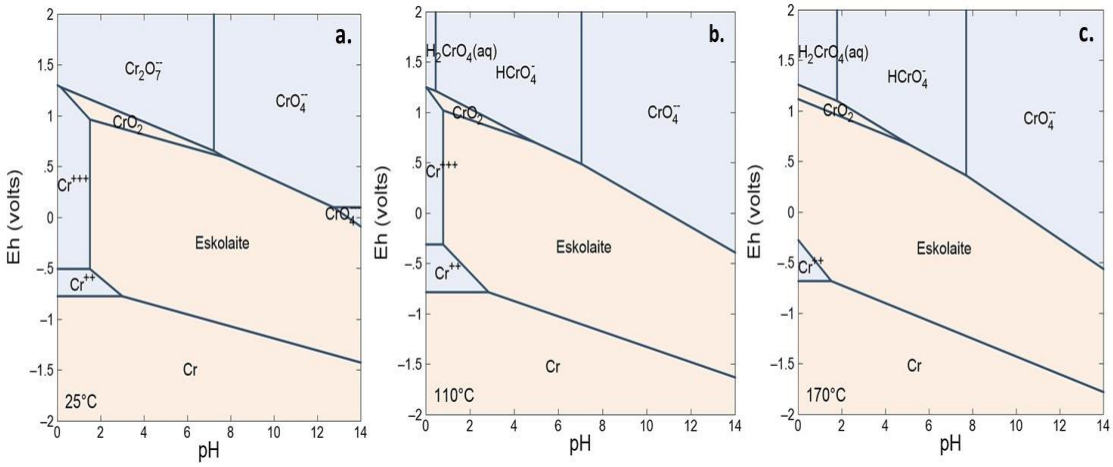

Fig. 2-9 Pourbaix diagram showing Cr speciation as a function of pH and Eh at **a.** 25°C and **b.** 110°C **c.** 170°C. Diagrams were calculated by using Geochemists WorkBench© v10.0.05.

A summary of the described product layers is listed in Table 2-5. All samples were analysed under the techniques described in Section 2.2 for the grain surfaces and cross-sections, but only some results are highlighted. Solids were compared after 4 days at 110°C and 170°C. All rim thickness are approximated averages based on SEM-BSE and high-resolution TIMA images. TIMA images for 110°C experiments are presented in Appendix C. Complementary information for short term 170°C experiments is presented in Appendix A.

Table 2-5. Summary of solid product layers after 4 days of reaction in different solutions at 110°C and 170°C (characterised by XRD, SEM-EDS, QEMSCAN and TIMA analyses).

System	Products formed after 4 days at 110°C	Products formed after 4 days at 170°C
$FeCl_3$+HCl	Only sulfur formed. Solid, porous and brittle sulfur replaced major portions of chalcopyrite without covering the entire surface. Surface cracks formed.	The cuboid had dissolved, and only dense molten sulfur was present.
$CuCl_2$+HCl	Sulfur replaced chalcopyrite as uneven patches around the pyrite particles.	Copper-enrichment phases in the form of digenite ($Cu_{1.8}S$) appeared as a major replacement of the chalcopyrite (rims 167 μm) with major surface cracks. External digenite rim converted to porous sulfur.
$Fe_2(SO_4)_3$+H_2SO_4	After four days, sulfur formed isolated zones of tight, thin (< 1 μm) layers. No product was found internally, and sulfur penetration was shallow.	Molten sulfur recrystallised in cracks and rims as tight sulfur layers (maximum thickness 27 μm). No porous texture resulted.
$CuSO_4$+H_2SO_4	A total surface replacement of chalcopyrite by digenite ($Cu_{1.8}S$) occurred. Cross-sections showed a thin (1.5 μm) replacement rim.	Chalcopyrite was covered by a layer of digenite ($Cu_{1.8}S$) with a 70-μm-thick rim. Fractures formed only near the replacement rim.
$K_2Cr_2O_7$+HCl	Sulfur formed during the first day and replaced chalcopyrite showing a	A covellite rim (29 μm) formed around chalcopyrite cracks, followed by hematite (7 μm)

	porous texture and cracks. After 4 days all solid was dissolved.	formation and a thick layer of non-porous chromium-oxide (Cr_2O_3).
O_2+glycine H_2O_2+glycine	At 60°C, chalcopyrite was transformed into an even copper-deficient layer. Cross-sections showed a continuous rim of hematite (15 µm) and hematite inside cracks.	At 60°C, hematite (Fe_2O_3) formed as a thin even rim (5 µm) and occurred inside cracks as fine precipitate. At 170°C, a 5 µm copper-enrichment layer of bornite (Cu_5FeS_4) formed, coated by hematite (Fe_2O_3) (10 µm).
$Fe(MSA)_3$*	Small zones of chalcopyrite surface were covered with tight sulfur layers. The sample perimeter showed pitting, but no product was found inside the cross-sections.	
$NaNO_3$+H_2SO_4	Superficial zones of globular sulfur resulted. Cross-sections showed minor sulfur zones (<1 µm). The cuboid perimeter was pitted because of sulfur loss from the rim.	
H_2O_2+H_2SO_4	Sulfur with surface cracks was the only patchy product. No product was found in cross-sections.	
$(NH_4)_2SO_4$+NH_4OH+$Na_2S_2O_8$	The surface was covered with fine-grained iron precipitates. Cross-sections showed a thin hematite replacement rim (Fe_2O_3) (5 µm) and bornite (Cu_5FeS_4) (< 1 µm). Major cracks were filled with iron precipitates. Pyrite portions showed thin layers of iron oxide (hematite).	

Notes: all rim thickness are approximated averages based on SEM-BSE images, * ferric methanesulfonate

2.3.3.1.5. Mechanisms of mineral transformation

Characterisation indicated that product formation was dependent on pH and Eh and was influenced significantly by fluid chemistry, as evidenced by the different products

that formed under similar pH and Eh conditions. Product phases ("leached layers") result from the selected removal of ions from the structure conserving the morphology and structure of the mineral (e.g., iron removal from chalcopyrite leaving bornite as product) (Burkin, 1969). Therefore, chemical gradients exist in solid rims and transformations occur by interaction of the fluid with the grain boundaries. Crundwell (2015) also presented a different understanding of chalcopyrite dissolution mechanism in which the dissolution behaviour is directly related to the n-type semiconductor structure and the preferential dissolution was attributed to the weak bound of iron with the surface because of its association with the anti-bonding orbitals of the valence band. However, in the course of the reaction the stoichiometric dissolution conditions will prevail.

Differing from the vision of preferential dissolution of species as the dissolution mechanism of sulfides a new mechanism for mineral transformation to copper-enriched phases has been proposed (Cai et al., 2011; Zhao et al., 2014). The mechanism is called interfacial coupled dissolution–reprecipitation (ICDR) and suggest that the formation of deficient layer obey to re-equilibration processes between the interfacial fluid and the solid in the mineral interface. The concept of interfacial–coupled dissolution–reprecipitation (ICDR) has been explained as a re-equilibration process that occurs when a solid is out of equilibrium with a fluid, starts to dissolve stoichiometrically and when the interfacial fluid becomes supersaturated, a product phase is precipitated (Putnis, 2002; Putnis, 2009). The main features of this mechanism include: 1) a preservation of the initial morphology, 2) a sharp chemical interface between the parent and product, 3) development of porosity and permeability, 4) crystal information of the parent is inherent in the product. Unlike solid-state diffusion, this mechanism is related closely to chemical variability where the most important chemistry is that of the interfacial layer that is formed between the parent and product phases. Our results suggest that ICDR may be the mechanism for formation of several phases that were present after leaching. Features that correlate with this mechanism include: (i) the replacement of chalcopyrite by porous digenite or bornite, (ii) the product phase showed a sharp chemical interface (confirmed by EDS line measurements) (Fig. 2-10a and c) and (iii) variability in product solids depending on interfacial chemistry of the fluid even in solutions with similar pH and Eh range (such as in the glycine and ammonia solutions) (Fig. 2-10b and c).

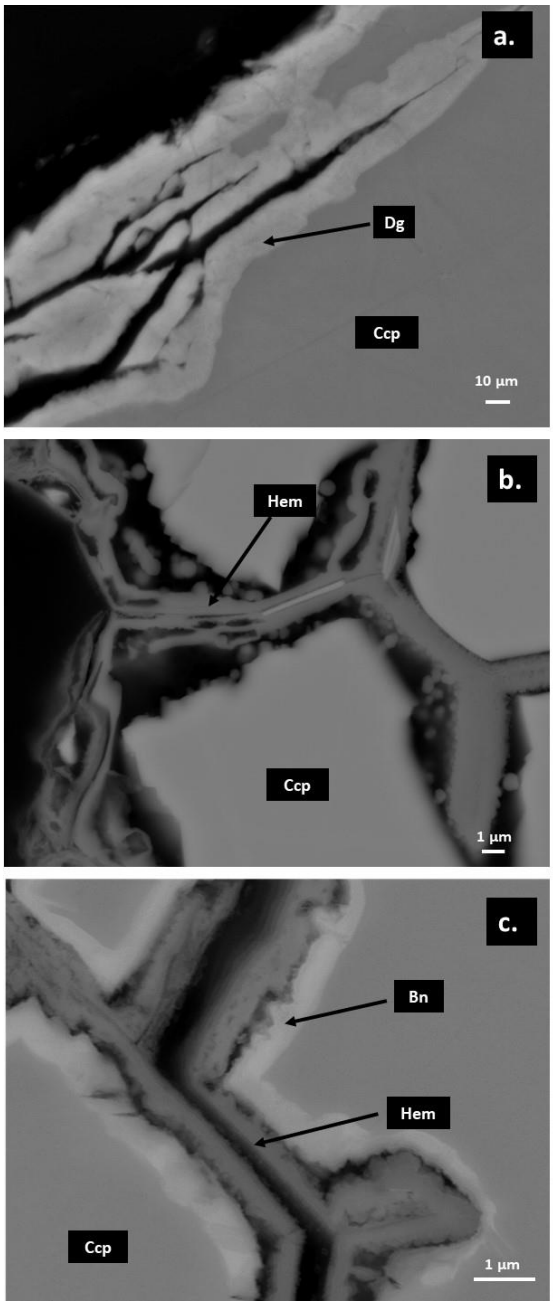

Fig. 2-10 SEM-BSE images of chalcopyrite cuboid samples after leaching with different systems showing characteristic features of ICDR pseudomorphic replacements, **a.** chalcopyrite sample after reaction in $CuSO_4$+H_2SO_4 solutions after 4 days at 110°C, chalcopyrite-digenite sharp chemical interface with porous texture, **b.** chalcopyrite sample after reaction in O_2+glycine solution after 4 days at 60°C, chalcopyrite-hematite showing gaps between phases due to volume changes during the replacement, **c.** chalcopyrite sample after reaction in $(NH_4)_2SO_4$+NH_4OH+$Na_2S_2O_8$ solution after 4 days at 110°C, chalcopyrite-bornite and bornite-hematite interfaces.

2.3.4. Morphological changes

2.3.4.1. Gangue dissolution

Selective dissolution of value metal over gangue mineral dissolution is important when mining low-grade ores to maximise economic recovery and avoid possible side reactions. In this study, gangue minerals included pyrite and minor quantities of magnetite. Pyrite dissolution was slower than chalcopyrite dissolution, as was noted previously by Chandra and Gerson (2010). Pyrite transformation to sulfur was achieved by using the strongest oxidants at 110°C, such as $FeCl_3$+HCl and $K_2Cr_2O_7$+HCl (Fig. 2-11). In contrast, alkaline solutions showed a low interaction with the gangue. Surface analysis indicated that a loose thin layer of iron oxide formed on top of pyrite pieces but disappeared after cross-sectional polishing. The interaction with gangue may be advantageous (for example, pyrite may enhance copper leaching by increasing the fluid progress into the core, as was presented by Dutrizac et al. (1971)), or be detrimental (such as reagent consumption in carbonate dissolution (Sinclair and Thompson, 2015)), depending on the gangue type. In this study, pyrite dissolution was considered advantageous and increased the extent of fractures when dissolved.

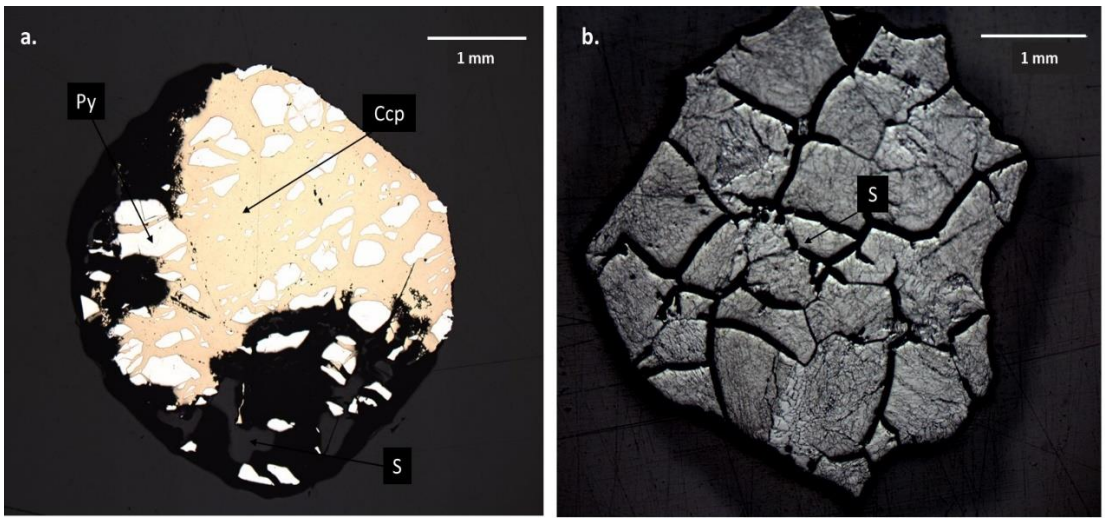

Fig. 2-11 Optical microscopy images of post-leached samples, **a.** general view of chalcopyrite–pyrite sample partially replaced by sulfur after four days of reaction in $FeCl_3$+HCl solution at 110°C showing that pyrite is oxidised to sulfur, **b.** overview of

chalcopyrite–pyrite sample that was replaced by sulfur after one day of leaching in $K_2Cr_2O_7$+HCl solutions at 110°C.

2.3.4.2. Accessibility enhancement

Experiments with $CuCl_2$+HCl solutions showed an increase in sample porosity that was recorded by various techniques (SEM, CT, and TIMA). The sample leached in $CuCl_2$+HCl at 170°C showed major fracturing after the original chalcopyrite was transformed into digenite (Fig. 2-12). Replacement started by an expansion of the original microfractures, which increased the reaction pathways. The newly formed phase had a porous texture (SEM analysis), and no passivation behaviour was evidenced in the copper-dissolution plot (Fig. 2-4b).

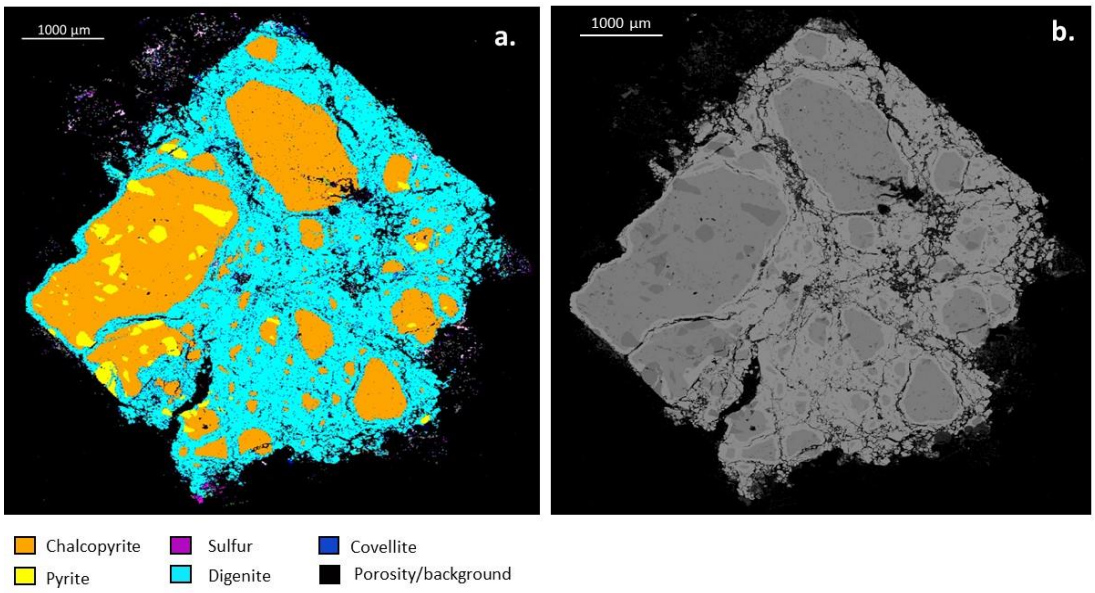

Fig. 2-12 QEMSCAN and SEM images of chalcopyrite cuboids after leaching with $CuCl_2$+HCl at 170°C for 4 days **a**. QEMSCAN phase identification **b**. SEM-BSE image showing major cracks around chalcopyrite replaced by digenite.

CT scans were conducted pre- and post-leaching to determine the development of porosity and volume changes in cuboids leached with $CuCl_2$+HCl solution for four days at 110°C. Only brittle sulfur replaced chalcopyrite and was evident in the upper face of the cuboid (Fig. 2-13a and b). Chalcopyrite showed morphological changes

and a rough texture (Fig. 2-13c and d). Pyrite did not show changes in morphology (Fig. 2-13e and f). These changes occur as dissolution at the sample surface (i.e., all changes are related to the sample destruction and created porosity that is connected to the outer sample surface). The registered porosity increase was 10.3% with a 95.6% increase in surface area. The change in surface area was a good proxy for the increased sample surface complexity as leaching progresses.

Analysis of the void space in SEM cross-sectional images showed that the cuboid in the $K_2Cr_2O_7$+HCl solutions dissolved completely, the next highest change in void area (20%) resulted for the $FeCl_3$+HCl system and the lowest change occurred for the $Fe_2(SO_4)_3$+H_2SO_4 and $Fe(MSA)_3$ solutions (1% and 3%, respectively). Alkaline solutions showed changes in void space between 12% (O_2+glycine) and 18% ($(NH_4)_2SO_4$+NH_4OH+$Na_2S_2O_8$) (See Fig. 2-15 accessibility enhancement).

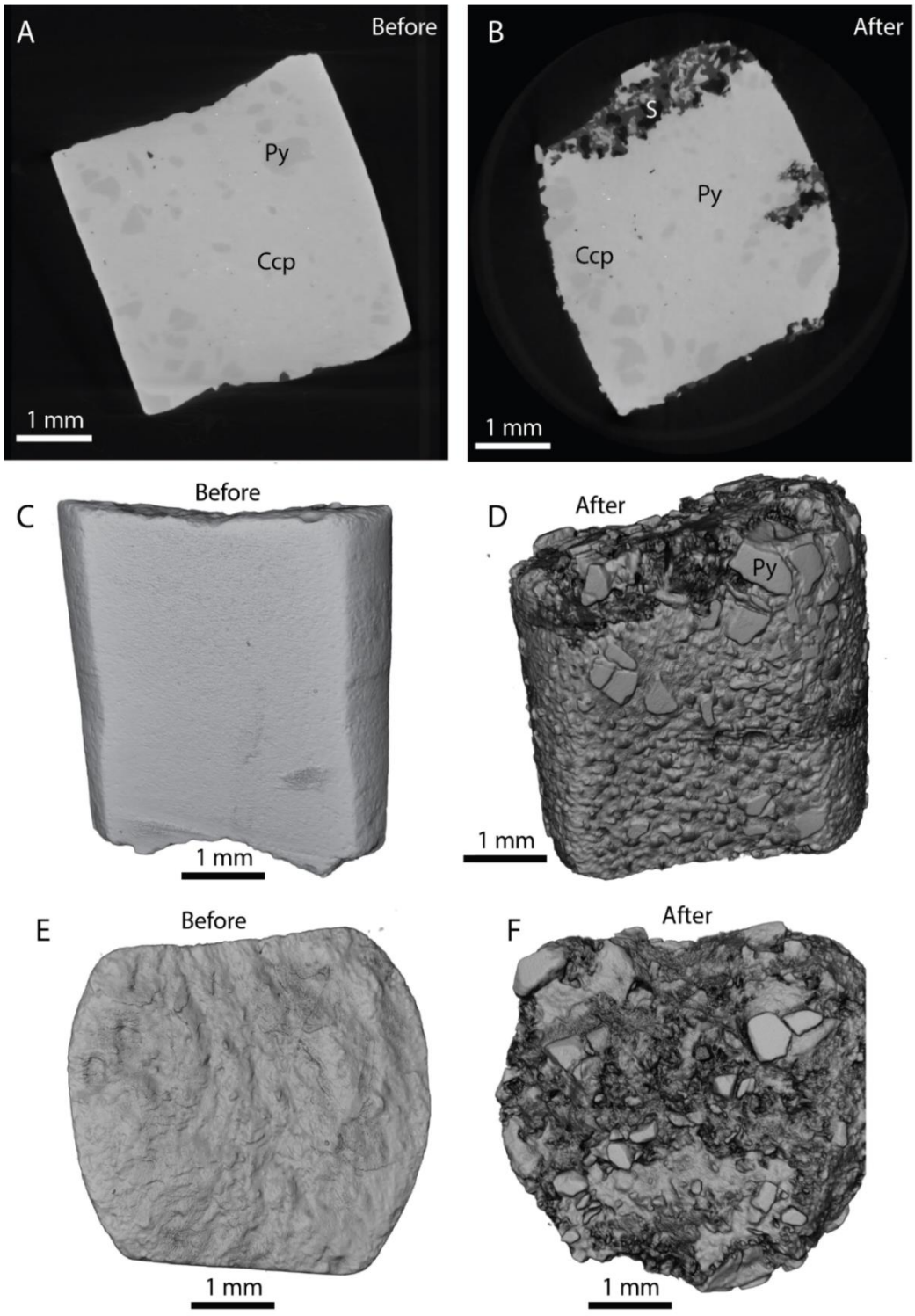

Fig. 2-13 Computed tomography images of cuboid sample pre- and post-leaching with $CuCl_2$+HCl solution at 110˚C for 4 days, **a. and b.** SEM-BSE images of unreacted and reacted sample showing a pitted perimeter and sulfur formation on the upper face of the cuboid, **c. and d.** 3D Reconstruction of external sample morphology before and after leaching showing major changes in the appearance of the solid and a decrease in volume, **e. and f.** 3D Images of top

face showing sulfur morphology, pieces of undissolved pyrite and changes in cuboid perimeter.

2.3.5. Implications for ISR

Many of the results obtained in this study have relevance to the choice of a lixiviant system (see Fig. 2-14) for use in an ISR application.

2.3.5.1. Lixiviant/oxidant temperature stability

Temperature influences the (i) pregnant leach solution stability (leads to precipitation) and (ii) lixiviant decomposition rates and oxidant solubility. The precipitation of secondary phases that can passivate mineral surfaces may result from an increase in temperature (with all other conditions remaining the same), as was evidenced in the $K_2Cr_2O_7$+HCl system by the formation of an impermeable Cr_2O_3 layer (eskolaite precursor). Although no jarosite phases formed in our experiments, a similar behaviour (iron hydrolysis) occurs with an increase in temperature (Dutrizac, 1982; Hidalgo et al., 2019b). Precipitation could be detrimental to ISR operation because of passivation and fracture clogging, as was seen in the Cr_2O_3 layer. This precipitation might be irreversible if formed in ore at ISR conditions because of the resistance to corrosion and to high thermal stress that make it insoluble in acid at elevated temperatures (Routschka and Wuthnow, 2008).

Reagents in the H_2O_2+H_2SO_4, $(NH_4)_2SO_4$+NH_4OH+$Na_2S_2O_8$ and H_2O_2+glycine systems decomposed and became less soluble at a higher temperature. A pressure increase of up to 400 kPa resulted because of oxidant decomposition. Hydrogen peroxide decomposition is accelerated above 60°C and in the presence of metal cations (Agacayak et al., 2014; Chiriţă, 2007). With an increase in temperature, ammonium-hydroxide vapour pressure is increased (Bell et al., 1995). The nitrate stability diagrams show the production of NO_2 and N_2 gases at moderate Eh (> 0.5 V) and above 110°C (Shiers, 2016). Evidence for glycine decomposition occurred in the H_2O_2+glycine solution screening stages with chalcopyrite at 170°C and in fluid stability tests (no chalcopyrite) at 90°C, 110°C, 130°C and 170°C; FTIR fluid analysis showed that no glycine was present in the final solutions. Reagent decomposition

increased when hydrogen peroxide was used, as has been documented elsewhere (Berger et al., 1999; Tanda, 2017). Gas dissolvers may be required should hydrogen peroxide and ammonia decomposition occur, such as those proposed by Litz (1982), to avoid a reduction in reaction rate, but dissolver addition may be costly. Although low copper dissolutions resulted for the H_2O_2+H_2SO_4 and $(NH_4)_2SO_4$+NH_4OH+$Na_2S_2O_8$ systems at high temperature, high recoveries were obtained in other studies below 100°C for fine-grained solids (Agacayak et al., 2014; Beckstead and Miller, 1977). In an ISR operation, fluid decomposition to a low-solubility gas could affect copper dissolution, present a mechanical hazard, block pores or channels, affect well casings or production tubing by cavitation and pose a health risk.

2.3.5.2. Accessibility enhancement

In an ISR operation, to improve fluid contact, accessibility to the minerals of interest in the ore may need to be enhanced. To achieve access, industry has focused on artificial processes, such as blasting (Sekisov and Lavrov, 2019), hydraulic fracturing and low-energy technologies (De Silva et al., 2018). Lixiviant interaction with the rock may also enhance accessibility by volume changes or mineral replacement by more permeable phases, as evidenced from the previously discussed solid analyses. To ensure effective mass transport, effective porosity is required. Therefore, the pore geometry, distribution and connectivity of the resulting porosity in product phases are important to determine possible flow interruptions (Nikkhou et al., 2019). Reaction-induced porosity has been evidenced by Putnis (2015) from ICDR, which proposes that a transient porosity forms because of the fluid–rock chemical re-equilibration process that allows for continuous fluid–rock interaction between the parent phase and the fluid. This porosity may heal with time, as was evidenced by Hidalgo et al. (2019a) in bornite sulfur layers, which may provide an explanation for the plateau stages that were reached for certain solutions after product-layer formation and growth ceased. An increase in void space and surface area by solid transformation through the formation of product phases (e.g., sulfur, copper-enrichment phases) and gangue dissolution increases the accessibility of the target mineral and may supplement mechanical enhancement.

2.3.5.3. Environmental impact

Subsurface water contamination and the undesired interaction of leach solutions with the environment must be avoided in ISR. Despite achieving good copper extraction, some systems may impact the environment, especially at elevated temperatures. For example, alkaline $(NH_4)_2SO_4$+NH_4OH+$Na_2S_2O_8$ solution is volatile, produces ammonia gas, is poisonous to aquatic life even at low concentrations and its toxicity increases with temperature and pH because of ammonia ionisation (NH_4^+), which causes cellular damage in fish (Levit, 2010). Ammonia has an unpleasant smell, and gas leaks may be toxic to plant life and to respiratory and skin systems (Minesota, 2019; Tanda, 2017). Although the best dissolution resulted for the $K_2Cr_2O_7$+HCl system, this reagent may pose several environmental issues in an ISR operation because of its high toxicity in water sources. Therefore, the use of these reagents is not recommended for ISR where subsurface water may contact the fluid and the temperature exceeds 30°C. The O_2+glycine system poses the best environmental option, as the most common amino acid with a low environmental hazard to humans, aquatic life and plants. However, when NaOH is used in solution to maintain pH, the environmental hazard increases and, in the same manner, the environmental advantage is lost if the working temperature does not remain below 60°C due to decomposition to ammonia.

2.4. Recommendations for fluid selection

Optimum temperature and pH ranges for the different reagent systems were based on the fluid and solid analysis after the experiments. These data are relevant to fluid–rock interactions at high temperatures and to coarse particle sizes, both of which are relevant to ISR (which may also occur in a pressurised environment with limited oxygen availability). The ranges were determined based on the thermal stability, possible reaction products formed and optimum copper dissolution. The recommended ranges for primary sulfide dissolution by the different lixiviants tested are presented in Fig. 2-14; these ranges may be increased or decreased based on target mineral analysis and will be specific to each ISR application.

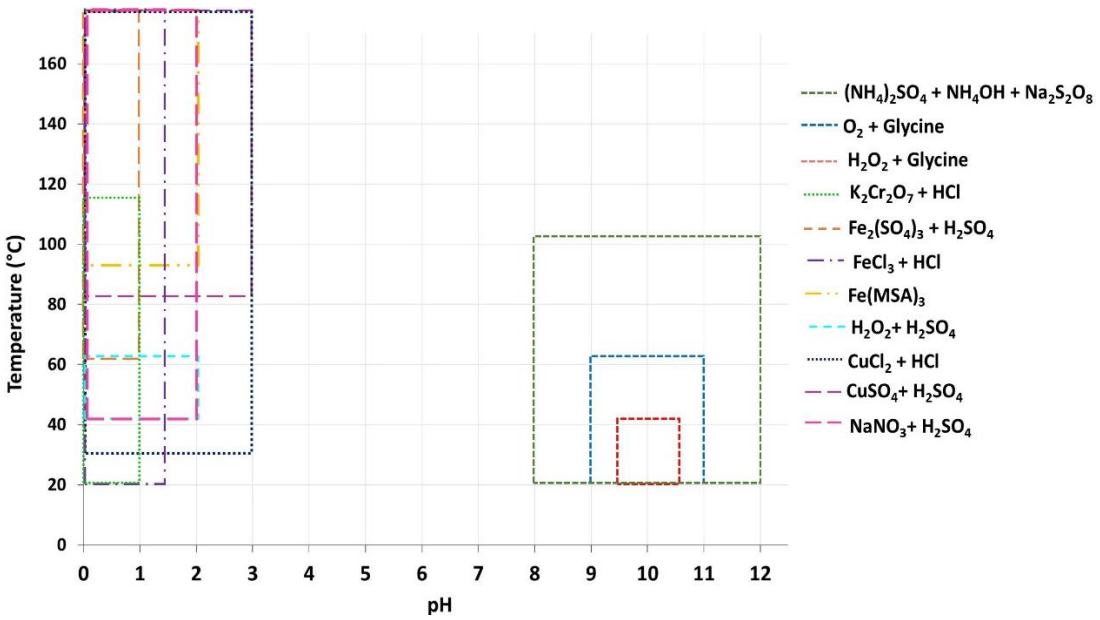

Fig. 2-14 Optimal temperature and pH conditions for 11 fluid solutions tested. Showing the optimal working windows to obtain maximum copper recovery without thermal instability or major precipitations. Acid solutions show an optimal pH range between 0 and 3, and alkaline solutions between 8 and 12.

Based on the experimental results and literature analysis, seven categories were used to compare the systems tested in this study in terms of their suitability to coarse-chalcopyrite-particle leaching under possible ISR conditions (Fig. 2-15). The categories included 1) copper dissolution at 110°C and 170°C; 2) temperature stability when considering the fluid decomposition and product precipitation; 3) environmental impact based on safety, possible gas production, biodegradability, extended human exposure and corrosion; 4) selectivity based on gangue pyrite dissolution; 5) passivation behaviour based on product-layer-formation morphology, texture and effect on copper dissolution; 6) accessibility enhancement from fracture and porosity analysis of the superficial textures and cross-sections and 7) reagent costs.

Fluid selection can be based on the requirements for specific applications. For example, if copper dissolution and the reaction-related enhancement of initial permeability are important, the best lixiviant option would be the $FeCl_3$+HCl solution. Based on the solid transformations, $CuSO_4$ oxidant increased the copper content of the solid instead of dissolving it, and therefore, this oxidant may need to be combined with other oxidants to be effective. The initial transformation did not show passivation

behaviour and could be used as a tenor enhancement into a more reactive solid to avoid chalcopyrite passivation with the second-stage oxidant. However, this implies extra time and cost. In an ISR scenario, the injection of mixed oxidants in stages with "soaking" times would facilitate the interaction of the injected oxidant and the recovered copper as part of the leaching system. It is important to understand the required reaction times of the systems with the intention of extrapolating these data to operational times. The reactions of chalcopyrite even above 170°C are slow. The "alternative" systems provided similar results to the "common" systems in industry and therefore, reagent selection will depend on other aspects, such as environmental concerns or costs.

The $Fe_2(SO_4)_3$+H_2SO_4 system, which is most common conventionally, showed disadvantageous behaviour for most criteria (Fig. 2-15). However, this system provides the best option if cost reduction is the most critical constraint. ISR operations have several cost advantages, such as a reduction in capital investment compared with conventional methods. ISR-associated costs depend mainly on the achieved flow rates, metal recovery and solid–liquid ratio (Seredkin et al., 2016). Costs may be reduced by oxidant regeneration by bio-oxidation and the use of saline water (such as sea water) (Paulson, 1992; Watling, 2015; Watling et al., 2014). Increased costs may discourage the use of some of the most efficient leach solutions, such as chloride solutions, which corrode stainless steel and generate pitting corrosion in pipes (Zhou et al., 2018), especially with increased temperature. The selection of resistant materials, such as production pipes, artificial lift systems, casings, tanks and surface facilities that contact the fluid, may increase operational costs. Supplementary information for Fig. 2-15 is presented in Appendix C.

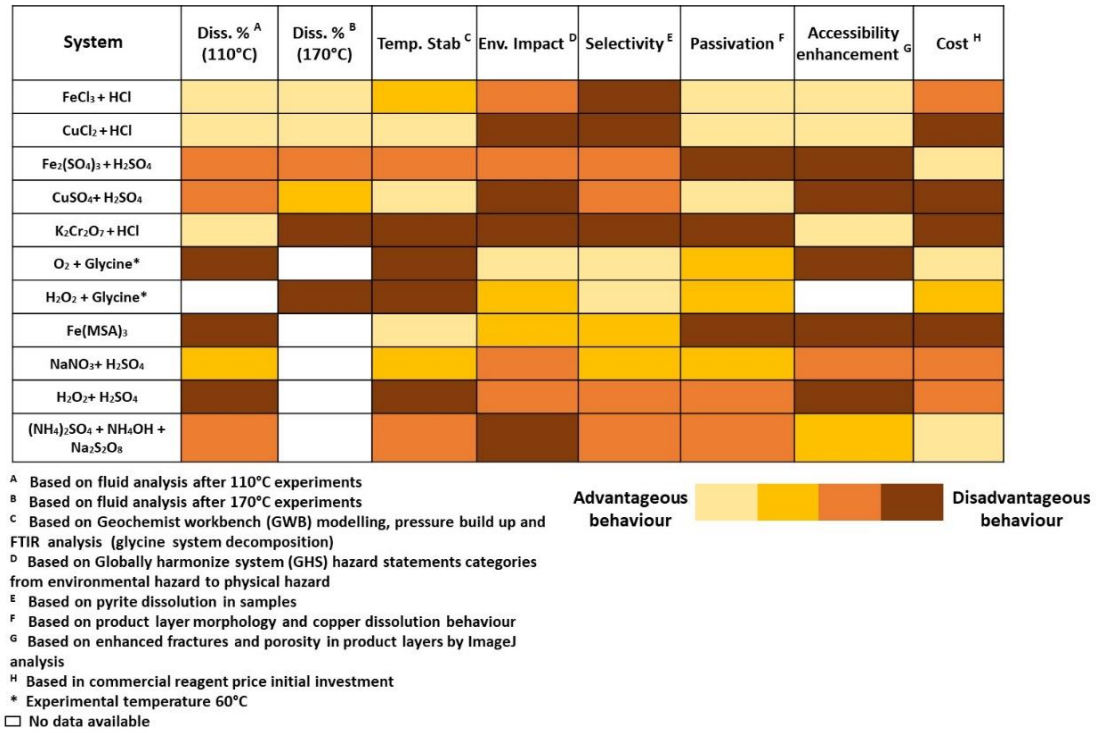

Fig. 2-15 Matrix of analysis of advantages and disadvantages of the solutions tested, showing the diverse strengths of the different systems, the ferric chloride and sodium nitrate solutions being the ones with more advantageous behaviours.

2.5. Conclusions

Screening tests on cuboid samples with several oxidants under the same conditions indicated that the alternative systems tested do not offer an improved leaching rate compared with more traditional systems. The stabilities of the alternative solutions, such as $K_2Cr_2O_7$+HCl and H_2O_2+glycine, indicated a major probability of decomposition or product formation related to an increased temperature, which affected the copper dissolution rate. Copper recovery was enhanced for chloride-containing systems ($FeCl_3$+HCl and $CuCl_2$+HCl). A change in product layer texture (including reaction-related fractures around product phases) with improved flow and sample accessibility resulted with the use of cupric-chloride and ferric-chloride oxidants. Each system has an optimal operating window, and the same conditions did not affect all systems equally. The selection of a suitable leaching system must be based on the specific characteristics of each deposit and operating requirements (depth, mineralogy, temperature, pressure, and surface facilities). Table

2-6 summarises the key advantages and disadvantages of all systems tested for application to ISR (based on our results and literature analysis).

Table 2-6. Advantages and disadvantages of different systems tested

System	Advantages	Disadvantages
$FeCl_3$+HCl $CuCl_2$+HCl	- High reaction rate for wide range of temperatures - Sample accessibility enhanced by reaction - Could be used with other oxidants as a mixed system	- Low compatibility with operating materials (e.g. stainless steel) - High acidity required to avoid precipitation of ferric-containing phases
$Fe_2(SO_4)_3$+H_2SO_4 $CuSO_4$+H_2SO_4 $Fe(MSA)_3$	- Improved kinetics at high underground temperatures, suitable for deep/hot bodies - Possible oxidant regeneration - More compatible with construction materials than other systems - Copper sulfate could be used as pre-treatment to enhance the copper grade without passivation behaviour, to be follow by a strong leaching solution for total dissolution	- Sulfur passivation-layer formation, possible path clogging above molten sulfur point - Slow kinetics below 100°C - Precipitation of phases at low acidities (e.g., jarosite)
$K_2Cr_2O_7$+HCl	- Low concentrations required - Aggressive rapid dissolution if chromium precipitations do not occur (170°C) - Dissolves gangue to form reaction-induced fractures (Eh > 650 mV vs standard hydrogen electrode)	- Precipitation (Cr_2O_3) at pH > 1 and temperatures > 90°C - Passivation layer formation restricts leaching - Toxic and corrosive chemicals with possible contamination of underground water
H_2O_2+glycine O_2+glycine	- Low environmental impact, biodegradable - No lixiviant consumption with gangue	- Decomposition at medium to high temperatures, excess peroxide required - Fractures required - Low oxygen solubility in deep ore bodies - Slow kinetics
$NaNO_3$+H_2SO_4	- Stable for wide pH range > 60°C - Relatively cheap reagents	- High concentrations of oxidant required for enhanced dissolution rate

		- Formation of non-porous sulfur coating layer - May decompose to generate NOx gases
H_2O_2+H_2SO_4	- Relative lower environmental risk - No secondary mineral formation or passivation layers - Compatible with acid and alkaline backgrounds	- Additives required to avoid peroxide decomposition (e.g., ethylene glycol) - Decomposes at higher temperatures (> 60°C) and in the presence of iron (III) - Rapid decomposition reduces copper dissolution rate
$(NH_4)_2SO_4$ + NH_4OH + $Na_2S_2O_8$	- Does not react with acid-consuming gangue - Low corrosion - Cleaner liquors for metal separation	- Volatile ammonia losses from reactive handling and injection - Vapour pressure generated with increasing temperature - Product layer passivation by ferric oxide - Toxic fumes and environmental contamination of underground water

Acknowledgments

MRIWA (Project M488), BASF, Curtin University and CSIRO are gratefully acknowledged for funding this work. The authors would like to thank Dr. Belinda Godel, Dr. Martijn Woltering, Peter Austin and Michael Verrall for their help with the mineralogical analysis; Dr Denis Shiers for reviewing a draft of this manuscript and the reviewers for their valuable additions to the final document.

References

Agacayak, T., Aras, A., Aydogan, S. and Erdemoglu, M., 2014. Leaching of chalcopyrite concentrate in hydrogen peroxide solution. Physicochemical Problems of Mineral Processing 50(2): 657–666.

Ahn, J., Barton, I.F., Shin, D. and Lee, J., 2018. The study of copper leaching from conichalcite and chalcopyrite using alternative lixiviants. Materials Processing Fundamentals 2018,Springer,Phoenix, Arizona, pp. 171–180.

Aksu, S. and Doyle, F.M., 2001. Electrochemistry of copper in aqueous glycine solutions. Journal of The Electrochemical Society, 148(1): B51.

Antonijević, M.M., Janković, Z. and Dimitrijević, M., 1994. Investigation of the kinetics of chalcopyrite oxidation by potassium dichromate. Hydrometallurgy, 35(2): 187–201.

Aydogan, S., Ucar, G. and Canbazoglu, M., 2006. Dissolution kinetics of chalcopyrite in acidic potassium dichromate solution. Hydrometallurgy, 81(1): 45–51.

Baba, A.A., Ghosh, M. K., Pradhan, S. R., Rao, D. S., Baral, A., Adekola, F. A., 2014. Characterisation and kinetic study on ammonia leaching of complex copper ore. Transactions of Nonferrous Metals Society of China, 24(5): 1587–1595.

Beckstead, L.W. and Miller, J.D., 1977. Ammonia, oxidation leaching of chalcopyrite -reaction kinetics. Metallurgical Transactions B, 8(1): 19–29.

Bell, S.L., Welch, G.D. and Bennett, P.G., 1995. Development of ammoniacal lixiviants for the in-situ leaching of chalcopyrite. Hydrometallurgy, 39(1): 11–23.

Berger, P., Karpel Vel Leitner, N., Doré, M. and Legube, B., 1999. Ozone and hydroxyl radicals induced oxidation of glycine. Water Research, 33(2): 433–441.

Bonan, M., Demarthe, J., Renon, H. and Baratin, F., 1981. Chalcopyrite leaching by $CuCl_2$ in strong NaCI solutions. Metallurgical Transactions B, 12(2): 269–274.

Burkin, A., 1969. Solid-state transformations during leaching. Mineral science Engineering 1(1): 4–14.

Cai, Y., Chen, X., Ding, J. and Zhou, D., 2011. Leaching mechanism for chalcopyrite in hydrochloric acid. Hydrometallurgy, 109–118.

Chandra, A.P. and Gerson, A.R., 2010. The mechanisms of pyrite oxidation and leaching: A fundamental perspective. Surface Science Reports, 65(9): 293–315.

Chiriţă, P., 2007. A kinetic study of hydrogen peroxide decomposition in presence of pyrite. Chemical and Biochemical Engineering Quarterly, 21(3): 257–264.

Córdoba, E.M., Muñoz, J.A., Blázquez, M.L., González, F. and Ballester, A., 2008. Leaching of chalcopyrite with ferric ion. Part I: General aspects. Hydrometallurgy, 93(3): 81–87.

Cruz-Espinoza, A., Ibarra-Galván, V., López-Valdivieso, A. and González-González, J., 2012. Synthesis of microporous eskolaite from Cr(VI) using activated carbon as a reductant and template. Journal of colloid and interface science, 374(1): 321–324.

Crundwell, F. K., 2013. The dissolution and leaching of minerals: Mechanisms, myths and misunderstandings. Hydrometallurgy 139:132–148

Crundwell, F., 2015. The semiconductor mechanism of dissolution and the pseudo-passivation of chalcopyrite. Canadian Metallurgical Quarterly: Hydrometallurgy. 54(3):279–288 .

De Silva, V.R.S., Ranjith, P.G., Perera, M.S.A., Wu, B. and Wanniarachchi, W.A.M., 2018. A low energy rock fragmentation technique for in-situ leaching. Journal of Cleaner Production, 204: 586–606.

Dutrizac, J.E., 1981a. Ammoniacal percolation leaching of copper ores. Canadian Metallurgical Quarterly, 20(3): 307–315.

Dutrizac, J.E., 1981b. The dissolution of chalcopyrite in ferric sulfate and ferric chloride media. Metallurgical Transactions B, 12(2): 371–378.

Dutrizac, J.E., 1982. Jarosite-type compounds and their application in the metallurgical industry, 3rd International Symposium on Hydrometallurgy, GECAMIN, Atlanta, Georgia, pp. 531–551.

Dutrizac, J.E., 1990. Elemental sulfurformation during the ferric chloride leaching of chalcopyrite. Hydrometallurgy, 23(2): 153–176.

Dutrizac, J.E., Macdonald, R.J.C. and Ingraham, T.R., 1971. Effect of pyrite, chalcopyrite and digenite on rate of bornite dissolution in acidic ferric sulfate solutions. Canadian Metallurgical Quarterly, 10(1): 3–7.

Eksteen, J.J., Oraby, E.A. and Tanda, B.C., 2017. A conceptual process for copper extraction from chalcopyrite in alkaline glycinate solutions. Minerals Engineering, 108: 53–66.

Fridleifsson, I.B., 1996. Present status and potential role of geothermal energy in the world. Renewable Energy, 8(1): 34–39.

Godel, B., 2013. High-resolution X-Ray computed tomography and its application to ore deposits: from data acquisition to quantitative three-dimensional measurements with case studies from Ni-Cu-PGE deposits. Economic geology, 108(8): 2005–2019.

Hackl, R.P., Dreisinger, D. B., Peters, E., King, J. A., 1995. Passivation of chalcopyrite during oxidative leaching in sulfate media. Hydrometallurgy, 39(1): 25–48.

Halpern, J., Milants, H. and Wiles, D.R., 1959. Kinetics of the dissolution of copper in oxygen-containing solutions of various chelating agents. Journal of the Electrochemical Society, 106(8): 647–650.

Harmer, S.L., Thomas, J.E., Fornasiero, D. and Gerson, A.R., 2006. The evolution of surface layers formed during chalcopyrite leaching. Geochimica et Cosmochimica Acta, 70(17): 4392–4402.

Hidalgo, T., Kuhar, L., Beinlich, A. and Putnis, A., 2018. Kinetic study of chalcopyrite dissolution with iron(III) chloride in methanesulfonic acid. Minerals Engineering, 125: 66–74.

Hidalgo, T., Kuhar, L., Beinlich, A. and Putnis, A., 2019a. Kinetics and mineralogical analysis of copper dissolution from a bornite/chalcopyrite composite sample in ferric-chloride and methanesulfonic-acid solutions. Hydrometallurgy, 188: 140–156.

Hidalgo, T., McDonald, R., Kuhar, L., Beinlich, A. and Putnis, A., 2019b. Staged leaching of bornite with acidic solutions at moderate temperature in an in-situ recovery environment, ALTA in-situ recovery (ISR) symposium, ALTA Perth, Western Australia.

Hirato, T., Majima, H. and Awakura, Y., 1987. The leaching of chalcopyrite with cupric chloride. Metallurgical Transactions B, 18(1): 31–39.

Hiroyoshi, N., Miki, H., Hirajima, T. and Tsunekawa, M., 2000. A model for ferrous-promoted chalcopyrite leaching. Hydrometallurgy, 57(1): 31–38.

Holmes, P., Crundwell, F., 2013. Polysulfides do not cause passivation: Results from the dissolution of pyrite and implications for other sulfide minerals. Hydrometallurgy. 139:101–110

Lázaro, I. and Nicol, M.J., 2003. The mechanism of the dissolution and passivation of chalcopyrite: An electrochemical study. A. Young, C. Anderson, A. James, D. Dreisinger, B. Harris (Ed.), Hydrometallurgy 2003. The Minerals, Metals and Materials Society, Vancouver, Canada, pp. 405–417.

Levit, S.M., 2010. A literature review of effects of ammonia on fish., Center for Science in Public Participation (CSP^2), Bozeman, Montana USA.

Li, Y., Kawashima, N., Li, J., Chandra, A.P. and Gerson, A.R., 2013. A review of the structure, and fundamental mechanisms and kinetics of the leaching of chalcopyrite. Advances in Colloid and Interface Science, 197–198: 1–32.

Litz, L.M., 1982. In-situ uranium mining with oxygen. Society of Mining Engineers of AIME; Littleton, CO; American Institute of Metallurgical Engineers meeting; Las Vegas, NV, USA.

Liu, Z.X., Yin, Z.L., Hu, H.P. and Chen, Q.Y., 2012. Leaching kinetics of low-grade copper ore with high-alkality gangues in ammonia-ammonium sulfate solution. Journal of Central South University of Technology (English edition), 19(1): 77–84.

Lundström, M., Aromaa, J., Forsén, O., Hyvärinen, O. and Barker, M.H., 2005. Leaching of chalcopyrite in cupric chloride solution. Hydrometallurgy, 77(1): 89–95.

Mahajan, V., Misra, M., Zhong, K. and Fuerstenau, M.C., 2007. Enhanced leaching of copper from chalcopyrite in hydrogen peroxide–glycol system. Minerals Engineering, 20(7): 670–674.

McDonald, R.G. and Muir, D.M., 2007. Pressure oxidation leaching of chalcopyrite. Part I. Comparison of high and low temperature reaction kinetics and products. Hydrometallurgy, 86(3): 191–205.

Meyer, M.C., Austin, P. and Tropper, P., 2013. Quantitative evaluation of mineral grains using automated SEM–EDS analysis and its application potential in optically stimulated luminescence dating. Radiation Measurements, 58: 1–11.

Minesota, S., 2019. Ecological effects of ammonia. Minesota Deparment of Agriculture.

Moyo, T., Petersen, J., Franzidis, J.P. and Nicol, M., 2015. An electrochemical study of the dissolution of chalcopyrite in ammonia–ammonium sulfate solutions. Canadian Metallurgical Quarterly, 54(3): 269–278.

Munoz, P.B., Miller, J.D. and Wadsworth, M.E., 1979. Reaction mechanism for the acid ferric sulfate leaching of chalcopyrite. Metallurgical Transactions B, 10(2): 149–158.

Murr, L. and Hiskey, J., 1981. Kinetic effects of particle-size and crystal dislocation density on the dichromate leaching of chalcopyrite. Metallurgical Transactions B, 12(2): 255–267.

Muszer, A., Wódka, J., Chmielewski, T. and Matuska, S., 2013. Covellinisation of copper sulfide minerals under pressure leaching conditions. Hydrometallurgy, 137(C): 1–7.

Nicol, M. and Zhang, S., 2017. The anodic behaviour of chalcopyrite in chloride solutions: Potentiostatic measurements. Hydrometallurgy, 167: 72–80.

Nikkhou, F., Xia, F. and Deditius, A.P., 2019. Variable surface passivation during direct leaching of sphalerite by ferric sulfate, ferric chloride, and ferric nitrate in a citrate medium. Hydrometallurgy, 188: 201–215.

Olubambi, P.A. and Potgieter, J.H., 2009. Investigations on the mechanisms of sulfuric acid leaching of chalcopyrite in the presence of hydrogen peroxide. Mineral Processing and Extractive Metallurgy Review, 30(4): 327–345.

Oraby, E., Eksteen, J., 2014. The selective leaching of copper from a gold–copper concentrate in glycine solutions. Hydrometallurgy, 150: 14–19.

Padilla, R., Pavez, P. and Ruiz, M.C., 2008. Kinetics of copper dissolution from sulfidised chalcopyrite at high pressures in H_2SO_4–O_2. Hydrometallurgy, 91(1): 113–120.

Parker, G.K., Woods, R. and Hope, G.A., 2008. Raman investigation of chalcopyrite oxidation. Colloids and surfaces A: Physicochemical and Engineering Aspects, 318(1): 160–168.

Paulson, S., 1992. Effects of fluid recycling on leach solution composition: implications for copper in situ mining. In situ recovery of minerals II, Edited by S.A. Swan and K.R.Coyne, New York, pp. 51–80.

Petrović, S.J., Bogdanović, G.D. and Antonijević, M.M., 2018. Leaching of chalcopyrite with hydrogen peroxide in hydrochloric acid solution. Transactions of Nonferrous Metals Society of China, 28(7): 1444–1455.

Putnis, A., 2002. Mineral replacement reactions: from macroscopic observations to microscopic mechanisms. Mineralogical Magazine, 66(5): 689–708.

Putnis, A., 2009. Mineral replacement reactions. Reviews in Mineralogy and Geochemistry, 70(1): 87–124.

Putnis, A., 2015. Transient porosity resulting from fluid-mineral interaction and its consequences, Reviews mineral geochemistry, pp. 1–23.

Routschka, G. and Wuthnow, H., 2008. Refractory Materials: Pocket Manual ; Design, Properties, Testing. Vulkan & Verlag, Germany.

Ruiz, M.C., Montes, K.S. and Padilla, R., 2011. Chalcopyrite leaching in sulfate–chloride media at ambient pressure. Hydrometallurgy, 109(1-2): 37–42.

Saxena, N.N. and Mandre, N.R., 1992. Mixed control kinetics of copper dissolution for copper ore using ferric chloride. Hydrometallurgy, 28(1): 111–117.

Schlesinger, M., King, M., Sole, K., Davenport, Wi., 2011. Extractive Metallurgy of Copper 5th edition. Elsevier: Oxford: England.

Schneider, C.A., Rasband, W.S. and Eliceiri, K.W., 2012. NIH Image to ImageJ: 25 years of image analysis. Nature Methods, 9(7): 671–675.

Sekisov, A.G. and Lavrov, A., 2019. Applicability of in-situ leaching and divided blasting combination. IOP Conference Series: Earth and Environmental Science, 262: Challenges for Development in Mining Science and Mining Industry 1–5 October 2018, Novosibirsk, Russian Federation

Seredkin, M., Zabolotsky, A. and Jeffress, G., 2016. In situ recovery, an alternative to conventional methods of mining: Exploration, resource estimation, environmental issues, project evaluation and economics. Ore Geology Reviews, 79: 500–514.

Shiers, D.W., 2016. Review of lixiviants and their suitability for in-situ recovery: Copper sulfides, CSIRO, CSIRO Mineral Resources Perth.

Shiers, D.W., Collinson, D.M., Kelly, N.J. and Watling, H.R., 2016. Copper extraction from chalcopyrite: Comparison of three non-sulfate oxidants, hypochlorous acid, sodium chlorate and potassium nitrate, with ferric sulfate. Minerals Engineering, 85: 55–65.

Sinclair, L. and Thompson, J., 2015. In situ leaching of copper: Challenges and future prospects. Hydrometallurgy, 157: 306–324.

Skrobian, M., Havlik, T. and Ukasik, M., 2005. Effect of NaCl concentration and particle size on chalcopyrite leaching in cupric chloride solution. Hydrometallurgy, 77(1): 109–114.

Sokić, M.D., Marković, B. and Živković, D., 2009. Kinetics of chalcopyrite leaching by sodium nitrate in sulphuric acid. Hydrometallurgy, 95(3-4): 273–279.

Solís-Marcíal, O.J. and Lapidus, G.T., 2014. Chalcopyrite leaching in alcoholic acid media. Hydrometallurgy, 147–148(C).

Tanda, B., Eksteen, J., Oraby, E. and O'Connor, G., 2019. The kinetics of chalcopyrite leaching in alkaline glycine/glycinate solutions. Minerals Engineering 135: 118–128.

Tanda, B.C., 2017. Glycine as a lixiviant for the leaching of low grade copper-gold ores, Thesis disertation, Curtin university, Perth, Australia.

Turan, M.D. and Altundogan, H., 2013. Leaching of chalcopyrite concentrate with hydrogen peroxide and sulfuric acid in an autoclave system. Metallical Materials Transactions B. 44(4): 809–819.

Turan, M.D., Arslanoğlu, H. and Altundoğan, H.S., 2015. Optimisation of the leaching conditions of chalcopyrite concentrate using ammonium persulfate in an autoclave system. Journal of the Taiwan Institute of Chemical Engineers, 50: 49–55.

Velásquez-Yévenes, L., Nicol, M. and Miki, H., 2010. The dissolution of chalcopyrite in chloride solutions: Part 1. The effect of solution potential. Hydrometallurgy, 103(1): 108–113.

Vracar, R., Vuckovic, N. and Kamberovic, Z., 2003. Leaching of copper(I) sulfide by sulphuric acid solution with addition of sodium nitrate. Hydrometallurgy, 70(1-3): 143–151.

Wallace, A.B., 1979. Possible signatures of porphyry-copper deposits in middle to late tertiary volcanic rocks of Western Nevada, Papers on mineral deposits of western north America: The International Association on the Genesis of Ore Deposits Ffth Quadrennial Symposium Proceedings. Nevada Bureau of Mines and Geology, University of Nevada, Reno, pp. 69–76.

Warren, G.W. and Wadsworth, M.E., 1984. The electrochemical oxidation of chalcopyrite in ammoniacal solutions. Metallurgical Transactions B, 15(2): 289–297.

Watling, H., 2015. Review of biohydrometallurgical metals extraction from polymetallic mineral resources. Minerals, 5(1): 1–60.

Watling, H.R., 2013. Chalcopyrite hydrometallurgy at atmospheric pressure: 1. Review of acidic sulfate, sulfate–chloride and sulfate–nitrate process options. Hydrometallurgy, 140: 163–180.

Watling, H.R., Shiers, D.W., Li, J., Chapman, N.M. and Douglas, G.B., 2014. Effect of water quality on the leaching of a low-grade copper sulfide ore. Minerals Engineering, 58: 39–51.

Whitney, D. and Evans, B., 2010. Abbreviations for names of rock-forming minerals. American Mineralogist, 95: 185–187.

Yu, P.H., Hansen, C.K. and Wadsworth, M.E., 1973. A kinetic study of the leaching of chalcopyrite at elevated temperatures. Metallurgical Transactions, 4(9): 2137–2144.

Zhao, J., Brugger, J., Ngothai, Y. and Pring, A., 2014. The replacement of chalcopyrite by bornite under hydrothermal conditions. The American Mineralogist, 99(11–12): 2389.

Chapter 3. Kinetic study of chalcopyrite dissolution with iron(III) chloride in methanesulfonic acid

The suitability of methanesulfonic acid as a copper lixiviant with ferric chloride as an oxidant was studied by analysing the leaching kinetics and by characterising solid residues from leach tests on a chalcopyrite-rich ore sample. The effects of temperature, initial acidity, ferric-ion concentration and particle size were determined. The leach kinetics were dependent on the temperature and particle size, whereas the acid and ferric concentrations had a minimal impact on the leaching rate within the ranges studied. Although a sulfur layer formed on the solid residue, the reaction mechanism could be modelled with the shrinking-core model with surface chemical-reaction control, which implies that lixiviant flow through the sulfur layer did not control the reaction rate. The apparent activation energy was 101 kJ mol^{-1} as calculated by the Arrhenius and 'time-to-a-given-fraction' methods. The activation parameters of the reaction were an enthalpy (ΔH^{++}) of 99.4 kJ mol^{-1}, and an entropy (ΔS^{++}) of –197 J $mol^{-1}K^{-1}$ as calculated by using transition state theory and the Eyring equation.

3.1. Introduction

Pure or alloyed copper is used extensively in society in agriculture, construction, electric appliances and equipment, transport, machinery and medicine (Barceloux, 1999). The increasing demand for this metal and the imbalance between its extraction and the discoveries of copper deposits require the exploitation of refractory and low-grade ores that have previously been regarded as uneconomical (Northey et al., 2014; Tilton and Lagos, 2007). Hydrometallurgical methods have become a feasible approach for copper production, with heap leaching being a common hydrometallurgical technique for low-grade metal extraction (Bartlett, 1997). In-situ recovery (ISR) has been suggested as a profitable alternative to recover copper from inaccessible, deep ore bodies (Northey et al., 2013). Refractory chalcopyrite ($CuFeS_2$) is the most common copper-bearing mineral and represents more than half of global copper mineral reserves (Wang, 2005). Copper extraction from chalcopyrite requires the addition of an oxidant and lixiviant. Several lixiviant–oxidant systems have been tested to provide rapid copper extraction without iron-hydroxy-product-precipitate and

passivation-layer formation (Córdoba et al., 2009). Ferric oxidant has proven to be a viable oxidant for chalcopyrite leaching, particularly in bioleaching systems, and has already been implemented in industrial copper-extraction processes, such as the BioCop, Sepon and Geocoat™ applications (Kowalczuk and Chmielewski, 2008).

Equations (1) to (3) present the reactions between chalcopyrite and ferric chloride in an acid environment. Chalcopyrite oxidation results in sulfur-layer formation, which could result in a coating of the chalcopyrite surface. This sulfur may be oxidised by excess ferric oxidant to form sulfate at a significantly slower rate than the chalcopyrite dissolution. Complete sulfur oxidation within a limited experimental time scale occurs only if the temperature is sufficiently high and if sufficient oxidant is present in the system.

$$CuFeS_2 + 4FeCl_3 \rightarrow CuCl_2 + 5FeCl_2 + 2S^0 \quad (1)$$

$$S^0 + 6FeCl_3 + 4H_2O \rightarrow SO_4^{2-} + 6Fe^{2+} + 8H^+ + 18Cl^- \quad (2)$$

$$CuFeS_2 + 16FeCl_3 + 8H_2O \rightarrow CuCl_2 + 2H_2SO_4 + 17FeCl_2 + 12HCl \quad (3)$$

In the absence of oxidant, chalcopyrite may react with acid to yield soluble copper as shown in Equation (4). This reaction is not spontaneous but has been observed experimentally (Lu et al., 2016).

$$CuFeS_2 + 4H^+ \rightarrow Cu^{2+} + Fe^{2+} + 2H_2S \quad (4)$$

Previous studies with hydrochloric acid and ferric chloride have shown that the main reaction product is elemental sulfur, which forms rapidly during the leaching reaction. Minimal further oxidation of S^0 to sulfate results, despite extended leaching times (Dutrizac, 1990; Jones and Peters, 1976). Equation (1) is believed to be the dominant reaction, followed by a slow conversion of some of the elemental sulfur to sulfate, as was identified by Dutrizac (1990), where more than 95% of the sulfur in sulfide converted to elemental sulfur, and less than 5% sulfate formed. This result was found to be independent of oxidant and acid concentrations.

Several kinetic studies have been conducted over a range of temperatures and pH conditions below 2.5 in the presence of hydrochloric and sulfuric acids to evaluate copper extraction (Table 3-1). Chalcopyrite leaching with ferric chloride is reported to be controlled by an electrochemical reaction at the surface of the mineral. This reaction requires a high energy input because strong chemical bonds in the crystalline structure of the chalcopyrite result in a significant energy consumption by the displacement of ions from bulk of the particle to the surface (Córdoba et al., 2008). The formation of a sulfur surface coating could result in a diffusion-controlled reaction. However, as shown in Table 3-1, most researchers have reported a chemical-reaction-control mechanism rather than diffusion control. Therefore, this sulfur layer appears to allow for continued lixiviant access to the reaction interface, which may indicate that the coating has an elevated porosity (Havlík et al., 1995; Hirato et al., 1986; Rath et al., 1988). Activation energies that have been calculated for chalcopyrite dissolution with ferric chloride vary from 15 kJ mol^{-1} to 93 kJ mol^{-1}, and the reaction kinetics are dependent on the material type (natural or synthetic), particle size and gangue content (Dutrizac, 1981).

Table 3-1. Review of literature on chalcopyrite dissolution with ferric-ion oxidant.

T (°C)	Iron (III) con. (mol L^{-1})	Acid con. (mol L^{-1})	Particle size (µm)	Leach media	E_a (kJ mol^{-1})	Mechanism	Reference
70–100	1	1	– 150+105	Iron(III) chloride in hydrochloric acid	92.8	Surface chemical-reaction control	(Rath et al., 1988)
45–100	0.2	0.3	–20+14	Iron(III) chloride in hydrochloric acid	42	Surface chemical-reaction control	(Dutrizac, 1981)
3.5–80	0.5 – 1	0.25–1	– 315+200	Iron(III) chloride in hydrochloric acid	55	Surface chemical-reaction control	(Havlík et al., 1995)
23–40	0.28	0.25	Disk electrode specimen	Iron(III) chloride in hydrochloric acid	86.4		(Orth and Liddell, 1990)
52–85	0.1	0.2	Disk electrode specimen	Iron(III) chloride in hydrochloric acid	69	Electrochemical kinetics	(Hirato et al., 1986)
75–96	0.1	1	–37+44	Iron(III) chloride in hydrochloric acid	83	Surface chemical-reaction control	(Palmer et al., 1981)
55–94	0.1	0.2	Disk electrode specimen	Iron(III) chloride in hydrochloric acid	69	Surface chemical-reaction control	(Majima et al., 1985)
55–85	0.004	5	-75+38	Iron(III) sulfate in sulfuric acid	22(< 10 h) 73 (>10 h)	Diffusion from the interface to the bulk solution and surface chemical-reaction control	(Kaplun et al., 2011)
52–90	0.25	0.5	< 38	Iron(III) sulfate in sulfuric acid	79.5	Surface chemical-reaction control for monosized particles	(Al-Harahsheh et al., 2005)
45–100	0.2	0.3	–20+14	Iron(III) sulfate in sulfuric acid	75	Diffusion through a product layer	(Dutrizac, 1981)
40–85	1	0.2	Disk electrode specimen	Iron(III) sulfate in sulfuric acid	76.8–87.7	First stage transport control, second stage chemical-reaction control	(Hirato et al., 1987)
35–68	0.08	pH 1.8	70	Iron(III) sulfate in sulfuric acid	130.7	Surface chemical-reaction control	(Córdoba et al., 2008)
60–90	0.25–0.03	1–0.01	12 and 4	Iron(III) sulfate in sulfuric acid	83.7	Electron transport through a product layer	(Munoz et al., 1979)

There has been an increasing interest in hydrometallurgical applications, such as ISR and heap leaching, because of more stringent environmental controls for copper-ore/concentrate processing by conventional pyrometallurgical techniques, which are associated with hydrogen-sulfide and sulfur-dioxide production, and because of the prospect of an increased exploitation of otherwise non-profitable ores (Feng et al., 2015a; U.S Congress, 1988). A major concern related to ISR and heap leaching is the risk of water and soil contamination from the lixiviant and pregnant leach solution (Seredkin et al., 2016), and, therefore, the selection of a lixiviant of low toxicity for subterranean use is desired.

The use of lixiviants with a lower environmental impact is attractive in copper hydrometallurgical applications, such as heap leaching and in-situ recovery, especially if these circumvent potential toxic gas production and surface and groundwater contamination. Hydrochloric or sulfuric acid lixiviants have been used in the ferric-ion system, because the presence of a strong acid accelerates chalcopyrite dissolution (Lu et al., 2000; Lundstrom et al., 2008; Wang, 2005). Despite the potential for use of these acids in heap-leaching and ISR applications, an alternative environmentally friendly lixiviant that is less corrosive than hydrochloric acid would be useful for heap leaching and would facilitate the application of the ISR technology (Noor and Al-Moubaraki, 2008). The environmental advantages of methanesulfonic acid (MSA) include an elevated degradability, a low corrosivity and a lack of hazardous volatile products generation, which make it 'greener' compared with hydrochloric, sulfuric, fluoroboric and nitric acids. Its increasing importance as an electrolyte system (Gernon et al., 1999; Florence et al., 2011) has improved MSA's commercial availability for bulk industrial applications. The average cost of one metric ton of MSA (70% purity) is more than 50% of the cost of sulfuric acid (98% purity) and hydrochloric acid (32% purity). MSA may be perceived to be an expensive reactant and, as such, has not been used extensively in metal-extraction applications. Nonetheless its strong acidity, potential for recycling and its environmental advantages make it a viable alternative for applications such as heap leaching and ISR.

In the presence of MSA, ferric methanesulfonate may form by Equation (5) with subsequent proposed reactions as shown in Equations (6) to (8).

$$FeCl_3 + 3CH_3SO_3H \rightarrow Fe(CH_3SO_3)_3 + 3HCl \quad (5)$$

$$CuFeS_2 + 4Fe(CH_3SO_3)_3 \rightarrow Cu(CH_3SO_3)_2 + 5Fe(CH_3SO_3)_2 + 2S^0 \quad (6)$$

$$S^0 + 6Fe(CH_3SO_3)_3 + 4H_2O \rightarrow SO_4^{2-} + 6Fe^{2+} + 8H^+ + 18CH_3SO_3^- \quad (7)$$

$$CuFeS_2 + 16Fe(CH_3SO_3)_3 + 8H_2O \rightarrow Cu(CH_3SO_3)_2 + 2H_2SO_4 + 17Fe(CH_3SO_3)_2 + 12CH_3SO_3H \quad (8)$$

Organic acids are a possible alternative as less harmful lixiviants, but requirements for a strong acid have limited their applicability (Feng et al., 2015a). Methanesulfonic acid is an organic acid that is formed by the atmospheric oxidation of dimethyldisulfide. Its high dissolving strength and acid strength compared with other organic acids make it suitable for the extraction of heavy metals such as lead and copper. MSA's acid dissociation constant is –1.92, which is higher than that of nitric acid (–1.3) and close to that of sulfuric acid (–2). This strong organic acid is almost 99.8% ionised in a 0.1 mol L^{-1} solution (BASF, 2012; Gernon et al., 1999; Feng et al., 2015a; Patai and Rappoport, 2006; Wu et al., 2014). MSA is readily biodegradable, with sulfate, water, biomass and carbon dioxide being generated as a product of biological activity. MSA's lack of odour, its low toxicity and corrosiveness and the fact that it is unlikely to generate harmful gases during its use make it a "greener" alternative to the sulfuric- and hydrochloric-acid leaching of chalcopyrite and potentially attractive for use in heap-leaching or ISR applications (Hasan and Rohan, 2010). Despite the environmental benefits of this acid having been analysed for other applications, such as electrowinning, catalysts and polymer solvents (Commarieu et al., 2002; Gernon et al., 1999; Florence et al., 2011; Hasan and Rohan, 2010), limited studies have been conducted on the effectiveness of MSA as a lixiviant in hydrometallurgical processes, focused principally on carbonate disolution (Feng et al., 2015a; Feng et al., 2015b; Wu et al., 2014), and its applicability to the leaching of refractory copper minerals such as chalcopyrite has not yet been evaluated. This study aimed at understanding the reaction kinetics of the ferric chloride/MSA system in the dissolution of a natural chalcopyrite sample with gangue inclusions at low to moderate temperatures (< 90°C) to elucidate its possible application in hydrometallurgical processing.

3.2. Experimental

3.2.1. Materials

A chalcopyrite-bearing sample was ball milled and dry sieved. Sized samples were blended with a ball mill and riffle split into representative fractions. Because of the economic advantage of ferric ion as oxidant, the possible biological regeneration of such an oxidant and its compatibility with MSA (Wu et al., 2014), screening experiments with MSA (0.5 mol L^{-1}) and stoichiometric amounts of ferric chloride and ferric sulfate as iron-based oxidants were conducted at 60°C. Copper extractions of 50% were achieved with ferric chloride after 24 h, and the copper extraction with sulfate solution was 20%. Based on these screening tests, ferric chloride was selected as the preferred oxidant in this study.

Stock solutions (3 mol L^{-1} and 0.5 mol L^{-1} free acid, pH –2.44, 707 mV) were prepared in deionised water from analytical-grade anhydrous ferric chloride (98%, Chem Supply, Australia) and MSA (100%, BASF, Germany). The sample mineralogy was determined using a PANalytical Empyrean X-ray diffractometer equipped with a Bragg-Brentano HD incident monochromator. The incident beam working parameters were a 0.5^{o} divergence slit at 40 kV, 40 mA and 0.02 rad soller slits and a 1^{o} antiscatter slit. A pixel three dimensions (3D) array detector in scanning one dimension (1D) mode with 0.125° antiscatter slit and 0.02 rad soller slits were used for the diffracted beam. The scan was performed using theta/theta geometry, with a 3–120^{o} scan range, and a 2-h scanning time. Sample mineral identification was performed using High Score Plus 3.0d.

3.2.2. Methods

Experiments were conducted in a closed tumbling water bath (15 inversions min^{-1}) using 15-mL Nalgene bottles that contained 1 g chalcopyrite-containing sample and 10 mL of lixiviant solution. The baseline experimental conditions are described in Table 3-2. Series of experiments were conducted in which one of the four different parameters investigated (particle size, ferric concentration, MSA concentration and temperature) was varied while the other baseline conditions were maintained constant.

MSA concentrations were varied at 0.05, 0.1, 0.5 and 0.75 mol L^{-1}. A 200% excess of ferric ions was used at concentrations of 1.5, 2, 2.5 and 3 mol L^{-1}. Particle sizes of –106+75 µm, –75+53 µm, –53+45 µm, –45+38 µm and –38 µm and temperatures of 40°C, 50°C, 60°C, 70°C and 90°C were studied.

Table 3-2. Baseline experimental conditions.

Chalcopyrite mass	**1 g**
Solution volume	10 mL
Particle size	–38 µm
$FeCl_3$ concentration	3 mol L^{-1}
MSA concentration	0.5 mol L^{-1}
Solids loaded	10% w/w
Temperature	90 C

The bottle headspace was flushed with high-purity nitrogen gas to minimise the amount of oxygen in the system. Each kinetic data point was determined from an individual experiment. The final solution pH and Eh were measured using a TPS WP-80 pH/ORP meter with double-junction Ag/AgCl/saturated KCl probe. After reaction, solutions were filtered and diluted 300-fold before copper and iron concentrations were determined using an Agilent 240/280 atomic absorption spectrophotometer (AAS) (4–5 mA, 222.6–217.9 nm for copper and 386–392 nm for iron). Solid residues were filtered, rinsed and dried using a vacuum filter and a standard oven at 30°C, and weighed. Solid samples were analysed by quantitative X-ray diffractometry (QXRD), using the same conditions that were used for the initial chalcopyrite sample. Coarse-grained solid residues (–106+75 µm) were mounted on a stub and epoxy mounts and studied by scanning electron microscopy equipped with energy-dispersive spectroscopy (SEM–EDS) using a JEOL-JSM-7001 field emission scanning electron microscope, Bruker Esprit 1.9 EDS system, Bruker 10 mm SDD EDS detector with 125 eV resolution, 20 kV accelerating voltage and a 10-mm working distance in backscattered electron imaging mode.

3.3. Results and discussion

A portion of the initial sample was digested using aqua regia and the solution chemical composition was analysed by inductively coupled plasma–atomic emission

spectroscopy (ICP–AES) (see Table 3-3). The QXRD analysis correlated with the chemical analysis revealed that the initial sample consisted of 67.2% chalcopyrite ($CuFeS_2$), 24.4% quartz (SiO_2) and 8.4% sphalerite (ZnS) (Fig. 3-1).

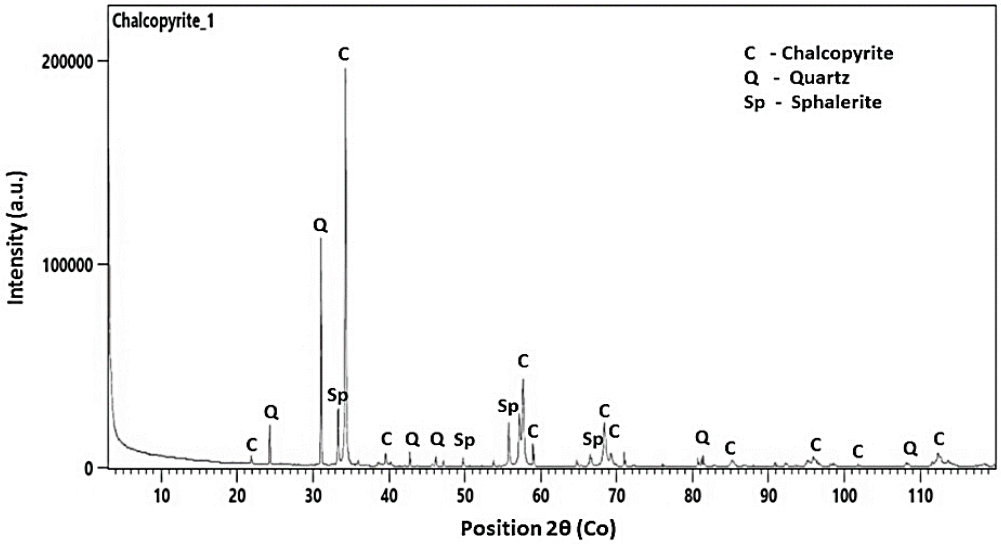

Fig. 3-1. X-ray diffractogram of the initial sample, showing the presence of chalcopyrite, quartz and sphalerite.

Table 3-3. Chemical composition of the initial chalcopyrite sample.

Element	Si	Fe	Al	Ca	Cu	Zn	Ni	Pb	S
wt%	12.1	19.4	0.423	1.39	21.9	4 99	0.833	0.054	24.4

3.3.1. Effect of initial acid concentration

The copper extraction as a function of initial MSA concentration did not vary significantly for the MSA concentrations tested (Fig. 3-2a). The order of the relationship between the MSA concentration and the chalcopyrite dissolution was 0.18, which implies that the dissolution is independent of the initial acid concentration. Ferric and ferrous ions (Fe^{+3} and Fe^{+2}) are highly soluble in MSA (saturation concentrations are 502 g/L and 690 g/L at 23°C, respectively) because of the formation of soluble methanesulfonates, even under neutral pH conditions (BASF, 2012). Therefore, the principal role of the MSA may be to prevent iron hydrolysis by the formation of highly soluble ferrous methanesulfonate $Fe(CH_3SO_3)_2$. If MSA were considered to be active in the formation of copper complexes, a stoichiometric MSA concentration of 0.26 mol L^{-1} would be required for dissolution. In this study, a lower

concentration of MSA than that stoichiometrically required resulted in similar copper extractions, and dissolution is therefore not expected to proceed by the complexation mechanism but rather by Equations (1)–(3) and (5)–(8). However, a minimum MSA concentration of 0.05 mol L^{-1} was required to avoid iron precipitation upon solution cooling to room temperature. The largest difference in leaching occurred for the experiments with 0.1 and 0.5 mol L^{-1} MSA and 4 h, with a difference of 17.5% copper extraction. All experiments that were conducted for 24 h achieved 100% copper extraction, with the final solution pH being below –0.5. This represents an advantage in terms of acid usage because a similar leaching extent can be achieved at a low acid concentration. A similar minor effect of acid concentration has also been observed for lead mineral dissolution, in which strong oxidative mineral attack occurred at low acid concentrations (Wu et al., 2014). We conducted an experiment with 0.5 mol L^{-1} MSA under anaerobic conditions. The result from this text is shown in Fig. 3-2b, in which the copper dissolution was less than 4% during the first 48 h and remained below 30% after more than 10 days of leaching at 90°C. Hydrogen sulfide was generated, which indicates that the reaction proceeded according to Equation (4) and emphasizes the requirement for an oxidant to dissolve the mineral.

3.3.2. Effect of initial iron(III) concentration

The influence of ferric-ion concentration is shown in Fig. 3-2b. The leaching rate increased slightly with an increase in ferric-chloride concentration, but because high initial concentrations were used, this change was small. Hirato et al. (1986) found that, in a hydrochloric-acid system, total copper extractions were more sensitive to ferric-ion concentrations below 1 mol L^{-1}. Complete copper extraction was achieved for all tested concentrations. The relationship between the leaching rate constants and the ferric-chloride concentration is linear with a slope of 0.43, which indicates that the reaction is almost half order with respect to the initial iron concentration, and which is consistent with previously reported slopes of 0.3 to 0.5 and 0.8. It is likely that the different slopes resuleted from variations in solid reactant composition (Ammou-Chokroum et al., 1979; Dutrizac, 1981; Hirato et al., 1986; Majima et al., 1985; Rath et al., 1988).

3.3.3. Effect of particle size

In our experiments, copper extraction was highly dependent on grain size (see Fig. 3-2c). Small increases in the size fraction increased the reaction time to achieve complete copper recovery by several hours. For example, the coarsest particle size required 120 h to achieve total dissolution compared with 8 h that for the finest particle size. The reaction rate of ferric ions and MSA with chalcopyrite was slower than with galena (Wu et al., 2014) but comparable with studies using ferric ion as an oxidant in hydrochloric or sulfuric acids under conditions similar to this study (Munoz et al., 1979; Rath et al., 1988).

3.3.4. Effect of temperature

The effect of temperature is shown in Fig. 3-2d. Copper extraction increased with an increase in temperature because Eq. (1) is endothermic, and energy addition is an important requirement for dissolution. Although a maximum dissolution was not achieved after 168 h at 40^{o}C, Fig. 3-2d suggests that the sample continued to react beyond 168 h. Under established standard conditions, a 120-h time difference to maximum dissolution existed between 90^{o}C and 70^{o}C, a slight increase in temperature has a strong effect on the reaction kinetics. This behaviour may be an indicator of the reaction mechanism because chemical-reaction-controlled processes exhibit large differences for small changes in temperature (Dreisinger and Abed, 2002).

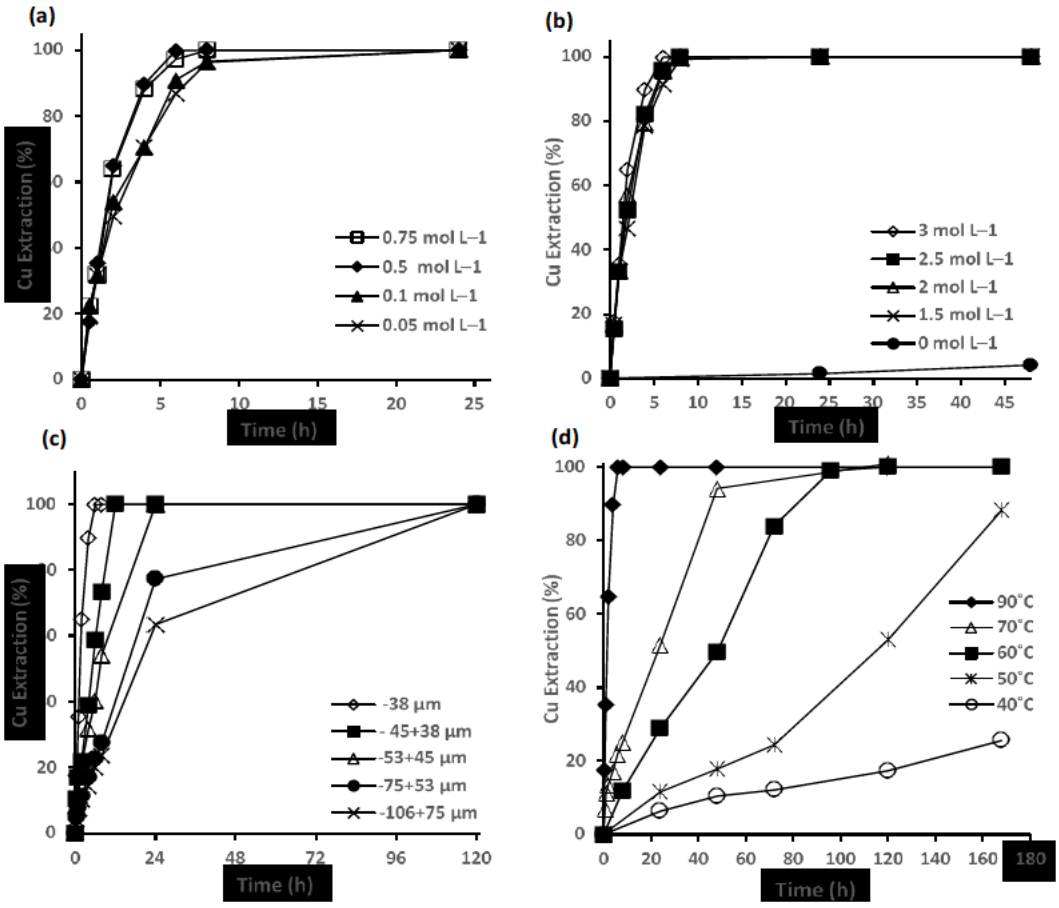

Fig. 3-2. Effect of experimental parameters on copper extraction from chalcopyrite: **a.** MSA concentration, **b.** ferric-ion concentration, **c.** particle size, **d.** temperature.

3.3.5. Kinetic analysis by shrinking-core models

Because chalcopyrite dissolution under acidic conditions is a heterogeneous reaction and depends on the reactant concentration and its change during the reaction, a rate equation can be established to provide the relationship between the experimental data and time. Such functions are usually empirical and are used to determine the reaction mechanism and rate constant (Putnis 1992). The model as given by Eq. (9) provides an integrated rate equation, where k_c is the rate constant, t is the reaction time, x is the fraction transformed and $g(x)$ is a function that describes the variation of x with time.

$$g(x) = k_c t \tag{9}$$

A shrinking-core model was selected, in which the reaction front commences at the outer particle surface and moves into the remaining bulk solid. The reaction rate will

be controlled by the diffusion of reactant to the reaction interface through the surrounding solution, infiltration and diffusion of the reactant within pores to the mineral surface, surface chemical reaction with the solid and element transport from the reaction interface into the bulk solution (Levenspiel, 1999).

Empirical rate equations for heterogeneous reactions have been developed to constrain the reaction control steps and we analysed our experimental data using six equations (Table 3-4). The data that were fitted to the film-diffusion-control model showed the poorest correlation and were discarded. The highest determination coefficients were obtained for the chemical-reaction control equation (with temperature data shown in Fig. 3-3), which confirms the mechanism as suggested by the effect of temperature on the reaction rate and agrees with other published kinetic analyses using ferric ion as an oxidant (Al-Harahsheh and Kingman, 2007; Córdoba et al., 2008; Dutrizac, 1981; Majima et al., 1985; Palmer et al., 1981; Rath et al., 1988). Elemental sulfur in chloride systems is reported to form a porous layer that allows for continued contact with reactants (Hirato et al., 1986; Palmer et al., 1981; Rath et al., 1988), which likely allows for continued lixiviant access to the reaction interface and element transport.

Table 3-4. Determination coefficients (R^2) for six kinetic experimental equations for selected experimental variables

	R^2					
	Film diffusion control	Diffusion control through a product layer (cylindrical particles)	Diffusion control through a product layer (spherical particles)	Surface chemical-reaction control (spherical small or large particles)	Film diffusion control (spherical small particles)	Film diffusion control (spherical large particle)
Variable	x	$x+(1-x)\ln(1-x)$	$1-3(1-x)^{2/3}+2(1-x)$	$1-(1-x)^{1/3}$	$1-(1-x)^{2/3}$	$1-(1-x)^{1/2}$
			Fe^{3+} concentration (mol L^{-1})			
3	0.70	0.98	0.96	0.99	0.87	0.94
2.5	0.81	0.97	0.97	0.99	0.94	0.99
2	0.79	0.99	0.97	0.99	0.93	0.98
1.5	0.83	0.98	0.96	0.99	0.95	0.98
			Particle size (µm)			
38	0.70	0.98	0.96	0.99	0.87	0.94
45	0.97	0.90	0.88	0.99	0.99	0.99
53	0.95	0.92	0.91	0.98	0.99	0.97
75	0.91	0.97	0.97	0.94	0.97	0.93
106	0.97	0.98	0.97	0.92	0.97	0.97
			MSA concentration (mol L^{-1})			
0.75	0.70	0.98	0.99	0.99	0.88	0.95
0.5	0.70	0.98	0.96	0.99	0.87	0.94
0.1	0.78	0.98	0.97	0.98	0.93	0.96
0.05	0.82	0.98	0.96	0.99	0.93	0.97
			Temperature (°C)			
90	0.70	0.98	0.96	0.99	0.87	0.94
70	0.93	0.90	0.88	0.97	0.97	0.98
60	0.99	0.80	0.77	0.94	0.98	0.96
50	0.97	0.73	0.72	0.94	0.96	0.95
40	0.90	0.97	0.97	0.91	0.91	0.91

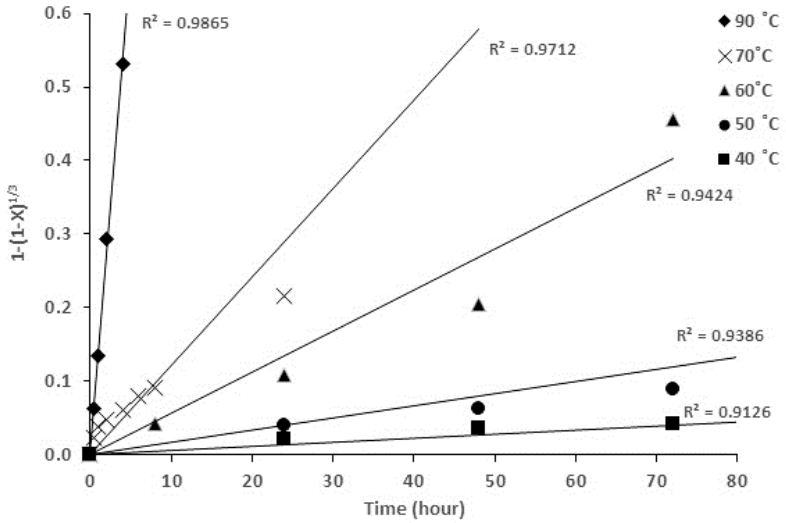

Fig. 3-3. Plot of fitted temperature data by using the chemical-reaction-control model $1\text{-}(1\text{-}x)^{1/3}$

In chemical-reaction control, the rate is proportional to the unreacted core surface area. The reactant concentration in the bulk solution may be considered to be fixed because of the excess that was used. Equation (6) describes the integrated rate equation for chemical-reaction-controlled processes for spherical particles (Levenspiel, 1999), where x is the fraction of reacted solid, τ is the time required to reach complete conversion of the core ($r = 0$) and k_c is the kinetic rate constant given by the inverse of τ (Eq. (10)).

$$\frac{t}{\tau} = k_c t = 1 - (1 - x)^{\frac{1}{3}} \tag{10}$$

The activation energy *(Ea*) was determined by Arrhenius's law (Eqs (11)) (Levenspiel, 1999). The rate constants (k_c) for each temperature were obtained from the slopes of the lines in Fig. 3-4. A plot of ln k_c versus *1/T* (Eq. (12)) allows for the value of the apparent activation energy and the frequency factor (*A*) to be calculated (Fig. 3-4a).

$$k_c = Ae^{-\frac{Ea}{RT}} \tag{11}$$

Rearranging the equation for plotting purposes yields:

$$ln\, k_c = -\frac{Ea}{R}\left(\frac{1}{T}\right) + ln\, A \tag{12}$$

Other activation parameters were estimated by using the transition-state theory. The relationship between the temperature and the reaction rate constant is given by the Eyring equation (Eq. (13)) (Kuhn, 2000). The differential form of this equation relates the activation enthalpy term to the activation energy (Eq. (14)).

$$k_c = \frac{k_b T}{h} e^{\frac{-\Delta G^{++}}{RT}} \quad (13)$$

$$Ea = \Delta H^{++} + RT \quad (14)$$

Linearisation to give Eq. (15) allows for a determination of the activation parameters (enthalpy and entropy) from a plot of $T\ x\ ln\ (k_c/T)$ versus T for the calculation of ΔH^{++} from the intercept and ΔS^{++} from the slope (Lente et al., 2005) (Fig. 3-4b). The Boltzmann and Planck constants were $k_b = 1.381 \times 10^{-23}$ J K^{-1} and $h = 6.626 \times 10^{-34}$ J s, respectively.

$$T\ ln\left(\frac{k_c}{T}\right) = T\left[ln\left(\frac{k_b}{h}\right) + \frac{\Delta S^{++}}{R}\right] - \frac{\Delta H^{++}}{R} \quad (15)$$

ΔH^{++} and ΔS^{++} can be used to obtain the free energy as shown in Eq. (16).

$$\Delta G^{++} = \Delta H^{++} - T\Delta S^{++} \quad (16)$$

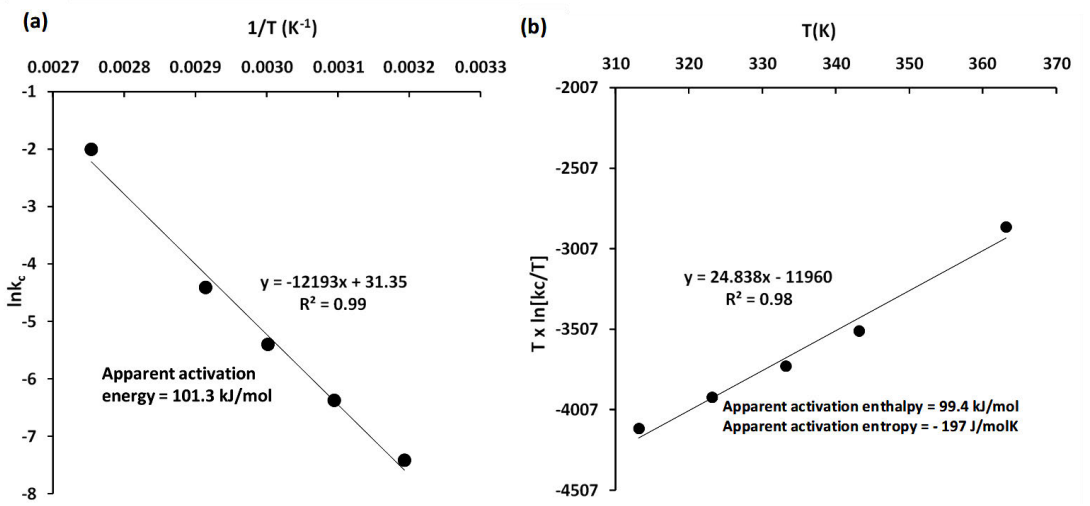

Fig. 3-4. Activation parameter determination. **a.** Arrhenius plot for chalcopyrite dissolution using data from the experimental kinetic equation for a chemical-reaction-controlled model, **b.** Eyring plot for chalcopyrite leaching.

The apparent activation energy as calculated using the shrinking-core model was 101.3 kJ mol^{-1}. This value is consistent with the selected empirical equations that were used to describe the reaction mechanism, even though it exceeds 55 to 88 kJ mol^{-1} as found previously for the ferric oxidant (Table 3-1)**.** However, it is closer to the 131 kJ mol^{-1} and 93 kJ mol^{-1} values that were determined for ferric-ion leaching by Córdoba et al. (2008) and Rath et al. (1988), respectively. Dutrizac (1981) described the gangue content or non-copper-containing minerals in the sample as a 'complication factor' that may influence the activation energy if the gangue minerals are reactive. Because our sample contained 33% non-copper-containing minerals, a higher activation energy compared with the fairly pure chalcopyrite concentrate that was analysed in previous studies appears to be reasonable. The use of impure chalcopyrite for kinetics analysis provides a more realistic representation of a potential practical application. The current high value could also be explained by the crystal structure of chalcopyrite and its semiconductor nature, where ion transport to energy vacancies and electrons (Fe^{+2} and Cu^{+}) through the crystal lattice to the surface requires a high energy consumption (Córdoba et al., 2008; Hiskey, 1993; Parker et al., 1981). The frequency of the collisions as a determinant factor of the reaction speed was found to be 4.12×10^{13} h^{-1} by using the Arrhenius law, which indicates a slow reaction, as evidenced in practice. The activation enthalpy and entropy values as calculated from the transition-state-theory Eyring plot were 99.4 kJ mol^{-1} and -197 J $mol^{-1}K^{-1}$, respectively. The small difference between this value and the activation energy of 101.4 kJ mol^{-1} is reasonable for a near-ambient temperature, where Ea $\cong$ ΔH^{++} (see Eq. (14)). The entropy is in the same range as that obtained by Dreisinger and Abed (2002) for reductive leaching of chalcopyrite in sulfate and chloride media (–212.4 J $mol^{-1}K^{-1}$ and –242 J $mol^{-1}K^{-1}$, respectively). The negative value of the entropy and positive free energy and enthalpy is indicative of a non-spontaneous reaction at any temperature and the formation of a transition-state complex.

The activation-energy estimation as based on empirical mechanism equations has the disadvantage of being dependent on the subjective selection of a rate function. The determined rate constant has a significant impact on the activation energy. This limitation and the inability to identify changes in mechanism and hence activation

energy values during the reaction suggest the necessity for an alternative verification methodology (Putnis, 1992). An independent method, which is termed the 'time to a given fraction' is based on the relationship between the reacted fraction x and the time t (Eq. (17)), where time is a dependent variable, as shown in Eq. (18).

$$\frac{dx}{dt} = k_c . f(x) \tag{17}$$

$$dt = {k_c}^{-1} . f^{-1}(x)\, dx \tag{18}$$

Integration between the initial and final fractions yields Eqs (19) to (21), where Ea represents the apparent activation energy in the specific time required to reach a certain reaction progress.

$$t_x = {k_c}^{-1} \int_{x=0}^{x=x_1} f^{-1}(x) dx \tag{19}$$

$$t_x \propto A^{-1}\, e^{-\frac{Ea}{RT}} \text{ If } t_x \propto {k_c}^{-1} \tag{20}$$

$$\ln t_x = const - \ln A + \frac{Ea}{R}\left(\frac{1}{T}\right) \tag{21}$$

Similar to an Arrhenius plot, the plot of ln t_x versus *1/T* produces a line with slope *Ea/R*, from which it is possible to calculate the activation energy for a specific reacted fraction *x*. The calculation of *Ea* for different fractions enables the monitoring of possible changes in the reaction mechanism (Putnis, 1992; Qian et al., 2017). Two fractions were analysed. The points at 20% and 50% represent the initial and midpoint in the reaction, respectively, where no points of inflexion were found (Fig. 3-5). The calculated Ea values were 101.2 kJ mol^{-1} and 94.9 kJ mol^{-1}, respectively, which confirmed the choice of chemical reaction as the rate-controlling step. Table 3-5 summarizes the calculated rate constants for both methods. The experimental points fit all linear regressions plots, and the determination coefficients exceed 0.98.

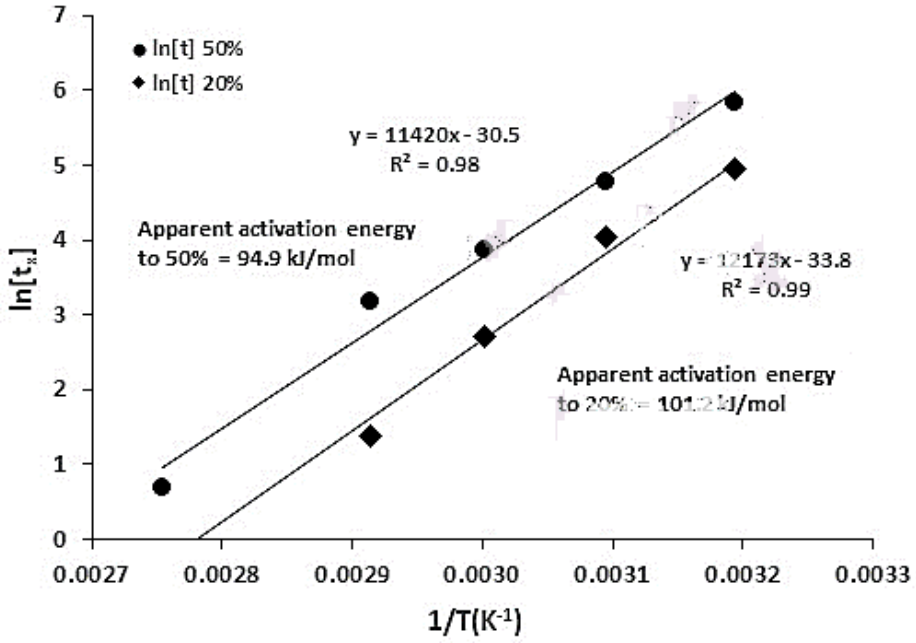

Fig. 3-5. Temperature data plotted as time-to-50% and -20% chalcopyrite leaching (x = 0.5 and x = 0.2) versus 1/T using the 'time-to-a-given-fraction' method for activation-energy determination.

Table 3-5. Kinetics rate constants for chalcopyrite dissolution as a function of temperature for the Arrhenius and 'time-to-a-given-fraction' methods

T (°C)	T (K)	1/[T] (K^{-1})	Rate constant k (h^{-1})	ln k	ln (k/T)	Time to 50% Cu (h)	Time to 20% Cu (h)	ln t_x to 50% Cu (h)	ln tx to 20% Cu (h)
90	363.15	2.75×10^{-3}	1.34×10^{-1}	-2.01	-7.91	2	0.8	0.69	-0.22
70	343.15	2.91×10^{-3}	1.21×10^{-2}	-4.41	-10.25	24	4	3.18	1.39
60	333.15	3.00×10^{-3}	4.50×10^{-3}	-5.40	-11.21	48	15	3.87	2.70
50	323.15	3.09×10^{-3}	1.70×10^{-3}	-6.38	-12.16	120	57	4.79	4.04
40	313.15	3.19×10^{-3}	6.00×10^{-4}	-7.42	-13.17	345	140	5.84	4.94

3.3.6. Residue characterisation

Residue samples from the –106+75 µm chalcopyrite fraction were studied by qualitative XRD and SEM. Samples were taken after 0.5 h, 1 h, 2 h, 4 h, 6 h and 8 h of leaching, as shown in Fig. 3-6. The main chalcopyrite peak at 34.24° existed in all patterns, but the peak intensity decreased by ~74% between the initial and final curves. The main sulfur peak at 26.87° increased in the first 8 h in proportion to the decrease in chalcopyrite.

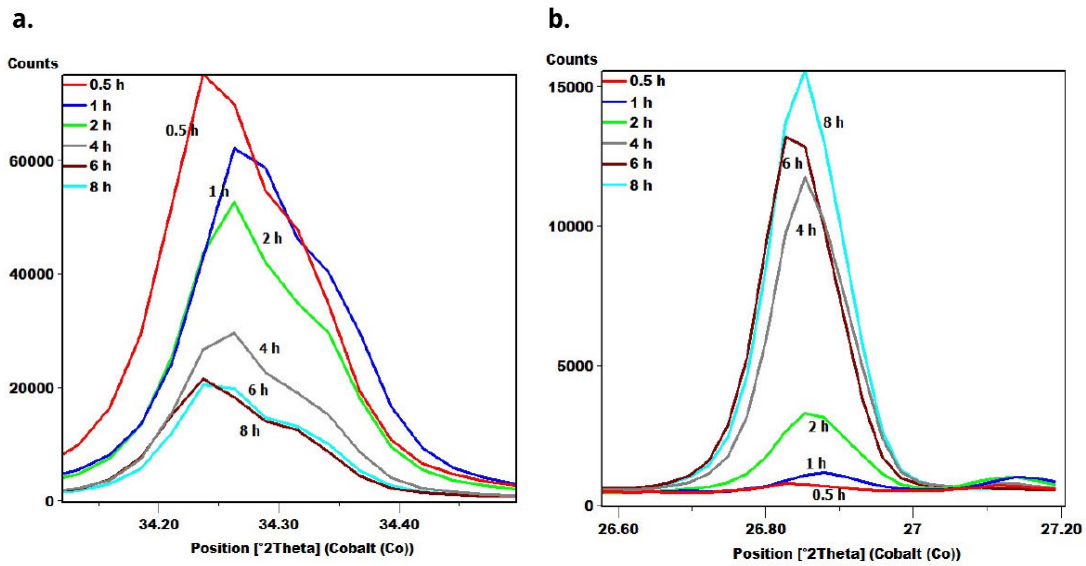

Fig. 3-6. X-ray diffractogram showing changes in peak intensity for six reaction times (0.5 h, 1 h, 2 h, 4 h, 6 h and 8 h) and for the –106+75-µm fraction at 90°C: **a**. Main chalcopyrite peak at 34.24° **b.** Main elemental sulfur peak at 26.87°.

The identification of sulfur as a reaction product was corroborated by SEM. Figures 3-7a to 3-7b show images of unpolished chalcopyrite grains after 8 h of leaching. Entire grains were covered by irregular interconnected globular grains of sulfur. The layer morphology had an intergranular porosity that allows for continuous flow between the bulk reactant and the chalcopyrite. As the leaching progressed, open spaces in the chalcopyrite decreased as is evident in the micrographs. However, fluid diffusion through the product layer was not the rate-controlling step in the reaction, because the product layer was sufficiently porous and did not provide a barrier to continuous leaching, as was observed by Majima et al. (1985). No other phases, such as secondary copper sulfides or oxides, were found in cross sections of the samples. Such an observation may correspond to the stoichiometric dissolution of iron and copper or to the rapid formation and dissolution of intermediate phases, which may only be identified in in-situ experiments.

Cracks in the chalcopyrite particles were visible in cross-sectional SEM micrographs; these may be reaction-enhanced fractures that form from volume reduction after copper and iron leaching and may allow for sulfur retention or promote reagent access via generated rather than natural fractures.

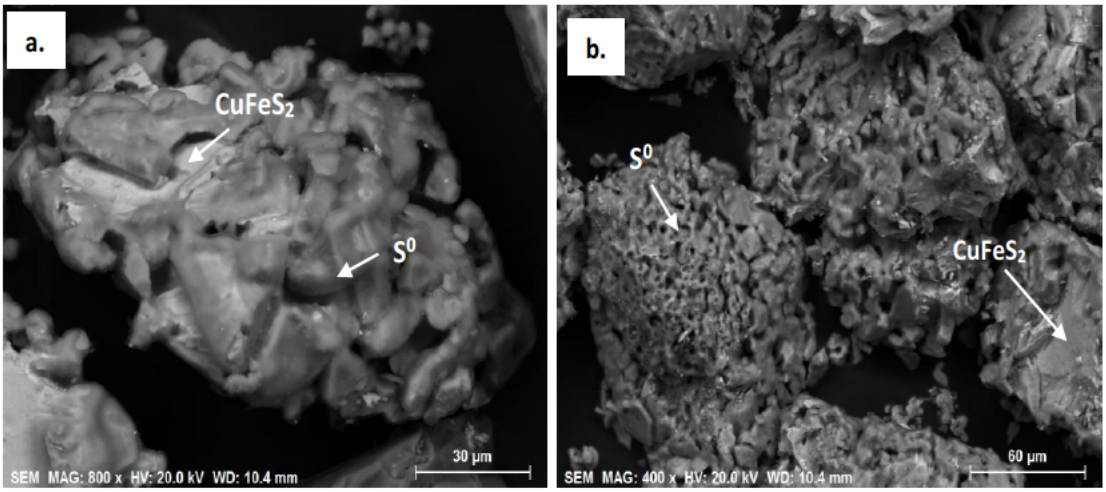

Fig. 3-7. Scanning electron photomicrographs of –106+75 µm chalcopyrite after 8 h leaching under baseline conditions **a**. Magnified chalcopyrite particle that is encased almost entirely with a sulfur layer of 'cap head' globular masses with interconnected spaces. Pores in the sulfur allow for flow between the sample and the bulk reactant. **b.** Covered chalcopyrite particles with internal spaces in the sulfur that allow for flow between the sample and the bulk reactant.

3.4. Concluding remarks

The leaching kinetics for an impure chalcopyrite sample with ferric-chloride solution in MSA was studied as a function of four parameters. The MSA concentration had a minor influence on the leaching rate and copper extraction was possible even at the lowest acid concentration. Because excess oxidant was provided, no ferric-ion regeneration was required, and the principal role of the acid was to prevent hydrolysis. Additional experiments are required to determine the lowest acid concentration prior to which iron hydrolysis becomes problematic. The ferric-ion concentration did not have a major influence on the kinetics within the range tested (1.5–3 mol L^{-1}) and there is an approximately half-order dependence on the ferric-ion concentration. The particle size and temperature had a significant influence on the kinetics, with large changes in reaction rate occurring for small variations in time. Temperature data analysis indicated that the reaction kinetics are controlled by chemical reaction. This finding was supported by a calculation of the apparent activation energy by different methods. The average apparent activation energy was 101.3 kJ mol^{-1} as determined by the Arrhenius equation, and 94.95 kJ mol^{-1} and 101.21 kJ mol^{-1} for 20% and 50%

dissolutions, respectively, by the ‘time-to-a-given-fraction’ method. Globular elemental sulfur encapsulated entire chalcopyrite particles with intergranular porosity that allowed for lixiviant access to the reaction interface. MSA addition did not appear to influence the texture of the reacted chalcopyrite. For hydrometallurgical applications, such as in a heap-leaching or an ISR application, the use of a biodegradable and recyclable acid, together with ferric ions and chloride-containing brine would constitute a reliable option for chalcopyrite extraction. Because of its environmental advantages, such as its low corrosiveness and biodegradability, MSA could represent a viable option for ISR operations.

Acknowledgments

MRIWA (Project M488), BASF, Curtin University and CSIRO are gratefully acknowledged for funding this work. The authors would like to thank Peter Austin and Milan Chovancek for their help with the analysis, and Denis Shiers and Robbie McDonald for reviewing a draft of this manuscript.

Nomenclature

A	pre-exponential factor
b	stoichiometric coefficient
Ea	activation energy
ΔG^{++}	Gibbs energy of activation
h	Planck's constant
ΔH^{++}	enthalpy of activation
k_B	Boltzmann's constant
k_c	apparent reaction rate constant
r	radius of unreacted particle at time t
r_0	initial particle radius
R	ideal gas constant
ΔS^{++}	entropy of activation
t	time
t_x	time to transform a given fraction
T	recorded temperature

τ time to completely consume the particle

x fraction reacted

References

Al-Harahsheh, M. and Kingman, S., 2007. The influence of microwaves on the leaching of sphalerite in ferric chloride. Chemical Engineering; Processing: Process Intensification, 46(10): 1246–1251.

Al-Harahsheh, M., S. Kingman, N. Hankins, C. Somerfield, S. Bradshaw & W. Louw, 2005.., 2005. The influence of microwaves on the leaching kinetics of chalcopyrite. Minerals Engineering, 18(13): 1259–1268.

Ammou-Chokroum, M., Sen, P. and Fouques, F., 1979. Electro-Oxidation of chalcopyrite in an acid chloride medium. I.--Merit and kinetics of the reaction (In French). Revue de Métallurgie / Mémoires et Études Scientifiques, Apr. 1979: 47.

Barceloux, D.G., 1999. Copper. Journal of Toxicology: Clinical Toxicology, 37(2): 217–230.

Bartlett, R.W., 1997. Metal extraction from ores by heap leaching. Metallurgical and Materials Transactions B, 28(4): 529–545.

BASF, 2012. Lutropur - the friendly acid. Chemical & Engineering News Archive, 90(36): 41.

Commarieu, A., Hoelderich, W., Laffitte, J.A. and Dupont, M.-P., 2002. Fries rearrangement in methane sulfonic acid, an environmental friendly acid. Journal of Molecular Catalysis A: Chemical, 182-183(Supplement C): 137–141.

Córdoba, E.M., Muñoz, J.A., Blázquez, M.L., González, F. and Ballester, A., 2008. Leaching of chalcopyrite with ferric ion. Part II: Effect of redox potential. Hydrometallurgy, 93(3): 88–96.

Córdoba, E.M., Muñoz, J.A., Blázquez, M.L., González, F. and Ballester, A., 2009. Passivation of chalcopyrite during its chemical leaching with ferric ion at 68 °C. Minerals Engineering, 22(3): 229–235.

Gernon, M., Wu, M., Buszta, T. and Janney, P., 1999. Environmental benefits of methanesulfonic acid. Comparative properties and advantages. Green Chemistry, 1(3): 127–140.

Dreisinger, D. and Abed, N., 2002. A fundamental study of the reductive leaching of chalcopyrite using metallic iron part I: kinetic analysis. Hydrometallurgy, 66(1): 37–57.

Dutrizac, J., 1990. Elemental sulfur formation during the ferric-chloride leaching of chalcopyrite. Hydrometallurgy, 23(2-3): 153–176.

Dutrizac, J.E., 1981. The dissolution of chalcopyrite in ferric sulfate and ferric chloride media. Metallurgical Transactions B, 12(2): 371–378.

Feng, Q., Wen, S., Zhao, W., LV, C. and Bai, X., 2015a. Leaching of copper from malachite with methane-sulfonic acid. Solvent Extraction Research and Development, Japan, 22: 1037.

Feng, Q., Wen, S.M., Zhao, W., Bai, X. and Chen, Y., 2015b. Dissolution regularities of smithsonite in methane sulfonic acid. Russian Journal Non-Ferrous Metals, 56(4): 365–371.

Florence, F., Nisha, S., Rajendran, K.N., Srinivasan, S. and John, S., 2011. Studies on electrodeposition of copper from methanesulphonic acid bath. International Journal of ChemTech Research, 3(3): 1318–1325.

Hasan, M. and Rohan, J.F., 2010. Cu electrodeposition from methanesulfonate electrolytes for ULSI and MEMS applications. Journal of the Electrochemical Society, 157(5): D278–D282.

Havlík, T., Škrobian, M., Baláž, P. and Kammel, R., 1995. Leaching of chalcopyrite concentrate with ferric chloride. International Journal of Mineral Processing, 43(1-2): 61–72.

Hirato, T., Kinoshita, M., Awakura, Y. and Majima, H., 1986. The leaching of chalcopyrite with ferric chloride. Metallurgical Transactions B, 17(1): 19–28.

Hirato, T., Majima, H. and Awakura, Y., 1987. The leaching of chalcopyrite with ferric sulfate. Metallurgical Transactions B, 18(3): 489–496.

Hiskey, J., 1993. Chalcopyrite semiconductor electrochemistry and dissolution, In: The Paul E.Queneau International Symposium. Extractive Metallurgy of Copper, Nickel and Cobalt. Published by Minerals, Metals, & Materials Society, pp. 949–969.

Jones, D.L. and Peters, E., 1976. Leaching of chalcopyrite with ferric sulfate and ferric chloride., In: Yannapolous, J.C., Agarwal. J.C. (Ed.),Extractive Metallurgy of Copper, pp. 633–653.

Kaplun, K., Li, J., Kawashima, N. and Gerson, A.R., 2011. Cu and Fe chalcopyrite leach activation energies and the effect of added Fe^{3+}. Geochimica et Cosmochimica Acta, 75(20): 5865–5878.

Kowalczuk, P. and Chmielewski, T., 2008. Search for a New Technology Producing Copper from Chalcopyrite, Interdisciplinary Topics in Mining and Geology, 7th Ph.D. Studies Scientific Conference, Wroclaw, pp. 94–100.

Kuhn, H., 2000. Principles Of Physical Chemistry : Understanding Molecules, Molecular Assemblies, Supramolecular Machines. Wiley, Chichester, U.K.

Levenspiel, O., 1999. Chemical Reaction Engineering. Wiley, New York.

Lu, D., Wang, W., Chang, Y., Xie, F. and Jiang, K., 2016. Thermodynamic analysis of possible chalcopyrite dissolution mechanism in sulfuric acidic aqueous solution. Metals, 6(12): 303.

Lu, Z.Y., Jeffrey, M.I. and Lawson, F., 2000. The effect of chloride ions on the dissolution of chalcopyrite in acidic solutions. Hydrometallurgy, 56(2): 189–202.

Lundstrom, M., Aromaa, J., Forsen, O. and Barker, M., 2008. Reaction product layer on chalcopyrite in cupric chloride leaching. Canadian Metallurgical Quarterly, 47(3): 245–252.

Majima, H., Awakura, Y., Hirato, T. and Tanaka, T., 1985. The Leaching of chalcopyrite in ferric chloride and ferric sulfate solutions. Canadian Metallurgical Quarterly, 24(4): 283–291.

Munoz, P.B., Miller, J.D. and Wadsworth, M.E., 1979. Reaction mechanism for the acid ferric sulfate leaching of chalcopyrite. Metallurgical Transactions B, 10(2): 149–158.

Noor, E.A. and Al-Moubaraki, A.H., 2008. Corrosion behavior of mild steel in hydrochloric acid solutions. International Journal of Electrochemical Science, 3(7): 806–818.

Northey, S., Haque, N. and Mudd, G., 2013. Using sustainability reporting to assess the environmental footprint of copper mining. Journal of Cleaner Production, 40(Supplement C): 118–128.

Northey, S., Mohr, S., Mudd, G.M., Weng, Z. and Giurco, D., 2014. Modelling future copper ore grade decline based on a detailed assessment of copper resources and mining. Resources, Conservation and Recycling, 83(Supplement C): 190–201.

Orth, R.J. and Liddell, K.C., 1990. Rate law and mechanism for the oxidation of copper(I) by iron(III) in hydrochloric acid solutions. Industrial & Engineering Chemistry Research, 29(7): 1178–1183.

Palmer, B.R., Nebo, C.O., Rau, M.F. and Fuerstenau, M.C., 1981. Rate phenomena involved in the dissolution of chalcopyrite in chloride bearing lixiviants. Metallurgical Transactions B, 12(3): 595–601.

Parker, A.J., Paul, R.L. and Power, G.P., 1981. Electrochemical aspects of leaching copper from chalcopyrite in ferric and cupric salt solutions. Australian Journal of Chemistry, 34: 13–34.

Patai, S. and Rappoport, Z., 2006. The Chemistry of Sulphonic Acids, Esters and their Derivatives. Wiley, pp. 1–1121.

Putnis, A., 1992. Introduction to Mineral Sciences. Cambridge University Press, 310–321 pp.

Qian, G., Li, Y., Li, J. and Gerson, A.R., 2017. Consideration of enthalpic and entropic energy contributions to the relative rates of chalcopyrite dissolution in the presence of aqueous cationic impurities. International Journal of Mineral Processing, 159: 42–50.

Rath, P.C., Paramguru, R.K. and Jena, P.K., 1988. Kinetics of dissolution of sulfide minerals in ferric chloride solution, 1: Dissolution of galena, sphalerite and chalcopyrite. Transactions of the Institution of Mining and Metallurgy, 97: 150–158.

Seredkin, M., Zabolotsky, A. and Jeffress, G., 2016. In situ recovery, an alternative to conventional methods of mining: Exploration, resource estimation, environmental issues, project evaluation and economics. Ore Geology Reviews, 79: 500–514.

Tilton, J.E. and Lagos, G., 2007. Assessing the long-run availability of copper. Resources Policy, 32(1): 19–23.

U.S Congress, O.O.t.a., 1988. Copper, Technology & Competitiveness. DIANE Publishing, Washington D.C.

Wang, S., 2005. Copper leaching from chalcopyrite concentrates. Journal of the Minerals, Metals & Materials Society (JOM), 57(7): 48–51.

Wu, Z., Dreisinger, D.B., Urch, H. and Fassbender, S., 2014. The kinetics of leaching galena concentrates with ferric methanesulfonate solution. Hydrometallurgy, 142: 121–130.

Chapter 4. Kinetics and mineralogical analysis of copper dissolution from a bornite/chalcopyrite composite sample in ferric-chloride and methanesulfonic-acid solutions

Ore samples contain a variety of copper-bearing and gangue minerals that affect the leach kinetics. The kinetic behaviour of a natural ore sample (that contained 48.7% bornite and 15.8% chalcopyrite) in a solution of methanesulfonic acid and ferric chloride was studied. The dependence of the reaction kinetics on the acid and oxidant concentrations, temperature and particle size was investigated. The reaction activation energy was calculated using two methods, by empirical kinetic equations and by the 'time-to-a-given-fraction' method. The shrinking-core-model was fitted according to diffusion through a product layer, and an average apparent activation energy of 79.3 kJ mol^{-1} was obtained. Three apparent activation energies were obtained by the 'time-to-a-given-fraction' method; that for a copper extraction below 20% was 15.6 kJ mol^{-1} for copper intermediate formation, that between 20% and 50% copper extraction was 42.3 kJ mol^{-1} associated with sulfur formation and that for dissolution above 50% was 76.5 kJ mol^{-1} for the final stage when the sulfur layer is covering the entire particle surface. The presence of chalcopyrite in the sample increased the average activation energy by 69% compared with a pure bornite sample. The leach products had different textures; the sulfur formed from chalcopyrite showed a more porous texture than that formed from bornite. These differences in texture are expected to affect the lixiviant access.

4.1. Introduction

Copper is a versatile material with specific properties, including a high conductivity and malleability (Barceloux, 1999). The continuous demand for copper in conjunction with the depletion in accessible reserves require alternative processing routines for low-grade and abandoned ores (Ata et al., 2001). However, hydrometallurgical processing of certain copper-bearing minerals, such as refractory sulfides, remains challenging. Oxide leaching is conducted by acid dissolution (Kelm and Helle, 2005; Khalezov et al., 1979; Nicol, 2018), but because of the high acid consumption, alkaline systems are also being considered as a viable leaching alternative (Aracena et al., 2018;

Ekmekyapar et al., 2015; Tanda et al., 2017). The processing of refractory copper sulfides is important, because these minerals comprise a large proportion of global copper. Chalcopyrite ($CuFeS_2$) is the world's most abundant copper mineral, and, together with chalcocite (Cu_2S) and bornite (Cu_5FeS_4), may represent the main source of copper when easily processed copper ores have been depleted. Bornite is frequently found in mixed deposits, together with other refractory copper minerals, such as chalcopyrite and chalcocite (Dutrizac et al., 1970; Wang et al., 2016). Kinetic studies are often conducted on pure mineral samples to provide a fundamental understanding of dissolution behaviour. However, in practice, natural samples contain a distribution of mineral types, which may host the same element of interest. An understanding of composite-sample leaching kinetics provides useful information for application to hydrometallurgical operations where the selection of pure minerals is not an option, such as in in-situ recovery (ISR) processing.

A sample that contained copper minerals in the form of bornite and chalcopyrite was used in this study. Although reviews exist on chalcopyrite leaching (Li et al., 2013), no extensive recent review has been provided on bornite leaching. For this reason, relevant studies in this field are presented chronologically below.

Studies on bornite kinetics date back to the 1930s, when Sullivan (1931) studied pure natural bornite dissolution in ferric-sulfate solution. He found that a rapid first-stage mineral dissolution occurred before sulfur formation, with a leaching rate that was strongly dependent only on temperature changes. The mechanism that determines the rate equation, the activation energy and the mineralogical transformations has been under discussion ever since. Lowe (1970) found that the rate is affected by time and that the activation energies differed depending on the residue depth in relation to the sample surface. Dutrizac and MacDonald (1973) confirmed that the role of the acid is to "assist" with ferric solubility, and it does not participate actively in the reaction.

Ugarte-Alverez (1971) described a variation in leaching behaviour above and below 40°C, and suggested idaite (Cu_3FeS_4) as the principal product of bornite leaching. He also found that at high temperature, two stages resulted; the first showed a rapid copper extraction of 40% without sulfur formation and no iron leaching, followed by a slower dissolution stage where an intermediate solid phase was covered by elemental sulfur product. Price and Chilton (1981) identified two products only during the

electroleaching of pure bornite when using sulfuric-acid solutions; $Cu_{2.5}FeS_4$ formed when current was applied and Cu_2S formed under controlled experiments without current. Pesic and Olson (1983) found similar results for chloride solutions compared with those for sulfate systems, but with a faster first-stage dissolution. The reaction was divided into two main stages with an interim transition period. Dutrizac et al. (1985) defined products that formed at different times and temperatures as non-stoichiometric bornite, digenite, chalcopyrite and an intermediate isotropic copper sulfide with a chalcopyrite-like structure and a variable composition from $Cu_{4.1}FeS_4$ to Cu_3FeS_4. These minerals yielded soluble copper and sulfur as the final products.

Table 4-1 presents a summary of the bornite kinetic-leaching studies in which activation energies and reaction mechanisms were reported. Additional recent studies on bornite leaching behaviour, such as by Lundström et al. (2016), Veloso et al. (2016), Yang et al. (2018) and Zhao et al. (2015) have not been included in Table 4-1, as these studies did not report activation energies.

Wall et al. (2011) investigated bornite dissolution by real-time *in-situ* x-ray powder diffraction (XRD), which showed a significant unit-cell variation during its dissolution in ferric-sulfate solution. The results included a real-time analysis of product formation and indicated a significant variation of the unit cell during the first 7% copper dissolution. The leaching of impure samples with different contents of bornite and gangue minerals has not been studied extensively, but most recent studies note the co-presence of chalcopyrite as a sample phase. Other studies have been performed to understand the interaction of chalcopyrite and bornite on the enhanced rate of bornite leaching by using mixed or separate samples (Dutrizac et al., 1971; Lu and Dreisinger, 2013; Wang et al., 2016) but the influence of the presence of other copper minerals on the kinetic mechanism and activation-energy requirements has not been determined.

Table 4-1. Review of literature on bornite kinetics and reported activation energies and leaching mechanisms.

Leach media	Activation energy (kJ/mol)	Mechanism	Product phases	Reference
Iron(III) chloride in hydrochloric acid	24.78 (0.5–30 C) 76.80 (> 30 C) and 40% 30 (> 30 C) and 55%	Mixed-control diffusion of ferric ions across solution boundary and chemical-reaction control (< 40%) Diffusion through a sulfur product layer (> 40%)	Copper extraction Cu_3FeS_4 (< 28%) Copper extraction Cu_3FeS_4 and S_0 (28% to 40%) Copper extraction S_0 (> 40%)	Pesic and Olson (1983)
Iron(III) sulfate in sulfuric acid	26.94 to 51.33	Solid-state diffusion	Cu_3FeS_4 and S_0	Lowe (1970)
Iron(III) sulfate in sulfuric acid	22.17 (> 40 C) 25.94 (< 40 C)	Liquid diffusion control	Non-stoichiometric bornite, Cu_3FeS_4, high sulfur content chalcopyrite and S_0 (> 40 C) Cu_3FeS_4 (< 40 C)	Dutrizac et al. (1970)
Iron(III) sulfate in sulfuric acid	8.78 (> 40 C)	Liquid diffusion of copper ions (> 40 C) Chemical reaction (< 40 C)	Idaite and S_0 (> 40 C) Non-stoichiometric bornite and idaite (< 40 C)	Ugarte-Alverez (1971)
Sulfuric acid electrokinetics	21	Solid state diffusion (< 50 C) Chemical reaction (> 50 C)	No current Cu_2S and $Cu_{1.8}S$ Current applied $Cu_{2.5}FeS_4$	(Price and Chilton, 1980; Price and Chilton, 1981)
Oxygen and sulfuric acid	35.9	Surface chemical reaction	Cu_3FeS_4 and CuS	Pesic and Olson (1984)
Ammonia/ammonium sulfate solution with sodium persulfate	15.6	Mixed kinetics interface transfer and diffusion through a product layer	Hematite and sulfur	Liu et al. (2014)

As mentioned previously, in this study, a sample that contained mainly bornite, chalcopyrite and sphalerite was used. The sample was leached in methanesulfonic acid (MSA) with ferric chloride as the oxidant. The relevant dissolution reactions for bornite, chalcopyrite and sphalerite and information on MSA are presented below.

As described above, bornite dissolution occurs in stages (Pesic and Olson (1983) (Equations (1) to (4), shown for a chloride system). The first stage involves the removal of cuprous ions from the bornite by ferric-ion oxidation to produce an intermediate Cu_3FeS_4 copper-deficient phase (Manning, 1967; Pesic and Olson, 1983). The second stage consists of complete dissolution with the production of elemental

sulfur. Sulfur oxidation with residual oxidant may yield sulfate, however, only a small (from 1.5 to 5.2%) amount of sulfate has been reported from bioleaching experiments (Wang et al., 2018).

Stage I

$$Cu_5FeS_4 + 4FeCl_3 \rightarrow Cu_3FeS_4 + 2CuCl_2 + 4FeCl_2 \quad (1)$$

Stage II

$$Cu_3FeS_4 + 8FeCl_3 \rightarrow 9FeCl_2 + 3CuCl_2 + 4S^0 \quad (2)$$

$$S^0 + 6FeCl_3 + 4H_2O \rightarrow SO_4^{2-} + 6Fe^{2+} + 8H^+ + 18Cl^- \quad (3)$$

$$Cu_3FeS_4 + 32FeCl_3 + 16H_2O \rightarrow 3CuCl_2 + 4H_2SO_4 + 33FeCl_2 + 24HCl \quad (4)$$

In the absence of an oxidant, but above a solution potential of 250 mV versus the standard hydrogen electrode, bornite dissolves in acid to yield secondary-copper-enriched layers (Equations (5) to (6) (Zhao et al., 2015)). These equations can be considered as intermediate electrochemical reactions in the dissolution of bornite with an oxidant. Equation (5) shows the intermediate copper-deficient layers that have been identified in previous studies.

$$Cu_5FeS_4 \rightarrow Cu_{5-x}FeS_4 + xCu^{2+} + 2xe^- \quad (5)$$

$$Cu_{5-x}FeS_4 + 6H^+ \rightarrow CuS + (4-x)Cu^{2+} + 3H_2S + Fe^{3+} + (5-2x)e^- \quad (6)$$

The composite sample that was used in this study contained chalcopyrite, which reacts with ferric chloride according to Equation (7). The reaction kinetics and products that were obtained from chalcopyrite dissolution with ferric chloride under the same conditions as used in this study are provided in a previous publication (Hidalgo et al., 2018).

$$CuFeS_2 + 16FeCl_3 + 8H_2O \rightarrow CuCl_2 + 2H_2SO_4 + 17FeCl_2 + 12HCl \quad (7)$$

Although copper is the focus in this study, other metal sulfides, such as sphalerite, are often present in copper-sulfide samples, and these may dissolve in a ferric chloride system. The dissolution kinetics of sphalerite have been studied previously (Aydogan et al., 2005; Dutrizac and Macdonald, 1978), and sphalerite reacts according to:

$$ZnS + 2FeCl_3 \rightarrow ZnCl_2 + 2FeCl_2 + S^0 \quad (8)$$

MSA or methanesulfonic acid (CH_3SO_3H) is a relatively new, biodegradable organic-acid lixiviant that is used as an electrolyte for heavy metals and is formed from the oxidation of dimethylsulfide (Bork et al., 2014; Gernon et al., 1999). This acid has mostly replaced hydrofluoric acid as a complexing agent for industrial lead and tin electroplating, and has proven effective in copper baths (Florence et al., 2011).

- The benefits of MSA for industrial application include its usefulness as an electrolyte for heavy-metal salt dissolution and its conductivity, high stability and low toxicity (Gernon et al., 1999), which are positive characteristics for hydrometallurgical applications, especially for ISR processing, with environmental concerns related to groundwater.

- The ability of MSA to solubilise otherwise often normally insoluble metals has attracted recent research in hydrometallurgical applications as described in Table 4-2. The results obtained in previous research are encouraging (Wu et al., 2014a; Wu et al., 2014b), in that the effectiveness of MSA in terms of enhancing solubility is comparable with that of stronger acids, and its high heavy-metal solubility provides an opportunity for the treatment of copper–lead–zinc–containing ores in an ISR environment.

- MSA may also provide advantages in terms of iron product formation. Sulfate for jarosite formation (by reaction with ferric ions and monovalent cations) may originate from the oxidation of sulfide minerals. Sulfuric acid may also serve as a sulfate source for jarosite formation. However, because MSA is stable, forming methanesulfonate ions upon dissociation, less jarosite is expected to form, especially if the extent of oxidation of sulfide minerals to form sulfate ions is small.

- MSA shows promise in downstream processing after the extraction of valuable metal from concentrates. The oxidant/MSA fluid may be regenerated by anodic reaction in electrowinning, as proven at the bench scale for lead processing, which involves a fluid passing through a cell with graphite anodes and stainless

steel cathodes (Wu et al., 2014b). Lead is recovered at the cathode, whereas the ferrous iron is oxidised by electrolysis to regenerate ferric iron for recycle. In a copper system, it is anticipated that a similar approach could be used, with copper recovery at the cathode and ferric iron at the anode.

Because of the possible environmental and other advantages of this acid over other known acids, and with a view towards its application in an ISR environment, MSA was selected as the most suitable lixiviant in this work.

Table 4-2. Review of literature on kinetic studies using MSA.

T (°C)	Mineral	Oxidant con. (mol L^{-1})	Acid con. (mol L^{-1})	Particle size (µm)	Leach media	Activation energy (kJ/mol)	Acid dependence	Reference
20–80	Smithsonite	Not applicable	0.24–0.64	219 to 61	MSA	32.66	Direct correlation with leaching rate	Feng et al. (2015c)
25–65	Malachite	Not applicable	0.18–0.54	228–53	MSA	24.48	High dependence at lower concentrations	Feng et al. (2015b)
10–60	Cerussite	Not applicable	0.075–0.225	317–69	MSA	43.30 < 30 C 17.20 > 30 C	Direct correlation with leaching rate	Feng et al. (2015a)
25–85	Galena	0.5–0.05	0.25–1	–109 +75 –45 +38	Ferric sulfate with MSA	36.15	Acid concentrations below 3 mol L^{-1} have little or no influence on leaching rate	Wu et al. (2014b)
40–90	Chalcopyrite	0–3	0.05–0.75	–106 +75 –38	Ferric chloride with MSA	101.3	Little influence on leaching rate at concentration tested	Hidalgo et al. (2018)

The rationale of this study was to determine the kinetic behaviour of a natural composite bornite/chalcopyrite sample with ferric chloride in a MSA-based lixiviant,

analyse the resulting surface layers, and compare this analysis with previous work on pure chalcopyrite leaching under the same conditions (Hidalgo et al., 2018). This work aimed to identify the individual effects of the bornite and chalcopyrite in the sample on the kinetic parameters. In recent years, besides the standard empirical kinetics model approaches, kinetics in mineral transformations and replacements in aqueous solutions have been studied by using other models, such as the 'time-to-a-given-fraction' method (Di Lorenzo et al., 2014; Okada and Utsumi, 2003; Pedrosa et al., 2017; Perdikouri et al., 2011; Qian et al., 2017). This method has been applied to chalcopyrite kinetics because of the complexity of the refractory-mineral dissolution, and complements the shrinking-core model (Kuzmina et al., 2017). We have used conventional empirical models and the time-to-a-given-fraction model to calculate the reaction activation energies for the bornite/chalcopyrite sample dissolution.

4.2. Experimental

4.2.1. Materials and methods

A natural sulfide sample was used as the starting material for the experiments. The mineral-phase distributions were determined by quantitative X-ray diffraction (QXRD) using a PANalytical Empyrean X-ray diffractometer equipped with a Bragg-Brentano HD incident monochromator. The incident-beam working parameters were a 0.5° divergence slit at 40 kV, 40 mA and 0.02 rad soller slits and a 1° antiscatter slit. The QXRD analysis showed that the sample contained 48.8% bornite, 15.8% chalcopyrite, 16.1% sphalerite and several gangue minerals (see Fig. 4-1). The sample was prepared by ball milling, sieving and separation into five size fractions. The bulk-sample elemental distribution, as determined by inductively coupled plasma–atomic emission spectroscopy (ICP–OES), is presented in Table 4-3. The percent copper varied from 32.4% for the –38 µm particles to 36.6% for the –106+75 µm size fraction.

Iron was selected as a suitable oxidant based on economic considerations (compared with other more expensive oxidants that may be suitable for ISR). Screening experiments with ferric chloride and ferric sulfate were conducted to identify the most efficient oxidant for leaching. In preliminary tests, at 60°C, after 5 days of leaching, the maximum copper extraction with ferric-sulfate solutions was 33%, whereas that

with the ferric-chloride solution reached 70%. Based on these results, ferric chloride was selected as the oxidant in this work.

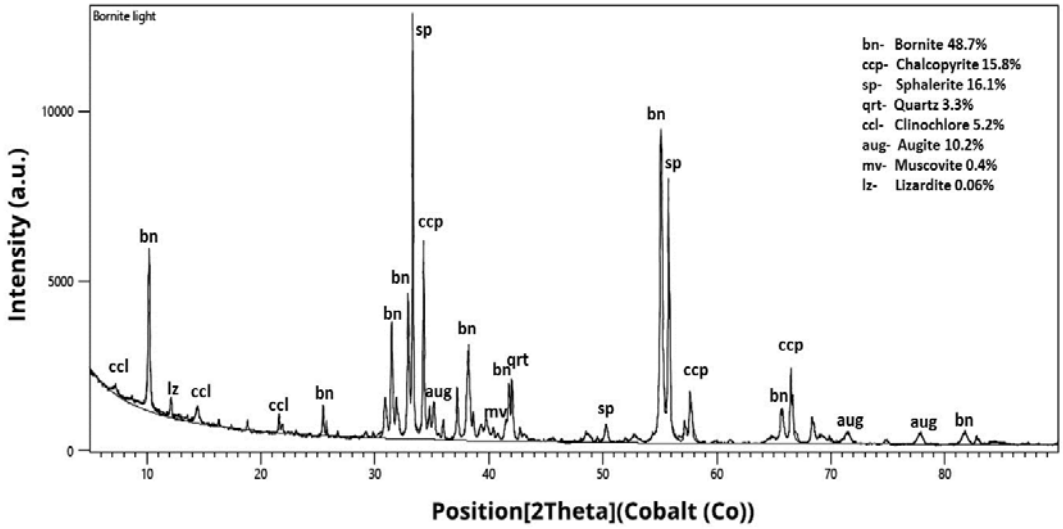

Fig. 4-1. X-ray diffractogram of the pre-leached sample (–38 µm), showing bornite as the predominant sulfide-containing mineral with chalcopyrite and sphalerite phases.

Table 4-3. Chemical composition of the initial bulk mineral sample.

Concentration [%]											
Al	**Ca**	**Cu**	**Fe**	**K**	**Mg**	**Na**	**Ni**	**Pb**	**S**	**Zn**	**Si**
1.45	3.43	35.5	11.3	0.497	1.25	0.007	<0.002	0.190	22.6	8.27	5.98

Different concentrations of ferric ions and acid were used to prepare stock solutions with analytical-grade anhydrous ferric chloride (98%, Chem Supply, Australia) and MSA (100%, BASF, Germany) in deionised water. Oxidant concentrations were based on calculations of total required copper oxidation (Equations 1 to 4), and an excess of 200% oxidant was used in the leach tests. A pulp density of 10% m/m solids was used and 1 g of sample was placed in 15 mL Nalgene bottles with 10 mL of solution. The bottle headspace was flushed with high-purity nitrogen gas and sealed. The bottles were placed in a tumbling water bath at a constant speed of 15 rpm. The baseline experimental conditions included a sample particle size of –38 µm, a 3 mol L^{-1} ferric concentration and acid concentration of 0.5 mol L^{-1} at 90°C. One of the four different parameters investigated (particle size, ferric concentration, MSA concentration and temperature) was varied to identify its effect on the reaction kinetics, while the other baseline conditions were kept constant (Table 4-4). Temperatures from 40°C to 90°C

were studied in 10°C increments and ferric-ion concentrations were varied between 0 and 3 mol L^{-1}. The particle size was varied from an upper size range of –106+75 µm to a lower range –38 µm and the acid concentration was varied from 0.75 mol L^{-1} to 0.05 mol L^{-1}. Replicate tests were conducted and a difference of less than 3% in repeatability was obtained.

Table 4-4. Baseline experimental conditions.

Chalcopyrite mass	1 g
Solution volume	10 mL
Particle size	–38 µm
$FeCl_3$ concentration	3 mol L^{-1}
MSA concentration	0.5 mol L^{-1}
Solids loaded	10% m/v
Temperature	90 C
Initial pH	2.44
Initial Eh	707 mV

Each experiment served as a unique data point in the reaction kinetics analysis. The final solids residue was filtered, the pH and Eh were measured and the copper concentration was determined by atomic absorption spectrophotometry (Agilent 240/280). Quantitative Evaluation of Minerals by Scanning Electron Microscopy (QEMSCAN) and scanning electron microscopy (SEM) images were used for the phase analysis. Solid samples were rinsed three times with deionised water, dried at 30°C and weighed. Reacted residues from tests at 90°C and 40°C and particle sizes of –106+75 µm and –38 µm were selected for mineralogical examination. The experimental plots contain between 9 and 10 total points per line distributed between 0.5 h and 96 h. The samples were analysed by mounting on stubs and in epoxy for SEM energy-dispersive X-ray spectroscopy (EDS) and QEMSCAN analysis, respectively, using a field emission scanning electron microscope (JEOL-JSM-7001) with a Bruker Esprit 1.9 EDS system. The measurement parameters were a 10-mm SDD EDS detector with a 125-eV resolution, a 20 kV accelerating voltage and a 10 mm working distance in backscattered electron imaging mode. QEMSCAN mineralogical analysis was performed by using an E430 unit with Idiscover 5.2 software. Target particle maps were developed by initial EDS identification and a CSIRO species identification protocol was run (Meyer et al., 2013).

4.3. Results and discussion

4.3.1. Kinetic results

4.3.1.1. Effect of initial acid concentration

Maximum extractions of ~90% copper were achieved (see Fig. 4-2a). The most marked difference in copper extraction occurred between 0.1 and 0.5 mol L^{-1}, whereas the 0.05 mol L^{-1} solution had a similar dissolution profile to the 0.1 mol L^{-1} solution. At acid concentrations below 0.05 mol L^{-1}, the reaction was almost entirely oxidative, and the role of the acid was to prevent iron hydrolysis.

4.3.1.2. Effect of initial iron(III) concentration

Figure 4-2b shows the effect of changes in ferric-ion concentration on copper extraction at 90°C (baseline temperature). As expected, the presence of an oxidant is mandatory for bornite dissolution. Experiments without oxidant showed that bornite did not react with acid during the first 48 h and reacted only slightly after this time. A significant decrease in copper extraction resulted for ferric concentrations below 1.25 mol L^{-1} and the increase in copper extraction was small for an increase in ferric concentration above 1.5 mol L^{-1}, which implies an independence from oxidant concentration above this value. Copper extraction was faster during the first 2 h of reaction for all concentrations, slowed down after 4 h of reaction and reached a plateau for concentrations below 1.25 mol L^{-1}. Concentrations above 1.5 mol L^{-1} provided an excess of oxidant and complete dissolution was expected; Pesic and Olson (1983) found this dependence more evident during the early stages of the reaction, with a first-order dependence on oxidant concentration during the first 30 min of leaching.

4.3.1.3. Effect of particle size

The inverse dependence of particle size and copper dissolution is shown in Fig. 4-2c. Within the first 2 h, a copper dissolution of 73% resulted for the –38 µm material, and this dissolution decreased to 55% for the –106+75 µm material. There was no major difference between particle sizes below –100 µm. A rapid initial dissolution was

observed for all grain sizes and the dependence was less than for pure chalcopyrite. A dependence on particle size was found by Ugarte-Alverez (1971) in the first stage of the reaction, and this was attributed to a reduction in particle size during the initial dissolution, but this dependence was more marked with very low oxidant concentrations (0.005 mol L^{-1}) (Pesic and Olson, 1983). This behaviour may indicate that bornite is a viable candidate target for ISR processing because a very fine grain size may not be required to achieve a relatively fast reaction at high ferric-ion concentrations. The leaching kinetics showed a significantly slower dissolution for chalcopyrite under the same conditions (Hidalgo et al., 2018).

4.3.1.4. Effect of temperature

The effect of temperature as measured between 40°C and 90°C indicated that two copper-extraction scenarios exist (Fig. 4-2d). The copper extractions for the 40°C and 50°C series and the 60°C to 90°C plots are close to each other. However, the two groups differ in the maximum copper extracted, with the lower-temperature experiments not achieving more than 80% copper dissolution. For all temperatures, the copper extraction up to ~30% was rapid and thereafter, it trended toward a plateau. The difference in extraction profiles as a function of temperature before and after 30% copper extraction may indicate that more than one reaction mechanism occurs and that copper dissolution from chalcopyrite is more rapid above 60°C. As shown in previous work on chalcopyrite leaching, the reaction kinetics are highly dependent on temperature changes and chalcopyrite dissolution increases markedly at higher temperatures (Dutrizac, 1981; Hirato et al., 1986). Dreisinger and Abed (2002) suggested that a difference between transport and chemical-reaction control is a noticeable enhancement of reaction kinetics even with small temperature increments, and mild changes in the separation between plots result from transport processes that control the reaction. Although chalcopyrite is present in the sample, the broad and even separation between temperature lines observed in previous work (Hidalgo et al., 2018) is not evident here, which implies that the bornite dissolution mechanism dominates the copper-extraction kinetics.

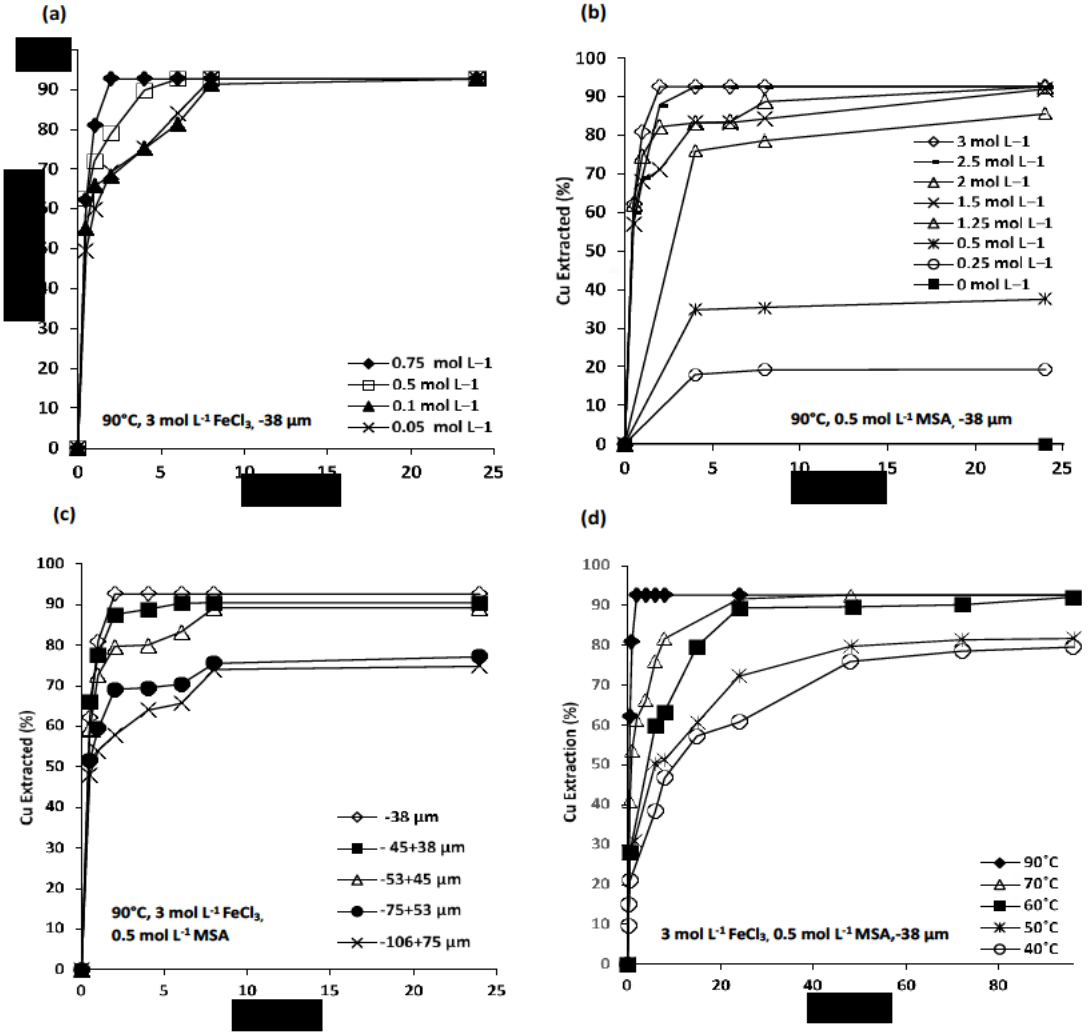

Fig. 4-2. Effect of experimental parameters on copper extraction for composite bornite/chalcopyrite sample: **a.** MSA concentration, **b.** ferric-ion concentration, **c.** particle size, **d.** temperature (different time scale for longer sampling times), maximum error as determined in replicate tests was 3% (excluded from the figure for clarity).

4.3.2. Kinetic analysis

4.3.2.1. Determination of kinetic parameters by using model-fitted methods

Empirical kinetic equations for heterogeneous reaction models are typically used to understand the reaction mechanism based on kinetic data. The shrinking-core model assumes that the reacting particle has a uniform radius and is surrounded by a reactant. The reactant penetrates the surface layer and continues into the remaining bulk of the particle until the shrinking core disappears. The heterogeneous reaction of bornite

leaching with acidic ferric chloride solution was modelled by using six different empirical equations to achieve a best fit as determined from the correlation coefficient (R^2). The integrated rate equation $g(x)$ relates the transformed fraction x and its variation with time t, where k_c is the apparent reaction rate constant, and is given by Equation (9).

$$g(x) = k_c t \tag{9}$$

Table 4-5 shows the fitting of the experimental data obtained with different diffusion-controlled and chemical-reaction-controlled equations. The best fit (highest R^2 values) was obtained for diffusion through a product layer ($R^2 \geq 0.88$), despite the poor fit for the initial reaction phase. The deviation from the straight-line plots (Fig. 4-3) suggests that a single mechanism may not apply to the entire reaction and that copper extraction from the chalcopyrite in the samples may be limited, especially at temperatures below 60°C. The fit lines were determined with 7 points (including the points between 0 and 2 h). Similar behaviour was found by the authors for the leaching of pure chalcopyrite samples at 50°C and 40°C, in which the copper dissolution was slower compared with the composite sample (Hidalgo et al., 2018). Previous studies also suggested that at low temperatures, an intermediate copper-mineral phase formation may limit the complete extraction of bornite, presumably by the formation of chalcopyrite or covellite (Pesic and Olson, 1983).

Table 4-5. Correlation coefficients (R^2) for six kinetic experimental equations applied to the copper leaching of a bornite/chalcopyrite composite sample at variable temperature for the shrinking-core model.

	R^2					
	Film diffusion control	Diffusion control through a product layer (cylindrical particles)	Diffusion control through a product layer (spherical particles)	Surface chemical-reaction control (spherical small or large particles)	Film diffusion control (spherical small particles)	Film diffusion control (spherical large particle)
g(x)	x	x+(1–x) ln(1–x)	$1–3(1–x)^{2/3}+2(1–x)$	$1–(1–x)^{1/3}$	$1–(1–x)^{2/3}$	$1–(1–x)^{1/2}$
	Temperature (°C)					
90	0.57	0.95	0.97	0.84	0.68	0.78
70	0.59	0.83	0.88	0.42	0.18	0.24
60	0.48	0.97	0.99	0.81	0.66	0.74
50	0.18	0.92	0.90	0.52	0.36	0.44
40	0.34	0.93	0.92	0.62	0.48	0.56

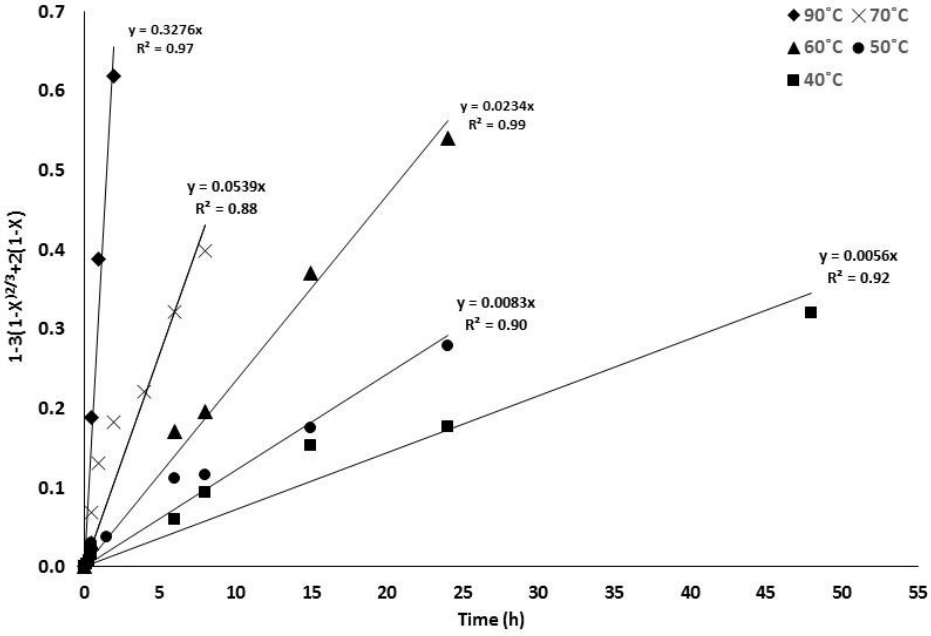

Fig. 4-3. Plots of fitted temperature data for bornite/chalcopyrite composite sample by diffusion through a product-layer-control model (spherical particles). Graphic shows the linear fit to plateau stage including the points of rapid dissolution between 0 and 2 h.

To obtain the activation parameters for the shrinking-core model, the best-fit equation was selected, and its integrated form is presented in Equations (10) to (11), where *x* is the fraction of reacted solid, τ is the time required to achieve complete conversion of the core (R = 0), k_c is the kinetic rate constant and D_e is the effective diffusion coefficient.

$$\frac{t}{\tau} = k_c t = 1 - 3(1 - x)^{\frac{2}{3}} + 2(1 - x) \quad (10)$$

$$k_c = \frac{1}{\tau} = \frac{\rho R^2}{6 b D_e C_a} \quad (11)$$

Arrhenius's law (Equations (12) to (13)) and the Eyring equation (transition-state theory, Equations (14) to (15)), were used to calculate the activation parameters, including the activation energy, enthalpy and entropy (Kuhn, 2000; Levenspiel, 1999). The activation energy was calculated by using the experimental rate constant that was obtained from a plot of ln k_c versus *1/T* (Fig. 4-4a). The enthalpy and entropy were obtained from a plot of $T \ln (k_c/T)$ versus T, with ΔH^{++} being derived from the intercept and ΔS^{++} from the slope (Lente et al., 2005) (Fig. 4-4b).

$$k_c = A e^{-\frac{Ea}{RT}} \quad (12)$$

$$\ln k_c = \ln A - \frac{Ea}{RT} \quad (13)$$

$$k_c = \frac{k_b T}{h} e^{\frac{-\Delta G^{++}}{RT}} \quad (14)$$

$$T ln\left(\frac{k_c}{T}\right) = T\left[ln\left(\frac{k_b}{h}\right) + \frac{\Delta S^{++}}{R}\right] - \frac{\Delta H^{++}}{R} \quad (15)$$

A final plot of the sample activation parameters is presented in Fig. 4-4. The apparent activation energy obtained from the Arrhenius plot was 79.3 kJ/mol, which is higher than that expected for a diffusion-controlled process. The activation energy is slightly higher than previously reported values with the same oxidant, which suggests that the presence of chalcopyrite in the system increased the activation energy (see also Table 4-2). The value is in agreement with that determined by Pesic and Olson (1983) for ferric-chloride solutions and temperatures above 40°C, and may indicate that the major influence on the thermodynamic behaviour of the sample is the bornite. The enthalpy

and entropy values from the Eyring plot are 77.3 kJ mol^{-1} and -197.1 J mol^{-1} K^{-1}, respectively. The entropy is very similar to that obtained for chalcopyrite under the same conditions and in other systems (Dreisinger and Abed, 2002; Hidalgo et al., 2018), and indicates that the reaction is not spontaneous at any temperature.

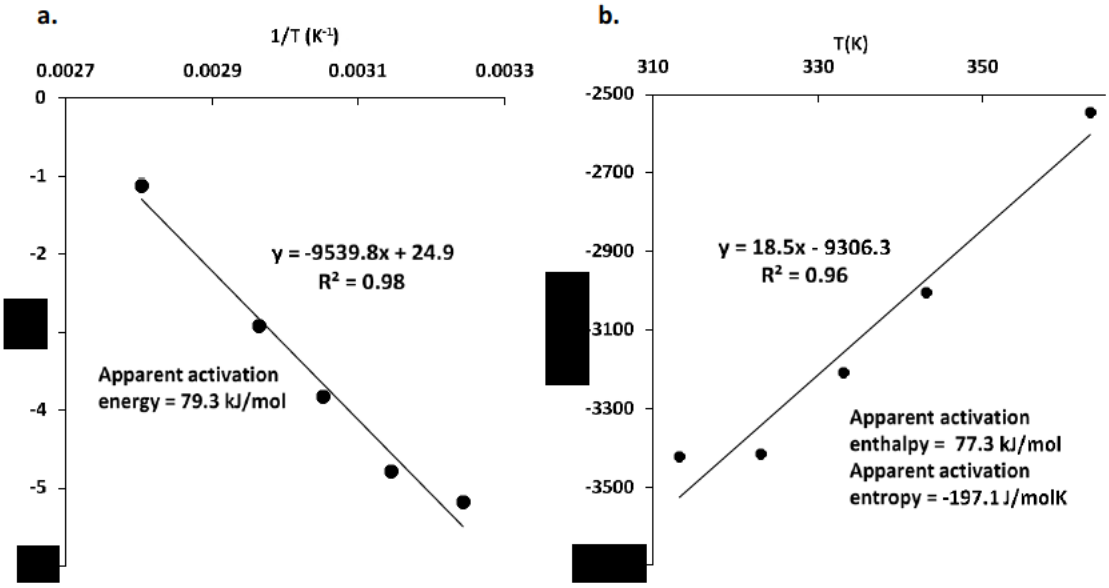

Fig. 4-4. Activation-parameter determination. **a.** Arrhenius plot for composite-sample dissolution using data from the experimental kinetic equation for diffusion through a product layer, **b.** Eyring plot.

The reaction orders for the other parameters were calculated from plots of ln k_c versus the ln of the parameters of oxidant concentration (CO), particle size (PS) and free acidity (FA). k_o was found by using the Arrhenius equation (Equation (12)) and the methodology presented by Feng et al. (2015a). All values were substituted into the kinetic equation of the dissolution kinetics for the composite sample of bornite and chalcopyrite, Equations (16) and (17), as follows (where lnA is the Arrhenius-equation intercept):

$$A = e^{intercept} = k_0 CO^{\propto} FA^{\emptyset} PS^{\beta} \quad (16)$$

$$1 - 3(1-x)^{\frac{2}{3}} + 2(1-x) = 6.77 \times 10^{11} CO^{0.45} PS^{-0.19} FA^{2.98} \exp\left(\frac{-79.3}{RT}\right) t \quad (17)$$

Equation 17 provides a formula to represent the shrinking-core model, which best describes the dissolution kinetics dependency on temperature, particle size and acid and oxidant concentrations for the bornite/chalcopyrite sample. Diffusion through a

product layer is the controlling step in the reaction; the product layer will grow rapidly at a higher temperature and reach a plateau rapidly, as is shown in the experimental results.

4.3.2.2. Individual contribution of bornite and chalcopyrite to copper dissolution by using model-fitted methods

In a composite sample where mineral separation is not possible (e.g., ISR operations) the ability to predict the effect of different copper minerals on the copper extractions would be extremely useful. The initial copper content of the sample used in this study was distributed between bornite (84.9% copper) and chalcopyrite (15.8%).

The copper extracted from the chalcopyrite can be predicted from Hidalgo et al. (2018):

$$1-(1-\mathrm{x})^{\frac{1}{3}} = 8.3\times10^{16}\mathrm{CO}^{0.44}\mathrm{PS}^{-2.19}\mathrm{FA}^{0.18}\exp\left(\frac{-101.4}{\mathrm{RT}}\right)\mathrm{t} \qquad (18)$$

The calculated copper extracted from chalcopyrite was subtracted from the total copper extracted to determine the copper extracted from pure bornite. The activation parameters for pure bornite were calculated by using the Arrhenius and Eyring plots, and a kinetic semi-empirical equation was determined for pure bornite (Equation (19)).

$$1-3(1-\mathrm{x})^{\frac{2}{3}}+2(1-\mathrm{x}) = 2.58\times10^{11}\mathrm{CO}^{0.79}\mathrm{PS}^{-0.72}\mathrm{FA}^{2.52}\exp\left(\frac{-72.02}{\mathrm{RT}}\right)\mathrm{t} \qquad (19)$$

The activation energy of 72 kJ mol^{-1} (see Fig. 4-5) for bornite alone was lower than that of the original sample and is close to that obtained in previous work on pure bornite (Pesic and Olson (1983). This lower value supports the conclusion that the chalcopyrite in the sample increases the energy requirement, though only marginally because bornite is the main phase that influences the curve shapes, and hence the results align more closely with pure bornite kinetic behaviour. In a previous analysis of the role of other copper minerals, such as digenite and chalcopyrite, on bornite dissolution, Dutrizac et al. (1971) found that the inclusion of less than 30% chalcopyrite in samples leached at 70°C did not change the shape of the dissolution

plots; however, when large amounts of chalcopyrite were added, at 15°C, the dissolution curves deviated from their initial form. The results in this work agree well with Dutrizac's results, including that the average activation energy was affected only slightly by the presence of 15.8% chalcopyrite in the sample. These results are relevant to an ISR scenario or to application at a larger scale, where the ratio of minerals in the ore modifies the kinetics and activation energy. The major copper-sulfide phase will dictate the leaching kinetics and potentially, as seen for chalcopyrite, limit the dissolution rate.

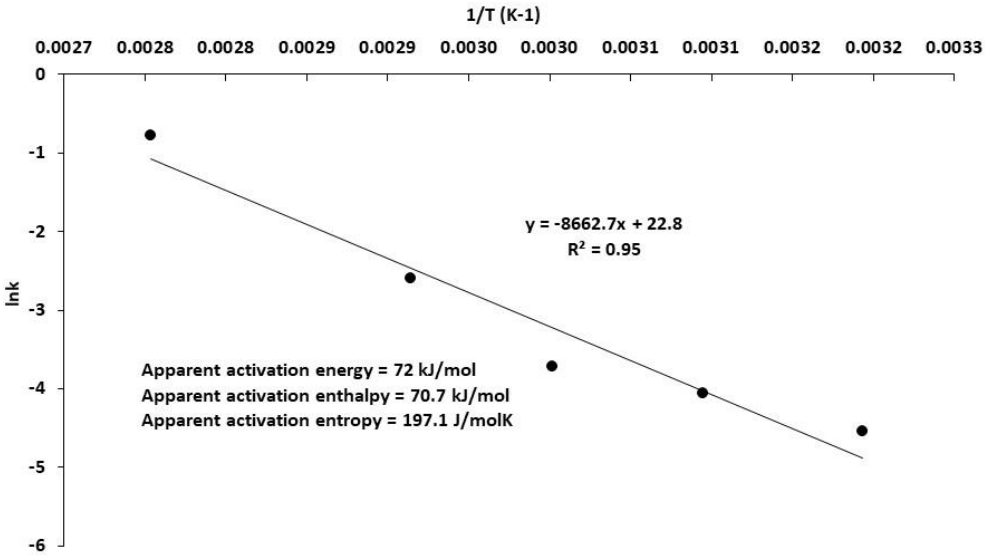

Fig. 4-5 Arrhenius plot for theoretical pure bornite dissolution using data from the kinetic equation for diffusion through a product layer.

4.3.2.3. Determination of kinetic parameters by using the time-to-a-given-fraction method

Although the model-fitted method (shrinking-core model) is used frequently to determine activation energies and reaction mechanisms based on empirical equations in hydrometallurgical kinetics analysis (as presented in Section 3.2.1), the main disadvantage of this approach is that an average activation energy is determined, which may obscure the presence of distinct reaction mechanisms. Hence, different reaction stages should be identified so that different model equations can be applied to each stage. Owing to the presence of both chalcopyrite and bornite in our samples, we expected a change in reaction mechanism, and we applied the time-to-a-given-fraction method to identify the time when this change occured in our experiments (Fig. 4-6).

The time-to-a-given-fraction approach relates the time (*t*) required to achieve mineral dissolution to the reaction progress. Equation (20) relates the reacted fraction *x* and a variable time *t*. The integrated equation, where *Ea* represents the apparent activation energy for the time required to reach a certain reaction progress, is given by Equation (21). The slope of the plot of ln t_x versus *1/T* was then used to calculate the apparent activation energy (Putnis, 1992).

$$dt = k_c^{-1}.f^{-1}(x)\,dx \tag{20}$$

$$\ln t_x = const - \ln A + \frac{Ea}{R}\left(\frac{1}{T}\right) \tag{21}$$

Plots of *ln(t)* as a function of *1/T* for various selected copper extractions are given in Fig. 4-6 and show that the slope changed with the reaction extent. A small slope change resulted between 20% and 30% extraction but a major change occurred between 30% and 50% copper dissolution. These changes in slope suggest that three stages of dissolution occur, as a first (below 20% copper dissolution), transition (between 20% and 50% copper dissolution) and second stage (above 50% copper dissolution). The changes also suggest that, between 30% and 50% copper extraction, chalcopyrite starts to dissolve and therefore, the activation-energy requirement increases.

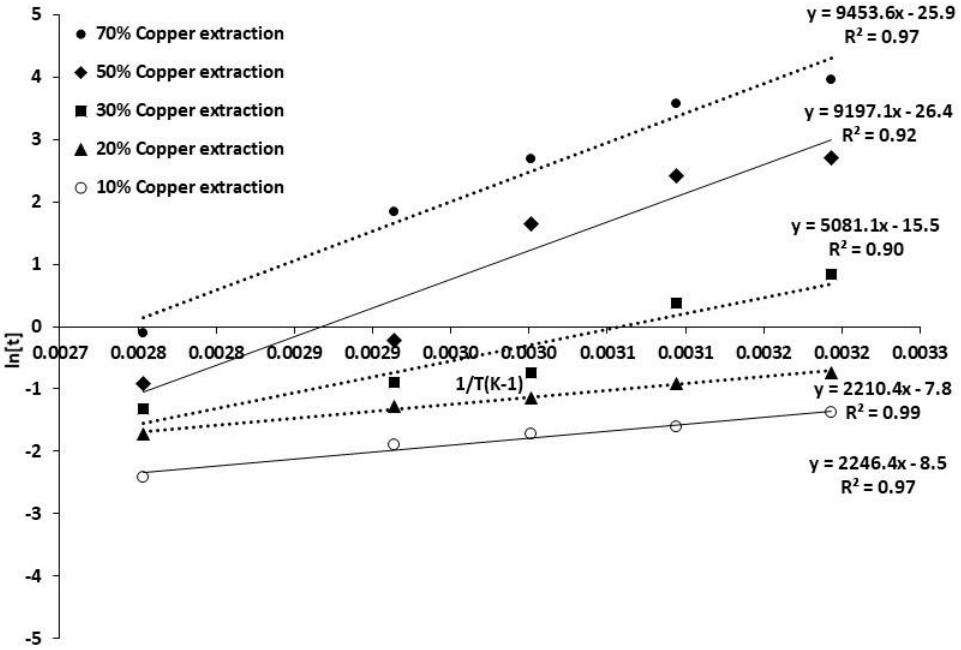

Fig. 4-6. Experimental temperature data for composite sample plotted as time-to-different percentages of copper recovery from experimental data (x = 0.1 to x = 0.7) versus *1/T* using the time-to-a-given-fraction method for activation-energy determination (the slopes were taken from the linearised equations next to each line).

The calculated energies for the original sample are almost constant (similar slope) for the first 20% copper dissolution with an apparent activation energy of ~15.7 kJ mol^{-1}. The energy increased to ~42.2 kJ mol^{-1} at 30% copper extraction. Activation-energy values for the first stage of the reaction varied between 21 to 51.3 kJ mol^{-1} for systems presented in the literature (see Table 4-1) and appears to correspond to bornite transformation to a copper-deficient phase. Pesic and Olson (1983) also suggested that low temperatures did not result in sulfur production, and therefore, the activation energy is low (24.78 kJ mol^{-1}) compared with the higher-temperature activation energies (30 kJ mol^{-1} for 40% extraction and –76.8 kJ mol^{-1} for 55% copper extraction, Table 4-1), as was also noted in the current study. Above 50% copper extraction, the activation energy increased slightly from ~76.5 kJ mol^{-1} to ~78.6 kJ mol^{-1} and was similar to the activation energy determined by the shrinking-core method. After 50% copper leaching, the calculated activation energy was similar to those found for covellite (71.5 kJ mol^{-1} and 74.4 kJ mol^{-1}) (Dutrizac and Macdonald, 1974; Miki et al., 2011), which may suggest the possible formation of covellite as an intermediate that may slow down the dissolution and increase the activation-energy requirement.

4.3.2.4. Individual contribution of bornite and chalcopyrite to copper dissolution by using the time-to-a-given-fraction method

Figure 4-7 provides plots of the theoretical pure bornite (Fig. 4-7a) and pure chalcopyrite (Fig. 4-7b) leaching using the time-to-a-given-fraction method. The change in activation energy between 30% and 50% copper dissolution for pure bornite leaching shows a two-stage mechanism (the mechanism below 30% and above 50% copper dissolution differs as shown by the change in slope in Fig. 4-7a), as has been presented previously in other studies with pure bornite (Dutrizac et al., 1970; Pesic and Olson, 1983; Ugarte-Alverez, 1971). Previously, these authors identified that chalcopyrite dissolution under the same conditions resulted in minimal changes in

measured activation energies, and this is evidenced by the small change in slopes of the chalcopyrite curves in Fig. 4-7b.

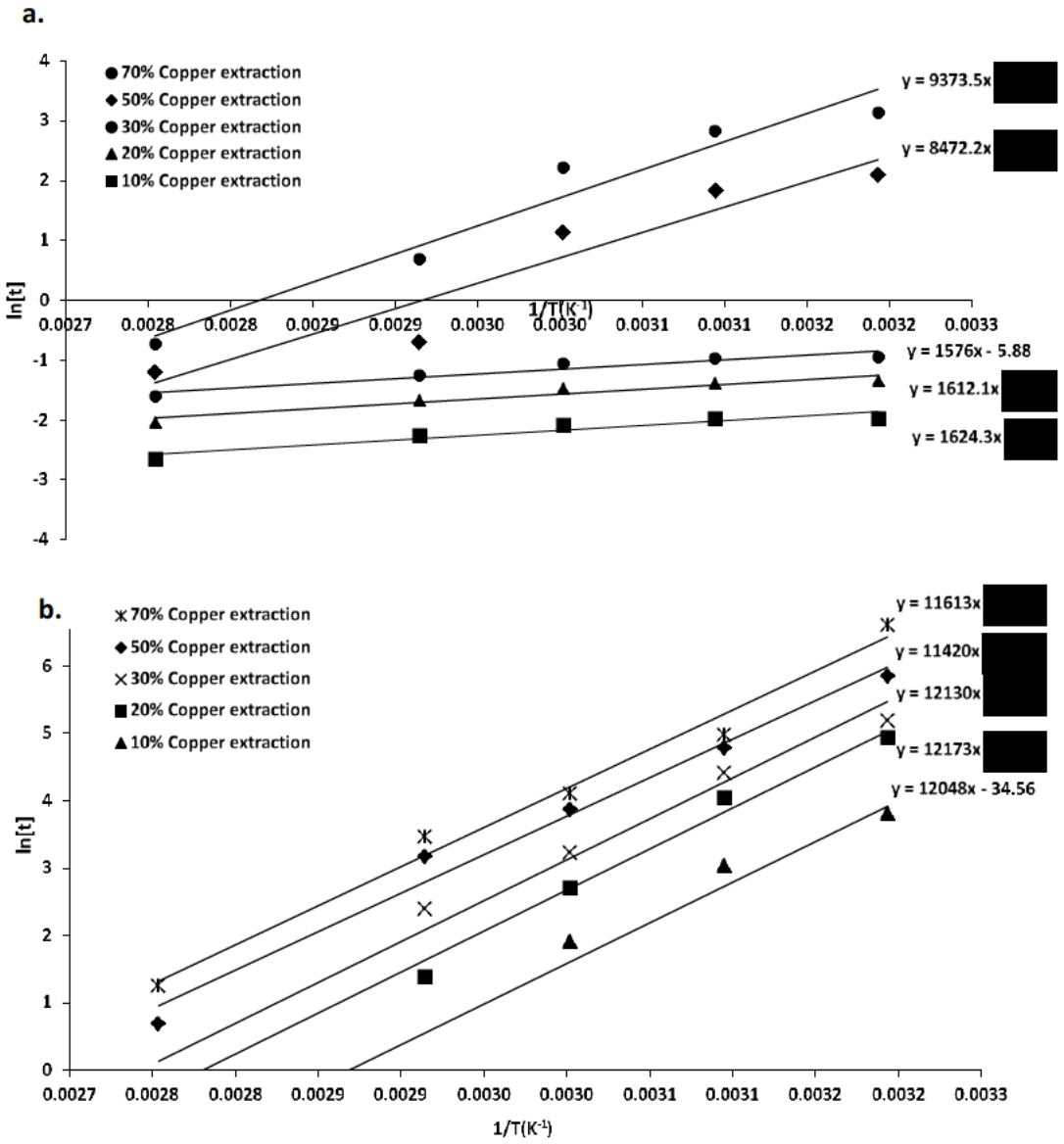

Fig. 4-7. Plots of copper leaching versus $1/T$ using the time-to-a-given-fraction method for activation-energy determination. **a.** theoretical pure bornite activation-energy behaviour showing the change in reaction requirement between 30% and 50% copper dissolution, **b.** pure chalcopyrite activation-energy behaviour showing a constant slope without major changes in the energy requirement.

Table 4-6 compares the activation parameters found for chalcopyrite (Hidalgo et al., 2018), bornite and the composite bornite/chalcopyrite sample from the Arrhenius, Eyring and time-to-a-given-fraction methods. The presence of chalcopyrite had only a

small impact on the activation energy, and the contribution by bornite dominates. Therefore, the chalcopyrite in the original sample did not affect the dissolution rate significantly (as evidenced by the similar slopes of the chalcopyrite dissolution lines in Fig. 4-7b) and as was also noticed by Dutrizac et al. (1971) for samples with a chalcopyrite content of up to 30%.

Table 4-6. Activation parameters calculated for pure chalcopyrite, pure bornite and bornite/chalcopyrite dissolution as a function of temperature for Arrhenius and time-to-a-given-fraction methods.

	Chalcopyrite	**Bornite**	**Bornite/chalcopyrite composite sample**
Ea Arrhenius (kJ/mol)	101.4	72	79.3
ΔH Eyring (kJ/mol)	99.4	69.1	77.3
ΔS Eyring (kJ/mol)	–197	–197.2	–197.1
Ea (as determined by the time-to-a-given-fraction method) (kJ/mol)			
10% copper dissolution	100.2	13.5	15.4
20% copper dissolution	101.2	13.4	15.7
30% copper dissolution	100.9	13.1	42.2
50% copper dissolution	94.9	70.4	76.5
70% copper dissolution	96.5	77.9	78.6

4.3.3. Mineralogical analysis

4.3.3.1. X-ray powder diffraction analysis

As evidenced by the kinetic data, two stages of bornite dissolution were identified (below 30% and above 50% copper dissolution) and several XRD analyses were performed during the reaction to obtain an indication of the intermediate and product phases. Sphalerite and chalcopyrite, which were present in the initial sample, were also present in the final sample. Therefore, complete copper recovery was not achieved from the chalcopyrite after 8 hours of leaching (see Fig. 4-8). Because this study focused on copper dissolution, detailed sphalerite leaching data are not presented, but chemical analysis confirmed that zinc was present in solution. For example, at 40°C,

56.2%, 74.9% and 91.5% of the sphalerite had leached at 6 h, 8 h and 15 h, respectively.

After 8 h, elemental sulfur was formed. An early reaction sample (30 min) showed no evidence of sulfur (Table 4-7), and the only product that was identified was an intermediate copper mineral that showed peak overlaps with chalcopyrite although solution chemistry indicated that copper was dissolved preferentially over iron. This mineral could not be classified as idaite based on XRD data only, as also shown by Ugarte and Burkin (1975). Because chalcopyrite was present in the initial sample, it is not possible for us to conclude whether chalcopyrite was a reaction product.

Table 4-7. Powder-diffraction data for the copper-deficient intermediate phase formed by leaching after 30 min (−106+75 µm), and reference patterns of idaite, chalcopyrite and bornite.

Intermediate phase (this work*)	**Idaite (Cu_5FeS_6) 00-013-0161 (Frenzel, 1959)**	**Chalcopyrite ($CuFeS_2$) 00-037-0471**	**Bornite (Cu_5FeS_4) 98-020-0424**
	d-spacing [Å]		
4.720	3 380	4 720	3 882
3.442	3 270 [1]	3 039 [1]	3 310
3.344	3 140 [1]	2 905	3 169
3.228	3 000	2 645	2 745[1]
3.125	2 820 [1]	2 606	2 519 [1]
3.030	2 700 [1]	2 307	2 455 [1]
2.997	2 420 [1]	1 955	2 241[1]
2.899	2 200 [1]	1 940	2 113
2.751	2 130	1 870 [1]	1 941
2.706	1 890 [1]	1 856 [1]	1 856
2.644	1 850 [1]	1 673	1 830 [1]
2.525	1 790	1 593 [1]	1 736
2.428 [2]	1 730	1 576 [1]	1 674
2.201	1 686	1 572	1 655
2.130 [2]	1 630 [1]	1 564	1 584
2.019	1 564 [1]	1 519	1 537 [1]
1.932	1 500	1 452	1 522
1.856	1 442	1 433	1 467
1.722	1 317	1 408	1 429
1.677	1 275	1 322	1 372
1.652	1 225 [1]	1 303	1 341
1.632 [2]	1 206 [1]	1 282	1 331 [1]
1.593	1 188	1 260	1 294
1.575	1 161 [1]	1 213	1 267
1.563	1 141	1 205	1 259
1.532	1 104	1 203	1 227
1.448	1 091	1 200	1 205
1.420	1 081	1 183	1 198
1.322	1 058	1 179	1 170
1.278	1 043	1 169	1 151
	1 017	1 153	1 120
	1 006	1 138	1 103
	0 987		1 098

[1] Main peak

[2] Possible **i**daite peak without interference

*Average chemical composition determined by EDS, QEMSCAN and confirmed from Cu/Fe ratios after chalcopyrite-content correction.

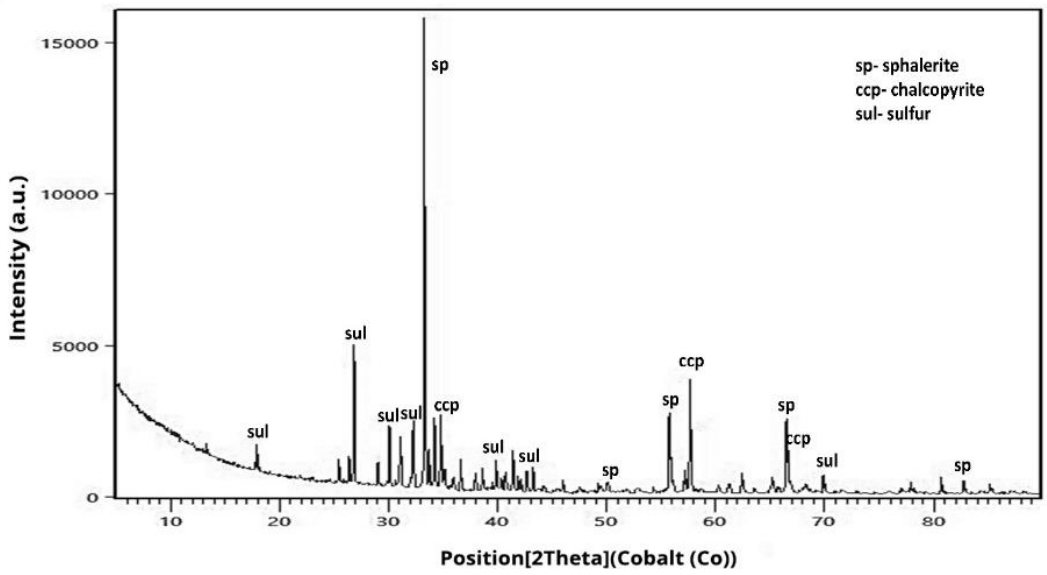

Fig. 4-8. Final X-ray diffractogram after 8 h of leaching and showing the final reaction products.

4.3.3.2. SEM analysis

The initial bornite particles were intact without any visible alteration product. The internal composition determined by SEM-EDS was constant through the entire particle for bornite and chalcopyrite. Textural changes to the bornite particle surface from 0.5 h to 8 h leaching for –106+75 µm particles at 90°C are shown in Fig. 4-9. It is possible to see sulfur forming, which encapsulated the particles after a period of time. In the first hour of the reaction, sulfur formation commenced via the development of a "beehive" or "skeletal" texture with internal openings that penetrated the particle via dissolution and generated cracks. After 2 h of reaction, a non-globular sulfur layer coated the particles and appeared to thicken after 4 h of reaction. As the experimental sampling times exceeded the time for 30% copper dissolution, sulfur production was evident. After 6 h of reaction, the particle appeared to be replaced entirely with sulfur.

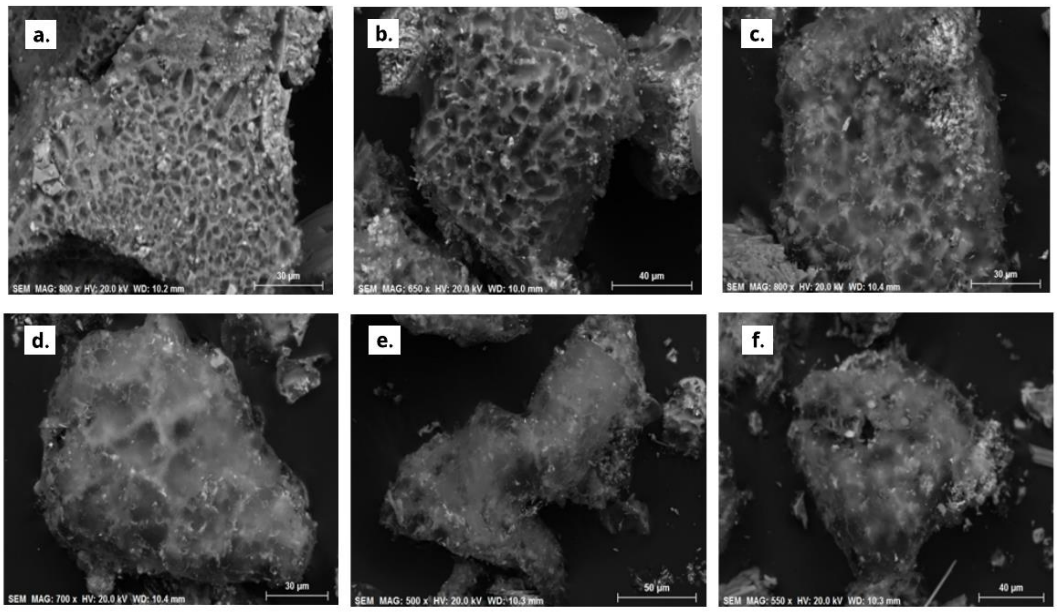

Fig. 4-9. Scanning-electron photomicrographs of –106+75 μm bornite particles mounted on stubs for 0.5 h, 1 h, 2 h, 4 h, 6 h and 8 h of leaching with a $FeCl_3$ (3 mol L^{-1}) and MSA (0.5 mol L^{-1}) solution at 90°C (from a to f, respectively).

The sulfur that coated the bornite particles appeared thick and not globular and may slow the diffusion of reactants. Figure 4-10 provides a comparative image of same-size chalcopyrite and bornite particles that were leached under the same conditions for 8 h. The chalcopyrite sulfur layer did not show textural changes with time and had evident porosity under the microscope. In contrast, the sulfur formed on bornite had an undefined form and the particle was encapsulated after 4 h of reaction. The difference in sulfur appearance may explain the different kinetic mechanisms found by the shrinking-core model for chalcopyrite and bornite under the same experimental conditions, namely, chemical control for chalcopyrite and diffusion through a product layer for bornite. If the sulfur coating is thick and apparently impermeable, transport through the product layer may control the reaction. A similar tight sulfur layer was found for chalcopyrite in sulfate systems and transport through a sulfur product layer has been suggested as a kinetics control step (Dutrizac et al., 1969; Munoz et al., 1979). Majima et al. (1985) found that the sulfur layer formed in ferric-chloride solution was considerably less dense (and therefore more porous) than that produced in ferric sulfate. It appears that the effect of the chloride on the texture of the produced sulfur is minor for bornite and, therefore, the sulfur coating is comparable to that found in sulfate systems for chalcopyrite.

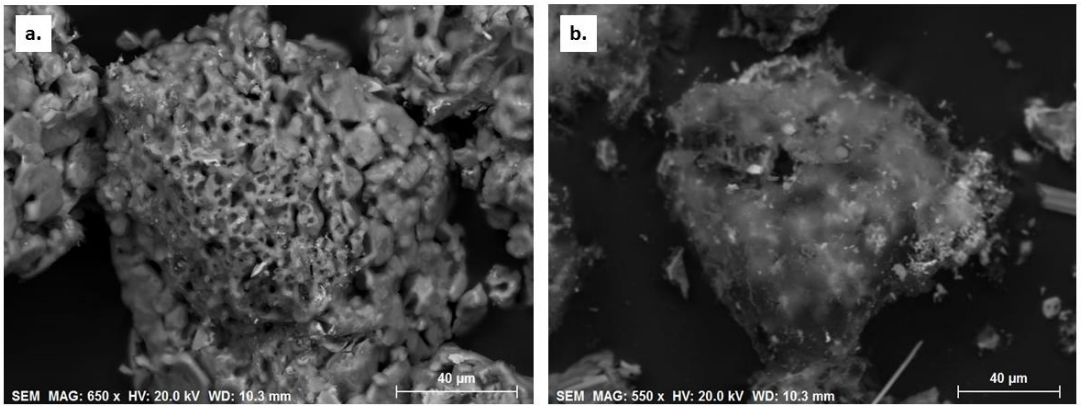

Fig. 4-10. Scanning electron photomicrographs of –106+75 µm chalcopyrite and bornite particles mounted on stubs after 8 h of reaction with a $FeCl_3$ (3 mol L^{-1}) and MSA (0.5 mol L^{-1}) solution. **a.** Chalcopyrite particle coated with porous globular elemental sulfur, **b.** bornite particle coated with sulfur layer without evident porosity.

The particle composition as a function of reaction time was studied by using polished cross-sections that were mounted in resin, with selected points studied by SEM-EDS. Images from 0.5 h to 8 h leaching are shown in Fig. 4-11 and the normalised chemical compositions are listed in Table 4-8. During the first 0.5 h of leaching, the particles were covered with small cracks from the sulfur at the surface into the center of the grains, which may have facilitated the mass transfer between the unreacted core and the solution. According to the chemical composition, almost 50% copper was lost from the original bornite during the initial 0.5 h. The iron-to-sulfur ratios remained constant during the first hour of the reaction. The new mineral that formed varied in composition from $Cu_{3.1}FeS_{3.8}$ to $Cu_{2.8}FeS_4$, Within the first half hour, the initial bornite was replaced by a copper-deficient mineral and sulfur formation commenced. After 4 h, almost the entire particle was replaced by sulfur and only small fragments of intermediate phase remained.

These findings agree with those of Pesic and Olson (1983), who found that after 49% copper dissolution, the residue composition was 51.0% copper, 14.0% iron and 30.5% sulfur. Dutrizac et al. (1970) described two different products that formed before sulfur in a sulfate-system, namely, non-stochiometric bornite with a composition of $Cu_{4.29}Fe_{0.99}S_4$ and a copper-deficient mineral with a composition between $Cu_{3.0}FeS_4$ and $Cu_{3.2}FeS_4$. This study also reported covellite grains and chalcopyrite lamellae as products.

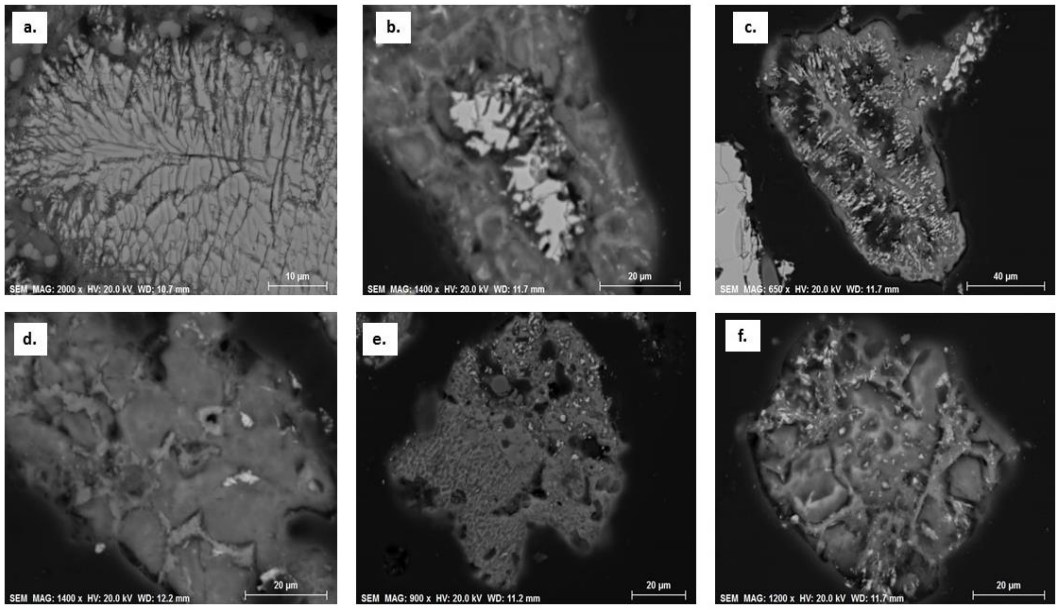

Fig. 4-11. Scanning electron photomicrographs of –106+75 μm bornite-particle cross-sections for 0.5 h, 1 h, 2 h, 4 h, 6 h and 8 h of reaction with a $FeCl_3$ (3 mol L^{-1}) and MSA (0.5 mol L^{-1}) solution at 90°C (from a to f, respectively).

Table 4-8. SEM-EDS chemical compositions of reacted residues of –106+75 μm bornite particles for 0.5 h, 1 h, 2 h, 4 h, 6 h and 8 h with a $FeCl_3$ (3 mol L^{-1}) and MSA (0.5 mol L^{-1}) solution at 90°C (stdv < 2).

Copper extracted (%)	Time (h)	EDS (m%)			
		Cu	Fe	S	Cu/Fe
0	0	67.9	13.6	18.3	4.9
49.39	0.5	52.8	14.9	32.3	3.5
55.72	1	54.6	19.4	25.9	2.8
59.61	2	24.1	10.5	65.4	2.3
65.92	4	24.9	9.4	65.7	2.6
67.66	6	7.1	3.9	88.9	1.8
76.31	8	1.5	0.8	97.7	1.7

After 30 min leaching at 40°C, no sulfur was detected. Instead, the surface texture was similar to that of the original bornite but with small surface cracks, and the mineral composition did not correspond to the original bornite, but its composition was in agreement with the copper-deficient mineral formed at high temperature. Cracks in the particle surface are believed to result from a volume reduction during the initial stage of the reaction (Dutrizac et al., 1985; Pesic and Olson, 1983). SEM images of the low-temperature intermediate product provide a good indication of the first stage of the

reaction where a small amount of copper was dissolved into solution and the entire particle changed into a copper-deficient mineral and yielded a friable and cracked particle without evident particle-surface changes. This result supports the fact that the control mechanism suggested by the shrinking-core model does not fit the low-temperature kinetics very well. Therefore, the time-to-a-given-fraction methodology is advantageous due to its independence of a selected model for the leaching mechanism, compared with the empirical equation model.

The role of chalcopyrite in the sample has been discussed from a kinetics perspective (section 4.3.2.). Some of the particles were composed of chalcopyrite and bornite, which provided an opportunity to identify differences in dissolution between these two minerals under the same conditions, as would be expected, for example, in an ISR environment, where the minerals co-exist and interact differently with the solution. Figure 4-12 shows the chemical composition and internal changes for a mixed-particle cross-section mount pre- and post-leaching at 90°C for 6 h. The initial sulfur compositions of the bornite and chalcopyrite differed slightly from the theoretical values (Pesic and Olson, 1983). The average bornite composition was 67.3% copper, 13.6% iron and 19.0% sulfur and for chalcopyrite the average was 34.0% copper, 31.5% iron and 32.9% sulfur. Chalcopyrite appeared to be intact after leaching, with no evident cracks or changes in the surface texture. The composition did not vary significantly. The bornite composition changed significantly after the reaction, with the internal texture appearing to be composed of bornite interspersed with sulfur. The composition of the cross-section leached particle varied from 58.3% copper, 18.0% iron and 23.7% sulfur to 49.0% copper, 11.8% iron and 39.2% sulfur, respectively. After two hours of reaction, the chalcopyrite did not dissolve further, more than 50% of the copper in bornite was dissolved and the particles were covered in sulfur. Therefore, it is possible to say that, for this sample, the energies calculated for the first 30% copper dissolution by the time-to-a-given-fraction method are applicable to just bornite without the influence of chalcopyrite in the sample.

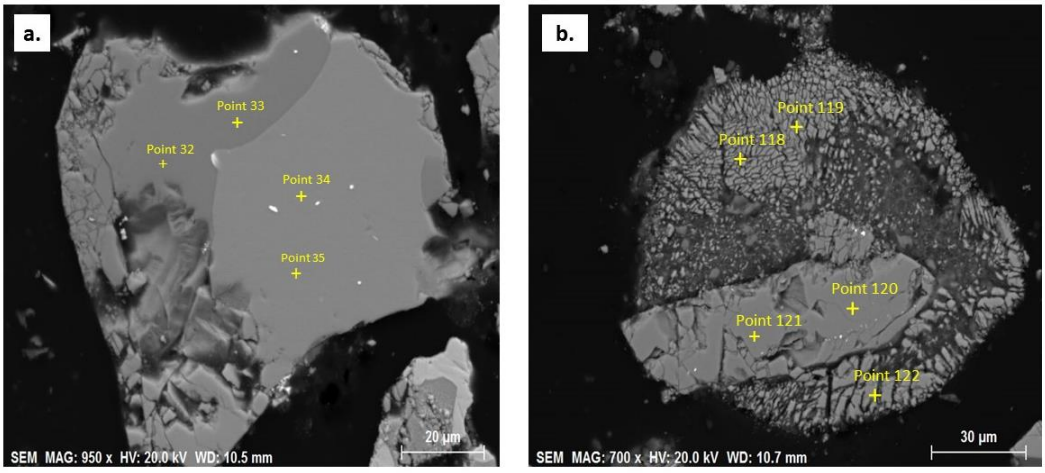

Fig. 4-12. Scanning-electron photomicrographs of –106+75 µm bornite mounted in epoxy and polished **a.** Initial sample before leaching, points 33 and 32 indicate chalcopyrite and points 34 and 35 correspond to the original bornite composition in the bulk sample. **b.** Bornite and chalcopyrite mixed particle after 6 h leaching with a $FeCl_3$ (3 mol L^{-1}) and MSA (0.5 mol L^{-1}) solution at 90°C. The chalcopyrite particle is surrounded by fragments of a copper mineral after the partial dissolution of bornite, and by elemental sulfur. Points 119 and 122 showed a copper-deficient composition, and points 120 and 121 showed a chalcopyrite composition (without changes from the unreacted composition).

4.3.3.3. QEMSCAN analysis

QEMSCAN particle mapping was used as an alternative technique to identify the intermediate phases formed by inferred chemical compositions. Figure 4-13 presents a partial map of the pre- and post-leached bornite and chalcopyrite in the sample analysed by SEM-EDS. An initial content of 2.47% of a mineral with the composition of idaite was identified in the original sample, which could be oxidised bornite, as identified in several natural bornite mineralisation zones (Hatert, 2005). After 30 min, the initial content of bornite was replaced almost entirely with a secondary unidentified copper mineral, with a composition that was not consistent with idaite or chalcopyrite, however, chalcocite/digenite existed in a reduced group of particles as a mixed intergrowth with the secondary copper mineral. Covellite was not identified in the sample. As expected, the chalcopyrite particles remained unchanged. Furthermore, under the leaching conditions used in these experiments, quartz was not expected to react, and therefore, quartz was used as a standard to measure the ratio of change in sample composition. The normalised data for the copper and iron mineral chemical

compositions of the initial sample and after 30 min of reaction are presented in Table 4-9. As expected, the bornite content was reduced by almost 88%, a new copper-sulfide phase of variable composition formed during this time and no production of idaite with a composition similar to that of the original sample resulted. There was a net decrease in chalcopyrite content, which suggests that some chalcopyrite started to dissolve, which also supports the conclusion that it is unlikely that chalcopyrite was generated.

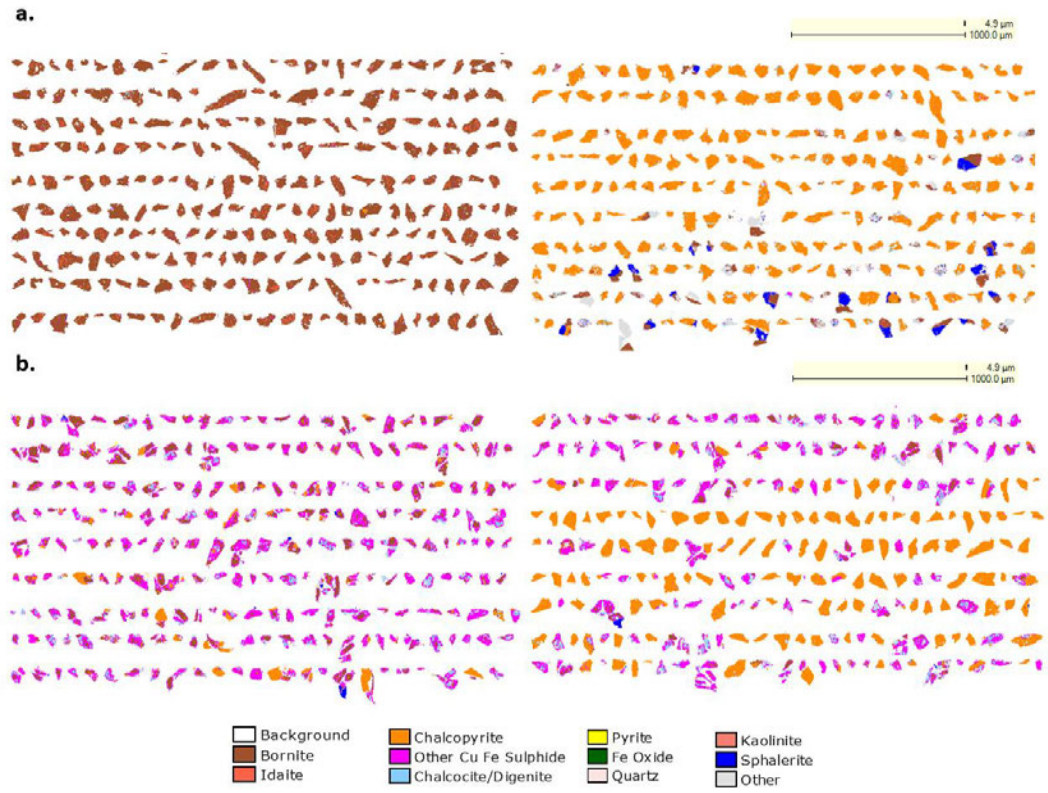

Fig. 4-13. QEMSCAN particle map for –106+75 μm sample at 0.5 h leaching with a $FeCl_3$ (3 mol L^{-1}) and MSA (0.5 mol L^{-1}) solution at 90°C. **a.** Initial map of copper minerals before leaching, **b.** post-leaching map of copper minerals.

Table 4-9. Normalised modal mineralogies (% area) for copper and iron and phases of the –106+75 μm sample before leaching and after 0.5 h leaching with $FeCl_3$ (3 mol L^{-1}) and MSA (0.5 mol L^{-1}). The quartz percentage was assumed to be constant and was used as a reference to determine changes in copper-containing minerals after leaching.

Mineral name	Pre-leached sample	0.5 h after leaching
	Mass %	Mass %
Bornite	52.45	5.85
Idaite	2.47	0.00
Chalcopyrite	6 96	5.30
Other Cu Fe sulfide	0 97	8.68
Chalcocite/digenite	2 19	2.65
Quartz	0.43	0.43

4.4. Conclusions

This study complements previous data on bornite leaching in ferric-chloride and MSA solutions, provides new information on the dissolution behaviour of composite mineral samples and presents a new kinetic-analysis methodology. The main conclusions are:

- The leaching of a composite bornite/chalcopyrite sample exhibited a low dependence on acid and oxidant concentrations, and the order of dependence of the bornite on ferric concentration was higher than that for chalcopyrite alone. MSA alone did not dissolve the copper in bornite within 48 h without the presence of an oxidant. Therefore, ferric chloride is the active oxidant in the reaction and the MSA prevents iron hydrolysis by maintaining a low pH. The dissolution was temperature dependent, particularly for temperatures below 60°C.

- The kinetic mechanism for the composite bornite/chalcopyrite sample leaching was found to be diffusion through a sulfur product layer and the average activation energy was calculated to be 79.3 kJ mol^{-1} by using the shrinking-core model.

- The leaching mechanism of the composite sample varied during the reaction and, therefore, the time-to-a-given-fraction kinetics analysis was used to obtain the kinetic parameters. Three reaction stages were identified for the composite sample:

for copper dissolutions below 20% the activation energy was 15.7 kJ mol^{-1}, between 20% and 50% it was 42.2 kJ mol^{-1} and above 50% it exceeded 76.5 kJ mol^{-1}. Bornite leached with a two-stage reaction mechanism; the first stage appeared to be the conversion of bornite into an intermediate without sulfur formation (13.5 kJ mol^{-1}) and a second stage occurred after the sulfur formed (70.4 kJ mol^{-1}). The activation energies obtained were similar to those of the composite sample, which indicated that the bornite leaching mechanism dominated the composite sample kinetics behaviour. The presence of chalcopyrite in the initial sample increased the activation energy between the 30% and 40% copper extractions.

- Mineralogical analyses of the resulting phases showed that the final reaction product was sulfur. An intermediate product was identified by chemical composition (Cu_3FeS_4). Chalcopyrite existed in the final residue, but because of its presence in the initial sample, it was not possible to confirm whether it was an intermediate reaction product.

- Based on the cumulative information, it is possible to differentiate bornite leaching into a rapid dissolution step where the initial bornite forms a copper-deficient phase with the same iron-to-sulfur ratio, and an intermediate 'idaite-type' copper mineral with a low activation energy (Equation 1). The second stage involves initial sulfur formation, and this coating results in a higher energy requirement for further dissolution (Equation 2). When the remaining particle is covered in sulfur, the activation energy exceeds 70 kJ mol^{-1} and the reaction is slower due to the formation of a low-permeable sulfur layer (Equations (2) to (7).

Acknowledgments

MRIWA (Project M488), BASF, Curtin University and CSIRO are gratefully acknowledged for funding this work. The authors would like to thank Robbie McDonald, Peter Austin and Matthew Rowles for their help with the mineralogical analysis, Robbie McDonald for his valuable contribution to this work, Denis Shiers for reviewing a draft of this manuscript, and the reviewers for their valuable additions to the final document.

Nomenclature

A	pre-exponential factor
b	stoichiometric coefficient
C_a	concentration in the main solution
CO	oxidant concentration
Ea	activation energy
FA	free acidity
D_e	effective diffusion coefficient of reactant in the product layer
ΔG^{++}	Gibbs free energy of activation
h	Planck's constant ($h = 6.626 \times 10^{-34}$ J s)
ΔH^{++}	enthalpy of activation
k_B	Boltzmann's constant ($k_b = 1.381 \times 10^{-23}$ J K^{-1})
k_c	apparent reaction rate constant
PS	particle size
r	radius of unreacted particle at time t
r_0	initial particle radius
R	ideal gas constant
ΔS^{++}	entropy of activation
t	time
t_x	time to transform a given fraction
T	recorded temperature
τ	time to complete leaching of the particle
x	fraction leached

References

Aracena, A., PÉRez, F. and Carvajal, D., 2018. Leaching of cuprite through NH_4OH in basic systems. Transactions of Nonferrous Metals Society of China (English Edition), 28(12): 2545–2552.

Ata, O.N., Çolak, S., Ekinci, Z. and Çopur, M., 2001. Determination of the optimum conditions for leaching of malachite ore in H_2SO_4 Solutions. Chemical Engineering & Technology, 24(4): 409–413.

Aydogan, S., Aras, A. and Canbazoglu, M., 2005. Dissolution kinetics of sphalerite in acidic ferric chloride leaching. Chemical Engineering Journal, 114(1): 67–72.

Barceloux, D., 1999. Journal of Toxicology: Clinical Toxicology, 37(2): 217–230.

Bork, N., Elm, J., Olenius, T. and Vehkamäki, H., 2014. Methane sulfonic acid-enhanced formation of molecular clusters of sulfuric acid and dimethyl amine. Atmospheric Chemistry and Physics, 14(22): 12023.

Di Lorenzo, F., Rodriguez-Galan, R.M. and Prieto, M., 2014. The kinetics of solvent-mediated transformation of hydromagnesite into magnesite at different temperatures and pressures, International: Goldschmidt Conference, Sacramento, California, pp. 557.

Dreisinger, D. and Abed, N., 2002. A fundamental study of the reductive leaching of chalcopyrite using metallic iron part I: kinetic analysis. Hydrometallurgy, 66(1): 37–57.

Dutrizac, J., Chen, T. and Jambor, J., 1985. Mineralogical changes occurring during the ferric ion leaching of bornite. Metallurgical Transactions B 16b(4): 679–693.

Dutrizac, J., Mac, D. and Ingraham, T., 1969. The kinetics of dissolution of synthetic chalcopyrite in aqueous acidic ferric sulfate solutions. Tansactions of the Metallurgical Society AIME, 245(5): 955–959.

Dutrizac, J., Macdonald, R. and Ingraham, T., 1970. The kinetics of dissolution of bornite in acidified ferric sulfate solutions. Metallurgical Transactions, 1(1): 225–231.

Dutrizac, J.E., 1981. The dissolution of chalcopyrite in ferric sulfate and ferric chloride media. Metallurgical Transactions B, 12(2): 371–378.

Dutrizac, J.E. and MacDonald, R.J.C., 1973. Percolation leaching of bornite ore, Proceedings, Australasian Institute of Mining and Metallurgy, Western Australia, pp. 25–31.

Dutrizac, J.E. and Macdonald, R.J.C., 1974. The kinetics of dissolution of covellite in acidified ferric sulfate solutions. Canadian Metallurgical Quarterly, 13(3): 423–433.

Dutrizac, J.E. and Macdonald, R.J.C., 1978. The Dissolution of sphalerite in ferric chloride solutions. Metallurgical Transactions B, 9(4): 543–551.

Dutrizac, J.E., Macdonald, R.J.C. and Ingraham, T.R., 1971. Effect of pyrite, chalcopyrite and digenite on rate of bornite dissolution in acidic ferric sulfate solutions. Canadian Metallurgical Quarterly, 10(1): 3–7.

Ekmekyapar, A., Demirkiran, N., Künkül, A. and Aktaş, E., 2015. Leaching of malachite ore in ammonium sulfate solutions and production of copper oxide. Brazilian Journal of Chemical Engineering, 32(1): 155–165.

Feng, Q.-C., Wen, S.-M., Wang, Y.-J., Cao, Q.-B. and Zhao, W.-J., 2015a. Dissolution kinetics of cerussite in an alternative leaching reagent for lead. Chemical Papers, 69(3): 440–447.

Feng, Q., Wen, S., Zhao, W., LV, C. and Bai, X., 2015b. Leaching of copper from malachite with methane-sulfonic Acid. Solvent Extraction Research and Development, Japan, 22: 159–168.

Feng, Q., Wen, S.M., Zhao, W., Bai, X. and Chen, Y., 2015c. Dissolution regularities of smithsonite in methane sulfonic acid. Russian Journal of Non-Ferrous Metals, 56(4): 365–371.

Florence, F., Nisha, S., Rajendran, K.N., Srinivasan, S. and John, S., 2011. Studies on electrodeposition of copper from methanesulphonic acid bath. International Journal of ChemTech Research, 3(3): 1318–1325.

Frenzel, G., 1959. Idait und "blaubleibender Covellin.". Neues Jahrb. Mineral 93: 87–132.

Gernon, M., Wu, M., Buszta, T. and Janney, P., 1999. Environmental benefits of methanesulfonic acid. Comparative properties and advantages. Green Chemistry, 1(3): 127–140.

Hatert, F., 2005. Transformation sequences of copper sulfides at Vielsalm, Stavelot Massif, Belgium. Canadian Mineralogist, 43(2): 623–635.

Hidalgo, T., Kuhar, L., Beinlich, A. and Putnis, A., 2018. Kinetic study of chalcopyrite dissolution with iron(III) chloride in methanesulfonic acid. Minerals Engineering, 125: 66–74.

Hirato, T., Kinoshita, M., Awakura, Y. and Majima, H., 1986. The leaching of chalcopyrite with ferric chloride. Metallurgical Transactions B, 17(1): 19–28.

Kelm, U. and Helle, S., 2005. Acid leaching of malachite in synthetic mixtures of clay and zeolite-rich gangue. An experimental approach to improve the understanding of problems in heap leaching operations. Applied Clay Science, 29(3): 187–198.

Khalezov, B., Kakovskii, I., Krushkol, O. and Kiseleva, V., 1979. Kinetics of dissolving azurite and malachite in aqueous sulfuric acid solutions. Metall(4): 29–32.

Kuhn, H., 2000. Principles of Physical Chemistry: Understanding Molecules, Molecular Assemblies, Supramolecular Machines. Wiley, Chichester, U.K.

Kuzmina, O., Symianakis, E., Godfrey, D., Albrecht, T. and Welton, T., 2017. Ionic liquids for metal extraction from chalcopyrite: solid, liquid and gas phase studies. Physical Chemistry Chemical Physics, 19(32): 21556–21564.

Lente, G., Fábián, I. and Poë, A.J., 2005. A common misconception about the Eyring equation. New Journal of Chemistry, 29(6): 759–760.

Levenspiel, O., 1999. Chemical Reaction Engineering, New York: Wiley, New York.

Li, Y., Kawashima, N., Li, J., Chandra, A.P. and Gerson, A.R., 2013. A review of the structure, and fundamental mechanisms and kinetics of the leaching of chalcopyrite. Advances in Colloid and Interface Science, 197–198:1–32.

Liu, Z.X., Yin, Z.L., Xiong, S.F., Chen, Y.G. and Chen, Q.Y., 2014. Leaching and kinetic modeling of calcareous bornite in ammonia ammonium sulfate solution with sodium persulfate. Hydrometallurgy, 144–145: 86–90.

Lowe, D.F., 1970. The kinetics of the dissolution reactions of copper and copper-iron sulfide minerals using ferric sulfate solutions, PhD thesis disertation, University of Arizona, Arizona.

Lu, J. and Dreisinger, D., 2013. Copper chloride leaching from chalcopyrite and bornite concentrates containing high levels of impurities and minor elements. Hydrometallurgy, 138: 40–47.

Lundström, M., Liipo, J., Taskinen, P. and Aromaa, J., 2016. Copper precipitation during leaching of various copper sulfide concentrates with cupric chloride in acidic solutions. Hydrometallurgy, 166: 136–142.

Majima, H., Awakura, Y., Hirato, T. and Tanaka, T., 1985. The leaching of chalcopyrite in ferric chloride and ferric sulfate solutions. Canadian Metallurgical Quarterly, 24(4): 283–291.

Manning, P.G., 1967. A study of the bonding properties of sulfurin bornite. The Canadian Mineralogist, 9(1): 85–94.

Meyer, M.C., Austin, P. and Tropper, P., 2013. Quantitative evaluation of mineral grains using automated SEM–EDS analysis and its application potential in optically stimulated luminescence dating. Radiation Measurements, 58: 1–11.

Miki, H., Nicol, M. and Velásquez-Yévenes, L., 2011. The kinetics of dissolution of synthetic covellite, chalcocite and digenite in dilute chloride solutions at ambient temperatures. Hydrometallurgy, 105(3): 321–327.

Munoz, P.B., Miller, J.D. and Wadsworth, M.E., 1979. Reaction mechanism for the acid ferric sulfate leaching of chalcopyrite. Metallurgical Transactions B, 10(2): 149–158.

Nicol, M.J., 2018. The kinetics of the dissolution of malachite in acid solutions. Hydrometallurgy, 177: 214–217.

Okada, T. and Utsumi, W., 2003. Kinetics of the graphite-diamond transformation in aqueous fluid determined by in-situ X-ray diffractions. Geochimica et Cosmochimica Acta, 67(18): A355–A355.

Pedrosa, E.T., Boeck, L., Putnis, C.V. and Putnis, A., 2017. The replacement of a carbonate rock by fluorite; kinetics and microstructure. American Mineralogist, 102(1): 126–134.

Perdikouri, C., Kasioptas, A., Geisler, T., Schmidt, B.C. and Putnis, A., 2011. Experimental study of the aragonite to calcite transition in aqueous solution. Geochimica et Cosmochimica Acta, 75(20): 6211–6224.

Pesic, B. and Olson, F.A., 1983. Leaching of bornite in acidified ferric chloride solutions. Metallurgical Transactions B, 14(4): 577–588.

Pesic, B. and Olson, F.A., 1984. Dissolution of bornite in sulfuric acid using oxygen as oxidant. Hydrometallurgy, 12(2): 195–215.

Price, D.C. and Chilton, J.P., 1980. The electroleaching of bornite and chalcopyrite. Hydrometallurgy, 5(4): 381–394.

Price, D.C. and Chilton, J.P., 1981. The anodic reactions of bornite in sulphuric acid solution. Hydrometallurgy, 7(1): 117–133.

Putnis, A., 1992. Introduction to Mineral Sciences. Introduction to mineral sciences, 1. Cambridge University Press, 310–321 pp.

Qian, G., Li, Y., Li, J. and Gerson, A.R., 2017. Consideration of enthalpic and entropic energy contributions to the relative rates of chalcopyrite dissolution in the presence of aqueous cationic impurities. International Journal of Mineral Processing, 159: 42–50.

Sullivan, J.D., 1931. Leaching copper from its ores. Journal of Chemical Education, 8(5): 829.

Tanda, B.C., Eksteen, J.J. and Oraby, E.A., 2017. An investigation into the leaching behaviour of copper oxide minerals in aqueous alkaline glycine solutions. Hydrometallurgy, 167: 153–162.

Ugarte-Alverez, F., 1971. Leaching of bornite, University of London, London, England, PhD disertation.

Ugarte, F.J. and Burkin, A.R., 1975. Mechanism of formation of idaite from bornite by leaching with ferric sulfate solution. Leaching and Reduct in Hydrometallurgy, Ed. A.R. Burkin, Institution of Mining and Metallurgy: 46–53.

Veloso, T., Paiva, P., Silva, C. and Leão, V., 2016. Leaching of bornite produced from the sulfurisation of chalcopyrite. Metallurgical and Materials Transactions B, 47(3): 2005–2014.

Wall, A., Mathur, R., Post, J. and Heaney, P., 2011. Cu isotope fractionation during bornite dissolution: An in situ X- ray Diffraction Analysis. Ore Geology Reviews, 42(1); 62–70.

Wang, J., L. Tao, H. Zhao, M. Hu, X. Zheng, H. Peng, X. Gan, W. Xiao, P. Cao, W. Qin, G. Qiu & D, 2016. Cooperative effect of chalcopyrite and bornite interactions during bioleaching by mixed moderately thermophilic culture. Minerals Engineering, 95: 116–123.

Wang, X., Hong, M., Liao,R., Zhao, C., Yu, S., Wang, J., Zhao,H., Gan, M., 2018. Synchrotron-based XRD and XANES study of bornite leached by mesophilic mixed bacteria, Characterisation of Minerals, Metals, and Materials 2018 Phoenix, AZ, USA,Springer, pp. 325–332.

Wu, Z., Dreisinger, D.B., Urch, H. and Fassbender, S., 2014a. Fundamental study of lead recovery from cerussite concentrate with methanesulfonic acid (MSA). Hydrometallurgy, 142: 23–35.

Wu, Z., Dreisinger, D.B., Urch, H. and Fassbender, S., 2014b. The kinetics of leaching galena concentrates with ferric methanesulfonate solution. Hydrometallurgy, 142: 121–130.

Yang, C.-R., Jiao, F. and Qin, W.-Q., 2018. Cu-state evolution during leaching of bornite at 50 °C. Transactions of Nonferrous Metals Society of China, 28(8): 1632–1639.

Zhao, H., Hu, M., Li, Y., Zhu, S., Qin, W.,Qiu, G., Wang, J., 2015. Comparison of electrochemical dissolution of chalcopyrite and bornite in acid culture medium. Transactions of Nonferrous Metals Society of China, 25(1): 303–313.

Every reasonable effort has been made to acknowledge the owners of copyright material. I would be pleased to hear from any copyright owner who has been omitted or incorrectly acknowledged.

Chapter 5. Replacement reactions of copper sulfides at moderate temperature in acidic solutions

Understanding mineral transformations of composite copper–sulfide ores and the associated reaction mechanism at low to medium temperatures in acidic solutions with oxidant restriction is important for in-situ recovery (ISR) operations because natural ore bodies typically comprise multiple sulfide species and their dissolution is oxidant consuming. However, the relevant reactions have scarcely been investigated. Here we present experimental observations on mineral replacement reactions of coarse-grained natural bornite–chalcocite samples in acidic solutions at 90°C and in the absence of oxidant. Transformations were found to follow a three-stage reaction sequence for bornite and one-stage for chalcocite. Bornite replacement commenced with the formation of digenite along fractures and surfaces. Bornite–digenite interfaces were sharp and digenite rims contained nanochannels that connected to the original bornite. When copper dissolution exceeded 30%, copper-deficient lamellae exsolved from the bornite by solid-state diffusion; this texture appeared only in stronger acidic solutions with extended times and did not occur in heating experiments without fluid. Chalcocite that was present together with bornite in the unreacted samples transformed into digenite characterised by laminar replacement textures. Finally, all phases were replaced by covellite accompanied by the formation of porosity. These replacements showed the concomitant operation of fluid-induced solid-state diffusion and fluid-mediated mineral replacement by coupled dissolution–precipitation reactions. The textures found in the resulting covellite showed a promising increase in porosity that could be beneficial for hard-rock ISR and suggest a pathway for refractory sulfide processing by acid pre-treatment.

5.1. Introduction

The recent decline in the frequency of discovered high-grade Cu deposits paired with stricter environmental regulations has encouraged the evaluation of alternative approaches for Cu extraction including *in-situ* recovery (ISR) (Sinclair and Thompson, 2015). Chalcopyrite and bornite represent the major proportion of currently known Cu resources (Zhao et al., 2015) and are thus of particular interest for ISR (Hidalgo et al., 2019a; Hidalgo et al., 2019b). In natural ore, chalcopyrite and bornite are commonly

associated with secondary sulfides, including chalcocite, digenite, and covellite. Since targeting of specific minerals during ISR operating in complex composite natural deposits is nearly impossible, the reactions between the lixiviant and secondary sulfide minerals must also be considered.

The hydrothermal enrichment of Cu by hydrothermal alteration of chalcopyrite and bornite into readily leachable minerals in the presence of copper sulfate or oxygen in acidic solutions and the possible viability of secondary sulfides as pre-treatment or purification processes have been addressed previously by Fuentes et al. (2009) and Cerda et al. (2017) . Under a variety of experimental conditions, both minerals were replaced by secondary copper-enriched phases, such as chalcocite, digenite and covellite (Bartlett, 1992; Muszer et al., 2013; Pesic and Olson, 1984). However, for the successful implementation of ISR, such sulfide mineral replacement reactions require further investigation under realistic conditions, including the effects of multiple reactants in composite samples, at medium to elevated temperatures, with coarse grained solids and restricted oxidant supply. In case of ISR, dissolution and precipitation of secondary Cu phases along the fluid (lixiviant and/or pregnant solution) flow paths and in the primary target zone may delay or enhance the recovery of Cu (Mallio et al., 1981). Hence, a better understanding of conditions that result in the formation of product layers on primary Cu-sulfide minerals and downstream from the lixiviant injection zone and the potential effect on porosity/permeability is critical for the implementation of ISR schemes.

The generation of secondary sulfide layers has been attributed to solid-state diffusion, and is described as the removal or replacement of certain ions while the underlying framework structure remains unaltered, e.g., chalcocite transformation into digenite and covellite by preferential dissolution of copper from the original phase (Burkin, 1969). Such ‘solid-state’ processes are broadly accepted as the mechanism of ‘leaching’ a metal from an ore body. However, in some cases, the replacement textures exhibit characteristics inconsistent with this mechanism, including replacement rates at moderate to low temperature, dependence on fluid composition, and a lack of diffusion profiles across replacement interfaces. Instead, these characteristics are indicative of fluid-driven mineral replacement by dissolution–precipitation reactions, as demonstrated for numerous systems (Altree-Williams et al., 2015; Hellmann et al., 2003; Putnis, 2002; Putnis and Putnis, 2007; Ruiz-Agudo et al., 2012; Ruiz-Agudo et

al., 2014) and demonstrated through the incorporation of species from a 'doped' solution in the secondary mineral (Geisler et al., 2005; Hövelmann et al., 2010; Labotka et al., 2002; Niedermeier et al., 2009).

Furthermore, recent observations suggest that the textures and chemical compositions of sulfide assemblages are consistent with mineral replacement by dissolution–precipitation reactions. For example, Zhao et al. (2014) investigated the fluid-mediated replacement of chalcopyrite by Cu-rich bornite between 200°C and 320°C in cuprous-chloride buffered solutions. Cai et al. (2011) described pseudomorphic replacement of chalcopyrite by Cl-bearing covellite and nantokite in acidic CuCl solutions below 100°C. In both examples, the solid product phases were characterised by an elevated porosity, which allowed for continued fluid transport to the reaction front.

The mineralogical changes in bornite (Cu_5FeS_4) in the presence of ferric oxidants have been reviewed by Dutrizac et al. (1985). In this analysis, bornite dissolution was found to be non-stoichiometric, which resulted in the formation of a Cu-deficient phase with a composition of Cu_3FeS_4. The phase was also identified by Ugarte-Alverez (1971), and was suggested to result from the extraction of ionically bound Cu atoms during the first stage of reaction, which leave behind a chalcopyrite-like unit cell that conserves the sulfur packing. Chalcocite dissolution in HCl at low to medium potentials (0 to 0.6 mV vs. standard hydrogen electrode (SHE)) was accompanied by the formation of several transient phases defined as $Cu_{2-x}S$. Covellite has been found to be the final product after sustained reaction of bornite and chalcocite in acidic solutions (Parikh and Liddell, 1990; Pesic and Olson, 1984). The transformation of primary Cu sulfides into covellite occurs with or without the presence of oxygen (Pesic and Olson, 1984; Price and Chilton, 1980; Price and Chilton, 1981) and has been attributed to the preferential dissolution of iron.

Bornite (Cu_5FeS_4), chalcopyrite ($CuFeS_4$) and digenite ($Cu_{1.8}S$) have a common structure based on the sphalerite stacking principle, which consists of cubic close-packing sulfur with alternative cation sites occupied. Chalcocite (Cu_2S) has a hexagonal sulfur close-packing with movable copper cations, Finally, the covellite structure is not described in terms of sulfur close-packing but is a coordinated copper layers that are limited by sulfur dimers and parallel to the hexagonal c-axis

(Makovicky, 2006). Thus, transformations from any of the other phases into covellite require a complete recrystallisation of the original phase.

To investigate further the reactions that occur along a reaction path from initial bornite and/or chalcocite to the final covellite at conditions relevant to ISR schemes, we present results from an experimental study conducted at 90°C, in acidic conditions and with low concentrations of dissolved oxygen. We used a coarse composite natural Cu-sulfide starting material to mimic the conditions anticipated during ISR.

5.2. Materials and methods

5.2.1. Experimental procedure

Experiments were conducted in 250 mL Nalgene bottles in a shaking water bath at 90°C with a constant speed of 150 rpm. Sample charges consisted of one cuboid cut from the bulk sulfide sample and 100 mL reactive fluid. Reactive fluids were prepared from deionised water and analytical-grade hydrochloric acid (HCl) and methanesulfonic acid (MSA) at concentrations of 0.5 mol L^{-1} without oxidant addition. The initial pH and Eh were 0.85 and 0.66, and 300 and 350 mV (vs. S. H. E), respectively. Reaction durations were 8 days, two weeks and 30 days. To minimize the amount of dissolved oxygen, nitrogen was bubbled continuously into the solutions for 3 hours before the experiments. Due to the production of H_2S during the experiments, intermittent pressure release was necessary by venting the gas and further bubbling of nitrogen directly into the fluid (tubing insertion) to flush the headspace. After the experiment, fluids were sampled through a 0.45 µm syringe filter and diluted for inductively coupled plasma-optical emission spectrometer (ICP-OES) analysis. Solid samples were washed three times with deionised water and dried overnight in a closed standard oven at 30°C. Additional dry runs were performed under the same conditions for comparison. The cuboid sample was placed in an empty Nalgene bottle flushed with nitrogen every 24 h and the bottle was placed in a closed incubator at 90˚C. The dry runs were run for 8 days, 2 weeks and 30 days.

5.2.2. Analytical methods

Characterisation of initial material was performed by a combination of methods, including optical microscopy, quantitative evaluation of minerals by scanning electron microscopy (QEMSCAN), scanning electron microscopy (SEM), electron backscatter diffraction (EBSD) and X-ray diffractometry (XRD) at the CSIRO Characterisation Laboratories, Western Australia. The samples were mounted in epoxy, polished and carbon coated prior to SEM analysis. A Nikon Eclipse EV100N POL microscope was used for optical imaging. Backscattered electron (BSE) and secondary electron (SE) imaging and energy-dispersive spectroscopy (EDS) analyses were conducted using a JEOL-JSM-7001 SEM fitted with a Bruker XFlash EDS system. SEM EDS spectra were collected at analysis points separated by at least 5 µm and the chemical compositions were calculated by averaging at least 35 points. Analyses of standard reference materials were carried out for quality control. Phase identification was performed on the polished surfaces using an E430 QEMSCAN at a 0.98 µm pixel spacing, and a PANalytical Empyrean X-ray diffractometer equipped with a cobalt X-ray tube operating at 40 kV, 40 mA, an incident monochromator, 0.5° divergence slit, and 0.02 rad soller slits. EDS mapping and EBSD measurements were undertaken using a Zeiss Ultra plus SEM fitted with an Oxford Symmetry EBSD and X-max EDS. High resolution maps and point analyses were collected at 5 keV to minimise the excitation volume and to obtain results for areas with fine textures. For the EBSD work, the SEM was typically operated at around 20 keV and 10 nA which gave a reasonable compromise of resolution, speed and beam damage to the sample.

Scanning transmission electron microscopy (STEM) imaging and EDS mapping was applied to specific samples for high-resolution investigation of the product–parent interfaces. Sample preparation was performed by focused ion beam (FIB) cutting using the FEI Helios Nanolab G3 CX DualBeam FIB/SEM at the Centre for Microscopy, Characterisation and Analysis (CMCA), The University of Western Australia. STEM analyses were performed with the Titan G2 80-200 TEM at 200 kV at CMCA using a double tilt specimen holder. Fluids were sampled after selected times of 4 h, 6 h, and from 1 to 30 days, and were analysed for Cu, Fe and S using the Varian Vista-Pro ICP-OES.

Mineral chemical compositions are expressed in mass percent unless stated otherwise. Mineral abbreviations in photomicrographs and electron images follow the recommendations by Whitney and Evans (2010).

5.2.3. Starting material

Natural Cu sulfide was cut and polished to form cuboid fragments with edge lengths of approximately 4 mm and an average mass of 0.34 g. The starting material was analysed for its mineral and chemical compositions by SEM-EDS, QEMSCAN and XRD (Fig. 5-1). The analysis of the starting material showed that the sulfide cubes had a homogeneous surface with minor cracks (Fig. 5-2) and well-defined grain boundaries, and were mainly composed of bornite (Cu_5FeS_4) (47% ± 1.3%) and chalcocite (Cu_2S) (20.6% ± 1.6%). Minor phases included chalcopyrite ($CuFeS_2$) (2.3% ± 0.8%), pyrite (FeS_2) (0.95% ± 0.4%), tennantite ($Cu_{12}As_4S_{13}$) (1.7% ± 0.7%), quartz (21.2% ± 2.1%), and negligible amounts of covellite (CuS) (0.1% ± 0.07%). The average chemical composition of the sulfide phases in the starting material were close to the theoretical values of bornite (Cu 63.7%, Fe 12.1%, S 24.5%) and chalcocite (Cu 79.9%, S 20.1%). Sulfide minerals in the starting material did not show evidence of compositional zonation in any of the major phases.

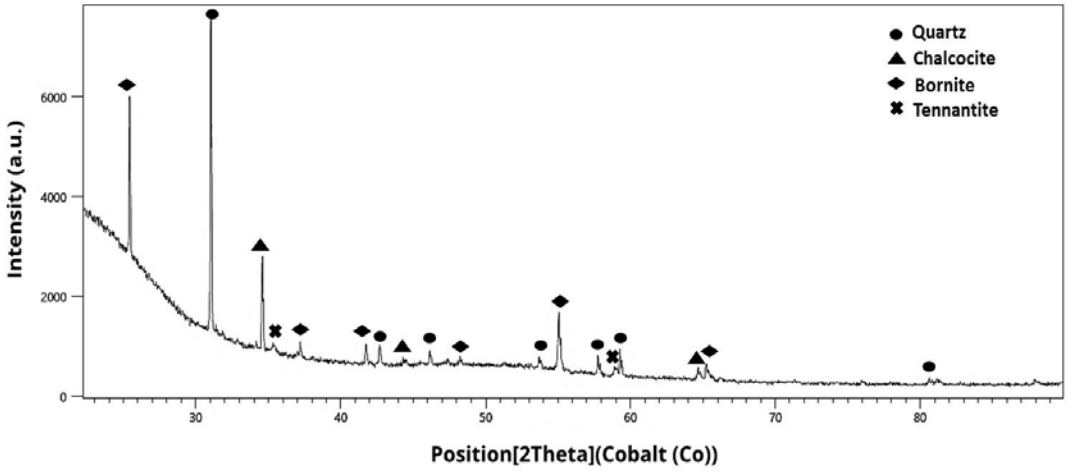

Fig. 5-1. X-ray diffractogram of the pre-leached sample, showing bornite, chalcocite and quartz as the dominant phases.

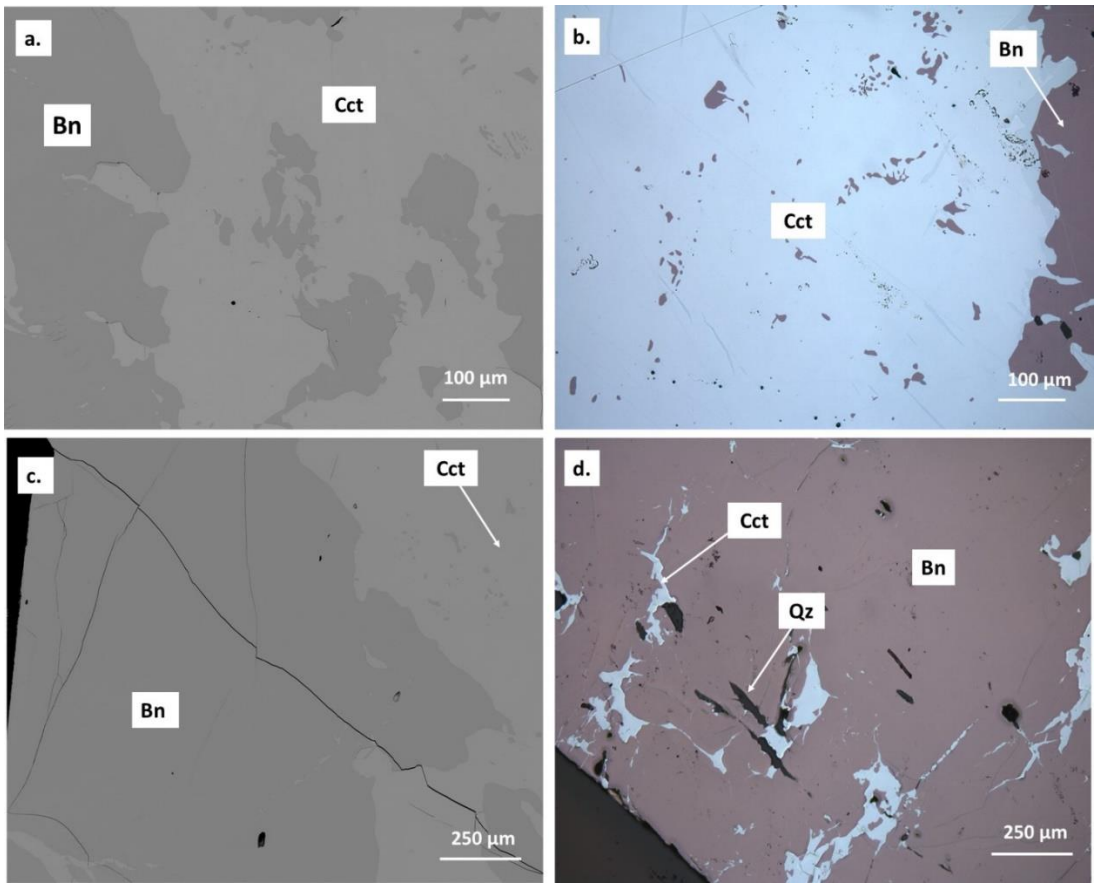

Fig. 5-2. BSE and optical images of the polished surface of bornite and chalcocite in an unreacted cuboid. **a.** SEM-BSE image indicating compositional homogeneity of the starting chalcocite. **b.** Reflected light photomicrograph showing a similar starting material sulfide assemblage as in Fig. 2a. without evident variations in colour. **c.** SEM-BSE image indicating compositional homogeneity of the starting bornite, absence of reaction rims or compositional changes around fracture zones. **d.** Reflected light photomicrograph showing a similar starting material sulfide assemblage as in Fig. 2c.

5.3. Results

5.3.1. Copper and iron dissolution rates

The experiments resulted in the release of Cu and Fe from the solids into the fluids. The percentages of Cu and Fe dissolved from the original samples in different acids for extended and reduced reaction times are plotted in Fig. 5-3. The shapes of the dissolution curve are similar for HCl and MSA, though a faster rate was obtained in the HCl solution. Iron release was faster than copper during the first ~72 h, at 12% for HCl and 4% for MSA solutions. The increase continued at slower pace from ~100 h

to ~600 h (Fig. 5-3c and f). A measurable release of Cu commenced after 6 hours, increased continuously until ~300 h and remained constant for longer experiment durations. A maximum of 38% of copper was dissolved in HCl and 23% in MSA solutions.

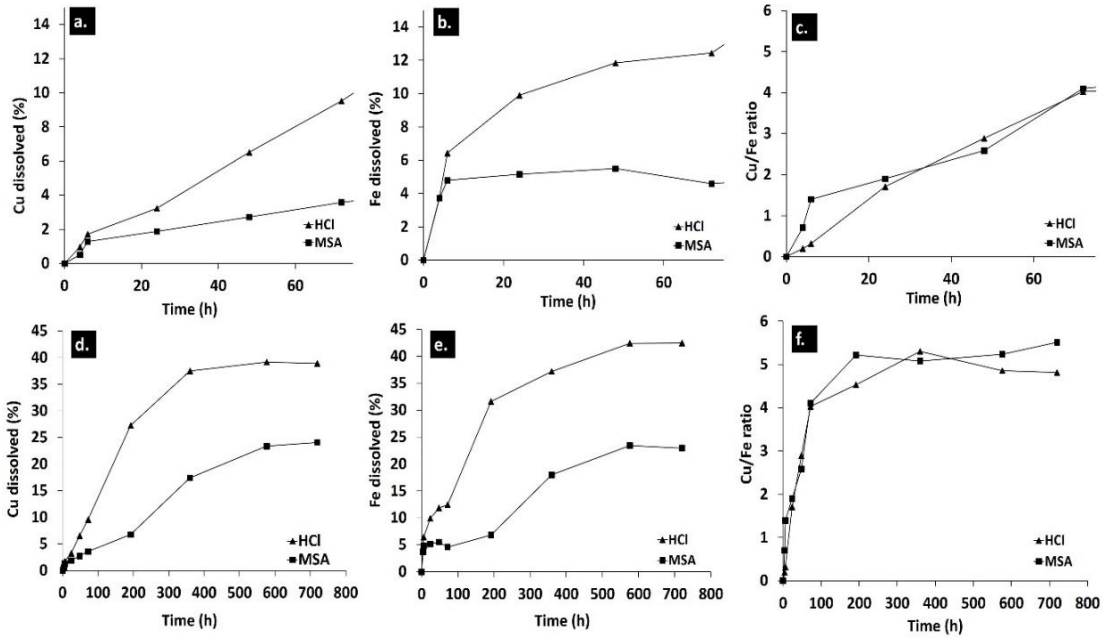

Fig. 5-3. Copper and iron extraction vs. time for composite sample in different acid solutions using the same acid concentration (0.5 mol L^{-1}) at 90°C. **a.** Copper dissolved in solution (%) for reduced reaction times (75 h). **b.** Iron dissolved in solution (%) for reduced reaction times (75 h). **c.** Molar Cu/Fe ratio in solution for reduced reaction times (75 h). **d.** Copper dissolved in solution (%) for extended times (720 h). **e.** Iron dissolved in solution (%) for extended reaction times (720 h). **f.** Molar Cu/Fe ratio in solution for extended reaction times (720 h).

5.3.2. Solid transformations

Under the experimental conditions, only bornite and chalcocite zones of the sample experienced mineralogical transformations. Chalcopyrite, although present at low percentage in some of the samples, showed minor replacement by digenite in the HCl solutions along fractures. For the purposes of this research, only bornite and chalcocite transformations are discussed. The compositions of the starting material and secondary phases are summarised in Table 5-1 and plotted in Fig. 5-4. Chemical formulae were calculated on a 4-sulfur and 1-sulfur basis (sulfur atoms constant) depending whether it formed after bornite or chalcocite as required for comparison.

Table 5-1. Chemical compositions and formulae of phases identified after reaction in acidic solutions at 90°C.

Mineral	Origin	Time of first occurrence		%Cu	sd (1σ) *	%Fe	sd (1σ) *	%S	sd (1σ) *	Calculated formula
		MSA	HCl							
Bornite	Unreacted sample	N.A.	N.A.	63.7	1.6	12.1	0.5	24.4	0.6	$Cu_{5.2}Fe_{1.1}S_4$
Chalcopyrite				35.9	1.4	32.5	0.9	31.6	1.9	$Cu_{1.1}Fe_{1.2}S_2$
Chalcocite				79.9	0.6	-	-	20.1	0.6	$Cu_{1.99}S$
Digenite	Chalcocite replacement	8 days	8 days	78.6	0.2	0	-	21.6	0.2	$Cu_{1.82}S$
Covellite		2 weeks		66.2	1.4	0	-	33.8	1.4	$Cu_{0.98}S$
Digenite	Bornite replacement	8 days		77.3	0.9	0.9	0.6	21.8	0.5	$Cu_{7.1}Fe_{0.1}S_4$
Covellite		2 weeks		65.9	1.3	0.2	0.5	33.9	1.7	$Cu_{3.9}Fe_{0.01}S_4$
X-bornite avg	Bornite exsolution	N.A.**	2 weeks	51.7	1.3	15.4	0.4	32.8	0.6	$Cu_{3.15}Fe_{1.08}S_4$
X-bornite Cu-deficient				41.1	1.1	27.3	1	31.6	0.1	$Cu_{2.6}Fe_{1.98}S_4$
X-bornite Cu-rich				65.1	0.9	6.5	0.7	28.4	0.4	$Cu_{4.58}Fe_{0.52}S_4$

* sd: standard deviation
** Exsolution was not evidenced in these samples
% are given in mass percentage of elements (wt %) based on SEM-EDS point analysis
x-bornite refers to the transformation of original bornite into exsolved phases

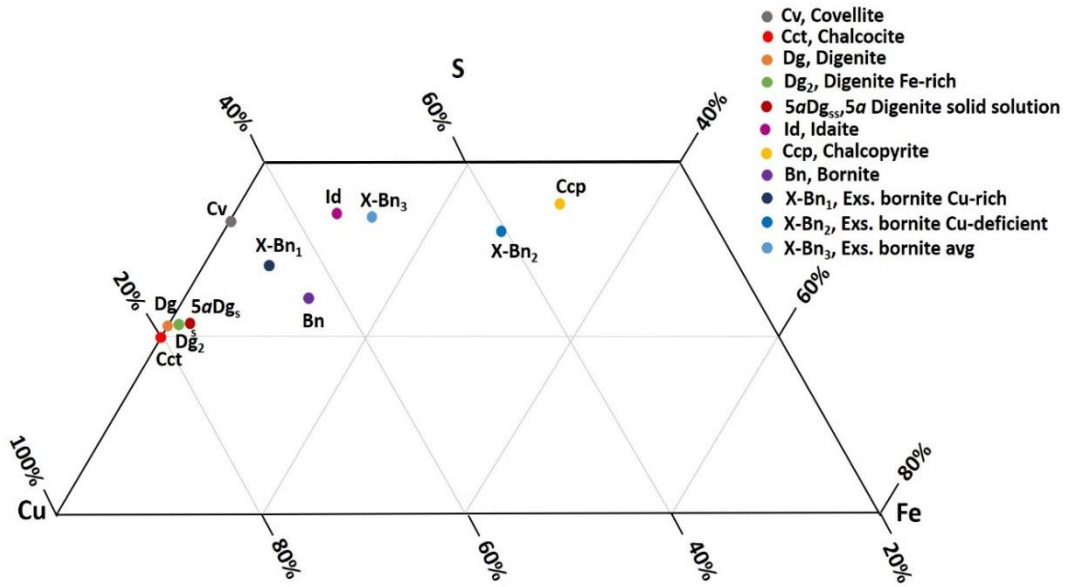

Fig. 5-4. Cu–Fe–S ternary diagram showing the observed changes in Cu-sulfide compositions. Additional phases: Dg_2: Fe-rich digenite from bornite replacement, 5*a*Dgss: 5a digenite solid solution (Grguric and Putnis, 1999), Id: idaite (Cu_3FeS_4) (Ugarte and Burkin, 1975), X-Bn_1: exsolved lamellae of Cu-rich bornite, X-Bn_2: exsolved lamellae of Cu-deficient bornite, X-Bn_3: bulk average composition of exsolution texture in bornite.

5.3.2.1. Chalcocite replacement

Of the two major sulfide phases in the solid reactant (chalcocite and bornite), chalcocite was the first to show signs of replacement. The optical image in Fig. 5-5a shows that chalcocite developed a reflection discolouration to light blue after 8 days of reaction time in MSA. This change in reflection colour was related to the removal of Cu during formation of dark blue lamellar digenite zones in the parent chalcocite (Fig. 5-5b). This change in composition and mineralogy was confirmed by SEM-EDS and XRD data. The transformation of chalcocite to digenite occurred more readily in the HCl solutions and after 8 days, iron free digenite (Fig. 5-5c) BSE imaging and EBSD analyses indicated the preservation of morphology and orientation during the replacement without the formation of detectable porosity.

For the extended experimental times, all MSA samples and HCl samples showed the formation of additional covellite. Initially, covellite replaced digenite along fractures and subsequently replaced the entire digenite areas. Complete replacement of digenite by covellite coincided with the reaction duration that was characterised by a constant Cu concentration in the fluid. The covellite had a fine grain size, and showed significant porosity and abundant shrinkage fractures (Fig. 5-5d). For the one-month HCl experiments, 34.7% covellite was present in the solid compared with 2.7% covellite in the solid for the experiment with MSA. Solid compositions are presented in Table 5-1.

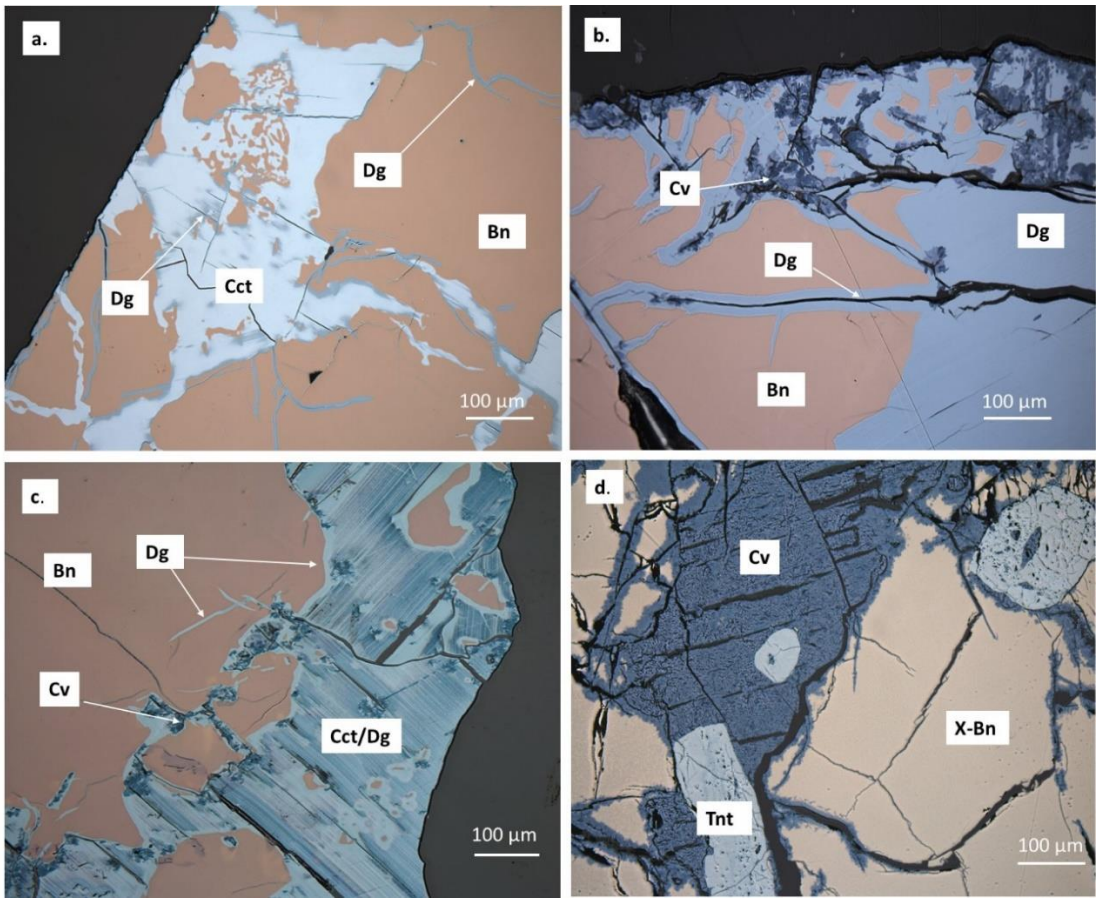

Fig. 5-5. Reflected light photomicrographs showing the transformation of chalcocite to digenite and covellite at 90°C. **a.** Chalcocite reacted in MSA after 8 days. Laminar texture reflects the presence of digenite accompanied by a minor variation in the Cu concentration. Copper-enriched zones were found as rims in bornite adjacent to chalcocite and along fractures in the bornite. **b.** Chalcocite reacted in MSA after 1 month. The original chalcocite was replaced by digenite, which in turn, was replaced by covellite. **c.** Partial chalcocite replacement by digenite in HCl after 8 days, showing strong laminar texture with copper-enriched digenite zones, covellite nucleation along fractures, and digenite rims along chalcocite-bornite grain boundaries. **d.** Covellite formation after one-month reaction in HCl showing abundant porosity and shrinkage features.

5.3.2.2. Bornite dissolution

Bornite replacement was found to be consistently slower than that of chalcocite in MSA and HCl. For example, bornite replacement commenced in the HCl solution only after 8 days. Generally, the textures and compositions of secondary phases formed from bornite evolved through three different stages. MSA solutions only showed one of these stages.

During the first stage, bornite replacement was restricted to the sample surface and the vicinity of fractures in the bornite, i.e., the contact zones with the reactive fluid, and resulted in the formation of secondary digenite (Fig. 5-6a). The composition of digenite after bornite was distinct from digenite after chalcocite because of its higher Fe content of ~0.8 at.% (Table 5-1), which placed it in the digenite–bornite solid solution region (Bn_4Dg_{96}) (Fig. 5-4). This zone was identified as 5*a* 'digenite solid solution', and was characterised by a cubic low-digenite structure with an Fe content between 0.4 at.% and 1.6 at.% (Grguric and Putnis, 1999). The digenite rims along cracks and the sample surface showed a consistent thickness of ~2.5 µm after 2 weeks and reached ~3.5 µm after one month in the MSA solution. At this time, covellite nucleation commenced. In the HCl solution, the digenite rim width reached ~2 µm after 8 days and ~3.7 µm after 2 weeks. After 2 weeks, digenite formation ceased and the reaction started to form secondary covellite. All experiments developed sharp concentration changes across the reaction interfaces between the bornite and secondary digenite (Fig. 5-6b and c). STEM high-angle annular dark field (HAADF) images and STEM-EDS show that the interface and concentration change was sharp on the nanometre scale (Fig. 5-7). Furthermore, STEM-HAADF investigation also showed that the replacement was accompanied by the protrusion of flame-shaped digenite from the reaction interface into the precursor bornite.

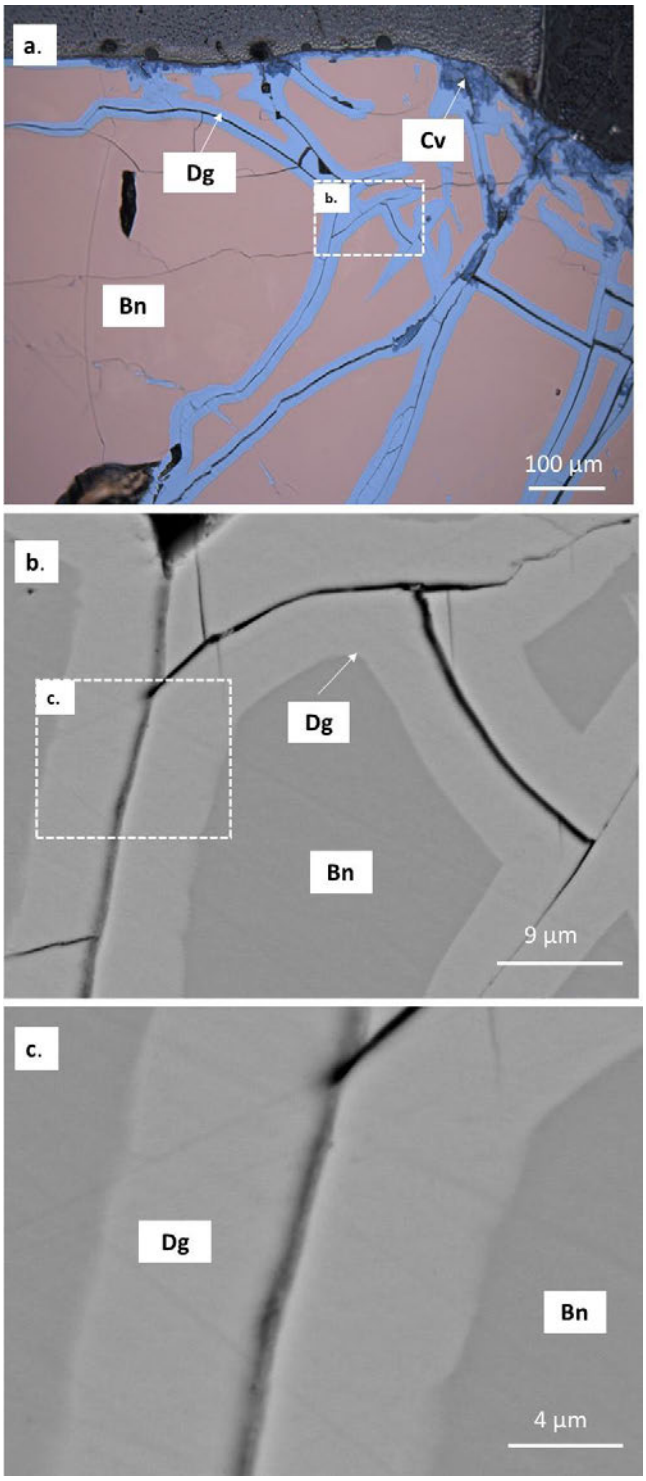

Fig. 5-6. Reflected light photomicrograph and BSE images of polished bornite sections after one month of reaction in MSA solutions at 90°C. **a.** Bornite sample after reaction. Internal cracks show continuous rims of digenite with additional covellite forming in the centre of the fractures. **b. and c.** SEM-BSE images showing details of sharp replacement fronts between dark-grey bornite and light-grey digenite without detectable phase-internal compositional and textural changes towards the interface. At this stage of reaction, bornite remains homogeneous and does not show exsolution textures.

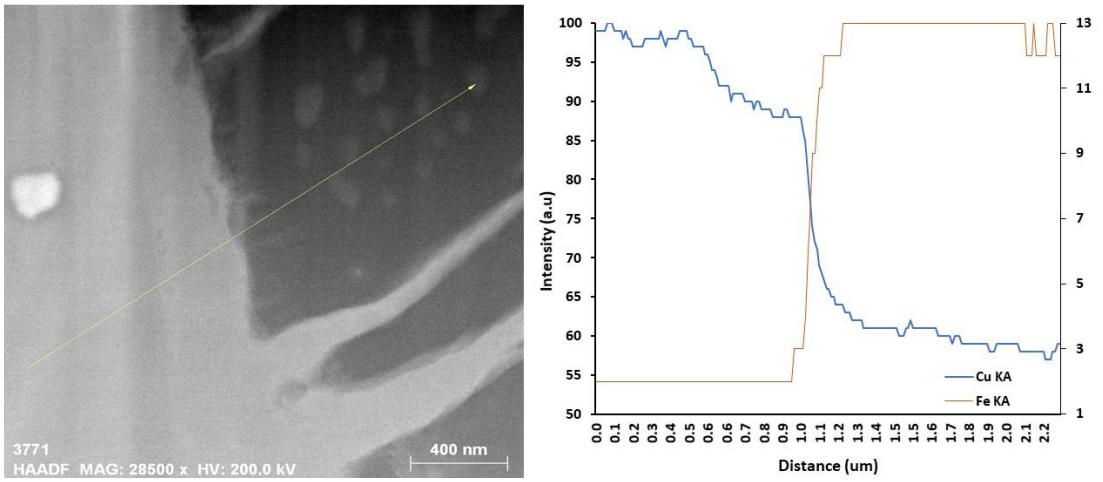

Fig. 5-7. STEM-HAADF image of the bornite–digenite replacement interface and a STEM-EDS concentration profile across the interface. The replacement interface between bornite (dark grey) and digenite zones (light grey) coincides with a sharp concentration change in Fe and Cu. The arrow in the STEM-HAADF image depicts the trace of the EDS line scan.

After two weeks of reaction in HCl solution, the second stage of bornite replacement was characterised by the termination of digenite formation from bornite and the development of a basket-weave exsolution texture in the bornite. Dry runs of the experiments did not show this exsolution texture under otherwise identical conditions and durations. Optical microscopy, SEM and QEMSCAN showed that bornite exsolved into two distinct phases with a texture consistent with exsolution from bornite (Fig. 5-8 to Fig. 5-10). Element mapping showed that the two exsolved phases were Cu-richer and Cu-poorer. Figure 5-9 also shows digenite replacing bornite along a fracture. Broad-beam SEM-EDS analysis suggests that the average composition of this altered bornite was copper-deficient compared with the original bornite and had a chemical formula ~Cu_3FeS_4, which is close to that reported from previous bornite leaching studies and has been identified as copper-deficient bornite or 'idaite' (Dutrizac et al., 1985; Pesic and Olson, 1983; Ugarte and Burkin, 1975). This average composition is labelled X-Bn_3 in Fig. 5-4. The two exsolved phases had approximate compositions of $Cu_{4.58}Fe_{0.52}S_4$ (X-Bn_2 in Fig. 5-4) and $Cu_{2.6}Fe_{1.98}S_4$ (X-Bn_1 in Fig. 5-4), respectively (Table 5-1). Given the fine size of the exsolution texture, the compositions determined by SEM-EDS reported in Table 5-1 should be considered as approximate. The Cu-poor lamellae had a composition close to mooihoekite

($Cu_9Fe_9S_{16}$), which was found by Wang et al. (2018) during bornite bioleaching and preceded the formation of chalcopyrite. Similar textures have been described from bornite solid solutions after dry annealing and quenching experiments (Brett and Yund, 1964; Grguric and Putnis, 1999; Zhao et al., 2017) and in natural ores (Ciobanu et al., 2017; Hatert, 2005).

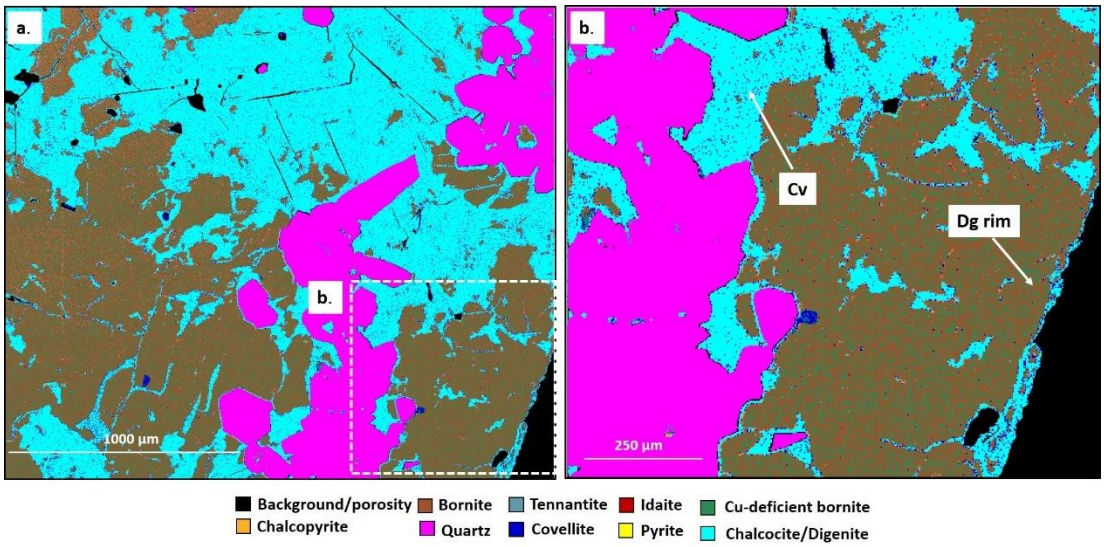

Fig. 5-8. QEMSCAN images of a bornite sample after 8 days of reaction in HCl solutions at 90°C. **a.** Reacted sample showing digenite rim formation surrounding fractures with covellite points spread on top, bornite zones show transformation into Cu-deficient bornite exsolution. **b.** Magnification of reacted solid sample showing zones of exsolution indexed as 'Cu-deficient bornite' showing patches of original bornite.

Additional EBSD analyses indicate that the Cu-enriched matrix of the exsolution texture was composed of orthorhombic bornite, whereas the Cu-deficient lamellae were composed of cubic bornite. The inverse pole map of the two phases indicates a preferred orientation to the 001 plane of the orthorhombic bornite and that the cubic bornite was orientated preferentially to the 010 plane. Point XRD results and EBSD map of the exsolution are presented in Appendix D.

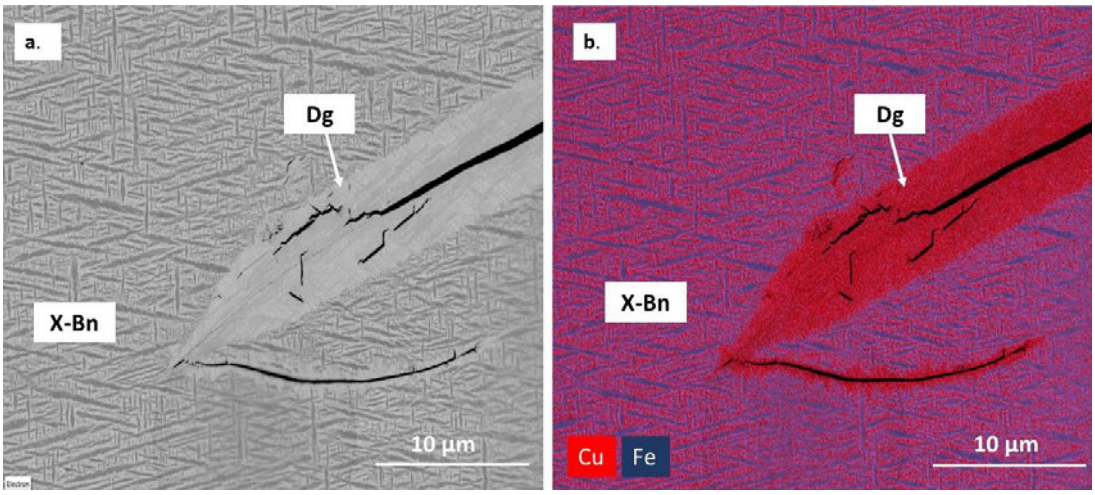

Fig. 5-9. SEM image and element distribution map of the bornite exsolution texture and digenite rim after reaction in HCl at 90°C for two weeks. **a.** BSE of the exsolution texture. **b.** EDS Cu concentration map showing lamellae of Cu-deficient bornite and the Cu-enriched digenite rim.

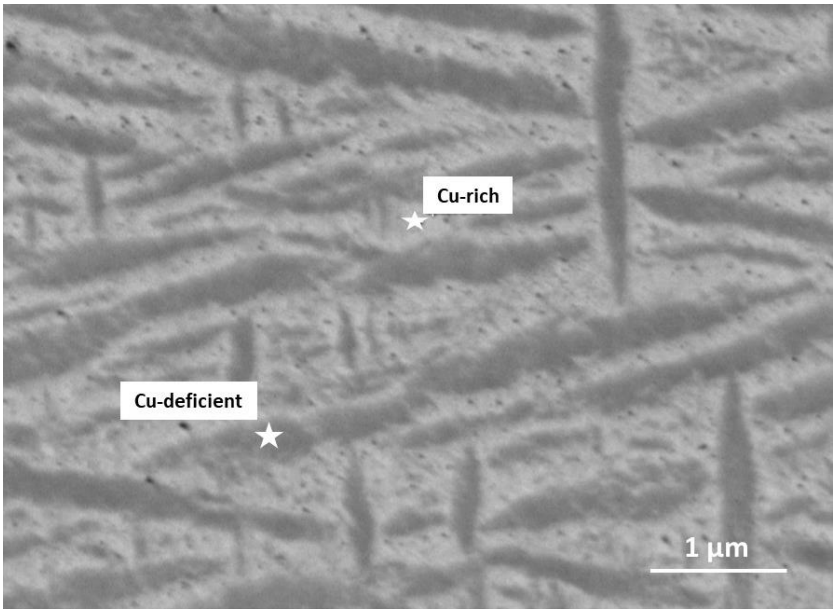

Fig. 5-10. SEM-BSE image of bornite after reaction in HCl at 90°C for two weeks showing an exsolution texture in the centre of the cuboid. SEM-EDS indicates that the dark lamellae have lower Cu concentrations, whereas the dark-grey matrix is depleted in Fe relative to unreacted bornite.

The third stage of the bornite reaction sequence was the increase in covellite formation, which was characterised by the replacement of earlier-formed digenite and the exsolved copper-deficient texture in the bornite. In our experiments, only the solids

leached with HCl reached this stage. The replacement of the rims went almost to completion and only relics of digenite were present in covellite after one month. At this time, more than 38% of the initial Cu in the system was dissolved in the fluid and covellite formed a major part of the sample. In contrast, reaction for one month in MSA formed chalcocite rims without concomitant exsolution from bornite (Fig. 5-11).

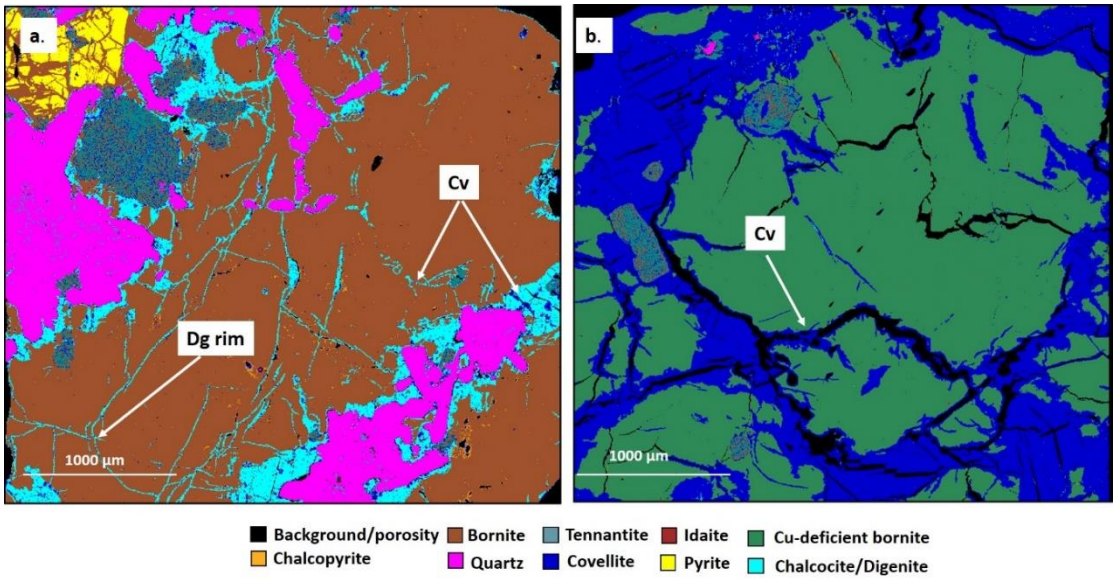

Fig. 5-11. QEMSCAN images of bornite samples after one-month reaction in acid solutions at 90°C. **a.** Solid sample reacted in MSA solution showing a thin sharp rim of digenite along bornite-quartz grain boundaries. Bornite zones do not show compositional changes and covellite nucleated on fracture joints. **b.** Bornite sample reacted in HCl solutions showing substantial replacement by covellite, which coincides with grain boundaries and fractures. Bornite shows compositional variations due to the presence of Cu-deficient bornite exsolution lamellae.

Despite extensive reaction, the former shape of the sulfide cuboids was preserved in all experiments. In optical photomicrographs, the covellite displays a dark-blue reflection colour and a relatively porous texture. Compared with the earlier digenite, covellite rims around fractures and at the sample surfaces were generally thicker and ranged from ~25 µm after two weeks to ~40 µm after one month of reaction (Fig. 12a to d). This implies that, at this stage of reaction, covellite not only formed from the precursor digenite but also directly from bornite. In contrast to digenite and covellite after chalcocite, covellite that formed after bornite contained detectable Fe (~0.2%;

Table 5-1). In a few places, fractures crosscut digenite rims and digenite-bornite interfaces. The orientation of these fractures aligned with the orientation of the exsolution (Fig. 5-12e and f).

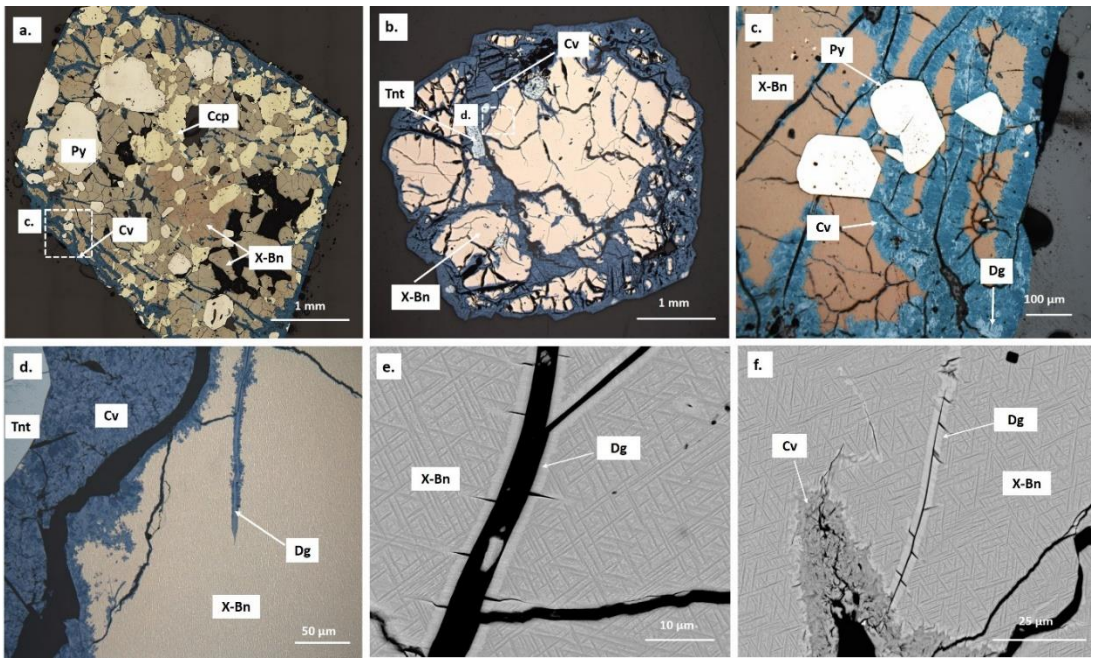

Fig. 5-12. Reaction textures of bornite after reaction in HCl solutions at 90°C. **a.** Reflected light photomicrograph showing covellite formation after reaction in HCl for two weeks. Covellite formation proceeded by replacement of digenite that formed initially from the original bornite along fractures. **b.** Reflected light photomicrograph showing covellite formation after reaction in HCl for one month, indicating continued covellite formation with experiment duration. **c.** Photomicrograph showing details of covellite formation in the area outlined in Fig. 12a. **d.** Photomicrograph showing details of covellite formation in the area outlined in Fig. 12b. **e**. Close-up SEM BSE image of the bornite exsolution texture after two weeks of reaction. The digenite rim shows fractures aligned with the orientation of the Cu-deficient exsolution lamellae. **f.** Close-up SEM BSE image of the bornite exsolution texture after one month of reaction, showing covellite replacing bornite containing the exsolution texture.

5.4. Discussion

5.4.1. Replacement mechanism

Diverse transformations were observed during the replacements of chalcocite and bornite in acidic solutions at 90°C. Owing the chosen temperature, the experimental observations should be directly relevant to ISR. The observed reaction textures are indicative for concomitantly operating solid-state diffusion and mineral replacement by dissolution–precipitation reactions. Although solid-state diffusion is generally considered slow, cation diffusion rates in Cu-sulfide minerals are relatively fast (Cherniak, 2010; Grguric and Putnis, 1999). Thus, mineral replacement driven by solid-state diffusion and by dissolution–precipitation may, theoretically, proceed at similar rates in sulfide minerals. The identification of the replacement mechanism must therefore rely on the analysis of reaction textures. The most important characteristics of the interface-coupled dissolution–precipitation mechanism (Putnis, 2009; Putnis and Putnis, 2007) include 1) a preservation of the parent-phase morphology and possible epitactic relations between the phases evidenced by transfer of crystallographic information from the parent, 2) a sharp and well-defined reaction front, 3) porosity and fractures in the product phase due to the relative solubilities and molar volumes of parent and product that allow the advective transport of fluid to the reaction front, and element transport through the interconnected fluid and 4) a dependence of the products on the chemical composition of the fluid at the reaction interface.

Upon initial reaction, chalcocite releases Cu incongruently into solution, which is accompanied by the formation of digenite. Subsequently, digenite is replaced by covellite, which is consistent with previous observations (Cheng and Lawson, 1991; Hackl et al., 1995; Muszer et al., 2013; Parikh and Liddell, 1990). The replacement of chalcocite by digenite requires a change in sulfur close-packing from hexagonal (hcp) to cubic (ccp) and thus cannot be reconciled with Cu depletion by solid-state diffusion. Consequently, we interpret digenite formation from chalcocite as fluid-mediated dissolution–precipitation reaction. Understanding the patchiness of the replacement (the light- and dark-blue domains in Fig.5-13b) is problematic but may indicate preferred fluid-induced reaction along close-packed layers in the chalcocite. The

texture formed when digenite is formed from bornite along fractures and along the grain boundary with chalcocite is consistent with a coupled dissolution–precipitation mechanism (Putnis, 2002; Putnis, 2009). The bornite–digenite reaction interface is sharp also on the nm-scale (Fig. 5-7) and Cu- and Fe-concentration profiles appear inconsistent with diffusion-dominated mass transport (Xia et al., 2009; Xia et al., 2008). Furthermore, the absence of void space between the parent and product indicates that the rate-determining step of the reaction is the dissolution rate of the parent phase, as has been demonstrated for chalcopyrite (Zhao et al., 2014). Similarly, sharp replacement interfaces have also been observed in dissolution–precipitation experiments using distinct starting materials (Janssen and Putnis, 2011; Niedermeier et al., 2009; Perdikouri et al., 2013; Zhao et al., 2014) and Hellmann et al. (2003) found that a distinctive sharp chemical boundary between parent and product phases is incompatible with an interdiffusion proton and cation model. Within this framework, the formation of secondary phases, including the ultimate formation of covellite, and hence also the release of Cu (and other elements) into solution, is controlled by the relative solubilities of primary and secondary sulfides and the fluid composition and saturation state.

In contrast to mineral replacement along fractures and at sample surfaces, the formation of the Cu-enriched and Cu-deficient bornite lamellae within coherent parts of the bornite (Fig. 5-13c and d) cannot be reconciled with a dissolution–precipitation reaction mechanism. Instead, similar exsolution textures have been linked to solid-state diffusion in natural samples (Ciobanu et al., 2017; Hatert, 2003; Schwartz, 1931; Schwartz, 1942) and were observed in annealing experiments at temperatures above 100°C (Brett and Yund, 1964; Grguric et al., 2000; Grguric and Putnis, 1999; Zhao et al., 2017). Fe and Cu diffusivities in sulfide minerals are faster than in silicate minerals and can result in a noticeable compositional and textural modification of the original bornite at the timescales and temperatures of our experiments, given a sufficiently strong driving force. The absence of exsolution lamellae in dry experiments on the same bornite reactant thus suggests that peripheral fluid-mediated mineral replacement creates an adequate chemical potential gradient to initiate re-equilibration of the cuboid internal composition by solid-state diffusion, thus forming the Cu-depleted bornite solid solution (X-Bn_3 in Fig.5-4). The probably thermodynamically unstable Cu-depleted bornite solid solution exsolves Cu- and Fe-depleted lamellae, resulting in

the basket-weave texture shown in Figs. 5-9 and 5-10. Similar observations were made by Zhao et al. (2017) and Li et al. (2018), who reported a several order-of-magnitude increase in the formation rate of sulfide exsolution textures in the presence of reactive fluid.

The exsolution found in our experiments depends on the alteration of the bornite composition, which in turn depends on the fluid composition. This is demonstrated by the absence of exsolution during dry experiments and at small reaction progress (MSA experiments and during the initial stage of HCl experiments) when the fluid composition remained relatively unaffected by the reactions.

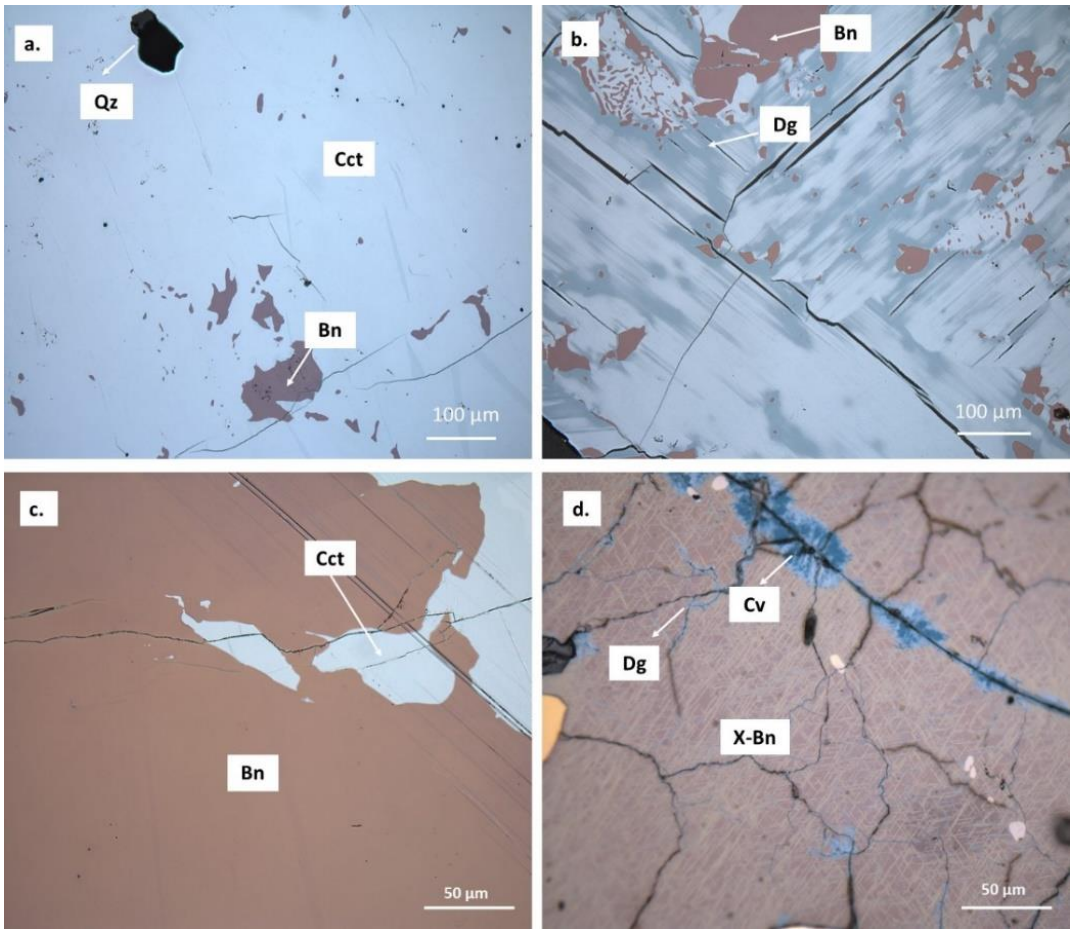

Fig. 5-13. Reflected light photomicrographs showing the comparison between unreacted solids and samples reacted for 2 weeks in HCl/MSA solutions at 90°C. **a.** Unreacted chalcocite zones without compositional changes. **b.** Chalcocite transformation after reaction in MSA solutions showing laminar texture of digenite replacement of chalcocite. **c.** Unreacted bornite zones showing uniform composition without obvious textural transformation. **d.** Exsolution

texture showing copper deficient lamellae and covellite nucleation on fracture zones after reaction in HCl solutions

5.4.2. Preservation of fluid pathways

Continuous reaction requires fluid and mass transport through newly formed replacement rims to the reaction interface through reaction-induced interconnected porosity. Covellite formation from digenite and bornite was clearly accompanied by the formation by µm-scale pore space that is visible in optical and BSE images, similar to that found in other replacement reactions described by this mechanism (Bowman et al., 2007; Janssen and Putnis, 2011; Xia et al., 2008; Zhao et al., 2013). This is consistent with extensive replacement of the precursor sulfide phases by covellite with increasing reaction duration (e.g. Figs 5-11b and 5-12b). In contrast to covellite, the replacement of bornite by digenite proceeded without discernible porosity formation, implying a pore size beyond microscope resolution, i.e. nano-porosity. At this scale nanofluidic transport phenomena can be significant and effectively govern mass transport (Plümper et al., 2017; Zheng et al., 2018). The difference in porosity between digenite and covellite is likely related to their difference in molar volume. The large molar volume of digenite (~130.7 cm^3/mol) may counteract significant porosity formation during replacement of bornite (~24.6 cm^3/mol), whereas isochemical replacement of digenite by covellite (~20.4 cm^3/mol) would be accompanied by a strong volume reduction (volumes from densities and molar mass). However, none of the observed replacement reactions proceed isochemically, thus complicating the quantification of mass transport and porosity formation.

Additional porosity may result from reaction-induced fracturing, which in turn may be driven by the volume change of mineral replacement and saturation state of the interfacial fluid (Jamtveit et al., 2009). Secondary fractures that can be related to the formation of digenite were observed in a few places (Fig. 5-12e and f). These fractures intersected the digenite–bornite reaction interface in regions where the bornite contained exsolution lamellae of Cu-deficient bornite. The fracture orientation generally followed the orientation of the exsolution lamellae and fracture rims in the bornite showed only thin or no secondary digenite, suggesting that fracture formation occurred relatively late.

5.5. Implications for *in-situ* leaching operations

In-situ leaching operations for copper sulfides have been avoided due to the refractory behaviour of the minerals and the challengingly low permeability and porosity of hard-rock ores. Successful implementation of ISR requires that Cu mineral surfaces remain accessible. On a macroscopic scale, this can be achieved by mechanical operations such as blasting and hydrofractruring. However, on the grain scale, access requires a tailored approach and knowledge about how reactions create or clog pore space to avoid passivation.

This research provides insight into the likely mechanisms of chalcocite and bornite transformations under restricted oxidant conditions in acid environments. Initial replacements showed a slower development of porosity and fractures. Above a fluid Cu concentration of ~0.01 mol L^{-1}, the replacement of precursor sulfides by covellite facilitated the total replacement. This advance was only achieved by using stronger acid (pKa HCl = –5.9 and pKa MSA = –1.9) and extended reaction times. Based on our results, we propose that the use of acidic pre-treatment without oxidant addition to achieve mineral replacement may be a useful option for reducing oxidant requirements, enhancing permeability and optimising the copper dissolution rate for *in-situ* leaching. For mixed ores that contain copper oxides or initial covellite, a mild acid solution may be suitable because the copper concentration could be increased by initial dissolution of the other phases. For refractory sulfides, the initial addition of a low concentration of copper sulfate may catalyse the reaction.

Porosity generation and fracturing provides the best opportunity for continuous interaction between the fluid and the mineral core, as evidenced by the increased replacement of the original phases. Experimental data suggest that for extended-time experiments, covellite would replace the original minerals and could have major repercussions for hydrometallurgical processing. Owing to its reactivity when compared with the original phases and the textural transformation observed in the final phase, the transformation of chalcopyrite or bornite into covellite by more economically viable pre-treatments represents an option for refractory copper sulfide processing.

A total transformation of primary copper sulfides into covellite as a pre-treatment may enhance the copper dissolution rate in otherwise refractory ores, as was tested in

related experiments by Hidalgo et al. (2019b) (see Appendix B), which found that resulting covellite increased the copper dissolution rate when it is subsequently leached with an oxidant. For ISR operations, the textural transformation in our results is promising, and suggests a close relationship between fluid accessibility to the solid and the fluid chemistry. A better understanding of these interactions could optimize the lixiviant selection and complement mechanical accessibility-enhancement techniques.

Acknowledgments

MRIWA (Project M488), BASF, Curtin University and CSIRO are gratefully acknowledged for funding this work. The experimental analysis was performed at CSIRO Mineral Resources (Waterford and Kensington) and at the University of Western Australia's Centre of Microscopy Characterisation and Analysis. The authors acknowledge the facilities, and the scientific and technical assistance of the Australian Microscopy and Microanalysis Research Facility at the Centre for Microscopy, Characterisation and Analysis (CMCA), the Australian Resources Research Centre (ARRC) and the University of Western Australia, which are facilities that are funded by the University, State and Commonwealth Governments. We thank Tuyen Pham and Peter Austin for help with the ICP and point-XRD analysis, respectively.

References

Altree-Williams, A., Pring, A., Ngothai, Y. and Brugger, J., 2015. Textural and compositional complexities resulting from coupled dissolution–reprecipitation reactions in geomaterials. Earth Science Reviews, 150: 628–651.

Bartlett, R., 1992. Upgrading copper concentrate by hydrothermally converting chalcopyrite to digenite. Metallurgical and Materials Transactions B, 23(3): 241–248.

Bowman, J.R., Valley, J.W. and Kita, N., 2007. Mechanisms of oxygen isotopic exchange and isotopic evolution of $^{18}O/^{16}O$-depleted periclase zone marbles in the Alta Aureole, Utah: USA insights from ion microprobe analysis of calcite. Contributions to Mineralogy and Petrology, 157: 77–93.

Brett, R. and Yund, R.A., 1964. Sulfur-rich bornites. American Mineralogist, 49(7-8): 1084–1098.

Burkin, A., 1969. Solid-state transformations during leaching. Mineral science Engineering 1(1): 4–14.

Cai, Y., Chen, X., Ding, J. and Zhou, D., 2011. Leaching mechanism for chalcopyrite in hydrochloric acid. Hydrometallurgy, 109–118.

Cerda, C., Taboada, M., Jamett, N., Ghorbani, Y. and C. Hernández, P., 2017. Effect of Pretreatment on Leaching Primary Copper Sulfide in Acid-Chloride Media. Minerals 8, 3–14.

Cheng, C.Y. and Lawson, F., 1991. The kinetics of leaching covellite in acidic oxygenated sulfate-chloride solutions. Hydrometallurgy, 27(3): 269–284.

Cherniak, D., 2010. Diffusion in carbonates, fluorite, sulfide minerals, and diamond, Reviews in Mineraogy and Geochemistry,Vol; 85, pp. 871–897.

Ciobanu, C.L., Cook, N.J. and Ehrig, K., 2017. Ore minerals down to the nanoscale: Cu-(Fe)-sulfides from the iron oxide copper gold deposit at Olympic Dam, South Australia. Ore Geology Reviews, 81(4): 1218–1235.

Dutrizac, J., Chen, T. and Jambor, J., 1985. Mineralogical changes occurring during the ferric ion leaching of bornite. Metallurgical Transactions B 16b(4): 679–693.

Fuentes, G., Viñals, J. and Herreros, O., 2009. Hydrothermal purification and enrichment of Chilean copper concentrates: Part 1: The behavior of bornite, covellite and pyrite. Hydrometallurgy, 95(1): 104–112.

Geisler, T., Pöml, P., Stephan, T., Janssen, A. and Putnis, A., 2005. Experimental observation of an interface-controlled pseudomorphic replacement reaction in a natural crystalline pyrochlore. American Mineralogist, 90(10): 1683–1687.

Grguric, B.A., Harrison, R.J. and Putnis, A., 2000. A revised phase diagram for the bornite-digenite join from in situ neutron diffraction and DSC experiments. Mineralogical Magazine, 64(2): 213–231.

Grguric, B.A. and Putnis, A., 1999. Rapid exsolution behaviour in the bornite-digenite series, and implications for natural ore assemblages. Mineralogical Magazine, 63(1): 1–12.

Hackl, R.P., Dreisinger, D.B., Peters, E. and King, J.A., 1995. Passivation of chalcopyrite during oxidative leaching in sulfate media. Hydrometallurgy, 39(1): 25–48.

Hatert, F., 2003. Occurrence of sulfides on the bornite-idaite join from Vielsalm, Stavelot Massif, Belgium. European Journal of Mineralogy, 15(6): 1063–1068.

Hatert, F., 2005. Transformation sequences of copper sulfides at Vielsalm, Stavelot Massif, Belgium. Canadian Mineralogist, 43(2): 623–635.

Hellmann, R., Penisson, J.M., Hervig, R.L., Thomassin, J.H. and Abrioux, M.F., 2003. An EFTEM/HRTEM high-resolution study of the near surface of labradorite feldspar altered at acid pH: evidence for interfacial dissolution-reprecipitation. Physics and Chemistry of Minerals, 30(4): 192–197.

Hidalgo, T., Kuhar, L., Beinlich, A. and Putnis, A., 2019a. Kinetics and mineralogical analysis of copper dissolution from a bornite/chalcopyrite composite sample in

ferric-chloride and methanesulfonic-acid solutions. Hydrometallurgy, 188: 140–156.

Hidalgo, T., McDonald, R., Kuhar, L., Beinlich, A. and Putnis, A., 2019b. Staged leaching of bornite with acidic solutions at moderate temperature in an in-situ recovery environment. ALTA ISR symposium, ALTA, Perth, Western Australia.

Hövelmann, J., Putnis, A., Geisler, T., Schmidt, B. and Golla-Schindler, U., 2010. The replacement of plagioclase feldspars by albite: observations from hydrothermal experiments. Contributions to Mineralogy and Petrology, 159(1): 43–59.

Jamtveit, B., Putnis, C.V. and Malthe-Sørenssen, A., 2009. Reaction induced fracturing during replacement processes. Contributions to Mineralogy and Petrology, 157(1): 127–133.

Janssen, A. and Putnis, A., 2011. Processes of oxidation and HCl-leaching of Tellnes ilmenite. Hydrometallurgy, 109(3): 194–201.

Labotka, T.C., Cole, D.R., Fayek, M. and Riciputi, L.R., 2002. Coupled cation and oxygen exchange between alkali feldspar and aqueous chloride solution. 12th annual V. M. Goldschmidt conference, Geochimica et Cosmochimica Acta, 66(15A): 1822–1825.

Li, K., Brugger, J. and Pring, A., 2018. Exsolution of chalcopyrite from bornite-digenite solid solution: an example of a fluid-driven back-replacement reaction. Mineralium Deposita, 53(7): 903–908.

Makovicky, E., 2006. Crystal structures of sulfides and other chalcogenides. Reviews in Mineralogy and Geochemistry, 61(1): 7–125.

Mallio, W., Pojasek, W., Park, W. and Rainville, G., 1981. Parameters and petrographic interpretation of In situ copper leaching. Process Mineralogy: Extractive Metallurgy, Mineral Exploration, TMS-AIME: 339–352.

Muszer, A., Wódka, J., Chmielewski, T. and Matuska, S., 2013. Covellinisation of copper sulfide minerals under pressure leaching conditions. Hydrometallurgy, 137(C): 1–7.

Niedermeier, D., Putnis, A., Geisler, T., Golla-Schindler, U. and Putnis, C., 2009. The mechanism of cation and oxygen isotope exchange in alkali feldspars under hydrothermal conditions. Contributions to Mineralogy and Petrology, 157(1): 65–76.

Parikh, R.S. and Liddell, K.C., 1990. Mechanism of anodic dissolution of chalcocite in hydrochloric acid solution. Industrial & Engineering Chemistry Research, 29(2): 187–193.

Perdikouri, C., Piazolo, S., Kasioptas, A., Schmidt, B. and Putnis, A., 2013. Hydrothermal replacement of Aragonite by Calcite: interplay between replacement, fracturing and growth. European Journal of Mineralogy, 25(2): 123–136.

Pesic, B. and Olson, F.A., 1983. Leaching of bornite in acidified ferric chloride solutions. Metallurgical Transactions B, 14(4): 577–588.

Pesic, B. and Olson, F.A., 1984. Dissolution of bornite in sulfuric acid using oxygen as oxidant. Hydrometallurgy, 12(2): 195–215.

Plümper, O., John, T., Podladchikov, Y.Y., Vrijmoed, J.C. and Scambelluri, M., 2017. Fluid escape from subduction zones controlled by channel-forming reactive porosity. Nature Geoscience, 10(2): 150–156.

Price, D.C. and Chilton, J.P., 1980. The electroleaching of bornite and chalcopyrite. Hydrometallurgy, 5(4): 381–394.

Price, D.C. and Chilton, J.P., 1981. The anodic reactions of bornite in sulphuric acid solution. Hydrometallurgy, 7(1): 117–133.

Putnis, A., 2002. Mineral replacement reactions: from macroscopic observations to microscopic mechanisms. Mineralogical Magazine, 66(5): 689–708.

Putnis, A., 2009. Mineral replacement reactions. Reviews in Mineralogy and geochemistry, 70(1): 87–124.

Putnis, A. and Putnis, C.V., 2007. The mechanism of reequilibration of solids in the presence of a fluid phase. Journal of Solid State Chemistry, 180(5): 1783–1786.

Ruiz-Agudo, E., Putnis, C., Rodriguez-Navarro, C. and Putnis, A., 2012. Mechanism of leached layer formation during chemical weathering of silicate minerals. Geology, 40(10): 947.

Ruiz-Agudo, E., Putnis, C.V. and Putnis, A., 2014. Coupled dissolution and precipitation at mineral–fluid interfaces. Chemical Geology.Vol:383, pp: 132–146

Schwartz, G.M., 1931. Textures due to unmixing of solid solutions. Economic Geology, 26(7): 739–763.

Schwartz, G.M., 1942. Progress in the study of exsolution in ore minerals. Economic Geology and the Bulletin of the Society of Economic Geologists, 37(5): 345–364.

Sinclair, L. and Thompson, J., 2015. In situ leaching of copper: Challenges and future prospects. Hydrometallurgy, 157: 306–324.

Ugarte-Alverez, F., 1971. Leaching of bornite, University of London, PhD disertation, London, England.

Ugarte, F.J. and Burkin, A.R., 1975. Mechanism of formation of idaite from bornite by leaching with ferric sulfate solution. Leaching and Reduct in Hydrometallurgy, pp: 46–53.

Wang, X., Hong, M., Liao, R., Zhao, C., Yu, S., Wang, J., Zhao,H., Gan, M., 2018. Synchrotron-based XRD and XANES study of bornite leached by mesophilic mixed bacteria, Characterisation of Minerals, Metals, and Materials 2018 Phoenix, AZ, USA,Springer, pp. 325–332.

Whitney, D. and Evans, B., 2010. Abbreviations for names of rock-forming minerals. American Mineralogist, 95: 185–187.

Xia, F., Brugger, J., Chen, G., Ngothai, Y., O'Neill, B., Putnis, A., Pring, A., 2009. Mechanism and kinetics of pseudomorphic mineral replacement reactions: A case study of the replacement of pentlandite by violarite. Geochimica et Cosmochimica Acta, 73(7): 1945–1969.

Xia, F., Zhou, J., Brugger, J., Ngothai, Y., O'Neill, B., Chen, G., Pring, A., 2008. Novel route to synthesize complex metal sulfides: Hydrothermal coupled dissolution-reprecipitation replacement reactions. Chemistry of Materials, 20(8): 2809–2817.

Zhao, H.-b., Wang, J., Gan, X.-w., Qin, W.-q., Hu, M.-h., Qiu, G.-z., 2015. Bioleaching of chalcopyrite and bornite by moderately thermophilic bacteria: an emphasis on their interactions. International Journal of Minerals, Metallurgy, and Materials, 22(8): 777–787.

Zhao, J., Brugger, J., Grguric, B.A., Ngothai, Y. and Pring, A., 2017. Fluid-Enhanced coarsening of mineral microstructures in hydrothermally synthesised bornite–digenite solid solution. ACS Earth and Space Chemistry, 1(8): 465–474.

Zhao, J., Brugger, J., Ngothai, Y. and Pring, A., 2014. The replacement of chalcopyrite by bornite under hydrothermal conditions. The American Mineralogist, 99(11–12): 2389.

Zhao, J., Brugger, J., Xia, F., Nogthai, Y., Chen, G., Pring, A. , 2013. Dissolution-reprecipitation vs. solid-state diffusion mechanism of mineral transformations in sylvanite, $(Au,Ag)_2Te_4$, under hydrothermal conditions. American Mineralogist, 98(1): 19–32.

Zheng, X., Cordonnier, B., Zhu, W., Renard, F. and Jamtveit, B., 2018. Effects of confinement on reaction-induced fracturing during hydration of periclase. Geochemistry, Geophysics, Geosystems, 19(8): 2661–2672.

Chapter 6. Effect of multistage solution–mineral contact for low-grade natural copper samples: extraction, acid consumption, gangue-mineral changes and precipitation

This study addresses some of the challenges that may occur during the in-situ recovery of ores, by understanding the multistage interaction of lixiviant with fresh ore samples. Our experiments aimed to simulate what may occur when leach solution travels through targeted regions of an ore deposit from injection to recovery well. The leaching of a low-grade natural ore that contained refractory copper sulfides mixed with gangue minerals was studied by using iron(III) as an oxidant in sulfuric, hydrochloric or methanesulfonic acids at 90°C. The leach solution was contacted over five successive stages with a new mass of ore every 72 h, without acid or oxidant replenishment. The solutions showed a decreased copper extraction capacity after two contact stages but leaching continued for the entire experiment. After three contact stages, precipitates formed in all solutions; iron and calcium precipitates formed from the beginning of the second contact stage for all systems (akaganeite precipitated in the chloride systems and jarosite and gypsum formed in the sulfate systems) and the extent of precipitation increased with an increase in temperature and pH.

6.1. Introduction

In-situ recovery (ISR) is an unconventional mining technique that requires the injection of a fluid (i.e., the lixiviant) in direct contact with subsurface ore to recover a valuable metal by the return of a pregnant solution to the surface for further processing. ISR may provide an alternative for processing low-grade reserves that are uneconomic to mine by conventional techniques. Besides being the primary global technique for the recovery of uranium (IAEA, 2016), ISR trials have been implemented mainly for oxide leaching, for example, at San Manuel, Casa Grande and Santa Cruz (Seredkin et al., 2016). Deep reduced copper orebodies that contain refractory chalcopyrite or bornite are challenging to leach by ISR as they require oxidant addition, may require elevated temperatures and the copper minerals may be difficult to access.

ISR requires continuous fluid–rock interaction prior to metal recovery from the fluid at the surface. Control limitations exist during processing because the interaction of the ore and fluid may occur over an extended distance between the injection and recovery wells (Mallio et al., 1981). The continuous transport of fluid between wells makes the maintenance of constant fluid conditions (such as pH and acid concentration) challenging, and soluble cation and anion uptake results in changes in solution properties (such as pH and solution potential, Eh), as occurs in recycled solutions in heap leaching. Solution recycle with processing at the surface in heap leaching may be more flexible than in an ISR environment and allows for pH control, acid replenishment, solid–liquid separation and washing (Nikoloski and Malley, 2018; Qian et al., 2014). Such controls may not be possible in an ISR application where fluid (of a changing composition) interacts with fresh solid until the fluid reaches the recovery point.

Continuous fluid–rock interactions will be accompanied by value and gangue mineral dissolution, precipitation of new phases and ion-exchange reactions. Precipitation of secondary minerals in a saturated solution is one of the main geochemical processes that reduces hydraulic conductivity, specifically when the precipitate obstructs fractures, reduces the porosity and thus impacts copper recovery and acid consumption (Sinclair and Thompson, 2015). Precipitation is affected by temperature, leaching solution composition and ore mineralogy (Schmidt et al., 1992), where higher temperatures are expected in deeper ore bodies. The subsurface temperature may also have an important impact on the chemistry of the final solution and solids after fluid transport, as the stability of certain cation/anion combinations changes with temperature.

To the best of our knowledge, only one study has investigated the recycling of lixiviants for ISR. Paulson (1992) conducted a series of laboratory experiments on 5-cm-diameter and 20-cm-long natural copper-oxide core samples with copper grades between 1.9% and 7.7%. Sulfuric acid was injected into the cores with a recycling frequency between 1 and 4 weeks. After filtration, acid was added before the solution was contacted with the solid again. Paulson evaluated the net effect of the dissolution–precipitation reactions and their effect on final core permeability. He found that metals

that were released from gangue minerals combined with sulfate from the lixiviant to form secondary mineral precipitates that significantly reduced the permeability.

The reuse of solutions that contain oxidant, at elevated temperatures and without make-up acid addition to simulate an ISR environment, has not been reported previously in the literature and is presented in this study. The aim was to characterize the fluid and solids after fluid–rock contact at estimated deep-ore-body temperatures (90°C) using samples that contained low-grade refractory copper and gangue minerals.

6.2. Experimental

6.2.1. Materials and characterisation

Samples of low-grade ore were ball milled, dry sieved and leached in acidic solutions containing ferric iron. Ferric iron was selected as the oxidant because it is affordable, soluble in a range of acid lixiviants and can be regenerated (Ferron, 2003). Five solutions containing either ferric chloride or ferric sulfate were prepared with deionised water and methanesulfonic acid (MSA, with and without sodium chloride, NaCl), hydrochloric acid (HCl) or sulfuric acid (H_2SO_4) (see Table 6-1) to represent sulfate and chloride lixiviant systems. The solution concentrations were selected to achieve complete oxidation.

Table 6-1. Summary of systems and conditions used in the leaching tests.

Solution number	Oxidant		Acid		Additive		Initial pH	Initial Eh (mV vs S. H. E)
	Type	Concentration (mol L^{-1})	Type	Concentration (mol L^{-1})	Type	Concentration (mol L^{-1})		
1	$FeCl_3$	0.5	MSA	0.3	-	-	0.21	719
2			HCl				0.11	723
3	$Fe_2(SO_4)_3$		MSA				0.34	719
4			H_2SO_4				0.28	696
5			MSA		NaCl	0.5	0.22	712

A particle size (P_{80}) of 68 µm (Brunauer–Emmett–Teller (BET) surface area of 3.2 m^2g^{-1}) was determined using a Malvern Mastersizer 3000 after the samples had been

placed in an ultrasonic bath for 20 min. The BET specific surface area analysis was performed by using a TriStar II automated gas adsorption analyser with nitrogen. Mineralogical identification was performed by using an E430 Pro Quantitative Evaluation of Minerals by Scanning Electron Microscopy (QEMSCAN). Samples were mixed with graphite in a ratio of 1:3 to separate the particles and mounted in resin using a protocol described by Meyer et al. (2013). The final data were processed with Idiscover 5.2 software. X-ray powder diffraction (XRD) data were collected in a PANalytical Empyrean X-ray diffractometer equipped with a Bragg-Brentano HD incident monochromator. The working parameters were: an incident beam at 0.5°, a divergence slit at 40 kV, 40 mA and 0.02 rad Soller slits and a 1° antiscatter slit with a diffracted beam pixel three dimensions (3D) array detector in scanning one dimension (1D) mode with a 0.125° antiscatter slit and 0.02 rad soller slits. Morphological and compositional analyses were performed by scanning electron microscopy-energy dispersive spectroscopy (SEM-EDS, JEOL-JSM-7001) with a 10 mm SDD detector and a resolution of 125 eV, 20 kV and a 10 mm working distance. All analyses and experiments were conducted at CSIRO Mineral Resources, Perth.

6.2.2. Contact test methods

Leach tests were performed in a shaking water bath at 90°C using sealed 250 mL Nalgene bottles, with a constant pulp density of 10% m/v. Each experiment consisted of five 72-h stages (total of 360 h). The duration of each stage (72 h) was selected in prior screening experiments, as this allowed for the maximum copper extraction to be reached using fresh lixiviant, and five stages were required to achieve changes in solid and fluid behaviour. The schematic in Fig. 6-1 shows how stages 1 to 5 aimed to represent a period during which target ore contacts pumped fluid in an ISR scenario until the recovery point is reached. After 72 h, the fluid was filtered, sub-sampled, and the remaining solution was contacted immediately with fresh solid at a 10% w/v pulp density. The solid residues were washed twice with distilled water and dried in a Binder BD56 standard incubator at 30°C. Triplicate experiments yielded an error of below 2%. Selected solids were digested with aqua regia after experiments for mass balance purposes and secondary element dissolution calculations (Na, Ca, K, Mg, Al and S). Fluid analysis was by inductively coupled plasma optical emission spectrometry (ICP-OES). pH and Eh values were obtained by using Ionode ORP and

pH (IJ44A and IJ64) combination electrodes. The dissolution per stage was calculated based on final solution analysis and from the elemental analysis of the fresh solid that was added at the beginning of the stage.

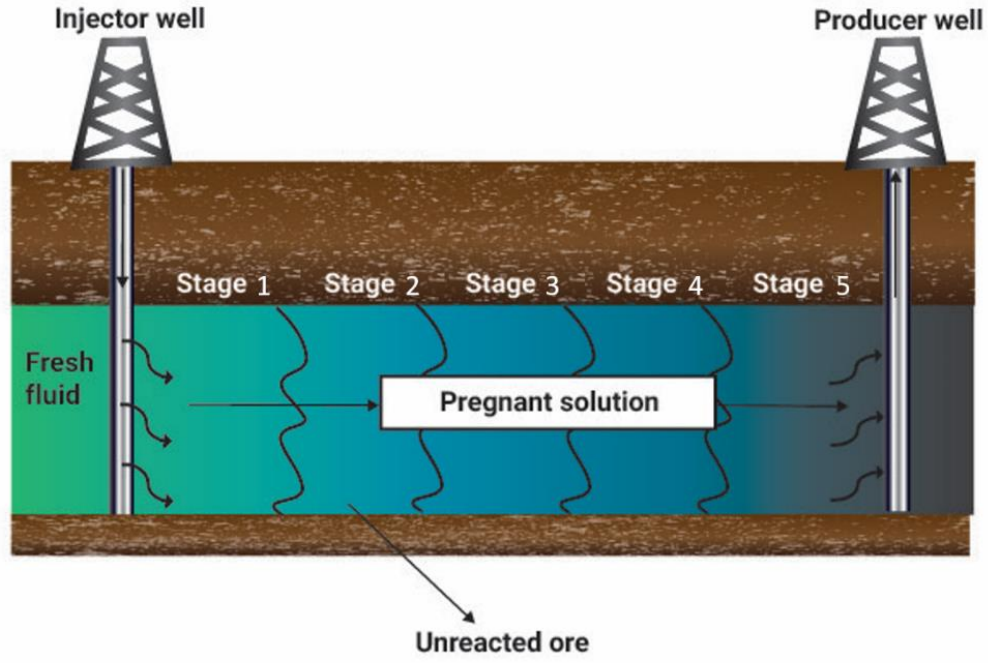

Fig. 6-1. Schematic of multistage fluid–rock interaction in an ISR scenario.

6.3. Results and discussion

6.3.1. Initial sample characterisation

Characterisation of the starting material by QEMSCAN inferred that the solids contained mainly feldspars, micas, clays and iron oxides. Chalcopyrite and chalcocite represented the main copper minerals, whereas bornite and covellite occurred in trace amounts (Table 6-2).

Table 6-2. Chemical and mineralogical composition of the initial bulk mineral sample by ICP-OES and QEMSCAN analyses.

Composition			
QEMSCAN		**ICP-OES**	
Mineralogy**	**mass %**	**Element**	**mass %**
Chalcopyrite	1.33	Al	8.18
Bornite	0.20	C***	0.388
Cu trap*	0.20	Ca	3.35
Pyrite	0.56	Co	0.003
Feldspars	54.13	Cr	0.014
Amphibole	10.24	Cu	0.397
Fe-oxide	7.19	Fe	7.25
Quartz	6.21	K	3.03
Chlorite	5.87	Mg	2.16
Epidote	3.40	Mn	0.071
Calcite	2.05	Na	3.15
Dolomite	0.13	Ni	0.002
Sphene	1.64	Si	26.4
Micas	1.33	S	0.37
Pyroxene	0.83	Zn	0.009
Garnet	0.73	Au (ppb)	1027
Phosphates	0.61		
Rutile/Anatase	0.35		
Talc	0.10		
Others	2.45		

*Copper-sulfide intermediates, mixtures and interactions with adjacent minerals

**Concentrations < 1 mass% were excluded unless confirmed by XRD analysis

*** Total inorganic carbon (TIC)

The XRD pattern of the original sample indicated that albite was the major phase with additional peaks of actinolite (amphibole), quartz and orthoclase (Fig. 6-2). Traces of calcite, chalcopyrite and muscovite were also found, which is consistent with the concentrations of calcium, sulfur and magnesium from the elemental analysis in Table 6-2.

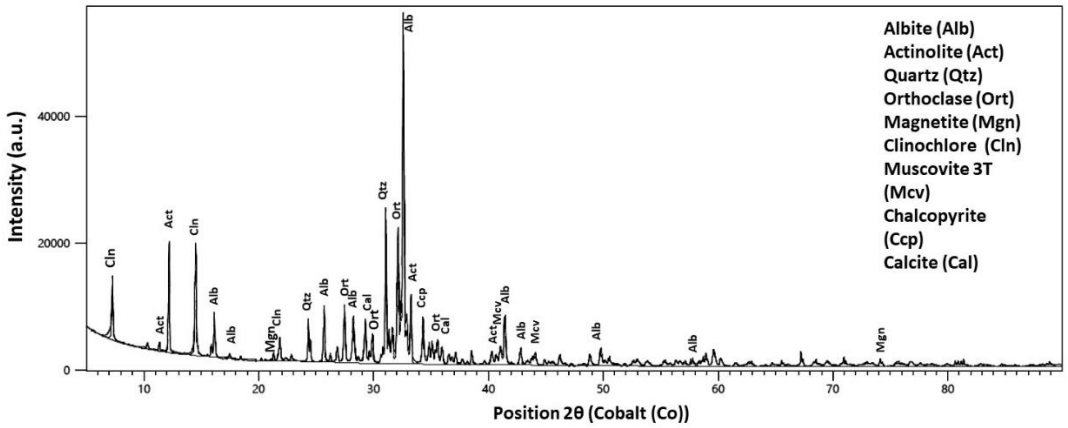

Fig. 6-2. X-ray diffractogram of the unreacted sample (P_{80} 68 µm), showing predominant phases of silicates and carbonates.

SEM analysis of the sample showed that copper sulfides were surrounded by gangue minerals (Fig. 6-3). Calcium was contained mainly in calcite. The Ca/Mg overlap may imply the existence of amphibole, as was confirmed by the XRD data. The iron and copper maps did not overlap completely because of the existence of magnetite in the sample. Sulfur overlapped with copper, which indicated the presence of copper sulfide minerals and Fe/S overlap confirmed the presence of pyrite.

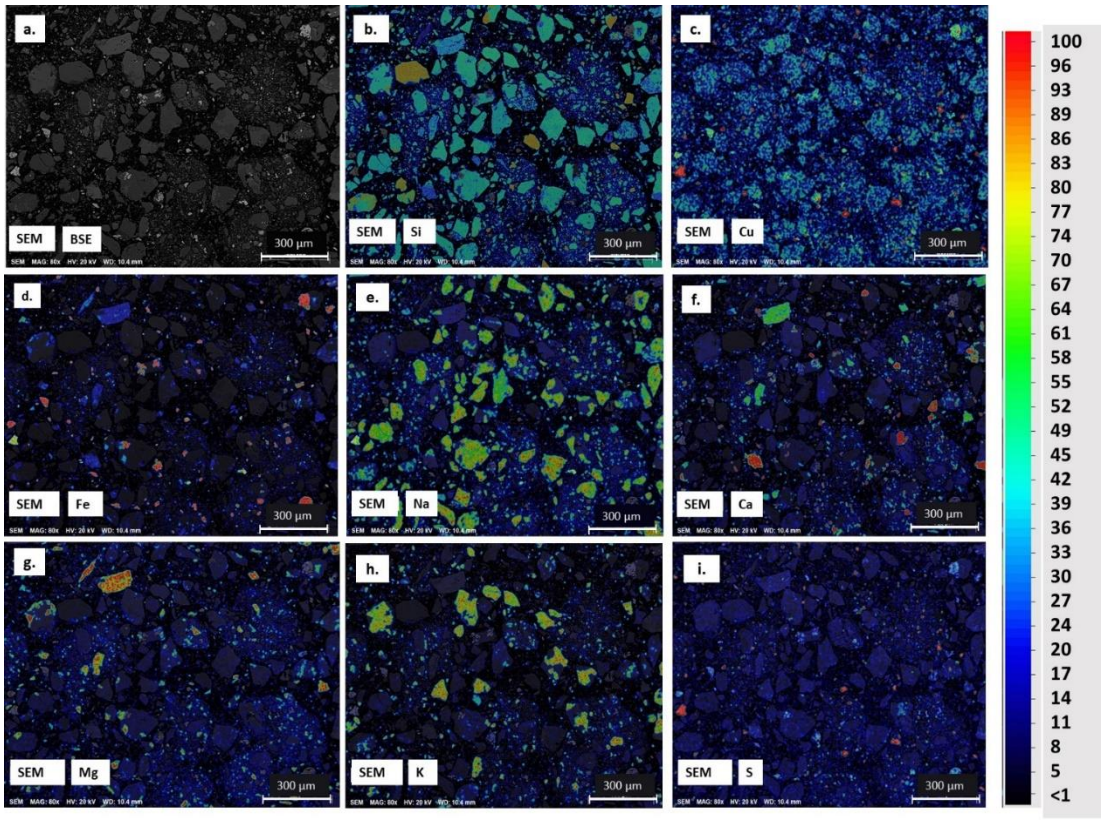

Fig. 6-3. SEM-EDS element distribution maps of the unreacted sample. **a.** unreacted solid, **b.** silica, **c.** copper**, d.** iron, **e.** sodium, **f.** calcium, **g.** magnesium, **h.** potassium, **i.** sulfur.

6.3.2. Fluid analysis

The solution Eh decreased on average by ~110 mV between stages 1 and 5 (Fig. 6-4a). The pH increased over the five stages but remained below 2 (Fig. 6-4b). The variation in pH between solutions is thought to reflect variations in the proportions of acid-consuming minerals (e.g., carbonates) and acid-producing minerals (e.g., jarosite). The maximum acid consumption between stages 1 and 3 was 57 kg sulfuric acid t^{-1} ore, 49 kg MSA t^{-1} ore with ferric sulfate addition, 36 kg HCl t^{-1} ore and 44 kg MSA t^{-1} ore with ferric chloride addition. The acid consumptions in the ferric-sulfate systems exceeded those for copper-oxide heap leaching with sulfuric acid of 18–47 kg t^{-1} (Azmayandeh et al., 2017). Based on the initial concentration of carbon (TIC), an average of 30 kg t^{-1} of acid would be consumed by carbonates if all were accessible, therefore most of the acid was expected to be consumed by the carbonates.

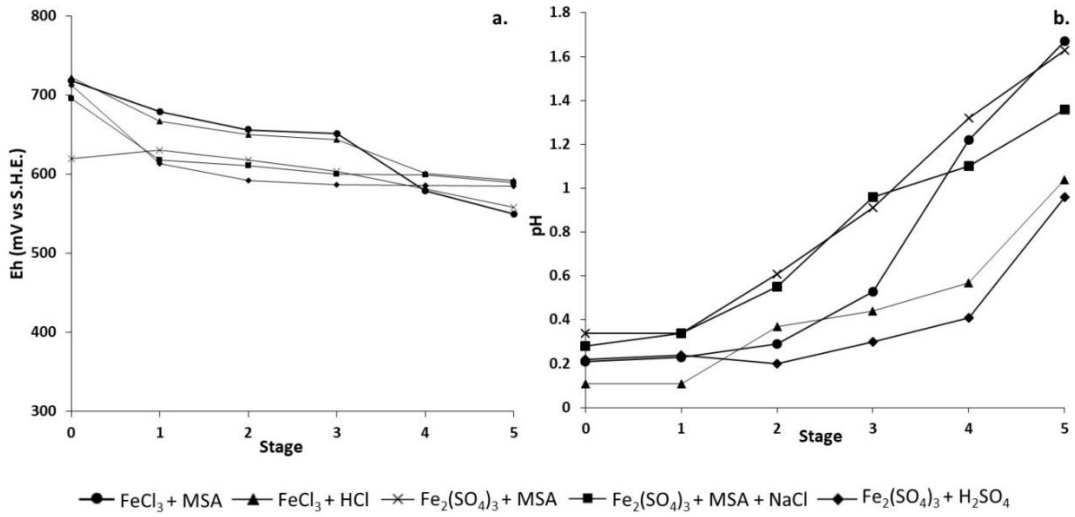

Fig. 6-4. a. Redox potential and **b.** pH change after five contact stages with fresh solid.

Copper in the pregnant leach solution originated primarily from chalcopyrite dissolution. Copper recovery increased during the first two stages for all solutions used. Figure 6-5a presents the copper leached per stage for each of the five solutions after contact with fresh solid sample in each stage. The peak copper recovery occurred in stage 2 and was highest in the ferric-chloride solutions with HCl and MSA (70% and 72%, respectively) compared with the ferric-sulfate solutions with MSA, MSA/NaCl and H_2SO_4 (54%, 38% and 41%, respectively). Copper dissolution in subsequent stages decreased. No copper dissolved after stage 3 in the $Fe_2(SO_4)_3/H_2SO_4$ solution. After stage 4, copper dissolved only in the $FeCl_3$/MSA and $FeCl_3$/HCl solutions. Iron dissolution was determined from the dissolved iron in solution minus the initial concentration of ferric iron from the oxidant (Fig. 6-5b). Negative values in Fig. 6-5b indicate that iron precipitated from solution. Iron dissolved in stages 1 and 2 (up to 96% iron dissolved in the $FeCl_3$/HCl system, Fig. 6-5b). Thereafter, iron precipitated in all systems, with up to 27% of the initial iron in the sample precipitating in the $Fe_2(SO_4)_3$/MSA/NaCl system.

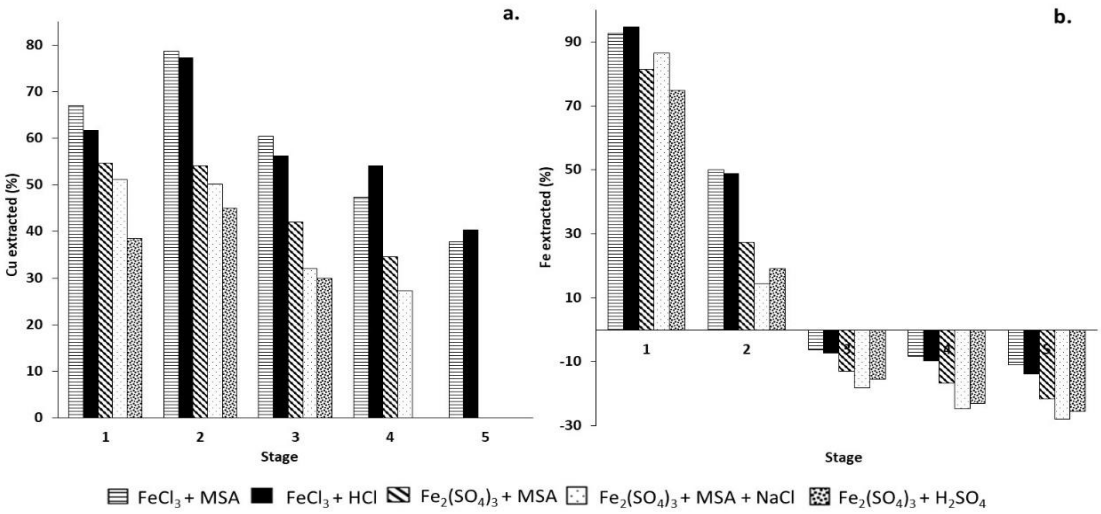

Fig. 6-5. a. Copper and **b**. iron extraction during the five experimental stages (72 h each stage) (no iron dissolution occurred after stage 2).

Figure 6-6 presents the dissolution of sulfur, calcium, aluminium, sodium, magnesium and potassium for selected stages (these elements were chosen based on experimental design and sample volume availability for analysis). Calcium dissolution occurred in all stages in the ferric-chloride systems ($FeCl_3$/HCl and $FeCl_3$/MSA) but precipitated in the ferric-sulfate systems ($Fe_2(SO_4)_3/H_2SO_4$, $Fe_2(SO_4)_3$/MSA/NaCl and $Fe_2(SO_4)_3$/MSA). The maximum aluminium and magnesium yields were low (< 20% and 55%, respectively) compared with these of the other metals, which may confirm that the calcium in solution originated mainly from calcite and only a small fraction was derived from amphiboles. Sodium and potassium dissolution decreased after stage 2 and precipitates formed in the final stages, because their solubility levels in the presence of both iron and sulfate were reached; this is discussed further below. High levels of dissolved impurities (K^+, Na^+, Ca^{2+}, Al^{3+} and Mg^{2+}) may increase precipitation and may also affect the rate of chalcopyrite dissolution. In our experiments, MSA and HCl solutions produced a higher solubility of heavy metals (e.g., Fe, Cu, Ni, Zn) than sulfuric acid, which may be disadvantageous in a multi-contact scenario.

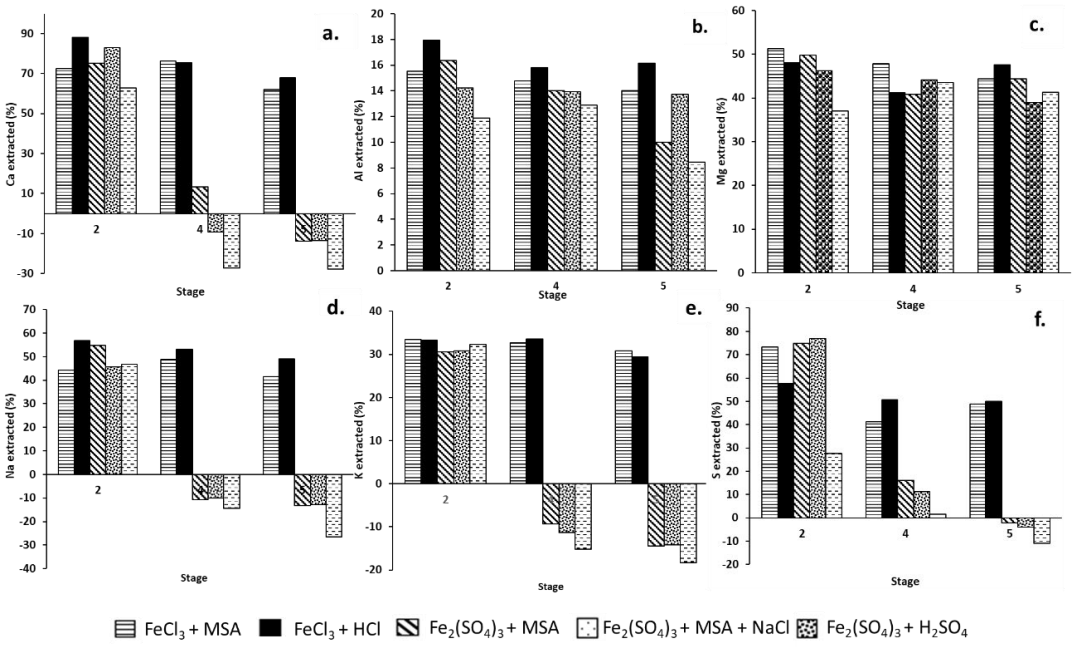

Fig. 6-6. Metal extraction at stages 2, 4 and 5, **a.** calcium, **b.** aluminium, **c.** magnesium, **d.** sodium, **e.** potassium, **f.** sulfur

To establish the theoretical effect of temperature and continuous leaching on element precipitation, stability diagrams for copper, iron and calcium and for all leaching systems were prepared using the Geochemist's Workbench® (GWB) software package. These diagrams allow for an understanding of the behaviour of the systems during the leaching stages. For example, the stability diagrams for copper, iron and calcium for the $Fe_2(SO_4)_3/H_2SO_4$ solution for stages 2 and 4 are shown in Fig. 6-7. Although copper is predicted to be soluble as Cu^{2+} for a pH below 4 and an Eh above 0.42 V (Fig. 6-7a and b) in stages 1 and 4, no additional copper dissolution occurred in the $Fe_2(SO_4)_3$/MSA/NaCl and $Fe_2(SO_4)_3/H_2SO_4$ systems in stage 4. The reduction in dissolution may result from surface passivation. The iron stability range decreased in stage 4; K-jarosite precipitation (Fig. 6-7c and d) was predicted above pH 1 in stage 1 and above pH 0.6 in stage 4. Calcium was soluble under stage-2 conditions (soluble calcium sulfate), but the calcium solubility limit was reached in stage 4 and gypsum precipitation was predicted (Fig. 6-7e and f).

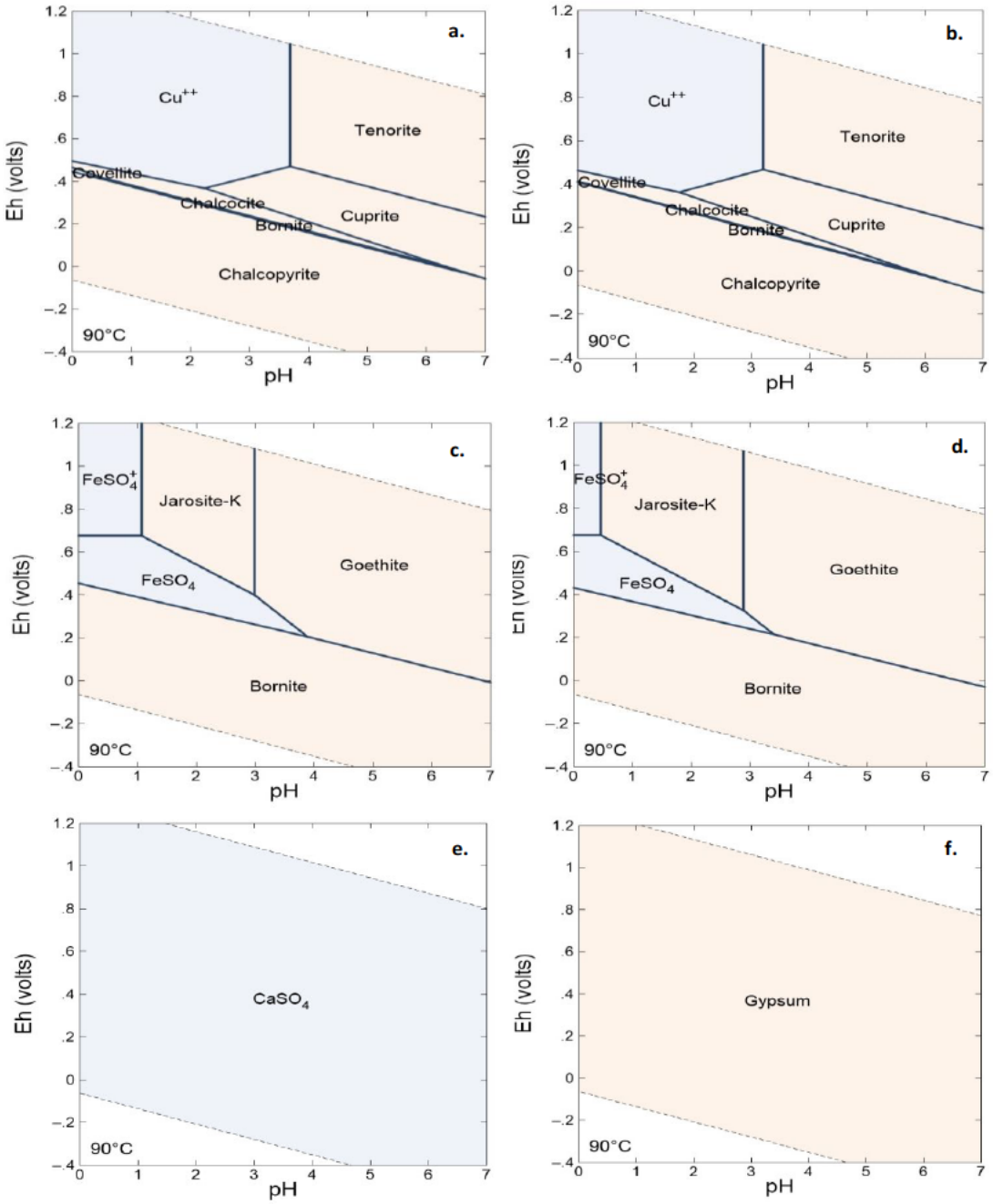

Fig.6-7. Eh–pH diagrams for **a, b.** copper, **c, d.** iron and **e, f.** calcium stability prepared by using the $Fe_2(SO_4)_3/H_2SO_4$ solution concentrations after stages 2 (left) and 4 (right) at 90°C and at atmospheric pressure.

6.3.3. Residue analysis

6.3.3.1. Solid product phases

QEMSCAN data that were normalised using quartz to allow for a comparison between leaching stages (Table 6-3) confirmed the dissolution of copper and gangue minerals

and precipitate formation (e.g., gypsum, jarosite and akaganeite), especially after stage 4. A more detailed description of these products that were formed in the chloride and sulfate systems is provided in Sections 3.3.2 to 3.3.4 and the reside morphology is described in Section 3.3.5.

Table 6-3. Normalised modal composition of solid residues (in % mass) after stages 1 and 4.

Minerals	**Initial**	$FeCl_3$/MSA		$FeCl_3$/HCl		$Fe_2(SO_4)_3$/MSA		$Fe_2(SO_4)_3/H_2SO_4$		$Fe_2(SO_4)_3$/MSA /NaCl	
		Stage									
		1	**4**	**1**	**4**	**1**	**4**	**1**	**4**	**1**	**4**
Copper minerals											
Chalcopyrite	0.214	0.009	0.002	0.054	0.005	0.092	0.01	0.048	0.078	0.003	0.008
Bornite	0.032	0	0.003	0.001	0.005	0.007	0	0	0.004	0	0.008
Cu trap*	0.032	0.003	0.001	0.01	0.005	0.018	0.005	0.029	0.004	0.006	0.014
Gangue minerals											
Feldspars	8.717	9.403	5.889	6.987	7.832	7.258	9.051	7.251	6.88	8.557	8.629
Amphibole	1.649	1.656	1.284	1.100	1.541	1.268	1.505	0.971	1.085	1.401	1.075
Fe-oxide	1.158	0.704	0.618	0.341	1.078	0.404	0.531	0.63	0.676	0.226	0.116
Quartz	1	1	1	1	1	1	1	1	1	1	1
Pyrite	0.09	0.001	0	0.008	0.003	0.001	0.008	0	0.164	0.008	0.019
Chlorite	0.945	0.382	0.394	0.167	0.292	0.014	0.092	0.004	0.031	0.008	0.014
Epidote	0.548	0.428	0.118	0.132	0.275	0.201	0.301	0.228	0.168	0.418	0.155
Calcite	0.33	0.042	0.015	0.024	0.018	0.018	0.023	0.023	0.022	0.019	0.014
Dolomite	0.021	0.016	0.026	0.005	0.019	0.013	0.02	0.018	0.02	0.025	0.028
Pyroxene	0.134	0.039	0.137	0.038	0.108	0.022	0.105	0.003	0.004	0.011	0.011
Precipitates											
Gypsum	0	0.001	0	0	0	0.001	0.232	0.001	0.365	0.006	1.285
Others**	0.395	0.829	0.711	0.654	3.220	0.333	8.607	0.31	8.694	6.983	9.122
Jarosite/Fe Intergrowth***	0	0.001	0.001	0.001	0	0.047	3.732	0.031	2.479	5.895	9.042
Akaganeite	0	0.047	0.057	0.034	0.055	0	0	0	0	0	0

*Copper-sulfide intermediates

** Includes agglomerated particles of jarosite, silica, gypsum and other intermediates

*** Includes ferric-sulfate precipitates

Figure 6-8 compares the change in mineral/precipitate mass percentage as the difference between the initial sample mineral masses and the precipitate masses in stages 1 and 4. Gypsum precipitated in the sulfate solutions (Fig. 6-8a) with maximum precipitation occurring in the $Fe_2(SO_4)_3/H_2SO_4$/NaCl solutions. Additional sodium in the initial solutions appeared to promote gypsum formation because of cation build up.

Calcium remained dissolved in the chloride solutions (Fig. 6-8b). A greater mass percentage of jarosite precipitated in the sulfate solutions (Fig. 6-8a) compared with the akaganeite in chloride solutions (Fig. 6-8b). These data may confirm that more iron precipitated in the sulfate solutions compared with the chloride solutions.

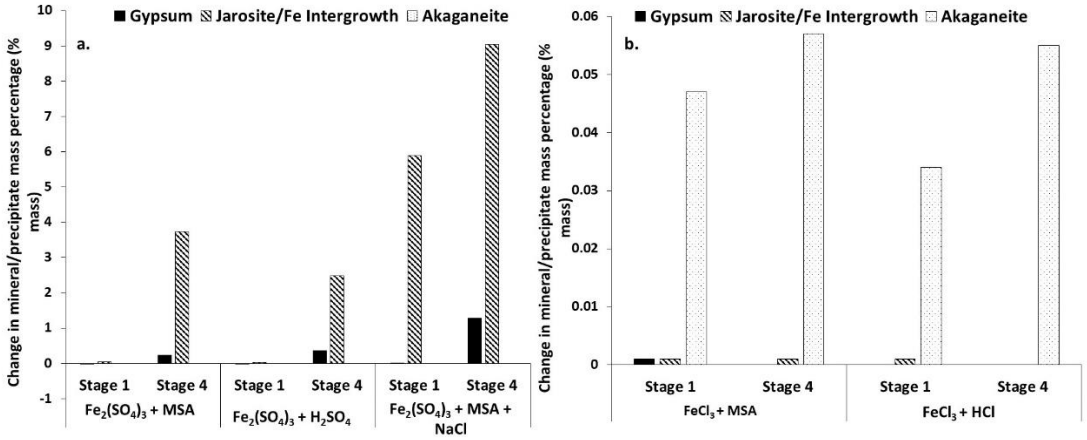

Fig. 6-8. Comparison of change in precipitate mass percentage (% mass) relative to the initial sample for gypsum, jarosite and akageneite **a.** sulfate solutions, **b.** chloride solutions

6.3.3.2. Chloride systems

Yellow solid residues formed in the chloride leaching systems ($FeCl_3$/HCl and $FeCl_3$/MSA). XRD indicated that akageneite (β-$Fe^{3+}O(OH,Cl)$), which is a chloride-containing ferric oxyhydroxide, formed in the ferric-chloride solutions (and more rapidly in HCl than in MSA solution, Fig. 6-9). Akaganeite occurs commonly in high chloride environments, as a corrosion product of iron materials and as a precipitate in inland acidic soils (Bibi et al., 2011; Jenssen et al., 2018). Its precipitation via iron hydrolysis requires the presence of Cl^- (> 0.1 M) and a low pH (< 3) (Peretyazhko et al., 2018).

$$FeCl_3 + H_2O \rightarrow Fe(OH)_{3-x}Cl_x + (3-x)HCl \quad (1)$$

Because of the fine grain size of akageneite (< 1 µm), a determination of the exact chemical composition was not possible. However, analysis of akaganeite particle agglomerates yielded an average chemical composition of 34.5% O, 59.4% Fe and 6.1% Cl, which agrees with the characterisation by Bibi et al. (2011). Most akageneite precipitates occurred as nanosized dispersed flakes and did not form thick superficial

layers. Others existed as thin rod-shaped layers attached to silicates after the first stage (Fig. 6-10a).

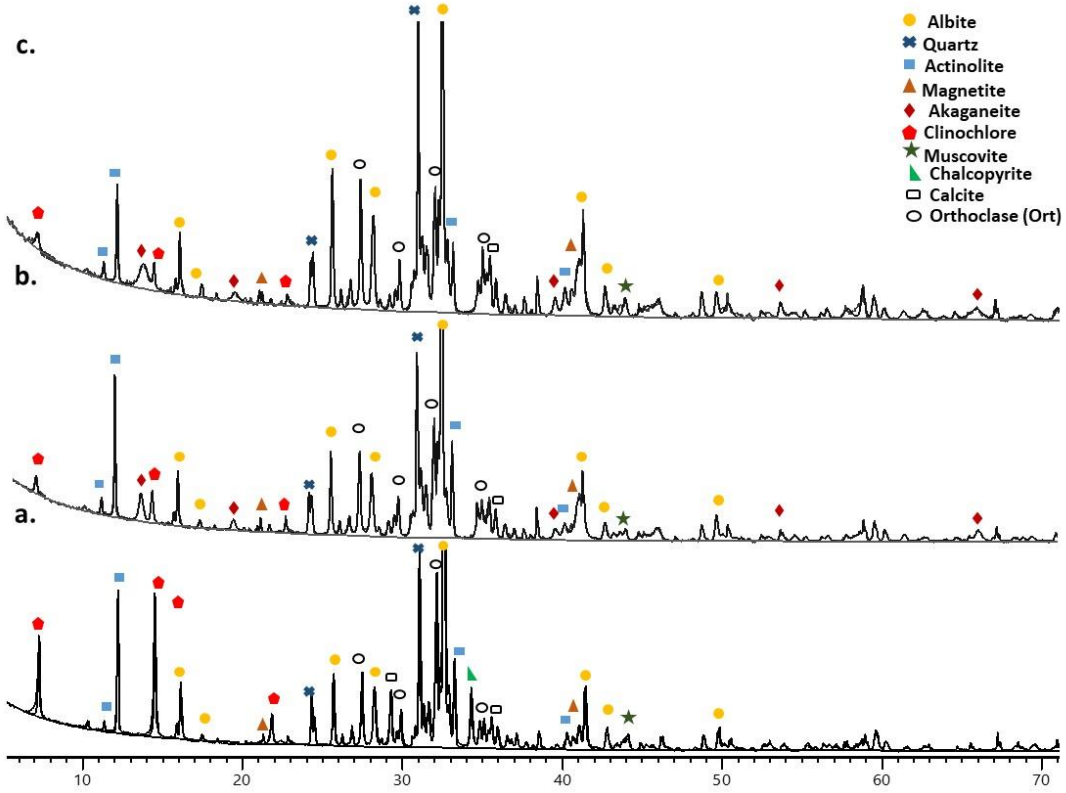

Fig. 6-9. X-ray diffractograms of **a.** unleached sample (P_{80} 68 µm) compared with **b.** stage 3 and **c.** stage 5 residues for $FeCl_3$/HCl solution. Akaganeite peaks appear after stage 3.

6.3.3.3. Sulfate systems

Residues from the sulfate leaching solutions ($Fe_2(SO_4)_3/H_2SO_4$ and $Fe_2(SO_4)_3$/MSA) were yellow. Abundant small rounded platy crystals of potassium jarosite ($KFe(SO_4)_2(OH)_6$, 45.2% O, 13.7% S, 5.3% K and 35.6% Fe, Fig. 6-10b) and a thick surface layer of rhombohedral Na-jarosite ($NaFe(SO_4)_2(OH)_6$, 47.3% O, 4.9% Na, 12.9%S and 34.8% Fe, Fig. 6-10c) were identified from the XRD and SEM images. The jarosite morphology agrees with that found in the literature (Cogram, 2018). Differences in jarosite morphology may be related to the formation rate and type of monovalent cations present (Sasaki and Konno, 2000). Jarosite, which precipitates by monovalent cation incorporation into the jarosite structure, results in acid formation (Equation 2) and occurs at ferric ion concentrations between 0.025–3 M in the presence of alkali metals, such as Na and K (Dutrizac, 1982), and between pH 0.9 and 2

(Córdoba et al., 2009; Lu et al., 2000). The initial iron plus the excess of iron dissolved during the first stages and alkali-metal dissolution from gangue facilitated jarosite precipitation when the pH exceeded 0.7. The decrease in dissolved iron, sodium and potassium after the first stage supports the observation of Na-jarosite and K-jarosite formation.

$$3Fe_2(SO_4)_3 + 12H_2O + 2A^* \rightarrow 2AFe_3(SO_4)_2(OH)_6 + 5H_2SO_4 + 2H^+ \quad (2)$$

*where A = H_3O^+, Na^+, Ag^+, ½Pb^{2+}, NH_4^+

Nanometre-sized colloidal silica precipitated and agglomerated on the surface of other minerals (also present in chloride systems) (Fig. 6-10d). All sulfate solutions showed gypsum precipitation after stage 2 in the form of large needles with an average composition of 56.6% O, 18% S and 25.3% Ca (Fig. 6-10e). Carbonate was confirmed, given the low dissolution of Mg (and in particular from amphibole), to be the main source of calcium. Carbonate dissolution consumes acid and can lead to gypsum precipitation at sufficiently high calcium and sulfate concentrations (Gomis-Yagües et al., 2000) (Equation 3).

$$Ca^{2+} + {SO_4}^{2-} + 2H_2O \rightarrow CaSO_4 \cdot 2H_2O \quad (3)$$

Such precipitation can result in flow rate reduction, as illustrated at the Twin Buttes heap-leaching operations and in ISR operations, such as the Cyprus Casa Grande operation (Bartlett, 1998; Earley and Jones, 1992).

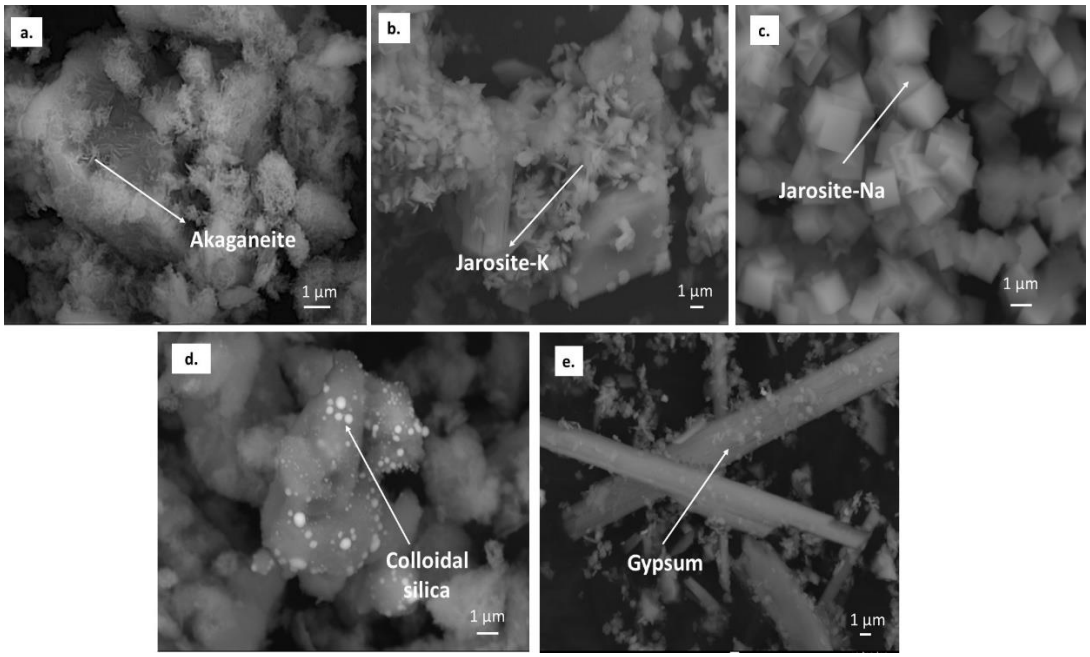

Fig. 6-10. SEM-BSE of precipitates in different solutions, **a.** spindle-shaped akaganeite particles attached to albite particles, **b.** K-jarosite particles, **c.** Na-jarosite crystals, **d.** gypsum needles.

6.3.3.4. Sulfate systems with added NaCl

The highest percentage of iron and calcium precipitation occurred in the $Fe_2(SO_4)_3/H_2SO_4/NaCl$ system after stage 2. Akaganeite did not form, possibly because of the higher concentration of SO_4^{2-} over Cl^- in solution. Rather, a layer of K-jarosite and Na-jarosite intergrowth remained after rinsing the precipitate (Fig. 6-11). Figure 6-12 compares the XRD pattern for the initial sample, with these of products that formed after stages 3 and 5 with ferric sulfate and sodium chloride in MSA solution. Major phases, such as albite and quartz, were still present in the sample, whereas calcite appeared to have dissolved completely. This type of precipitation occurs when copper dissolution stops, and, therefore, it is thought that agglomerates that coat the copper sulfide may inhibit copper dissolution.

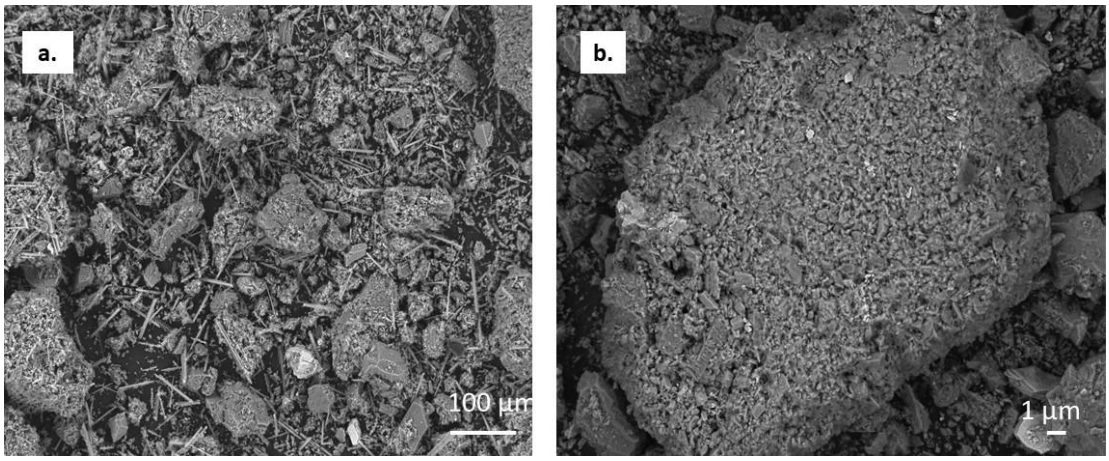

Fig. 6-11. SEM-BSE photomicrographs of the solid residue after leaching in $Fe_2(SO_4)_3$/MSA /NaCl solution. a. agglomerated particles surrounded by gypsum, b. magnification of a particle showing a layer composed of intergrown Na- and K-jarosite.

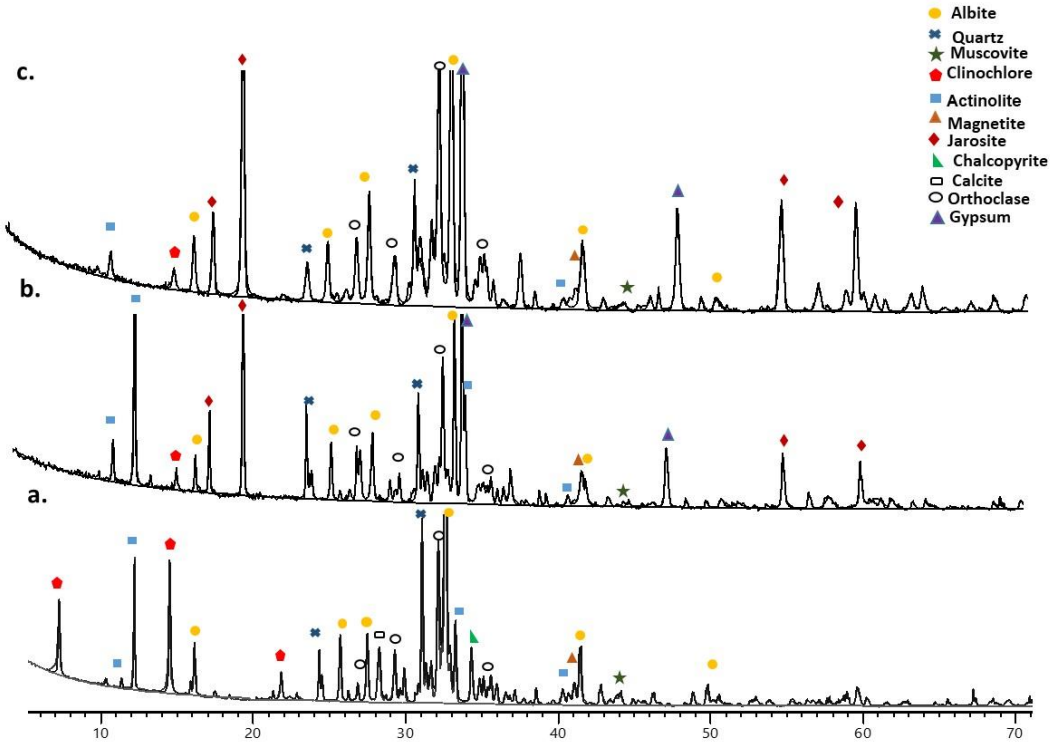

Fig. 6-12. X-ray diffractograms of **a.** unleached sample (P_{80} 68 µm) compared with **b.** stage 3 and **c.** stage 5 for $Fe_2(SO_4)_3$/MSA /NaCl. Jarosite and gypsum appear after stage 3.

SEM-EDS element distribution maps of the solid residues (Fig. 6-13) showed dispersed iron mixed with sulfur in jarosite zones (K-jarosite) and major gypsum precipitation.

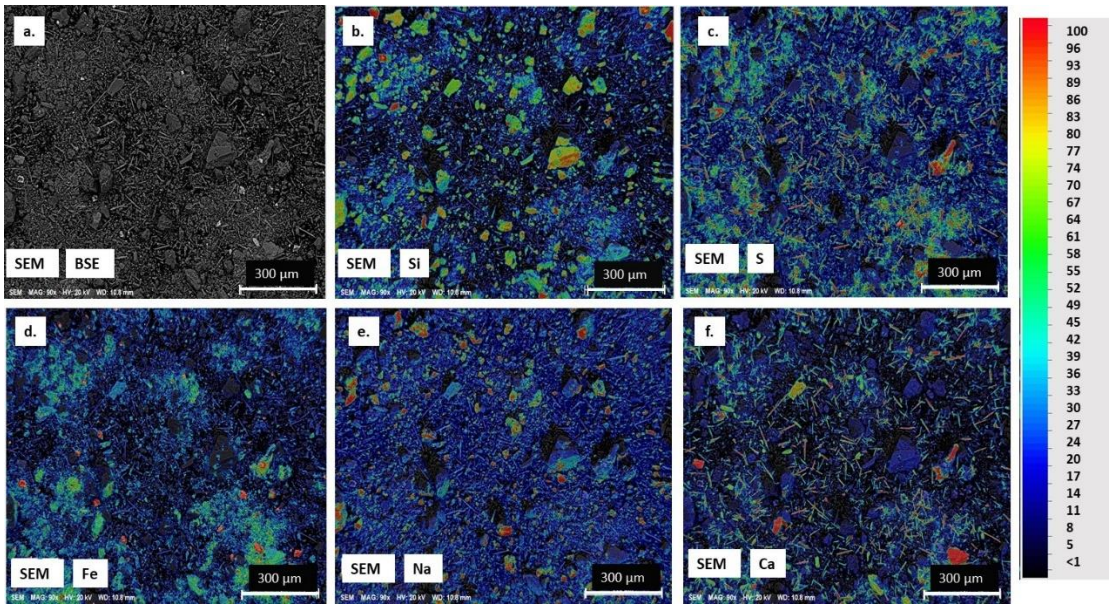

Fig. 6-13. Scanning-electron elemental maps of sample after stage 5 in $Fe_2(SO_4)_3$/MSA /NaCl showing partial elemental distribution, **a.** Initial sample, **b.** silica, **c.** sulfur**, d.** iron, **e.** sodium, **f.** calcium Note that the copper content in the residues was too low for visualisation.

6.3.3.5. Residue morphology

Leaching can result in particle-surface modification, sometimes without large changes in mass, which can increase the particle wettability and porosity (Suzany Ferreira dos Santos et al., 2019). Changes in particle-surface texture and increases in particle porosity have been observed previously for sulfide leaching (Hidalgo et al., 2019b). As an indicator of the development of particle "porosity", a measure of rugosity was applied, which is an indirect measure of the particle "non-sphericity" or roughness. The rugosity is the ratio between the intrinsic area (including the cracks and/or pores, as determined by BET) and the characteristic area, which is the surface that is projected as a plane (as a spherical particle, as determined by dynamic light scattering measurements or specific surface area (SSA)) (Du Preez, 2015). A higher ratio indicates a higher porosity or the presence of surface irregularities.

Figure 6-14 compares the particle size, surface area and rugosity. The particle size (P_{80}) decreased after five stages for all solutions, with the ferric sulfate in sulfuric acid yielding the smallest particle size. The surface area and rugosity both increased. Samples that were reacted with the chloride solutions ($FeCl_3$/MSA and $FeCl_3$/HCl)

had a rugosity that was five times larger than that of the original sample, possibly because of the reduced particle size after leaching and dispersed distribution of precipitates (e.g., micron-sized akaganeite flakes) that formed only in the chloride solutions.

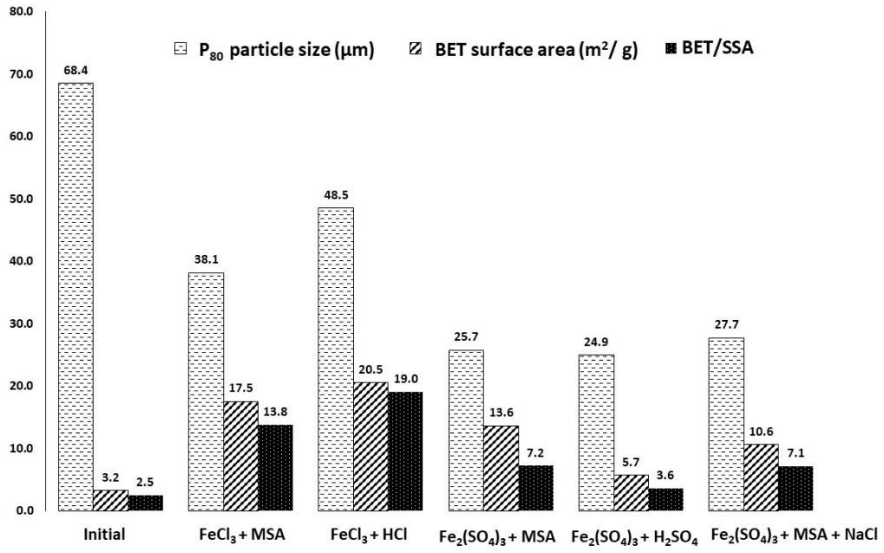

Fig. 6-14. Comparison of P_{80}, surface area (by BET) and rugosity (ratio of BET to SSA) for the unreacted sample and the residues after five stages.

6.4. Conclusions and implications for ISR

This study provides an indication of possible mineral behaviour in an ISR environment during flow of a saturated pregnant leach solution through unreacted low-grade natural ore. The main conclusions are:

- Solids analyses (XRD, SEM/EDS and QEMSCAN) showed three major precipitation phases, namely, jarosite and gypsum in the sulfate system and akaganeite in the chloride system. Precipitation occurred because of the increased cation concentrations in solution (Na^+, $Ca^{2+}$and K^+), the experimental temperature, and pH increase after stage 2.

- Less precipitation of iron occurred from the chloride solutions ($FeCl_3$/MSA and $FeCl_3$/HCl) than the sulfate solutions ($Fe_2(SO_4)_3$/MSA, $Fe_2(SO_4)_3/H_2SO_4$ and $Fe_2(SO_4)_3$/MSA/NaCl). Likewise, the presence of MSA reduced iron

hydrolysis and delayed precipitate formation compared with the sulfuric and hydrochloric acid systems.

- SEM imaging showed that precipitates in sulfate solutions formed agglomerates, and those in chloride solutions formed small particles, both of which can block microfractures. These precipitates formed after three stages of contact for the conditions used in this study.

- NaCl addition increased the precipitation from sulfate solutions and promoted the formation of gypsum and Na-jarosite.

- Increased initial ferric concentration promoted increased precipitation, especially when sulfate and alkali were present.

- Iron precipitates formed passivation layers and may hinder copper dissolution.

Because tests were conducted on finely ground material in this study, recommendations for future work include studies on changes in permeability (as a result of solid changes, such as precipitate formation) in wide horizontal columns that contain fractured material or cores above 60°C, with fluid monitoring at intermediate points along the column, to enable a closer approximation to a real ISR environment.

The most important implication for ISR from this study was the demonstration that precipitates will form as the lixiviant moves from the injection to the collection well. Precipitates may block narrow flow paths. As these precipitates are in chemical equilibrium with the pregnant solution, they are unlikely to redissolve during continued fluid flow and they may form preferential pathways, result in "short circuiting" (Sinclair and Thompson, 2015) or cause equipment failure (Zhang et al., 2017). Based on our results and information in the literature, recommendations for precipitation control in ISR processing include:

- MSA and hydrochloric acid use may be preferred to sulfuric acid use for ores with high alkali-metal contents.

- Addition of NaCl is not recommended when the solid contains high amounts of sodium-rich minerals and sulfate is present in solution, and/or in the presence of soluble iron minerals.

- Copper dissolution is related closely to iron precipitation; ideally, constant pH control is required and, between 40°C and 90°C, the pH should be below 1.8.

- Surfactant addition may prevent microfracture clogging and/or cationic polymer and clay swelling (Tan et al., 2014), but may be costly.

- Rinsing stages can dilute cation build up and dissolve soluble precipitates but would also incur additional operational costs.

- Well spacing will be a trade-off between close spacing to prevent precipitation and more cost-effective wider spacing. Furthermore, increased well spacing may not be counterbalanced by the use of higher oxidant concentrations (Bartlett, 1998).

Acknowledgments

The authors would like to acknowledge MRIWA (Project M488), BASF, Curtin University and CSIRO for funding this work; Tuyen Pham and Sophia Surin for assistance with the fluid and solid analysis; Drs Robbie McDonald and Denis Shiers for reviewing a draft of this manuscript and the reviewers for their valuable additions to the final document.

References

Azmayandeh, M., Aghazadeh, V. and Abdollahi, H., 2017. Investigation of affecting parameters on heap leaching performance and reducing acid consumption of low grade oxide-sulfide copper ore. International Journal of Mineral Processing and Extractive Metallurgy, 2: 40–45.

Bartlett, R.W., 1998. Solution mining : leaching and fluid recovery of materials. The Netherlands: Gordon and Breach Science Publishers.

Bibi, I., Singh, B. and Silvester, E., 2011. Akaganéite (β-FeOOH) precipitation in inland acid sulfate soils of south-western New South Wales (NSW), Australia. Geochimica et Cosmochimica Acta, 75(21): 6429–6438.

Cogram, P., 2018. Jarosite, Reference Module in Earth Systems and Environmental Sciences. Elsevier.

Córdoba, E.M., Muñoz, J.A., Blázquez, M.L., González, F. and Ballester, A., 2009. Passivation of chalcopyrite during its chemical leaching with ferric ion at 68 °C. Minerals Engineering, 22(3): 229–235.

Du Preez, C., 2015. A new arc–chord ratio (ACR) rugosity index for quantifying three-dimensional landscape structural complexity. Landscape Ecology, 30(1): 181–192.

Dutrizac, J.E., 1982. Jarosite-type compounds and their application in the metallurgical industry, 3rd International Symposium on Hydrometallurgy. Metallurgical Society of AIME, Atlanta ,Georgia, pp. 531–551.

Earley, D., III and Jones, P.M., 1992. Geochemical effects on the hydrology of in-situ leaching mining of copper oxide ore at the Cyprus Casa Grande Mine, Arizona. Littleton, CO, United States: Society for Mining, Metallurgy, and Exploration, pp. 60.

Ferron, C., 2003. Leaching of secondary copper minerals using regenerated ferric sulfate copper. VI: Hydrometallurgy of Copper. Montreal: Canadian Institute of Mining, Metallurgy and Petroleum: 337–352.

Gomis-Yagües, V., Boluda-Botella, N. and Ruiz-Beviá, F., 2000. Gypsum precipitation/dissolution as an explanation of the decrease of sulfate concentration during seawater intrusion. Journal of Hydrology, 228(1): 48–55.

Hidalgo, T., Kuhar, L., Beinlich, A. and Putnis, A., 2019a. Kinetics and mineralogical analysis of copper dissolution from a bornite/chalcopyrite composite sample in ferric-chloride and methanesulfonic-acid solutions. Hydrometallurgy, 188: 140-156.

Hidalgo, T., McDonald, R., Kuhar, L., Beinlich, A. and putnis, A., 2019b. Staged leaching of bornite with acidic solutions at moderate temperature in an in-situ recovery environment, ALTA ISR symposium, ALTA, Perth, Western Australia.

IAEA, 2016. In situ leach uranium mining: An overview of operations, International Atomic Energy Agency, Vienna.

Jenssen, I.B., Hines, M.A., Dotterud, O.M., Bøckman, O. and Andreassen, J.-P., 2018. Filtration properties of ferric hydroxide precipitate in nickel production. In: B.R. Davis et al. (Eds.), Extraction 2018. Springer International Publishing, Cham, pp. 1373–1381.

Lu, Z.Y., Jeffrey, M.I. and Lawson, F., 2000. Effect of chloride ions on the dissolution of chalcopyrite in acidic solutions, Hydrometallurgy: 56, pp.189–202

Mallio, W., Pojasek, W., Park, W. and Rainville, G., 1981. Parameters and petrographic interpretation of In situ copper leaching. Process Mineralogy: Extractive Metallurgy, Mineral Exploration, TMS-AIME. pp. 339–352.

Meyer, M.C., Austin, P. and Tropper, P., 2013. Quantitative evaluation of mineral grains using automated SEM–EDS analysis and its application potential in optically stimulated luminescence dating. Radiation Measurements, 58: 1–11.

Nikoloski, A.N. and Malley, G.P., 2018. The acidic ferric sulfate leaching of primary copper sulfides under recycle solution conditions observed in heap leaching. Part 1. Effect of standard conditions. Hydrometallurgy, 178: 231–239.

Paulson, S., 1992. Effects of fluid recycling on leach solution composition: implications for copper in situ mining. In situ recovery of minerals II, Edited by S.A. Swan and K.R.Coyne, New York, pp. 51–80.

Peretyazhko, T.S., Ming, D.W., Rampe, E.B., Morris, R.V. and Agresti, D.G., 2018. Effect of solution pH and chloride concentration on akaganeite precipitation: Implications for akaganeite formation on Mars. Journal of Geophysical Research: Planets, 123(8): 2211–2222.

Qian, G., Li, J., Li, Y. and Gerson, A.R., 2014. Probing the effect of aqueous impurities on the leaching of chalcopyrite under controlled conditions. Hydrometallurgy, 149: 195–209.

Sasaki, K. and Konno, H., 2000. Morphology of jarosite-group compounds precipitated from biologically and chemically oxidised Fe ions. Canadian Mineralogist, 38: 45–56.

Schmidt, R. D., D. Barley & M. J. Friedel, 1994. Dynamic influences on hydraulic conductivity during in situ copper leaching. In Swan, S. A. & K. R. Coyne (eds) In Situ Recovery of Minerals II. Engineering Foundation, New York. pp. 259–286.

Seredkin, M., Zabolotsky, A. and Jeffress, G., 2016. In situ recovery, an alternative to conventional methods of mining: Exploration, resource estimation, environmental issues, project evaluation and economics. Ore Geology Reviews, 79: 500–514.

Sinclair, L. and Thompson, J., 2015. In situ leaching of copper: Challenges and future prospects. Hydrometallurgy, 157: 306–324.

Santos, S., Lima, R., Cruz, C.,Pimentel, V., Ferreira, M., Cardoso, R., Rezende, M., Fook, V., 2019. PEEK Physical Surface Modification: Evaluation Of Particles Leaching Process. Materials Research 22.

Tan, K., Li, C., Liu, J., Qu, H., Xia, L.,Hu, Y., Li, Y., 2014. A novel method using a complex surfactant for in-situ leaching of low permeable sandstone uranium deposits. Hydrometallurgy, 150: 99–106.

Zhang, P., Chen, T., Wang, G. and Peng, C., 2017. Ocean economy and fault diagnosis of electric submersible pump applied in floating platform. International Journal of e-Navigation and Maritime Economy, 6: 37–43.

Chapter 7. Conclusions and recommendations for ISR application

This research serves as a component of work being undertaken to unlock the potential for hard-rock in situ recovery (ISR). Experiments focused on an analysis of fluids and solids that had been leached under simulated ISR conditions. Analytical techniques were used for solids characterisation and allowed for the identification of morphologies, chemistry and textures of the reacted solids. Conclusions were made based on the gaps in knowledge provided in Chapter 1 and are presented with recommendations for ISR implementation.

- **Mineral dissolution and fluid stability:** Under similar conditions, the various leaching fluids showed different copper leaching efficiencies, with chloride solutions showing the best performance for chalcopyrite dissolution above 60°C. At 90°C, other fluids that proved promising at lower temperatures were affected detrimentally (e.g., potassium dichromate). The accessibility was enhanced by certain fluids (e.g., ferric and copper chloride) and increased the number of fractures, the surface area and the porosity. When the fluid was negatively affected by changes in pH and acid consumption, this accessibility enhancement was compromised, and undesired precipitation reduced the solid permeability and copper dissolution rates. High-temperature experiments allowed for a comparison with low-temperature experiments and filled knowledge gaps. Tests to simulate low-oxygen environments that are expected in deep ore bodies showed copper dissolution in several solutions ($FeCl_3$ and $K_2Cr_2O_7$ in HCl). Therefore, ISR could be possible at high temperature even with a low oxygen solubility. Based on different selection criteria, $FeCl_3$+HCl was found to be the most efficient solution for chalcopyrite dissolution in the presence of pyrite above 90°C. High-temperature (170˚C) experiments were presented at the ALTA conference and the associated paper is attached as Appendix A.

- **Reaction kinetics and mechanism:** An understanding of the kinetics of composite samples is important for ISR because of the lack of selectivity in real operation. Activation energies were determined from kinetic studies of composite samples. The energy requirements changed when more than one phase was present. In these cases, empirical equations may not fit the experimental data, and an alternative method for energy calculation should be applied, such as the 'time-to-a-given-fraction' methodology. This method can be used to calculate the energy requirements for different reaction stages and composite samples with a high concentration of gangue and valuable mineral sources, which makes it a valuable tool for ISR leaching characterisation. Some product formation showed characteristic features of interface coupled dissolution–reprecipitation (ICDR), including a sharp chemical interface and porosity development in the newly-formed phases (Pollok et al., 2011; Putnis, 2002; Putnis, 2009; Putnis, 2015; Ruiz-Agudo et al., 2012; Ruiz-Agudo et al., 2014; Xia et al., 2009). At ISR temperatures, the coexistence of ICDR and solid-state diffusion was found; the specific characteristics of each mechanism have important implications on the resulting product textures and may affect the microscale permeability of the ores.

- **Compositional and morphological transformations:** The product layers were influenced by the local fluid chemistry and changed over the course of the reaction. Furthermore, under similar conditions and using the same solution, different product layers were found among copper sulfides (chalcopyrite, bornite and chalcocite). Sulfur was the main product that formed during leaching, as was also presented by Dutrizac (1990). The texture of the sulfur layers depends on the fluid chemistry and on the leached mineral. Sulfur porosity changed in the presence of chloride when chalcopyrite was leached and evolved with reaction time by healing the porosity as shown by the bornite solids. Copper-enrichment phases resulted from chalcopyrite oxidation and were produced mainly when copper was concentrated in fluids. The copper-enrichment phases showed no passivation; these phases also formed with depleted oxidant and with acid only present in the fluid and leached more rapidly with oxidant addition after the initial transformation (Appendix B). The

transformations followed the reactive zones and transformed the entire mineral, and in some cases the surrounding gangue minerals and impermeable zones. Fractures triggered the initial transformation and retained the effective permeability and porosity through contact with the ore. Passivation resulted when iron precipitates formed during multistage fluid–rock interactions in sulfate solutions because of the formation of jarosite that coated the chalcopyrite surface.

- **Low-grade ore dissolution and the effect of gangue minerals:** When a higher content of gangue was initially present and there was continuous fluid–rock interaction above 90°C, an increase in precipitations was evidenced. Precipitation resulted from the increase in concentration of anions and cations in solution even with a slight increase of pH. The increase in cation and anion concentrations in fluids caused iron hydrolysis, especially in sulfate solutions. The use of such solutions in the presence of gangue may induce fracture blockage and passivation of the reactive surfaces. Even though an increase of acidity and continuous pumping could counteract some of these effects, prolonged fluid–rock contact will accelerate acid consumption along the flow pathway. Thus, careful oxidant selection to minimise these adverse effects is vital.

The outcomes of this research highlight the importance of geometallurgical analysis for ISR operations. The analysis of fluid and rock behaviour is a valuable tool for initial fluid selection to avoid issues associated with reactions and solid transformations. The main conclusion from this research is that solid transformations are dynamic and are related closely to fluid chemistry.

Based on these results, recommendations for ISR operations include:

- **Optimal fluid selection:** Fluid selection should be based on copper dissolution, stability at a chosen temperature, passivation behaviour, environmental impact, accessibility enhancement and cost. Some fluids prove promising when assessed according to many of these points (e.g., ferric chloride, sodium nitrate and copper chloride). Although ferric sulfate solution

tends to be the preferred industry choice, this solution shows a low copper dissolution, passivation behaviour and temperature instability. The cost savings that are possible in ISR operations compared with conventional mining (Seredkin et al., 2016) may allow for a more expensive fluid selection.

- **Use of pre-treatments or mixed systems:** The use of mild hydrothermal solutions (e.g., low-concentration Cu^{2+} solutions or acidic solutions) results in enriched copper phases (Cai et al., 2011; Cerda et al., 2017; Zhao et al., 2014). This resulting phase may be soluble because the textural and morphological transformation increases the reactivity of the ore compared with the unreacted ore. Subject to time constraints, pre-treatment with affordable acidic hydrothermal solutions could be used to replicate natural transformations (geomimetics) followed by aggressive oxidation to increase the copper recovery rate and ore accessibility. Chalcopyrite transformed to copper-enriched phases in acidic solutions when fractures were present. Therefore, the simultaneous application of blasting with pre-treatment or staged dissolution may allow for an increased chalcopyrite replacement rate.

- **Composite solid kinetics:** In the case of composite solids with more than one source of valuable metal, kinetics were most affected by the dominant phase. The energy requirements (activation energies) changed during the reaction. The best approach for kinetic analysis is to use the ‘time-to-a-given-fraction’ method, which can be applied to ISR complex ores.

- **Reaction-driven accessibility enhancement:** Optimal leaching behaviours depend to a large extent on ensuring fluid–rock contact. Textural transformations occurred after all reactions, with the reaction-driven enhancement of initial fractures and the enhancement of fluid–rock contact being of significance. Aggressive solutions provided major fracture networks that enhanced the fluid pathways. Mechanical accessibility enhancement is mandatory for chalcopyrite leaching below 90°C. Fluid selection could assist microscale accessibility, generate effective porosity and increase the overall permeability.

- **Oxidant/lixiviant influence in precipitations:** Within the ranges tested, oxidant and acid concentrations did not significantly influenced the chalcopyrite and bornite dissolution kinetics. Higher oxidant concentrations were counterproductive for some solutions and increased precipitations resulted when pH and acid concentrations were not maintained. The use of saline or hypersaline water may increase cation and anion concentrations, which could cause jarosite/akaganeite/gypsum precipitation, especially at higher temperatures, which, in turn, could produce major blockages in hard-rock fracture channels, scale and corrosion in pipes. An increase in salinity and continuous contact with fresh solid resulted in an increase in acid consumption. Therefore, oxidant concentrations should be based on the initial copper concentration in the solid with limited excess. The use of saline water is not recommended when high concentrations of cation-containing gangue is present in the ore, especially when ferric sulfate in sulfuric acid is used as the leach solution. The monitoring of fluid changes by continuous sampling and, if possible, by real-time analysis of groundwater (such as by using new techniques, such as Sensei® sensors (Caruso et al., 2018)) could prevent precipitation, which could have important repercussions for hard-rock permeability.

This work provides a starting point in terms of the understanding of fluid–rock interactions under ISR conditions. In future, the geological identification of candidate samples for ISR processing and fluid selection should be applied to Australian copper ores. Similar studies could also be expanded to other commodities, such as nickel or gold. Differences were visible between fine-grained and cuboid samples. Work could be expanded to understand copper-sulfide leaching of cores, and hard-rock kinetic analysis could be conducted to understand the effect of a reduced surface area. Experimental apparatus may include column leaching and flow-through reactors. The extent of accessibility enhancement on copper dissolution by selected lixiviants should be compared with that of blasted solids, such as those that may be expected to be produced for in-mine recovery (IMR) (Mousavi and Sellers, 2019) and hard-rock ISR applications.

References

Cai, Y., Chen, X., Ding, J. and Zhou, D., 2011. Leaching mechanism for chalcopyrite in hydrochloric acid. Hydrometallurgy, 109–118.

Caruso, D. et al., 2018. Automating groundwater monitoring for in-situ recovery operations using CSIRO Sensei™ sensors. Emerging Sensing Technologies Summit 2018, SPIE, Melborune, Australia.

Cerda, C., Taboada, M., Jamett, N., Ghorbani, Y. and C. Hernández, P., 2017. Effect of Pretreatment on Leaching Primary Copper Sulfide in Acid-Chloride Media. Minerals 8. pp. 3-14.

Dutrizac, J., 1990. Elemental sulfur formation during the ferric-chloride leaching of chalcopyrite. Hydrometallurgy, 23(2-3): 153–176.

Mousavi, A. and Sellers, E., 2019. Optimisation of production planning for an innovative hybrid underground mining method. Resources Policy, 62: 184–192.

Pollok, K., Putnis, C. and Putnis, A., 2011. Mineral replacement reactions in solid solution-aqueous solution systems: Volume changes, reactions paths and end-points using the example of model salt systems. American Journal of Science, 311:211–236.

Putnis, A., 2002. Mineral replacement reactions: from macroscopic observations to microscopic mechanisms. Mineralogical Magazine, 66(5): 689–708.

Putnis, A., 2009. Mineral replacement reactions. Reviews in Mineralogy and Geochemistry, 70(1): 87–124.

Putnis, A., 2015. Transient Porosity Resulting from Fluid-Mineral Interaction and its Consequences, Reviews in Mineralogy and Geochemistry, pp. 1–23.

Ruiz-Agudo, E., Putnis, C., Rodriguez-Navarro, C. and Putnis, A., 2012. Mechanism of leached layer formation during chemical weathering of silicate minerals. Geology, 40(10): 947–950.

Ruiz-Agudo, E., Putnis, C.V. and Putnis, A., 2014. Coupled dissolution and precipitation at mineral–fluid interfaces. Chemical Geology.pp: 132–146.

Seredkin, M., Zabolotsky, A. and Jeffress, G., 2016. In situ recovery, an alternative to conventional methods of mining: Exploration, resource estimation, environmental issues, project evaluation and economics. Ore Geology Reviews, 79: 500–514.

Xia, F., J. Brugger, G. Chen, Y. Ngothai, B. O'Neill, A. Putnis & A. Pring, 2009. 2009. Mechanism and kinetics of pseudomorphic mineral replacement reactions: A case study of the replacement of pentlandite by violarite. Geochimica et Cosmochimica Acta, 73(7): 1945–1969.

Zhao, J., Brugger, J., Ngothai, Y. and Pring, A., 2014. The replacement of chalcopyrite by bornite under hydrothermal conditions. American Mineralogist, 99(11–12): 2389.

Appendix A. Comparative analysis of lixiviant/oxidant systems for chalcopyrite leaching from coarse samples at elevated temperature

Chalcopyrite ($CuFeS_2$) is the most common copper-bearing mineral and represents more than half of global copper mineral reserves (Wang, 2005). Refractory chalcopyrite requires the addition of an oxidant and lixiviant for dissolution. Although lixiviants have been evaluated in previous studies for conventional mining, limited information is available regarding their behaviour during the leaching of coarse samples at high temperatures, including their stabilities and what secondary products may form. We compared the thermal stability of a variety of lixiviants and their ability to leach copper from chalcopyrite with oxidant addition at set temperature, pressure and pH conditions. Tests were conducted at 170°C for 120 to 576 hours using solid cubes (4-mm sides) to simulate coarse samples found in heap leaching and in-situ recovery. Sealed batch reactors (closed-system conditions) were used to simulate an anaerobic environment that may be experienced in a subterranean application (such as an in-situ recovery environment). Lixiviants, including sulfuric acid, hydrochloric acid and glycine, and oxidants, including iron(III), copper, dichromate, permanganate and hydrogen peroxide, were screened for their suitability to leach copper from hard–rock copper-sulfide deposits.

This paper presents the findings from this study and includes a comparison of the leaching systems at high temperature based on an identification of products and passivation phenomena, and an analysis of surficial textures. Conclusions are provided on the possible suitability of the systems for use in high-temperature copper in-situ recovery processing based on the laboratory performance of the chosen systems.

A.1. Introduction

During the hydrometallurgical processing of copper-sulfide minerals, an oxidant such as Fe^{3+} or O_2 is used to oxidize sulfide to sulfate and release copper into solution for recovery and purification (Schlesinger et al., 2011). The selection of a suitable lixiviant/oxidant system can enhance the recovery rate, reduce the lixiviant

consumption and result in an overall increase in mining efficiency. Chalcopyrite leaching studies have attracted significant interest because of the global abundance of this mineral and its high copper content. A variety of oxidant/lixiviant combinations for the processing of reduced copper minerals under ambient conditions have been examined (Acero et al., 2007; Antonijević et al., 1994; Bonan, 1981; Córdoba et al., 2008; Eksteen, 2017; Li, 2010; Ruiz, 2011; Watling, 2013; Watling, 2014) and the outcomes from these studies highlight important aspects of primary-sulfide leaching at low- to medium-temperature conditions. Conventional systems include mainly Fe^{3+} as an oxidant. When leaching with Fe^{3+}, chalcopyrite is sensitive to temperature changes and its solubility increases with increasing pressure and temperature (Córdoba et al., 2008; Dutrizac, 1981; Munoz et al., 1979; Watling). Other authors studied the effect of copper as an oxidant and identified that Cl^- accelerates the leaching rate (Skrobian et al., 2005). Some alternative oxidant and lixiviant systems have been tested under low-temperature conditions using concentrated chalcopyrite, and these include ammonia, dichromate and glycine. These tests have shown promising results, e.g., potassium dichromate showed 80% copper extraction after 150 min at 90°C (Antonijević et al., 1994; Aydogan et al., 2006; Beckstead and Miller, 1977; Oraby and Eksteen, 2015). An understanding of the lixiviant/oxidant response beyond these known temperature (and pressure) regimes may be required in an in-situ recovery (ISR) environment. However, limited studies exist on different commercially proposed systems above 225°C (Ferron et al., 2000; McDonald and Muir, 2007; Yu et al., 1973).

The formation of surface layers, which is commonly termed "passivation", has an important influence on the leaching rate. In some cases, passivation layers may restrict lixiviant access to the reaction interface. However, surface layers that may form during the oxidation process, such as less refractory secondary copper-enrichment phases, may favour mineral dissolution (Li et al., 2010). Diverse types of product layers may form in different systems and/or under different conditions, which implies that more than one secondary phase can form during the same leaching process. A better understanding of the mechanisms of secondary-phase formation during leaching and its influence on the leaching rate will highlight optimal dissolution conditions. Therefore, an understanding of the matrix response to lixiviant/oxidant systems at the grain-scale is essential to evaluate possible operational issues, e.g., the potential for

pore-space clogging, which may induce blockage of the lixiviant flow path and prevent recovery from the pregnant leach solution.

In this paper, we discuss the leaching behavior of coarse pieces of a natural chalcopyrite sample in six different lixiviant/oxidant systems under similar conditions, using commercially available oxidants and lixiviants and its possible extrapolation to a practical operation.

A.2. Experimental conditions

Initial sample

Natural samples of chalcopyrite from a private collection without a specified origin were cut and polished to form ~4 mm × 4 mm × 4 mm cubes (~64 mm^3 volume). Initial samples were examined by scanning electron microscopy (SEM). The experimental average point chemical distribution in the blank cubes was measured to obtain an indication of their elemental abundance before leaching. These values served as a baseline for secondary-product identification. Surface X-ray diffraction (XRD) analysis and aqua–regia digestion with inductively coupled plasma–atomic emission spectroscopy (ICP–AES) were used to determine the sample mineralogy and chemical composition, respectively.

Leaching tests

Triplicate experiments were conducted using cubes with the lixiviant/oxidant systems listed in Table A-1. The cubes were covered with 5 ml of solution and sealed in in 10-ml Teflon-lined closed stainless-steel batch reactors. The reactors were heated to a set temperature in standard convection ovens at 170°C. Screening experiments were conducted at elevated temperature to accelerate the reaction with the coarse sample, identify the viability of the lixiviant/oxidant system and compare the effectiveness of the different lixiviants and oxidants under the same conditions. To simulate extreme conditions for deep ore bodies (relevant for ISR), no oxidant or oxygen replenishment occurred during the experiments. The experimental set up did not allow for pH or Eh monitoring or control during the experiment. The leaching time varied from one to three weeks, after which solids and fluids were sampled. The leachates were filtered

and diluted, the solid residues were washed and dry-mounted in epoxy resin and polished to obtain a cross section of the sample surface below and surface product.

The oxidant concentrations were calculated from the stoichiometric dissolution relationships with chalcopyrite (see Table A-1) and a factor of twice excess oxidant was added to the solution. Reagents were from BASF, Sigma Aldrich and Ajax Finechem. Most systems were stable under the temperature conditions that were tested; no precipitation or density changes resulted during the experiment, but the glycine decomposed above 60°C below pH 12.

Table A-1. Summary of systems and conditions used in the leaching tests.

Oxidant	Molar ratio $CuFeS_2$	Lixiviant	Concentration (mol L^{-1})	Density (g/mL)	Initial pH	Initial Eh (mV)
$FeCl_3$	16	HCl	0.5	1 36	-1.26	627
$Fe_2(SO_4)_3$	8	H_2SO_4	0.25	1 5	-0.18	566
$CuCl_2$	15	HCl	0.5	1 39	-1.07	654
$CuSO_4$	2	H_2SO_4	0.34	1.05	-0.6	587.4
$K_2Cr_2O_7$	2.8	HCl	0.4	1.09	0.65	863
H_2O_2	2	Glycine	1	1.07	12.83	-106

Characterisation

Reaction-product phases were analysed with a PANalytical Empyrean X-ray diffractometer and interpretation of the acquired pattern was performed using High score plus. Reacted cubes were studied by scanning electron microscopy-energy-dispersive X-ray spectroscopy (SEM-EDS) using a JEOL-JSM-7001 field emission SEM. The copper and iron contents in the leach solutions were analysed by using an Agilent 240/280 atomic absorption spectrophotometer (AAS) and inductively coupled plasma atomic emission spectroscopy (ICP–OES).

A.3. Results

Initial sample characterisation

XRD and solids analysis indicated that the sample was a mixture of fairly pure chalcopyrite with traces of pyrite and quartz. The average initial chemical distribution

was 35.2% Cu, 30.98% Fe and 33.83% S. Dispersed pyrite gangue was present in a portion of the cubes (see Fig. A-1).

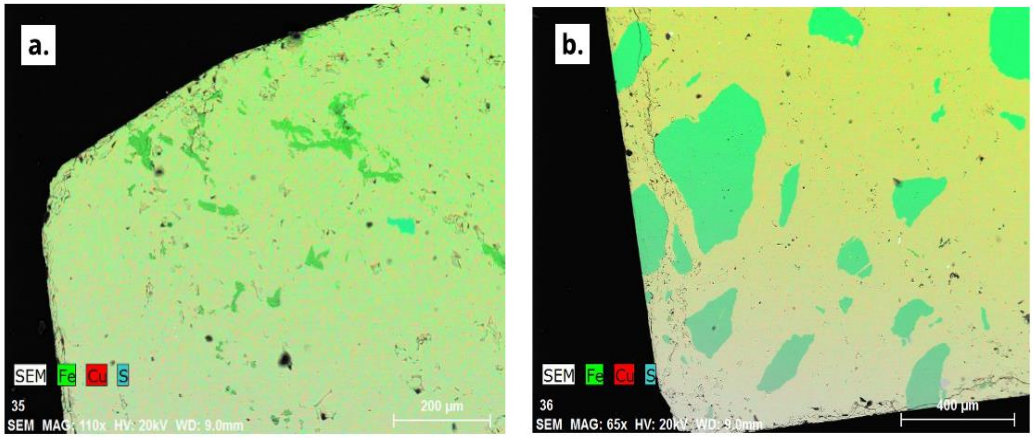

Fig. A-1. SEM elemental maps showing copper, iron and sulfur distributions in initial cube samples before leaching. **a.** No cracks existed at the peripheries of the sample, **b.** pyrite gangue distributed in the sample.

Copper dissolution

The copper dissolution from the chalcopyrite cubes at 170ºC after three weeks is shown in Fig. A-2. The chloride systems proved most effective at this temperature; the sample in the ferric-chloride system dissolved with only residual sulfur remaining and more than 80% copper extraction was achieved in the copper-chloride system after three weeks. The copper recovery was below 50% for all other lixiviant systems. The extent of copper leaching in the sulfate system, and specifically in the ferric-sulfate system, was similar to that seen previously in crushed and disk-milled samples (Dutrizac, 1981; Hirato et al., 1987; Munoz et al., 1979). The formation of a sulfur layer attached to the mineral surface limits continuous contact of the fresh mineral surface and the solution. Systems such as dichromate with hydrochloric acid and hydrogen peroxide with glycine showed a low copper extraction at higher temperatures. In the potassium-dichromate system, the initial solution Eh may have induced the formation of an impermeable manganese dioxide precipitate that reduced the copper recovery compared with expected results from previous studies. Recent studies demonstrate that hydrogen peroxide does not significantly enhance copper extraction, and, in fact, may degrade the lixiviant (Tanda, 2017). Because this study was based on literature available at the time, hydrogen peroxide was selected as an

oxidant. However, at the optimal glycine lixiviant system pH of 11, glycine decomposes above 60°C in the presence of hydrogen peroxide.

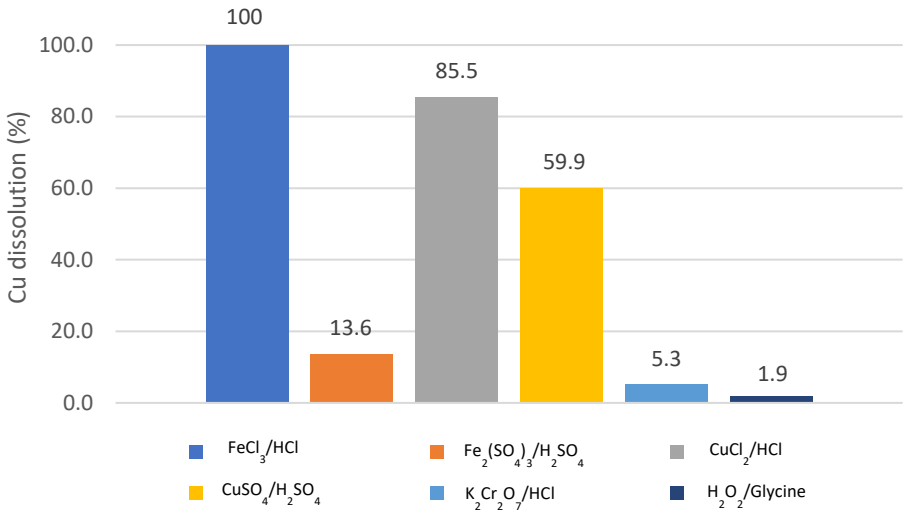

Fig. A-2. Final comparative Cu extractions from chalcopyrite (~64 mm^3 cube samples) at 170°C after three weeks of leaching.

Solid reaction products

Reaction product assemblages were mostly consistent for the three samples in each system. SEM analysis was used to examine the leach residues to understand the reaction mechanism and to explain the copper recovery in the four systems in which the copper extraction was lowest. The appearance of some reaction products in the cube experiments can be related to the different reaction rates and the presence of gangue inclusions in the starting material. The resulting solid phases included iron precipitates, copper-enrichment zones and other precipitates, such as hematite, covellite and bornite. The experimental temperature exceeded the melting point of sulfur (115°C), which resulted in sulfur adherence to surfaces and which could have created a surface-passivating effect.

Ferric-oxidant solutions showed sulfur only as a product layer. As mentioned above, the cube in ferric-chloride solution dissolved after 5 days to yield only S^0 by XRD analysis. A solid sulfur layer formed around the bulk mineral in the ferric-sulfate medium (see Fig. A-3a). Sulfur entered small cracks in the sample and replaced the dissolved chalcopyrite in the final stages of the experiment. No intermediate secondary

mineral phases were found. Pieces of chalcopyrite remained prior to the sulfur layer replacement. SEM images indicate that the sulfur layer as formed in the ferric-sulfate system appeared less porous than that formed in the ferric-chloride system, which may hinder solution access to the unreacted sample core.

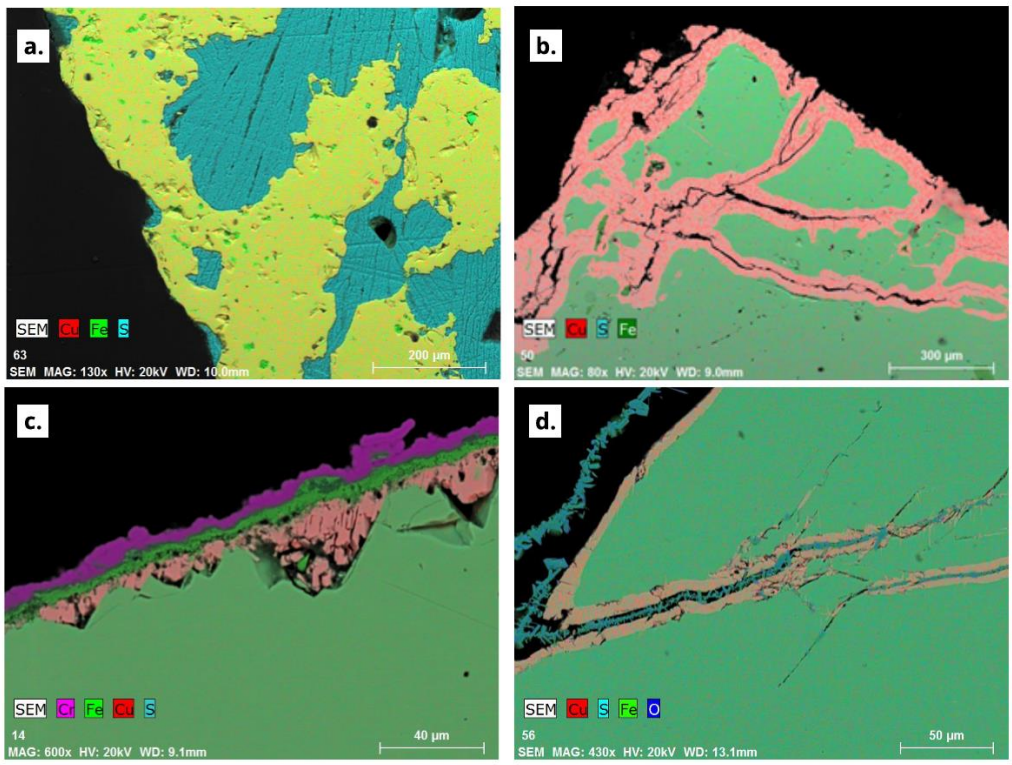

Fig. A-3. SEM elemental maps of chalcopyrite cube samples after leaching with different systems at 170°C for three weeks. The red areas represent a high copper concentration without iron in the product, green areas represent a high iron concentration and blue areas represent a high sulfur concentration. **a.** Cube leached with ferric sulfate and sulfuric acid showing sulfur precipitation in cavities; chalcopyrite that surrounded the sulfur areas had a higher sulfur content than the initial sample, **b.** cube after three weeks' leaching with cupric sulfate and sulfuric acid showing a digenite rim on the outer surfaces and along fractures, **c.** perimeter of a coarse cubic sample leached with potassium dichromate and hydrochloric acid; the three resultant layers include chromium (III) oxide (deep purple), hematite (deep green) and covellite (red), **d.** cube after reaction with glycine and hydrogen peroxide showing a bornite (orange) and goethite (deep green) layer that enters the internal fractures.

Both systems with cupric oxidant yielded secondary phases. The only difference between the systems was the thickness of the intermediate products and the speed of the reaction. Both reactions provided insight into copper enrichment in secondary

phases. Product phases included S^0 and Fe_2O_3 on the surface. Intermediate enrichment rims contained minerals, such as Cu_2S, $Cu_{1.8}S$ and CuS. These intermediate copper sulfides represent stages prior to the final dissolution of chalcopyrite and the recovery of Cu^{2+} in solution. A cross–section through a reacted chalcopyrite cube after three weeks in a copper-sulfate/sulfuric-acid system at 170°C is shown in Fig. A-3b. The map shows an enrichment zone where all iron has been extracted and a secondary copper compound, as identified by EDS and XRD, was found to be digenite with a standard composition of 22.7%S and 77.6% Cu. The chalcopyrite core had a higher iron content, but no other iron–copper minerals were found in the samples. For the chloride systems, the development of the rim was faster and the cube was replaced by a new iron-deficient layer after three weeks. Elemental sulfur replaced the digenite face for stronger oxidant concentrations before the complete dissolution of the sample **(**Fig. A-4).

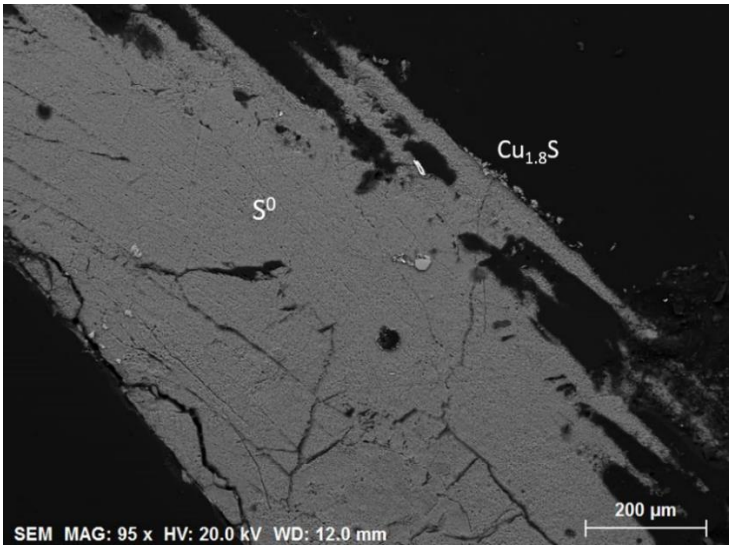

Fig. A-4. SEM image of cube sample after leaching with higher concentration of cupric chloride and hydrochloric acid at 170°C after 5 days, showing mostly elemental sulfur and a small piece of digenite attached to the external part of the residue.

A textural analysis of cubes in the potassium-dichromate system with chloride-ion addition in a hydrochloric-acid environment after three weeks revealed a layering of compositionally distinct reaction products on the cube surface. No sulfur was found as a product in this system. The inner layer was enriched in copper and an iron-deficient layer with an average composition of 24.3% S, 1.7% Fe and 74% Cu was present in

fractured areas. Outer parts of the cracks presented a composition that was similar to that of CuS (66% Cu and 34.18% S). The intermediate layer was copper-deficient and was identified by XRD as hematite with a composition of 69.3% Fe and 31% S. The outer layer was identified as Cr(III) oxide **(**Fig. A-3c). Limited information exists on product formation in such systems. Existing reports only provide information on systems below 97°C for concentrate and crushed sample, and no surface analysis of the mineral is available. According to the Pourbaix diagram for Cr speciation, at higher temperatures modelled by geochemist workbench (GWB), the range of pH where dichromate is stable decreases (See chapter 2), and the window for precipitation expands. Under the stoichiometric criteria of oxidant composition and the acidic conditions, the formation of Cr(III) is expected at the system solution potential (863 mV). In previous studies with milder oxidant conditions, the presence of this passivation layer was not found; instead, an elemental sulfur layer was found to surround the particles in a similar manner as occurs in ferric systems (Antonijević et al., 1994). The layers hinder dissolution.

Standard experimental conditions of 170°C were applied for all systems. Leaching in glycine was found to be highly dependent on pH and temperature conditions. Above 60°C, the solution pH decreased and at a low pH and high temperature, the glycine is thought to have decomposed to form ammonia. Glycine systems with oxygen or oxygen/peroxide as oxidant(s) are not ideal for use in batch reactors because pH control and oxidant replenishment are not possible. It is therefore possible that the initial oxidant was exhausted despite the excess addition, which yielded a poor final recovery after three weeks. The sample surface was coated with goethite and turned red but this layer did not appear to passivate the sample surface (Tanda, 2017). SEM-EDS analysis indicated the presence of a rim of goethite and bornite of uneven thickness (Fig. A-3d). Bornite was identified in all samples from 24 h to three weeks. No sulfur formation or gangue dissolution was evident and the variation in thickness of the bornite rim between the first and last experiment was negligible. In addition to the replacement rim at the outer parts of the reacted cube, replacement reactions resulted along fractures that extended into the cube interior. Fractures were frequently surrounded by a copper-enriched reaction halo even if they were not connected to the outside perimeter. These fractures may not be connected in the two-dimensional SEM images but may be connected in the third dimension (Fig. A-5).

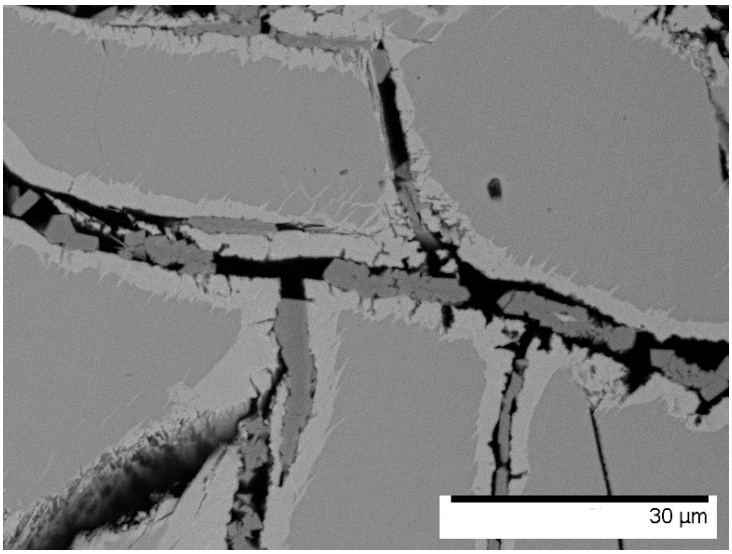

Fig. A-5. SEM images of cube samples after leaching with glycine and hydrogen peroxide after three weeks; lighter greys represent the bornite reaction rim around fractures and the iron-oxide product inside cracks.

A.4. Discussion

Each natural chalcopyrite cube differed between experiments and the chemical elemental distribution and the natural dissemination of gangue differed for each case. For coarse samples in heap leaching or natural samples in a subsurface ISR operation, the mineral is impure and is not crushed, and its accessibility is affected by the surrounding gangue and lack of natural fractures. The copper extractions that were obtained in some systems are encouraging, but, based on the cube size, reaction times for coarse material may be considerable, even at the high set point temperature (170°C).

Iron oxidants are used most commonly in hydrometallurgical processes because of their cost and availability. The results from the study with ferric oxidant confirm the temperature dependence of the copper extraction, which is especially important in sulfuric-acid environments where sample passivation with sulfur reduces the reaction rate. The introduction of sulfur into natural fractures obstructs access channels and surface contact with solution. Even though the sulfur layer appears not to impede flow, the time for recovery and maximum dissolution were affected. The difference in copper leaching between sulfate and chloride media and the product textures with copper and iron additions support the statement on changes in the product-layer morphology, where sulfur in the sulfate system was found to be more compact and

dense than that in the chloride system (Hirato et al., 1986; Hirato et al., 1987). It is possible that chloride-ion addition facilitates the breakdown of passive films and enhances chalcopyrite dissolution by maintaining continuous flow between the fluid and the core (Dreisinger, 2006), or the reactions and the form in which chalcopyrite is redistributed are different.

When cupric ions existed in the leaching environment, the dissolution of iron from the copper sulfide sample was higher than in any other system. In a $CuCl_2$ solution, for each mol of copper that enters the fluid, more than three times the iron was initially dissolved, followed by copper dissolution into solution and the appearance of elemental sulfur as a final product. However, the reaction rate did not appear to be affected or terminated by secondary-sulfide formation. Therefore, chalcopyrite underwent multiple dissolution stages with the formation of enriched products in the perimeter and cracks of the sample.

The potassium-dichromate and potassium-permanganate systems are not used commercially in the mining industry. Leaching information on these systems is restricted to a few publications and the results in this work. Potassium dichromate may present several environmental issues in an in-situ operation as it is toxic, corrosive and flammable under certain conditions (based on MSDS). This system proved prone to passivation-layer formation or precipitation under specific pH and Eh ranges, which could prevent dissolution and result in the blockage of access paths. Optimal pH and Eh control may be difficult to achieve in practice, because of fluid injection and recovery conditions at the surface, and the effect of residence time on the fluid pH and the initial contact with the formation. Precipitates that were identified in the initial experiments provide an indication of the possible concerns of the nature of these systems at high temperature. To better understand the real efficiency of copper recovery, these two systems require further experimentation under lower-temperature conditions and with higher acidities to confirm whether they perform better.

The glycine system is marketed as an environmentally friendly lixiviant alternative with a proven effectivity for heap leaching (Tanda, 2017). The conditions used on this test work and the oxidant type were sub-optimal and the copper recovery was affected. Hydrogen peroxide is not believed to be the most effective oxidant for glycine, however, alkaline systems are a good alternative to acid systems to avoid gangue

reactions (glycine did not react with pyrite in the sample). A different oxidant in the glycine system should provide better results. For example, the continuous injection of oxygen may act as a suitable oxidant for the system, as evidenced in studies that with other oxidants (Nicol, 2018; Oraby and Eksteen, 2014). Even though the selectivity of glycine is a favourable factor for heap-leaching operations, it could be deleterious for operations where the accessibility is low. The lack of natural fractures may limit the flow and subsequent reactions in this system. This implies a necessary introduction of new fractures in the mineral.

The greatest hindrance for some of the studied systems is the requirement for temperatures above 90°C and extended reaction times to achieve at least 40% recovery in the fairly impure chalcopyrite cube. Required copper oxidant concentrations were smaller than in any other system, and cupric- and ferric-ion regeneration may be possible.

Some of the results from extensive research into ferric-ion heap leaching under low to moderate temperatures have been corroborated in our initial experiments at high temperatures. The good results observed with ferric oxidant systems above 100°C and the temperature dependence postulate that this system is the best option for medium- to high-temperature ore processing. Other operational concerns may interfere with the lixiviant applicability because of the aggressive behaviour of the chloride environment and sulfur formation in the sulfate system.

In the ferric chloride/hydrochloric acid system, sample dissolution occurred in less than 5 days, including iron gangue dissolution. The final pH of the sample did not show a substantial variation in free acidity, which may imply a higher reagent consumption. In an ISR operation, this lack of selectivity could represent a kinetic advantage if the accessibility of the sample is low, but also a major operational problem because of possible subsidence from mineral dissolution, which may produce mechanical problems with casing, tubing or packers inside the well, and the contamination of surrounding water by solution leakage. The aggressive nature of this solution and its incompatibility with common materials, such as stainless steels, could require exotic high-cost materials with a shorter lifespan. The same concerns apply to copper-chloride solutions.

A possible application of copper as an oxidant may include its combination with other oxidants. In an ISR scenario, the injection of mixed oxidants in stages with "soaking" times would facilitate the interaction of injected oxidant and recovered copper as part of the leaching system. It is important to understand the required reaction times of the systems with the intention of extrapolating these data to operational times. The reactions of chalcopyrite even above 170°C are slow. Alternative systems were of similar success to these common of systems in industry, which indicates that experimentation should proceed with new mixed systems or staged treatment with different solutions.

Almost all systems generated a “passivation layer”, but the nature of these layers varied between systems. Copper-enriched sulfides are more readily leached, sometimes without oxidant addition. The continuous and large-scale conversion of chalcopyrite in an operation may be cheaper with less environmental damage with the use of environmentally friendly lixiviants.

A.5. Conclusions

Results from screening tests on cubic samples with several oxidants under the same conditions indicated that the alternative systems tested do not offer an improved leaching rate compared with more traditional systems. The stability of alternative oxidants, such as potassium dichromate and glycine, indicated a major probability of product formation that would affect fluid access to the mineral surface.

Chalcopyrite dissolution appeared to include the replacement of initial mineral by secondary copper-enrichment phases. This mineral form on the surface did not appear to hinder mineral dissolution; chalcopyrite leaching continued and formed product layers of iron-containing oxides on the sample surface. The type of copper sulfide that formed was related to the concentration and nature of the solution used.

Copper recovery was enhanced for systems that included chloride ions. The effect on texture of the product layer improved the continuous flow and the sample accessibility, as was evident for the cupric- and ferric-chloride oxidants.

Each system has a window of optimal operating parameters for optimal recovery, and the same conditions do not affect all systems equally. The selection of a suitable

leaching system must be based on the specific characteristics of each deposit (depth, mineralogy, temperature, pressure, and surface facilities).

Acknowledgments

MRIWA (Project M488), BASF, Curtin University and CSIRO are gratefully acknowledged for funding this work. Jian Li is thanked for reviewing a draft of this manuscript.

References

Acero, P., Cama, J. and Ayora, C., 2007. Kinetics of chalcopyrite dissolution at pH 3. European Journal of Mineralogy, 19(2): 173–182.

Antonijević, M.M., Janković, Z. and Dimitrijević, M., 1994. Investigation of the kinetics of chalcopyrite oxidation by potassium dichromate. Hydrometallurgy, 35(2): 187–201.

Aydogan, S., Ucar, G. and Canbazoglu, M., 2006. Dissolution kinetics of chalcopyrite in acidic potassium dichromate solution. Hydrometallurgy, 81(1): 45–51.

Beckstead, L. and Miller, J., 1977. Ammonia, oxidation leaching of chalcopyrite — reaction kinetics. Metallurgical Transactions B, 8(1): 19–29.

Bonan, M.D., J. M. Renon, H. Baratin, F., 1981. Chalcopyrite leaching by $CuCl_2$ in strong NaCI solutions. Metallurgical Transactions B, 12(2): 269–274.

Cerda, C., Taboada, M., Jamett, N., Ghorbani, Y. and C. Hernández, P., 2017. Effect of Pretreatment on Leaching Primary Copper Sulfide in Acid-Chloride Media. Minerals 8. pp. 3–14.

Córdoba, E.M., Muñoz, J.A., Blázquez, M.L., González, F. and Ballester, A., 2008. Leaching of chalcopyrite with ferric ion. Part I: General aspects. Hydrometallurgy, 93(3): 81–87.

Dreisinger, D., 2006. Copper leaching from primary sulfides: Options for biological and chemical extraction of copper. Hydrometallurgy, 83(1): 10–20.

Dutrizac, J.E., 1981. The dissolution of chalcopyrite in ferric sulfate and ferric chloride media. Metallurgical Transactions B, 12(2): 371–378.

Eksteen, J.J.O., E. A. Tanda, B. C. , 2017. A conceptual process for copper extraction from chalcopyrite in alkaline glycinate solutions. Minerals Engineering, 108: 53–66.

Ferron, C., Dymov, I., McKay-Davison, N. and Butcher, D., 2000. Kinetics and mechanisms of high temperature pressure leaching of Guelb Moghrein chalcopyrite concentrate. pp. 579–595.

Hirato, T., Kinoshita, M., Awakura, Y. and Majima, H., 1986. The leaching of chalcopyrite with ferric chloride. Metallurgical Transactions B, 17(1): 19–28.

Hirato, T., Majima, H. and Awakura, Y., 1987. The leaching of chalcopyrite with ferric sulfate. Metallurgical Transactions B, 18(3): 489–496.

McDonald, R.G. and Muir, D.M., 2007. Pressure oxidation leaching of chalcopyrite. Part I. Comparison of high and low temperature reaction kinetics and products. Hydrometallurgy, 86(3): 191–205.

Munoz, P.B., Miller, J.D. and Wadsworth, M.E., 1979. Reaction mechanism for the acid ferric sulfate leaching of chalcopyrite. Metallurgical Transactions B, 10(2): 149–158.

Nicol, M.J., 2018. A comparative assessment of the application of ammonium chloride and glycine as lixiviants in the heap leaching of chalcopyritic ores. Hydrometallurgy, 175: 285–291.

Oraby, E.A. and Eksteen, J.J., 2014. The selective leaching of copper from a gold–copper concentrate in glycine solutions. Hydrometallurgy, 150: 14–19.

Oraby, E.A. and Eksteen, J.J., 2015. The leaching of gold, silver and their alloys in alkaline glycine– peroxide solutions and their adsorption on carbon. Hydrometallurgy, 152: 199–203.

Ruiz, M.C.M., K. S. Padilla, R., 2011. Chalcopyrite leaching in sulfate–chloride media at ambient pressure. Hydrometallurgy, 109(1–2): 37–42.

Schlesinger, M.E., King, M.J., Sole, K.C. and Davenport, W.G., 2011. Extractive Metallurgy of Copper. Elsevier science.

Seredkin, M., Zabolotsky, A. and Jeffress, G., 2016. In situ recovery, an alternative to conventional methods of mining: Exploration, resource estimation, environmental issues, project evaluation and economics. Ore Geology Reviews, 79: 500–514.

Skrobian, M., Havlik, T. and Ukasik, M., 2005. Effect of NaCl concentration and particle size on chalcopyrite leaching in cupric chloride solution. Hydrometallurgy, 77(1): 109–114.

Tanda, B.C., 2017. Glycine as a lixiviant for the leaching of low grade copper-gold ores, Curtin university, PhD dissertation, Perth, Australia.

Watling, H.R., 2013. Chalcopyrite hydrometallurgy at atmospheric pressure: 1. Review of acidic sulfate, sulfate–chloride and sulfate–nitrate process options. Hydrometallurgy, 140: 163–180.

Watling, H.R., 2014. Chalcopyrite hydrometallurgy at atmospheric pressure: 2. Review of acidic chloride process options. Hydrometallurgy, 146: 96–110.

Yu, P., Hansen, C. and Wadsworth, M., 1973. A kinetic study of the leaching of chalcopyrite at elevated temperatures. Metallurgical Transactions, 4(9): 2137-2144.

Every reasonable effort has been made to acknowledge the owners of copyright material. I would be pleased to hear from any copyright owner who has been omitted or incorrectly acknowledged.

Appendix B. Staged leaching of bornite with acidic solutions at moderate temperature in an in-situ recovery environment

Sequential-staged leaching with different lixiviant and oxidant systems may be viable in an in-situ recovery (ISR) environment and may provide an opportunity for the leaching of refractory minerals if these can be converted into more readily leachable secondary products. An understanding of the leaching behavior of secondary products when in contact with a different lixiviant system from that used in the first leaching stage may provide valuable information for ISR operations. Bornite (Cu_5FeS_4) has been found to be replaced by secondary sulfides, such as covellite and chalcocite, when leached with acidic solutions with restricted oxidant. The secondary sulfide phases may be easier to oxidize or passivate the surface and reduce the reaction rate. The leaching of resulting products of chalcopyrite, such as the dissolution of bornite that formed from the sulfurisation of a chalcopyrite concentrate in the presence of gaseous sulfur has been addressed previously, but, to the authors knowledge, a sequential analysis of refractory coarse copper sulfide samples, such as bornite, which have been leached previously in acid solutions with a second-stage dissolution in oxidant/lixiviant solutions has not been undertaken. In ISR, mineral contact with acid may result in viable oxidant solutions for copper sulfide leaching; for example, after acid dissolution, iron oxides and hydroxides may provide a source of iron(III) oxidant.

A synthetic goethite sample was dissolved in methanesulfonic acid to obtain a ferric methanesulfonate lixiviant for bornite leaching. A natural sample of bornite with quartz was cut into coarse pieces and leached sequentially with two different solutions (hydrochloric acid followed by ferric methanesulfonate solution). The first stage was performed in a closed incubator for a maximum of 20 days and the second stage was conducted over two days in a Parr reactor at 110°C. Leaches were conducted with minimum oxygen present to simulate an ISR environment.

This paper presents results on the chemical composition of the solutions after each stage, and a cross-sectional analysis of the samples post-leaching, as determined by X-ray diffraction, scanning electron microscopy and quantitative evaluation of materials by scanning electron microscopy (QEMSCAN). Information is provided on the

dissolution efficiency, product identification and an analysis of final textures. This study provides guidance on the potential for application of sequential staged leaching to ISR and for the treatment of refractory copper sulfides in an ISR environment.

B.1. Introduction

Global reserves of copper ores have declined in recent years; average copper grades have fallen, and the global demand has increased. In 2016, the average copper grade in mines was 0.62% because of a reduction in the number of high-grade mines. In recent years, 10% of primary copper production has been by hydrometallurgical processing (Calvo et al., 2016). Further reductions in the number of shallow reserves are expected in future, which may make heap leach processing more difficult and, in many cases, uneconomic. In-situ recovery (ISR) represents an alternative for copper recovery in challenging mine sites (low–grade deep ore bodies, and residual mines). Even though ISR is well known for uranium processing and has been applied in pilot programs for treating copper oxide zones (Seredkin et al., 2016), the processing of refractory copper sulfides, such as chalcopyrite, bornite and enargite, by ISR presents a challenge that requires extensive research.

The slow dissolution and low total recovery of copper sulfides suggests that an extensive leaching period could be required in an ISR application. Extensive reaction times may incur additional costs, with higher oxidant and acid consumptions and the possible passivation by product layers because of fluid saturation and pH changes. Iron oxides and (oxy) hydroxides, such as goethite, may be present in supergene zones in copper deposits (Cook, 1988) or these may be a product of shallow weathering (Özdemir and Dunlop, 2000) and may constitute a source of iron for use as an oxidant in leaching. In hydrometallurgical processing, iron-containing minerals are often considered to be gangue minerals, and an alternative use of these may represent a cost saving in ISR operations. Ferric ions have been proven to be a viable oxidant for bornite leaching (Dutrizac et al., 1970; Pesic and Olson, 1983). Recently, methanesulfonic acid has attracted attention as a viable lixiviant for hydrometallurgical processing because of its high solubility of heavy metals and less corrosive character compared with other strong acids (Feng et al., 2015a; Feng et al.,

2015b; Gernon et al., 1999; Hidalgo et al., 2018; Wu et al., 2014a; Wu et al., 2014b). Therefore, the use of a solution with ferric ions from a mineral source, in methanesulfonic acid, may be a valuable alternative in economic and environmental terms for ISR operations. Sulfonate anions complex strongly with metal ions with the potential to form highly polymeric materials (Gernon, 1999; Haynes et al., 1981). Goethite was selected in this test work because it is a major component of terrestrial soils and it is soluble in acid according to Equation 1. This met one of the objectives of this work which was to prepare an oxidant in an acidic medium from the interaction between a natural source of iron and a strong organic acid for potential use in an ISR application.

$$\alpha FeOOH + 3CH_3SO_3H \rightarrow Fe(CH_3SO_3)_3 + 2H_2O \quad (1)$$

Bornite and chalcopyrite are the most abundant copper minerals and often co-exist naturally. Bornite and chalcopyrite dissolution in acid medium follow similar steps with bornite leaching more rapidly than chalcopyrite but being able to form the same product layers. The electrochemical dissolution of chalcopyrite in acid has been found to follow a consecutive reduction–oxidation process with bornite as an intermediate before the final formation of covellite (Zhao et al., 2015). The secondary formation of bornite as a product of chalcopyrite has been studied in hydrothermal solutions and from sulfurisation (Veloso et al., 2016; Zhao et al., 2014) and it has been found that the extent of copper dissolution from the resultant bornite is considerably higher than direct dissolution of the original chalcopyrite. Veloso et al. (2016) also found that the resultant bornite has comparable behaviour to natural bornite. Bornite transformation to covellite in acidic solutions has been observed during bornite leaching (Hidalgo et al., 2019; Muszer et al., 2013; Price and Chilton, 1980; Price and Chilton, 1981). The transformation may occur because of the direct oxidation of bornite (Equations 2 to 3). The dissolution of the resulting covellite has been noted as a fundamental aspect of overall bornite dissolution (Zhao et al., 2015).

$$Cu_5FeS_4 \rightarrow Cu_{5-x}FeS_4 + xCu^{2+} + 2xe^- \quad (2)$$

$$Cu_{5-x}FeS_4 + 6H^+ \rightarrow CuS + (4-x)Cu^{2+} + 3H_2S + Fe^{3+} + (5-2x)e^- \quad (3)$$

Pre-treatment is a technique that has been used to optimize the recovery of metals from heap leaching operations. Approaches have been proposed for curing and agglomeration via acid addition (Lu et al., 2017) and, more recently, an acidic sodium chloride pre-treatment has been tested to enhance the copper dissolution of mixed fine particles and concentrates of primary copper minerals (Bahamonde et al., 2017; Cerda et al., 2017). The application of a pre-treatment in ISR operations requires an improved understanding of the coarse sample response to the fluid and to the product layers that are formed. The aim of this research was to analyse resultant solution compositions and solid residues after a two-stage leaching treatment of coarse bornite particles process, namely, hydrochloric acid pre-treatment followed by contact with an acidified iron(III) solution at medium temperature.

Initial samples and analytical techniques

Natural samples of bornite from a private collection were cut into coarse pieces of ~64 mm^3 volume. A portion of the initial sample was milled for inductively coupled plasma–optical emission spectroscopy (ICP–OES) and X-ray fluorescence (XRF) analysis. Blank samples were mounted in resin and polished for X-ray diffraction (XRD) and scanning electron microscopy (SEM) measurements for initial sample characterisation. The initial energy-dispersive X-ray spectroscopy (EDS) analysis was used as a baseline for secondary-product identification. After leaching, the samples were mounted on stubs and examined by SEM to study the unpolished surfaces. Thereafter, polished epoxy mounts were prepared for XRD, SEM-EDS and QEMSCAN analysis. The instruments used included a PANalytical Empyrean X-ray diffractometer, JEOL-JSM-7001 field emission SEM-EDS and E430 Pro Quantitative Evaluation of Minerals by Scanning Electron Microscopy (QEMSCAN), respectively.

Fluid samples were filtered and analysed for free acidity by titration with 0.05 M sodium hydroxide after Ethylenediaminetetraacetic acid (EDTA) complexation and using a 904 Titrando. The concentration of iron(II) in solution was determined by titration with a 0.001 M potassium dichromate solution. Total iron, copper and sulfur concentrations were determined by ICP–OES analysis.

Leaching tests

Synthetic light-yellow goethite powder (68.9% Fe) was used as the iron source to prepare the oxidant solution. To obtain a solution of 1 mol L^{-1} ferric methanesulfonate, stoichiometric amounts of goethite were stirred at 150 to 200 rpm with methanesulfonic acid (100%) in a 300-mL titanium vessel at 140°C for up to three days. The solution was filtered before use and the total ferric iron concentration was determined by atomic absorption spectroscopy (AAS). The ferric methanesulfonate solution was prepared batchwise with a cumulative mass of 10 g of goethite and 100 mL of concentrated methanesulfonic acid. The ferric methanesulfonate solution that was used in the test work was obtained by dilution of the synthesised concentrated solution to a 1 mol L^{-1} ferric iron concentration.

Two-stage dissolution experiments were conducted with coarse cuboid samples of bornite (Cu_5FeS_4). In stage one, two sulfide cubes were placed in separate 250-mL Nalgene bottles with 30 mL of 0.1 mol L^{-1} hydrochloric acid solution with an initial pH of 0.83 (vs. S. H. E) and a solution potential (Eh) of 301.3 mV (vs. Ag/AgCl). The head spaces were flushed with high-purity nitrogen, sealed and placed into a closed orbital shaker incubator at 70°C and 100 rpm for 7 or 20 days. Replicate tests were conducted. A small amount of hydrogen sulfide gas was produced during the experiment (as evidenced by the odour). This gas was vented by opening the bottle at 24 h intervals and the head space was flushed with nitrogen each time to restrict oxygen ingress into the solution. After the selected time, the fluid was filtered for analysis and the solid sample was rinsed three times with deionised water and dried in a standard oven at 30°C. The 1 mol L^{-1} ferric methanesulfonate oxidant solution that was used in the experiments had an initial pH of 0.51 and an Eh of 530 mV (vs. Ag/AgCl).

The second stage of dissolution involved the leaching of the previously leached bornite pieces and was compared to a control piece that had not been subjected to prior treatment. The samples were placed into a 300-mL titanium Parr reactor, covered with 70 mL of ferric methanesulfonate solution and closed. Nitrogen was injected into the system at 0.2 MPa pressure to facilitate fluid sampling. The temperature was set to 110°C to represent potential ISR conditions for deep ore bodies and to accelerate the reaction. The reactor contents were stirred at 100–150 rpm. Final pH and Eh values

were measured after each experiment. Samples (2–4 mL) were taken at intervals until the final fluid was recovered after either one or two days. To avoid contamination from fluid in the sampling tube, an initial sample was taken (to flush the sampling port) and discarded. A second sample was retained for analysis. Once the final leach time had been reached, the sample was rinsed with deionised water and dried for further analysis.

B.2. Results

Initial Sample

XRD analysis of the unreacted material showed bornite as the major phase with traces of quartz and hematite. No other copper minerals were identified by XRD. Digenite ($Cu_{1.8}S$) was identified by SEM and QEMSCAN analysis in some samples. A bulk sample composition of 65% Cu, 16% Fe and 19% S was determined by ICP–OES and XRF analysis. The composition determined by SEM–EDS was 60.9% Cu, 11.5% Fe and 27.6%S for the bornite and 78.5% Cu and 21.8% S for the digenite phase. The particle surface showed no evidence of oxidation rims or sulfur products. The surface texture showed a minimum amount of natural fractures and no marked porosity (Fig. B-1). A sample cross-section showed a clean surface with veins of digenite but no evidence for sulfur formation, reaction rims or covellite being present.

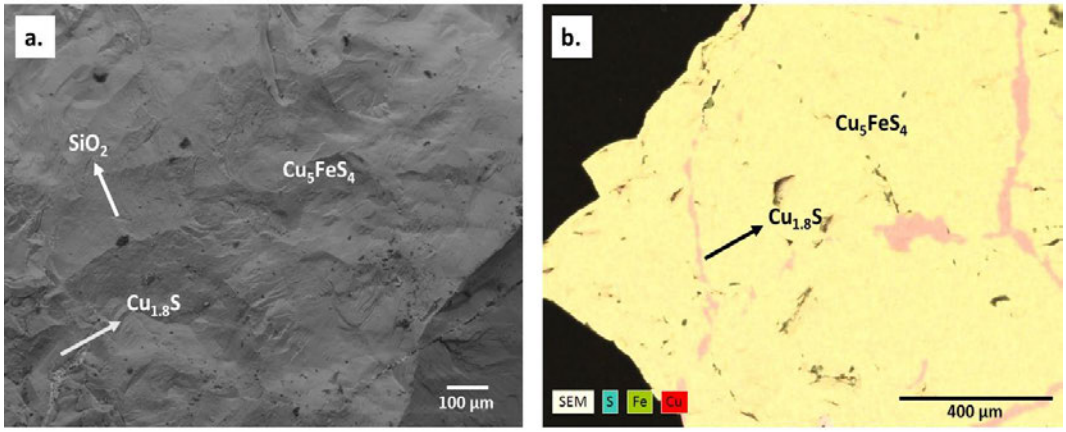

Fig. B-1. Scanning electron photomicrographs (SEM-BSE) of initial coarse sample, **a.** initial surface texture without major cracks or layers that coat the sample, **b.** elemental maps showing

copper, iron and sulfur distributions, yellow is the resulting bornite phase and red is the secondary sulfide digenite.

Goethite Dissolution

The resultant concentrated ferric methanesulfonate solution was dark purple and a small residual amount of black solids was recovered after filtration. XRD analysis of the resulting solids indicated that the solids were composed of hematite. The final iron concentration in solution was 1 mol L^{-1} and the acid concentration was 2.87 mol L^{-1}**.**

Acid Pre-Treatment

Samples with a similar cubic size and mass (between 0.17 and 0.20 g) were selected for acid pre-treatment with hydrochloric acid. The pre-treatment solution and contact time were selected based on previous experiments that indicated the formation of covellite after hydrochloric acid leaching in the absence of an oxidant (Hidalgo et al., 2019). The copper dissolution was slow; 6% and 15% copper extractions were achieved after 7 and 20 days, respectively. Iron was dissolved preferentially with more than 40% dissolution after 20 days. Final solids showed changes in composition and surface texture. After seven days of pre-treatment, the original bornite colour was replaced by a bright blue colour, and this colour darkened after 20 days. Samples showed pronounced cracks distributed over the surface and an increased number of surface cracks after 20 days of pre-treatment (Fig. B-2a). After seven days, an iron-depleted surface layer with a Cu/S ratio of 2.17 was formed (average concentrations of 65.9% Cu and 28.5% S). Iron was still present in regions of the sample, with average concentrations below 5%.

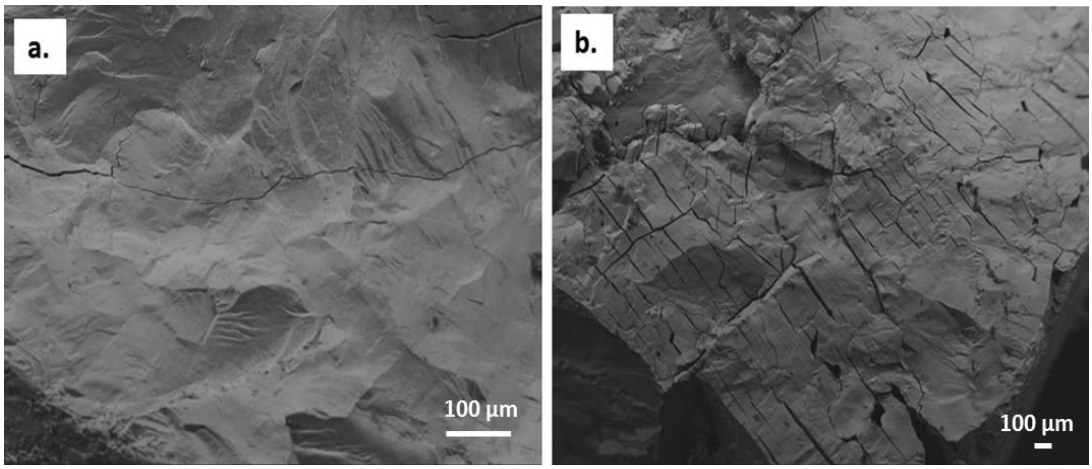

Fig. B-2. Scanning electron photomicrographs (SEM-BSE) of the sample surface after 0.1 M hydrochloric acid pre-treatment, **a.** surface texture after 7 days of treatment, **b.** surface texture after 20 days showing major cracks.

After 20 days of acid treatment, a cross–section of the sample showed a rim of covellite covering the perimeter and internal features (such as fractures) that came into contact with the fluid (Fig. B-3); other images not shown here confirm that the covellite was porous. The original bornite was almost entirely transformed into a copper-deficient layer (1.9 Cu/S ratio) with a lower copper average of 51% Cu. Sulfur formation occurred in the external fractures close to the covellite rim of the sample.

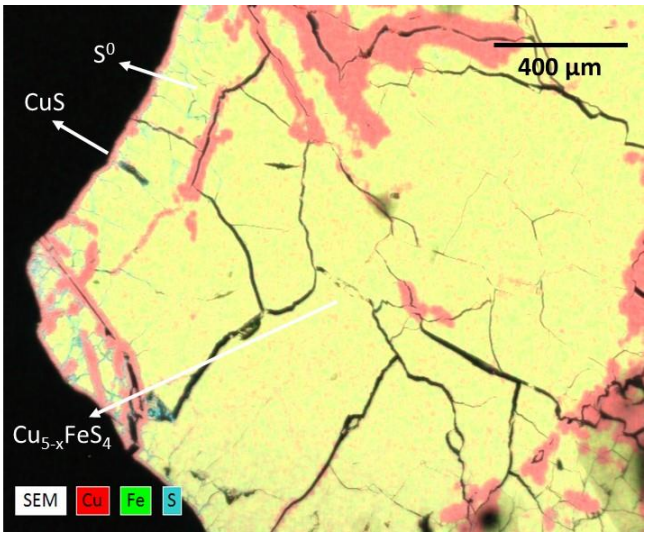

Fig. B-3. Scanning electron photomicrographs (SEM) composition map of the sample cross-section after 20 days of pre-treatment with 0.1 mol L^{-1} hydrochloric acid. Red zones represent covellite replacement, yellow zone copper-deficient bornite and blue zones sulfur formation.

Bornite Leaching by Ferric Methanesulfonate

Fluid Composition

Replicate untreated and acid pre-treated were leached, one of each for one and two days, with fluid sampling to obtain dissolution curves for comparison. For untreated samples, copper recovery was calculated relative to the initial sample copper concentration (ICP–OES determined); for treated samples the copper dissolved by pre-treatment was subtracted from that present in the initial sample. The copper recovery data are shown in Fig. B-4. Untreated samples showed between 74% copper dissolution after 48 h of leaching. The copper dissolution from samples that were pre-leached with hydrochloric acid for 7 days was 81%, with the first 50% of copper dissolution being obtained after 4 h, which was significantly more rapid than for the untreated sample. After 5 h, the dissolution rate decreased and started to match that of the untreated samples. Because of mineralogical differences between samples, a small difference in copper dissolution between replicates was expected. The difference in dissolution during the first 5 h of leaching between the untreated and pre-treated samples (Fig. B-4a) was found to be statistically significant (t-test, $p = 0.05$). The sample that had been pre-leached for 20 days showed an increase in copper dissolution over the shorter leaching time and reached an 87% final copper dissolution with a faster dissolution during the first six hours of leaching. Fig. B-4b compares the copper dissolution averages for the untreated and pre-treated samples. The standard deviation between replicates was below 3%.

The pre-treated samples showed a lower acid consumption during the second stage than the untreated samples. The pH values increased by 0.2 units during the reaction and the Eh values decreased from 530 mV to 493 mV (vs. Ag/AgCl). The total iron concentration was obtained by ICP–OES analysis, the ferrous concentration was determined by potassium dichromate titration, and the ferric consumption was determined by using the difference between these values. Similar ferric consumptions resulted for the untreated sample and pre-treated samples although the ferric consumption by the untreated sample was double that of the pre-treated sample during the initial 6 h of leaching. The final ferric consumption was between 8.7% and 11.5% for all samples after 48 h.

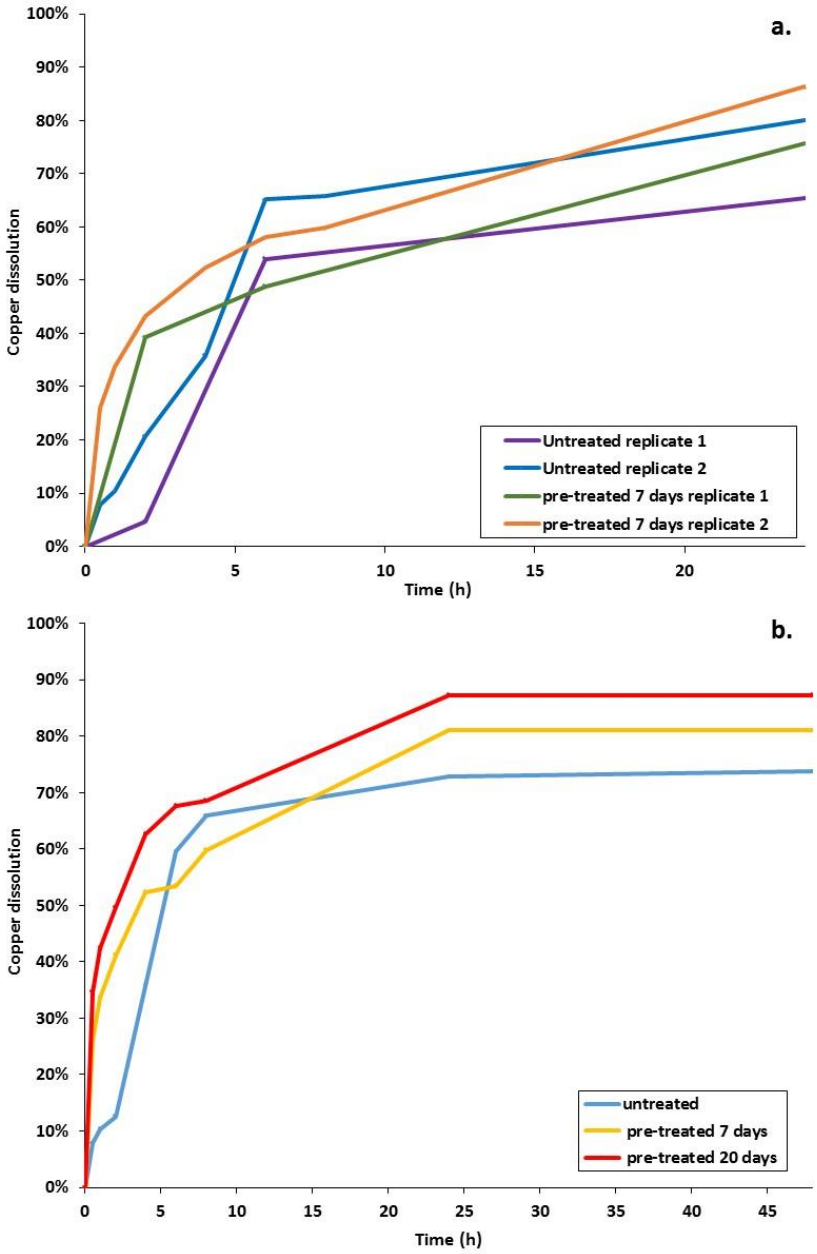

Fig. B-4. Replicates of comparative copper extractions for 1 mol L^{-1} ferric methanesulfonate leaching at 110°C of samples after pre-treatment versus untreated samples. **a.** Untreated sample compared with samples that had been pre-leached for 7 days, **b.** averages for the untreated and treated sample replicates up to 24 h; the extraction after 48 h (single sample) is given to indicate that leaching has plateaued.

Leach residue characterisation

Figure B-4 shows the resultant surface textures of the untreated and pre-leached samples, as observed by SEM and before cross-sectioning.

Untreated Sample

The untreated samples had the appearance of a dark-grey, rough solid that was brittle and broke easily. Surface analysis showed partial covering of the remaining bornite and minor parts of covellite product layers by sulfur. After 24 h, the sample had major fractures of the bornite and showed initial sulfur production. After 48 h, the sample consisted mainly of sulfur with some residual solids having chemistries that corresponded with high sulfur covellite (62.7% Cu with 37.3% S) and a $Cu_{5-x}FeS_4$ (average concentrations of 46.3%Cu, 14.7%Fe and 37.6%S). Digenite veins of the original sample were not present in the final solids, although covellite was found in the centre of the residue in the form of veins.

Seven-Day Pre-Treated Sample

The 7-day acid-treated sample presented similar features to the untreated sample; sulfur covered most of the solid with sections of undissolved copper enrichment in the form of covellite. After 24 h leaching, sulfur was present as only a small portion of solids with covellite existing at the perimeter between sulfur and the $Cu_{5-x}FeS_4$ intermediate. After 48 h of leaching the sample was dark grey and broke into pieces. SEM and QEMSCAN examination showed the main phase was sulfur and pieces of the remaining bornite with a low copper content and high concentrations of sulfur (47.9% Cu, 14.0% Fe and 37.9% S). Covellite was present in the sample as a rim that surrounded the bornite solids and replaced pieces that were enclosed by sulfur. After QEMSCAN analysis, a higher mass% of covellite was present in the final pre-treated sample than in the untreated sample (Fig. B-5).

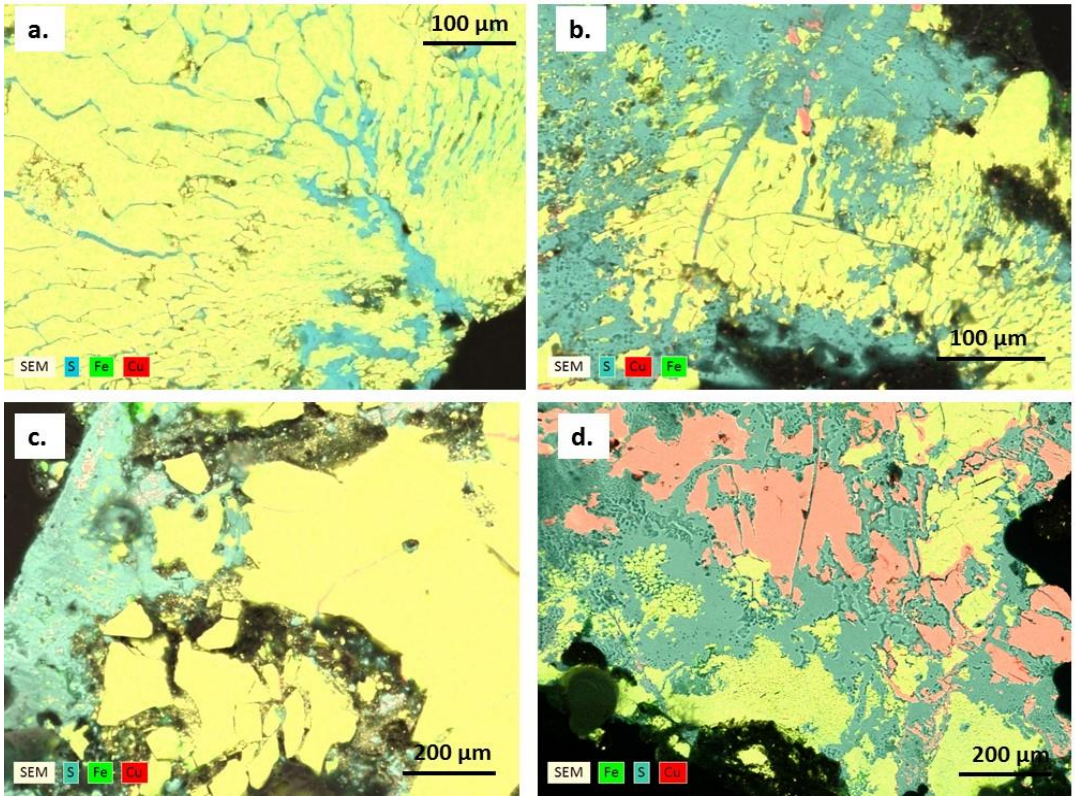

Fig. B-5. SEM cross-section elemental maps of bornite coarse samples after leaching with 1 mol L^{-1} ferric methanesulfonate solution at 110°C for two days. The red areas represent copper without iron in the product, yellow areas represent copper and iron and blue areas represent sulfur. **a.** untreated sample after 1 day of leaching showing fracturing and sulfur inclusions in fractures, no zones of copper enrichment, **b.** untreated sample after 2 days of leaching showing major replacement of bornite ($Cu_{5-x}FeS_4$) by sulfur with some isolated zones of covellite, **c.** sample pre-treated for 7 days after 1 day of leaching showing a thick sulfur rim with small areas of copper enrichment (covellite) next to copper-deficient bornite, **d.** sample pre-treated for 7 days after 2 days of leaching showing main phase of sulfur with pieces of bornite ($Cu_{5-x}FeS_4$) and covellite, some pieces of bornite showed a rim of covellite.

Twenty-Day Pre-Treated Sample

The sample surface and fractures were covered or filled with sulfur, respectively, after 20 days of pre-treatment, with minor amounts of covellite present at the perimeter (Fig. B-6). The sample that had been pre-treated for 20 days was almost entirely converted to sulfur and the remaining pieces of bornite showed copper dissolution and a very high concentration of sulfur because of the major transformation (average concentrations of 48.9% S, 12.8% Fe and 38.2%Cu).

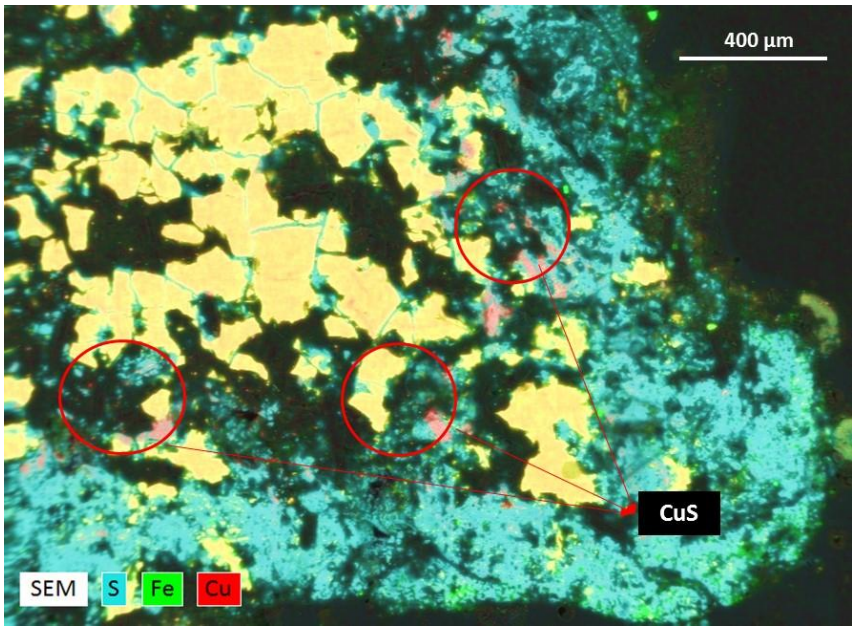

Fig. B-6. SEM cross-section elemental maps of 20 days acid pre-treated bornite coarse samples after leaching with 1 mol L^{-1} ferric methanesulfonate solution at 110°C for one day. Iron concentrations remained homogenous in the resulting solid residue, with sulfur filling the cracks between bornite pieces and covering the perimeter of the sample. Copper concentration occurred as covellite encased by sulfur at the outer rim.

B.3. Discussion

Commercial alternatives exist for the pre-treatment of copper sulfides for heap leaching applications, These include the CLEAR process, which involves a combination of chloride pre-treatment at 105ºC followed by pressure leaching at 150ºC, and Cuprochlor, which involves the leaching of chalcocite by the initial addition of calcium chloride as an agglomerant, and the addition of Cl^- and Cu^{2+} for subsequent leaching (Herreros et al., 2005). Two previous studies presented a low-temperature (20ºC to 50ºC) and fine-grained (below 150 µm) process for primary copper sulfides by pre-treatment with sodium chloride and sulfuric acid followed by leaching using Cu^{2+} in acidic solutions, and found an enhanced copper dissolution (Bahamonde et al., 2017; Cerda et al., 2017). The aim of this study was to trial pre-treatment conditions that may be applicable in an ISR environment, where the accessibility is limited. Therefore, a study of the resultant mineralogy from the fluid–rock interactions was undertaken, as this has not previously been considered in detail. Our study used chloride addition via hydrochloric acid without oxygen addition in the

first stage, to simulate the low oxygen solubility at higher temperatures in an ISR environment (Bartlett, 1998), followed by leaching with ferric ions as an oxidant.

It has been proposed that copper–enrichment layers passivate the surface of primary sulfides (Warren et al., 1992). Nevertheless, it is also well known that copper enrichment layers, such as covellite and chalcocite, are readily oxidised compared with chalcopyrite and bornite and that lower oxidation potentials are needed to achieve significant copper dissolution (Li et al., 2013; Warren et al., 1992). Figure B-7 shows a schematic of the solid residues found after the staged leaching process had been applied. The results from our experiments support the theory of the replacement of the original mineral by a more leachable rim phase.

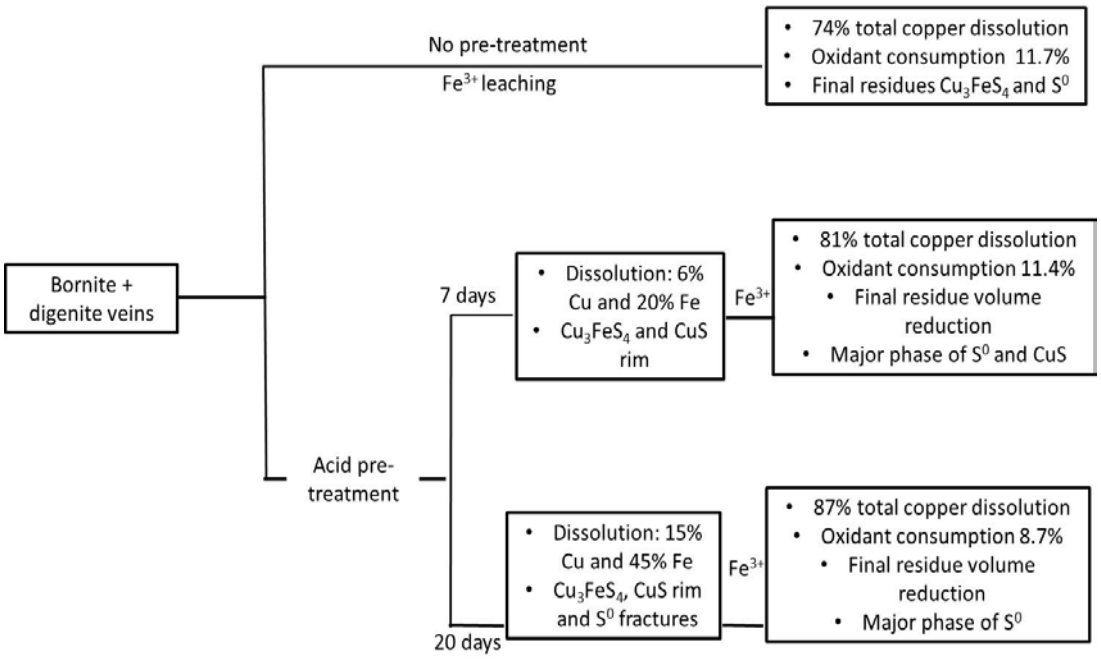

Fig. B-7. Schematic of pre-treatment outcomes compared to untreated samples.

Untreated Samples

Copper dissolution in the untreated samples reached more than 70% in all samples. The final products corresponded to those in the pre-treated samples. $Cu_{5-x}FeS_4$ was present in pieces that were surrounded by sulfur, as was evidenced previously in the ferric sulfate leaching of bornite (Dutrizac et al., 1985; Dutrizac et al., 1970; Ugarte-

Alverez, 1971; Ugarte and Burkin, 1975) Covellite was the major phase in the final residue and was found in sections of the sample and not as a rim of the original bornite.

The original sample was composed mainly of bornite, but pieces of the sample presented digenite veins. The digenite that was in contact with the lixiviant was converted to covellite and dissolved copper (Thomas et al., 1967), which may explain why the pre-treated and untreated samples presented the same final products. Covellite has also been identified in sulfate solutions in previous studies (Dutrizac et al., 1985) because of the interaction of Cu_3FeS_4 and copper in solution (Equation 4). It is possible too, that the presence of this phase enhanced the expected dissolution by addition of internal zones of readily leachable covellite.

$$Cu_3FeS_4 + Cu^{2+} \rightarrow 4CuS + Fe^{2+} \quad (4)$$

Pre-Treated Samples

After pre-treatment, a replacement of bornite by covellite occurred under all conditions. Such behaviour has been found previously for the contact of bornite with acid with and without oxygen (Hidalgo et al., 2019; Muszer et al., 2013; Pesic and Olson, 1984; Price and Chilton, 1981). SEM analysis showed a cracked sample surface, presumably because of the volume change during the reaction, and the resulting covellite showed a porous texture, which is presumed to have allowed the fluid to continue to contact the solid surface. Rapid iron dissolution resulted during the first days of the pre-treatment reaction followed by a minor dissolution of copper after three days. The copper in solution increased the dissolution of bornite and enhanced the formation of secondary products, such as copper-deficient bornite (Cu_3FeS_4) and more covellite, as explained by Pesic and Olson (1984). Extended pre-treatment times resulted in an increase in sulfur in the sample, possibly because of the copper in the chloride solution that reacted with the covellite rim and the internal bornite (Lundström et al., 2016).

Samples that were pre-treated showed better copper dissolution than the untreated samples. Pre-treated samples showed a noticeably higher dissolution during the first five hours of leaching. Five hours may be the time required to dissolve the covellite rim that formed and start the reaction with the internal bornite. Covellite dissolution is

faster and was found to leach preferentially in the presence of primary sulfides (Peters and Loewen, 1973; Petersen and Dixon, 2006). Equation 5 presents the expected dissolution of the newly formed covellite by ferric ions, with cupric ions and elemental sulfur as the products. The final dissolution was slightly higher for the pre-treated samples, which may correspond to the transformation to covellite (a higher mass % of covellite was found in the treated samples). After this new phase dissolved, an initial rapid dissolution of copper occurred to form a Cu_3FeS_4-type mineral that continued to dissolve and form sulfur (Dutrizac et al., 1985; Dutrizac et al., 1970; Pesic and Olson, 1983; Ugarte-Alverez, 1971), as was identified in all samples analysed.

$$5CuS + 10Fe^{3+} \rightarrow 5Cu^{2+} + 10Fe^{2+} + S^0 \quad (5)$$

Applicability to ISR

The results of this study highlight the applicability of acid pre-treatment for the in-situ leaching of primary copper sulfides. Copper enrichment, here found to occur via the formation of covellite, did not lead to passivation behaviour, and leaching was accelerated by the transformation of the initial sample. This has also been confirmed in experiments with fine-grained particles (Bahamonde et al., 2017; P. Cerda et al., 2017). Primary sulfide transformations are a key factor in the ISR of refractory sulfides. Transformations can occur even in the presence of minimum oxidant addition, and the resulting phases are easier to leach and are porous, which may improve the accessibility within the ore. For the ISR processing of a high-grade ore with problematic copper sources, such as chalcopyrite and bornite, pre-treatment is therefore a viable possibility. An extended treatment time is required, but, because of the low operational cost, it may be possible to perform a long-term pre-treatment and convert major parts of the ore into secondary phases followed by a short-term leaching stage enhanced by secondary phase formation, as demonstrated in this study. However, conversion alone by acid treatment (with the low accompanying levels of oxygen) may generate toxic gas (H_2S) at the subsurface, which is inconvenient from an operational perspective (e.g., pitting in tubing, overpressures) and unwelcome both environmentally and, more so, as a potential hazard to living organisms (i.e., leaks). Based on the results, the pre-treatment acceleration of leaching to enhance dissolution was used to transform the original sample to a more leachable form, which may also

induce fractures and increase the accessibility of the fluid (which is a major advantage for ISR). For low-grade ore ISR targets with acid-consuming gangue, the acid may also be consumed before the conversion of the primary copper sulfide phase is completed, which reduces the advantages of the initial acceleration of copper dissolution. In such a circumstance, it may be necessary to alternatively consider an alkaline pre-treatment.

B.4. Conclusions

After an assessment of the staged dissolution of bornite by acid pre-treatment and ferric methanesulfonate solution leaching, the main conclusions were:

- The use of iron as a natural oxidant source to generate leaching solutions represents a valuable topic for future research. More specifically, the use of more soluble iron-containing minerals as oxidant sources may reduce the acid strength that is required for dissolution, which, in turn, would make such an option more economically attractive.

- Acid pre-treatment of refractory copper minerals, i.e. bornite, increased their dissolution rate and yielded a higher copper recovery. In practice, the implementation of long-term pre-treatment stages to improve the conversion to secondary products before leaching represents a means to improve resource utilisation.

- Products from the bornite replacement showed a porous texture, which allowed for fluid interaction and increased accessibility in the system.

- The applicability of the staged dissolution of refractory copper minerals may present challenges in ISR operations because of the variable nature of the ores. For a chalcopyrite or bornite ore, the initial addition of a low concentration of Cu^{2+} as a replacement for oxygen may enhance the transformation into a copper enrichment phase and avoid hydrogen sulfide formation.

Acknowledgments

MRIWA (Project M488), BASF, Curtin University and CSIRO are gratefully acknowledged for funding this work. The authors would like to thank Sophia Surin and Tuyen Pham for their help with the analysis. Jian Li is thanked for reviewing a draft of this manuscript.

References

Bahamonde, F., Gómez, M., Navarro, P., 2017. Pre-Treatment with Sodium Chloride and Sulfuric Acid of a Bornitic Concentrate and Later Leaching in Chloride Solution. Hydroprocess, ICMSE 2017; Santiago de Chile.

Bartlett, R., 1998. Solution mining : leaching and fluid recovery of materials. 2nd ed. ed. Gordon and Breach Science Publishers.

Calvo, G., Mudd, G., Valero, A., 2016. Decreasing Ore Grades in Global Metallic Mining: A Theoretical Issue or a Global Reality. Resources, 5(36), pp.1–14

Cook, S., 1988. Supergene copper mineralisation at the Lakeshore Mine, Pinal County, Arizona. Economic Geology 83(2):297–309.

Dutrizac, J., Chen, T. and Jambor, J., 1985. Mineralogical changes occurring during the ferric ion leaching of bornite. Metallurgical Transactions B 16b(4): 679–693.

Dutrizac, J., Macdonald, R., Ingraham, T., 1970. The kinetics of dissolution of bornite in acidified ferric sulfate solutions. Metallurgical Transactions.1(1). pp:225–31.

Feng, Q., Wen, S., Zhao, W., Lv, C., Bai, X., 2015. Leaching of Copper from Malachite with Methane-sulfonic Acid. Solvent Extraction Research and Development, Japan 22(2):159–168.

Feng, Q., Wen, S., Wang, Y., Cao, Q., Zhao, W., 2015. Dissolution kinetics of cerussite in an alternative leaching reagent for lead. Chemical Papers. 69(3):440–7.

Gernon, M., Wu, M., Buszta, T., Janney, P., 1999. Environmental benefits of methanesulfonic acid. Comparative properties and advantages. Green Chemistry.1(3):127–40.

Gernon, M., 2017. The Preparation and Stoichiometric Synthetic Reactions of Metal Methanesulfonate Salts. Methanesulfonate Review.

Haynes, J., Sams, J., Thompson, R., 1981. Synthesis and structural studies of iron(II) and iron(III) sulfonates. Canadian Journal of Chemistry. 59(4):669–78.

Herreros, O., Bernal, N., Quiroz, R., Fuentes, G., Viñals, J., 2005. Lixiviación de concentrados de cobre utilizando NaCI y el cobre soluble aportado por el propio concentrado. Revista de Metalurgia Madrid; 41(5). pp.384–392.

Hidalgo, T., Beinlich, A., Verrall, M., Kuhar, L., Putnis, A., 2020. The replacement mechanism of bornite by covellite and chalcocite in acidic solutions. Ore Geology Reviews, accepted manuscript.

Hidalgo, T., Kuhar, L., Beinlich, A., Putnis, A., 2018. Kinetic study of chalcopyrite dissolution with iron(III) chloride in methanesulfonic acid. Minerals Engineering. 125:66–74.

Li, Y., Kawashima, N., Li, J., Chandra, A., Gerson, A., 2013. A review of the structure, and fundamental mechanisms and kinetics of the leaching of chalcopyrite. Advances in Colloid and Interface Science. 197–198:1–32.

Lu, J., Dreisinger, D., West-Sells, P., 2017. Acid curing and agglomeration for heap leaching. Hydrometallurgy. 167:30–5.

Lundström, M., Liipo, J., Taskinen, P., Aromaa, J., 2016. Copper precipitation during leaching of various copper sulfide concentrates with cupric chloride in acidic solutions. Hydrometallurgy. 166:136-42.

Muszer, A., Wódka, J., Chmielewski, T., Matuska, S., 2013. Covellinisation of copper sulfide minerals under pressure leaching conditions. Hydrometallurgy;137(C):1–7.

Özdemir, Ö., Dunlop, D., 2000. Intermediate magnetite formation during dehydration of goethite. Earth and Planetary Science Letters. 177(1):59–67.

Cerda, C., Taboada, M., Jamett, N., Ghorbani, Y., Hernández, C., 2017. Effect of Pretreatment on Leaching Primary Copper Sulfide in Acid-Chloride Media. Minerals; (8) pp. 1–14 .

Pesic, B., Olson, F., 1984. Dissolution of bornite in sulfuric acid using oxygen as oxidant. Hydrometallurgy. 12(2):195–215.

Pesic, B., Olson, F., 1983. Leaching of bornite in acidified ferric chloride solutions. Metallurgical Transactions B. 14(4):577–88.

Peters, E., Loewen, F., 1973. Pressure leaching of copper minerals in perchloric acid solutions. Metallurgical Transactions. 4(1):5–14.

Petersen, J., Dixon, D., 2006. Competitive bioleaching of pyrite and chalcopyrite. Hydrometallurgy. 83(1):40–9.

Price, D., Chilton, J., 1981. The anodic reactions of bornite in sulphuric acid solution. Hydrometallurgy. 7(1):117–33.

Price, D., Chilton, J., 1980. The electroleaching of bornite and chalcopyrite. Hydrometallurgy.5(4):381–94.

Seredkin, M., Zabolotsky, A., Jeffress, G., 2016. In situ recovery, an alternative to conventional methods of mining: Exploration, resource estimation, environmental issues, project evaluation and economics. Ore Geology Reviews. 79:500–14.

Thomas, G., Ingraham, T., Macdonald, R., 1967. Kinetics of dissolution of synthetic digenite and chalcocite in aqueous acidic ferric sulfate solutions. Canadian Metallurgical Quarterly. 6(3):281–92.

Ugarte, F., Burkin, A., 1975. Mechanism of formation of idaite from bornite by leaching with ferric sulfate solution. Leaching and Reduct in Hydrometall. 46–53.

Ugarte-Alverez, F., 1971. Leaching of bornite. London, England: University of London; PhD dissertation.

Veloso, T., Paiva, P., Silva, C., Leão, V., 2016. Leaching of Bornite Produced from the Sulfurisation of Chalcopyrite. Metallurgical and Materials Transactions B.47(3):2005–14.

Warren, G., Wadsworth, M., El-Raghy, S., 1992. Passive and transpassive anodic behavior of chalcopyrite in acid solutions. Journal of Electronic Materials. 21(1):571–9.

Wu, Z., Dreisinger, D., Urch, H., Fassbender, S., 2014. Fundamental study of lead recovery from cerussite concentrate with methanesulfonic acid (MSA). Hydrometallurgy. 142:23–35.

Wu, Z., Dreisinger, D., Urch, H., Fassbender, S., 2014. The kinetics of leaching galena concentrates with ferric methanesulfonate solution. Hydrometallurgy. 142:121–30.

Zhao, H., Hu, M., Li, Y., Zhu, S., Qin, W., Qiu, G., 2015. Comparison of electrochemical dissolution of chalcopyrite and bornite in acid culture medium. Transactions of Nonferrous Metals Society of China. 25(1):303–13.

Zhao, J., Brugger, J., Ngothai, Y., Pring, A., 2014. The replacement of chalcopyrite by bornite under hydrothermal conditions. The American Mineralogist. 99(11–12):2389.

Every reasonable effort has been made to acknowledge the owners of copyright material. I would be pleased to hear from any copyright owner who has been omitted or incorrectly acknowledged.

Appendix C. Complementary data chapter 2

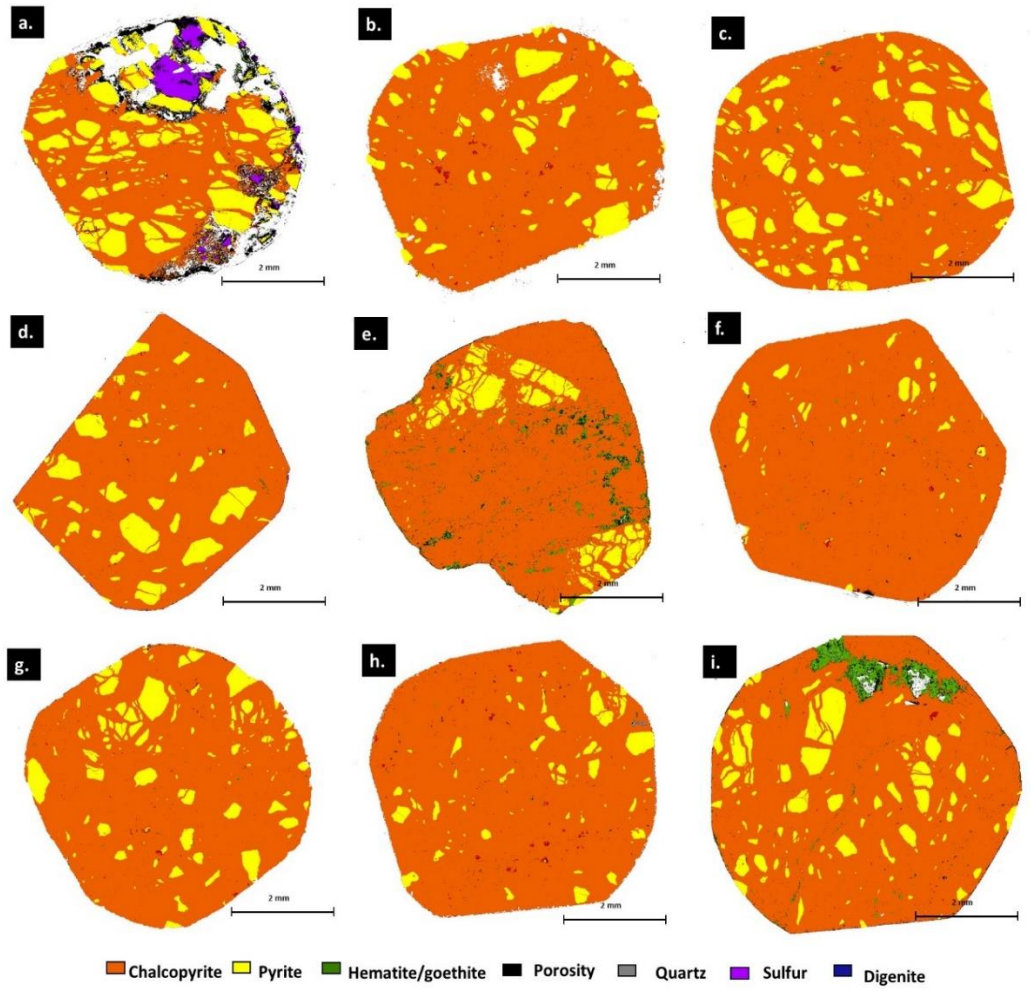

Fig. C-1. TIMA maps images of chalcopyrite samples after reaction in different lixiviant systems at 110°C for 4 days. **a.** solid after leaching in $FeCl_3$ + HCl. **b.** solid after leaching in $CuCl_2$ + HCl. **c.** solid after leaching in $Fe_2(SO_4)_3$ + H_2SO_4. **d.** solid after leaching in $CuSO_4$+ H_2SO_4. **e.** solid after leaching in O_2 + Glycine. **f.** solid after leaching in $C_3H_9FeO_9S_3$. **g.** solid after leaching in $NaNO_3$+ H_2SO_4. **h.** solid after leaching in H_2O_2+ H_2SO_4. **i.** solid after leaching in $(NH_4)_2SO_4$ + NH_4OH + $Na_2S_2O_8$.

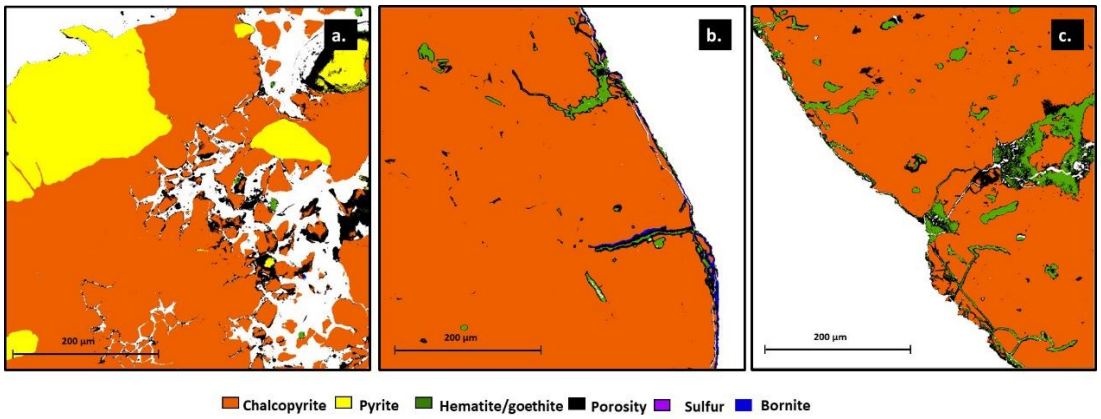

Fig. C-2. TIMA high resolution maps images of chalcopyrite samples after reaction in different lixiviant systems at 110°C for 4 days. **a.** solid after leaching in $FeCl_3$ + HCl showing the lack of enrichment phases next to fracture leached zones. **b.** solid after leaching in $CuSO_4$+ H_2SO_4 showing digenite rim. **c.** solid after leaching in $(NH_4)_2SO_4$ + NH_4OH + $Na_2S_2O_8$ showing zones of bornite and hematite. **d.** solid after leaching in O_2 + Glycine showing hematite in rim and fracture zones.

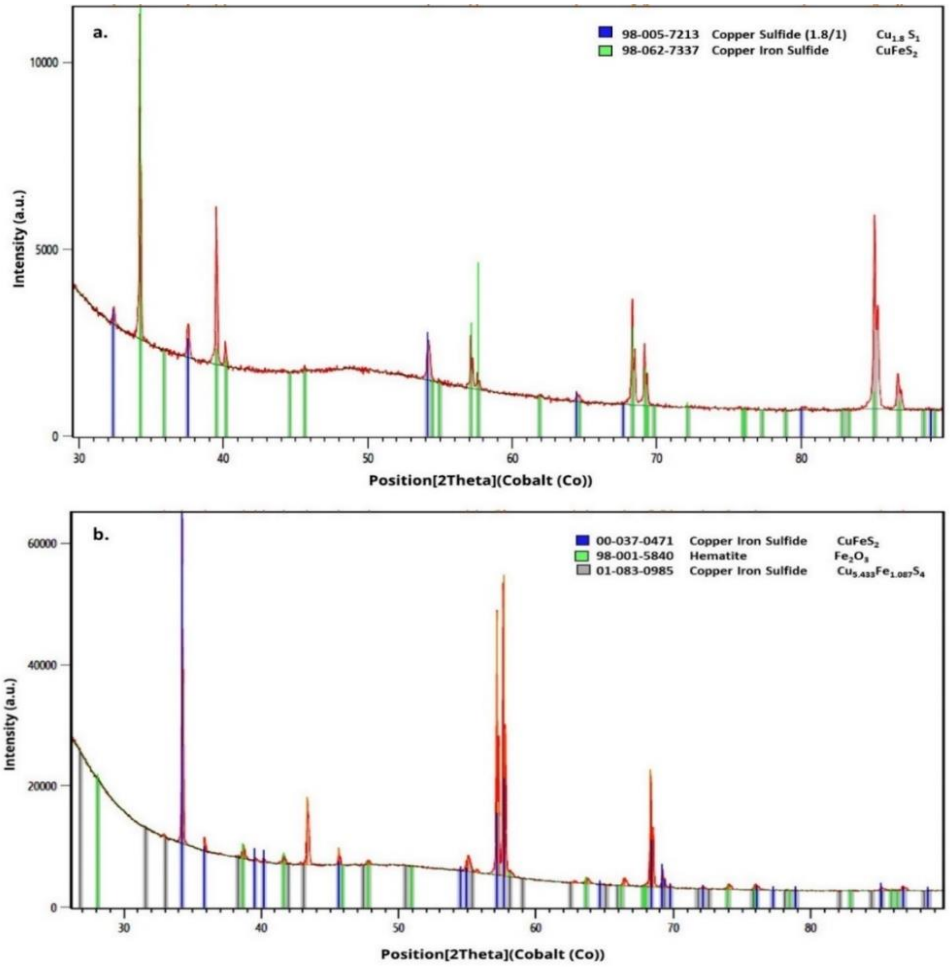

Fig. C-3. X-ray diffractogram of samples after leaching with selected lixiviant systems showing product phases after leaching. **a.** X-ray pattern after leaching in after 8 days at 170°C $CuSO_4$+ H_2SO_4 solution showing the presence of digenite and chalcopyrite. **b.** X-ray pattern after leaching in after 4 days at 110°C solution $(NH_4)_2SO_4$ + NH_4OH + $Na_2S_2O_8$ solution showing the presence of hematite, chalcopyrite and bornite.

Table C-1. Summary of pH after one and four days of reaction with different lixiviant systems for 110°C and 170°C showing the changes between initial and final pH.

Lixiviant System	**110 °C**				**170 °C**		
	Initial	**pH 1 day**	**pH 4 day**	**ΔpH**	**Initial**	**pH 8 day**	**ΔpH**
$FeCl_3$ + HCl	-0.07	0.01	0.04	0.11	-1.26	0.94	0.32
$CuCl_2$ + HCl	-0.02	0.31	0.44	0.42	-1.07	-0.93	0.14
$Fe_2(SO_4)_3$ + H_2SO_4	-0.03	0.36	0.48	0.45	-0.18	1.69	1.51
$CuSO_4$+ H_2SO_4	0 23	0.65	0.83	0.6	-0.6	0.52	0.08
$K_2Cr_2O_7$ + HCl	0 16	0.51	0.58	0.42	0.58	0.65	0.07
O_2 + Glycine / H_2O_2 + Glycine*	10.5	10.43	9.6	-0.9	11.2	10.85	-0.35
$C_3H_9FeO_9S_3$	-0.06	0.03	0.76	0.7	-	-	-
$NaNO_3$+ H_2SO_4	0 11	0.17	0.9	0.79	-	-	-
H_2O_2+ H_2SO_4	0 23	0.9	1.04	0.81	-	-	-
$(NH_4)_2SO_4$ + NH_4OH + $Na_2S_2O_8$	10.6	9.87	9.83	-0.77	-	-	-

*Experiments were performed at 60 C

Table C-2. Summary of categorised physical, health and environmental hazards for different reagents used in experiments.

Reagent	**Physical hazards**	**Health hazards**	**Environmental hazards**
$FeCl_3$	H290	H314, H302, H315, H318	H412
$CuCl_2$		H301, H302, H312, H315, H318, H319, H335	H400, H410, H411
$K_2Cr_2O_7$	H272	H301, H312, H314, H317, H330, H334, H340, H350, H360, H372	H400, H410, H411
$CuSO_4$		H302, H315, H319	H400, H410
$Fe_2(SO_4)_3$	H290	H302, H315, H317, H318, H319, H335	
$C_3H_9FeO_9S_3$		H301, H315, H318, H319, H335, H350	
$NaNO_3$	H272	H302, H319	
H_2O_2	H271	H302, H314, H332	
$(NH_4)_2SO_4$		H320, H315, H319, H335	

O_2		
HCl	H314, H331	
H_2SO_4	H314	
MSA	H314	
NH_4OH	H314	H400
Glycine		

H271 May cause fire or explosion; strong oxidizer
H272 May intensify fire; oxidizer
H290 May be corrosive to metals
H301 Toxic if swallowed
H302 Harmful if swallowed
H312 Harmful in contact with skin
H314 Causes severe skin burns and eye damage
H315 Causes skin irritation
H317 May cause an allergic skin reaction
H318 Causes serious eye damage
H319 Causes serious eye irritation
H330 Fatal if inhaled
H331 Toxic if inhaled
H332: Harmful if inhaled
H334: May cause allergy or asthma symptoms or breathing difficulties if inhaled
H335: May cause respiratory irritation
H340: May cause genetic defects
H350: May cause cancer
H360: May damage fertility or the unborn child
H372: Causes damage to organs through prolonged or repeated exposure
H400: Very toxic to aquatic life
H410: Very toxic to aquatic life with long-lasting effects
H411: Toxic to aquatic life with long-lasting effects
H412: Harmful to aquatic life with long-lasting effects

Table C-3. Summary of initial reagent cost for different lixiviant systems used in experiments.

Reagent	**Initial cost (USD/ ton)**	**Reagent**	**Initial cost (USD/ ton)**	**Total cost reagents (USD/ ton)**
$FeCl_3$	600	HCl	200	800
$CuCl_2$	1600	HCl	200	1800
$K_2Cr_2O_7$	1860	HCl	200	2060
$CuSO_4$	1700	H_2SO_4	195	1895
$Fe_2(SO_4)_3$	150	H_2SO_4	195	345
$C_3H_9FeO_9S_3$*			1814	1814
$NaNO_3$	400	H_2SO_4	190	590
H_2O_2	500	H_2SO_4	190	690
$NH_4)_2SO_4$	100	NH_4OH	300	400
O_2	0	Glycine	453 5	453.5

*Commercial ferric methanesulfonate

Table C-4. Summary of comparative of changes in fracture-porosity areas calculated by ImageJ 1.x on cross-sections of solids after leaching with different reagents for 4 days at 110°C.

Lixiviant System	Area (pixels)	Δ area (%)	Width (pixels)	Height (pixels)
Unreacted	135265		1307	1070
$FeCl_3$ + HCl	162562	20%	1309	1069
$CuCl_2$ + HCl	156524	16%	1310	1068
$Fe_2(SO_4)_3$ + H_2SO_4	136362	1%	1309	1068
$CuSO_4$+ H_2SO_4	141107	4%	1310	1068
O_2 + Glycine	151431	12%	1309	1068
Fe^{+3}MSA	139886	3%	1309	1069
$NaNO_3$+ H_2SO_4	153738	14%	1309	1068
H_2O_2+ H_2SO_4	139917	3%	1310	1068
$(NH_4)_2SO_4$ + NH_4OH + $Na_2S_2O_8$	159138	18%	1309	1068

Appendix D. Complementary data chapter 5

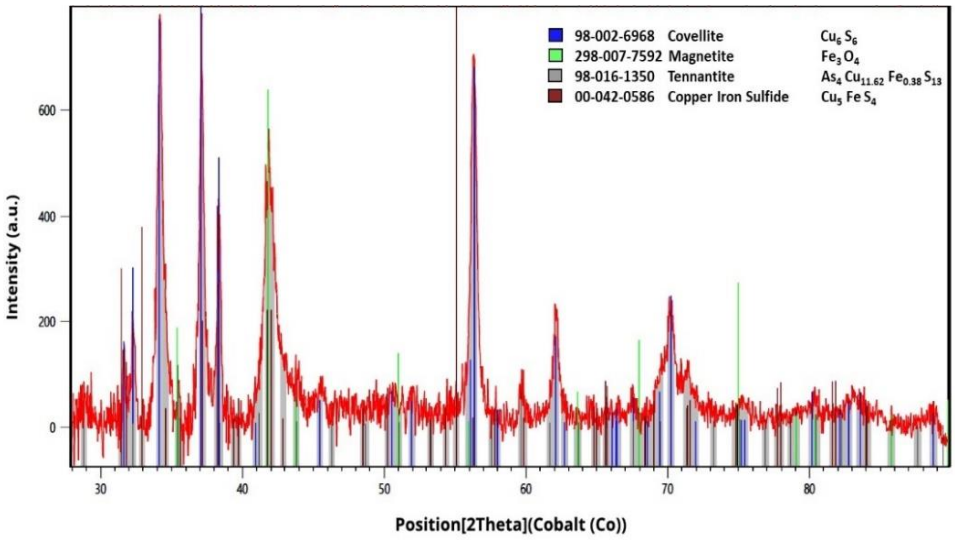

Fig. D-1. X-ray diffractogram of the bornite-chalcocite sample after reaction with HCl solutions for one month at 90°C, the major phase found was covellite with minor peaks of magnetite, tennantite and bornite.

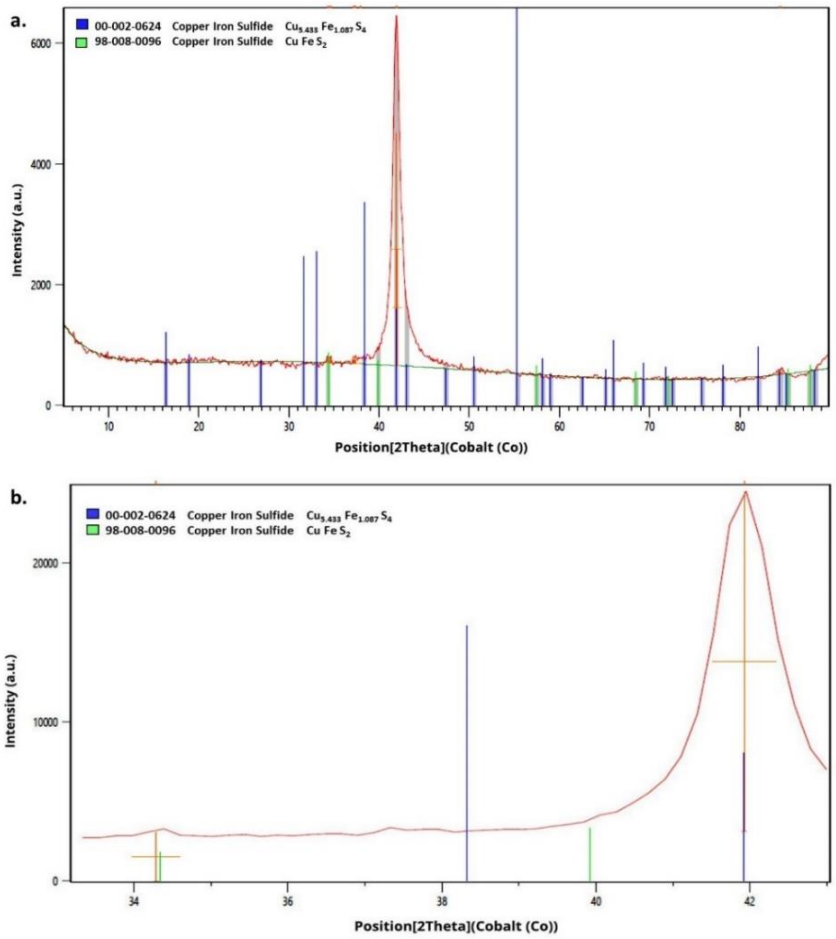

Fig. D-2. a. Point X-ray diffractogram (acquisition time 48 h) of the bornite-chalcocite sample after reaction with HCl solutions for one month at 90°C focused in exsolution texture. Only one peak from chalcopyrite was found. **b.** Point X-ray diffractogram (acquisition time 48 h) from 33 (2θ) to 45 (2θ) of the bornite-chalcocite sample after reaction with HCl solutions for one month at 90°C focused in exsolution texture. Showing the chalcopyrite peak found.

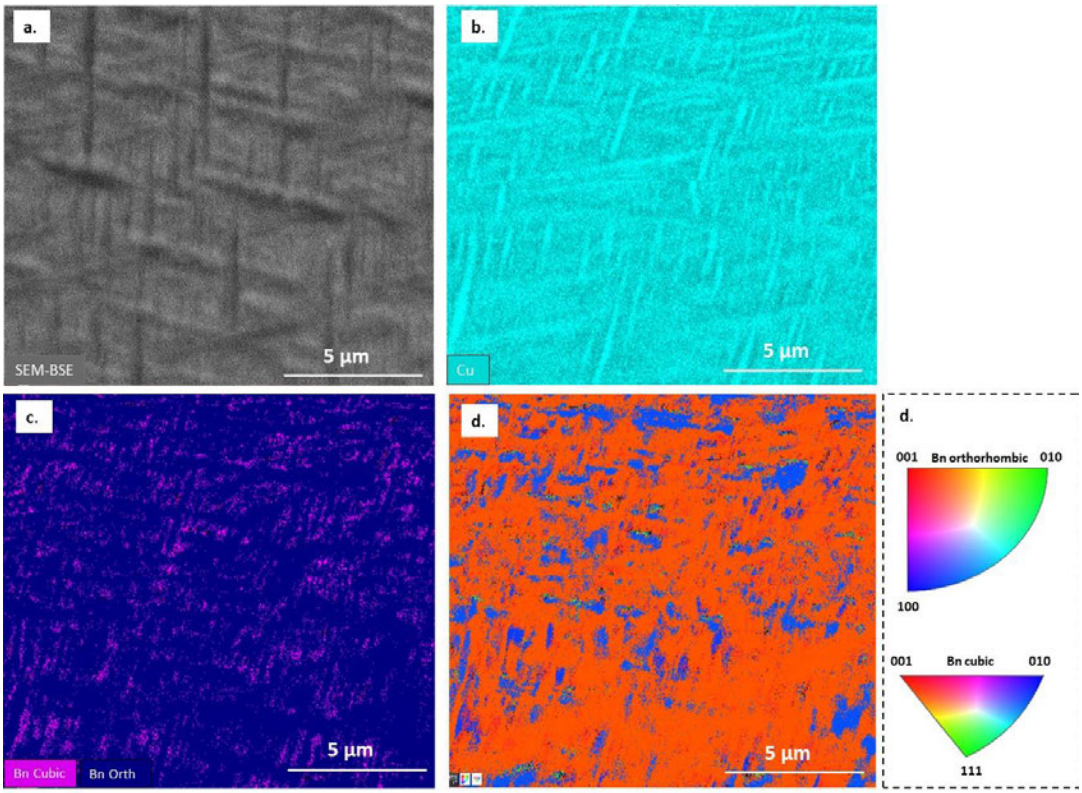

Fig. D-3. EBSD maps images of the bornite exsolution texture after reaction in HCl at 90°C for one month. **a.** Band contrast of the exsolution texture **b.** EDS Cu concentration map showing the lamellae of Cu-deficient bornite. **c.** Phase map showing the distribution of orthorhombic (blue) and cubic (fuchsia) bornite. **d.** Inverse pole figure (IPF) map showing the relative orientation of orthorhombic and cubic bornite (the orientation key is attached to the image).

Statements of Authorship

Chapter 2

Publication title: Comparative analysis of copper dissolution and mineral transformations in coarse chalcopyrite for different lixiviant/oxidant systems elevated temperature (110˚C to 170˚C).

Publication status: In preparation.

Publication details: To be submitted to hydrometallurgy.

Author's contributions

To whom it may concern,

By signing the Statement of Authorship, each author certifies that their stated contribution to the publication is accurate and that permission is granted for the publication to be included in the candidate's thesis.

Name of Principal Author: Tania Marcela Hidalgo Rosero

Contribution to the Paper (%): 70%

Signature: [redacted] **Date:** 19/11/2019

Name of Co-author: Dr. Robbie McDonald

Contribution to the Paper (%): 10%

Signature: [redacted] **Date:** 28/11/2019

Name of Co-author: Dr. Andreas Beinlich

Contribution to the Paper (%): 10%

Signature: [redacted] **Date:** 14/11/2019

Name of Principal Author: Dr. Laura Kuhar

Contribution to the Paper (%): 5%

Signature: [redacted] **Date:** 19/11/19

Name of Principal Author: Dr. Andrew Putnis

Contribution to the Paper (%): 5%

Signature: [redacted] **Date:** 14.11.19

Chapter 3

Publication title: Kinetic study of chalcopyrite dissolution with iron (III) chloride in methanesulfonic acid.

Publication status: Published.

Publication details: Hidalgo, T., Kuhar, L., Beinlich, A. and Putnis, A., 2018a. Kinetic study of chalcopyrite dissolution with iron (III) chloride in methanesulfonic acid. Minerals Engineering, 125: 66-74. https://doi.org/10.1016/j.mineng.2018.05.025.

Authors contributions

To whom it may concern,

By signing the Statement of Authorship, each author certifies that their stated contribution to the publication is accurate and that permission is granted for the publication to be included in the candidate's thesis.

Name of Principal Author: Tania Marcela Hidalgo Rosero

Contribution to the Paper (%): 80%

Signatur [redacted] **Date:** 19/11/2019

Name of Co-author: Dr. Laura Kuhar

Contribution to the Paper (%): 10%

Signature: [redacted] **Date:** 19/11/19

Name of Principal Author: Dr. Andreas Beinlich

Contribution to the Paper (%): 5%

Signature: [redacted] **Date:** 14/11/2019

Name of Principal Author: Dr. Andrew Putnis

Contribution to the Paper (%): 5%

Signature: [redacted] **Date:** 14.11.2019

Chapter 4

Publication title: Kinetics and mineralogical analysis of copper dissolution from a bornite/chalcopyrite composite sample in ferric-chloride and methanesulfonic-acid solutions.

Publication status: Published.

Publication details: Hidalgo, T., Kuhar, L., Beinlich, A. and Putnis, A., 2019a. Kinetics and mineralogical analysis of copper dissolution from a bornite/chalcopyrite composite sample in ferric-chloride and methanesulfonic-acid solutions. Hydrometallurgy, 188: 140-156. https://doi.org/10.1016/j.hydromet.2019.06.009.

Authors contributions

To whom it may concern,

By signing the Statement of Authorship, each author certifies that their stated contribution to the publication is accurate and that permission is granted for the publication to be included in the candidate's thesis.

Name of Principal Author: Tania Marcela Hidalgo Rosero

Contribution to the Paper (%): 75%

Signature [redacted] **Date:** 19/11/2019

Name of Principal Author: Dr. Laura Kuhar

Contribution to the Paper (%): 15%

Signature: [redacted] **Date:** 19/11/19

Name of Co-author: Dr. Andreas Beinlich

Contribution to the Paper (%): 5%

Signature: [redacted] **Date:** 14/11/2019

Name of Principal Author: Dr. Andrew Putnis

Contribution to the Paper (%): 5%

Signature: [redacted] **Date:** 14.11.19

Chapter 5

Publication title: Replacement reactions of copper sulfides at moderate temperature in acidic solutions.

Publication status: Submitted .

Publication details: To be submitted to Ore Geology reviews.

Authors contributions

To whom it may concern,

By signing the Statement of Authorship, each author certifies that their stated contribution to the publication is accurate and that permission is granted for the publication to be included in the candidate's thesis.

Name of Principal Author: Tania Marcela Hidalgo Rosero

Contribution to the Paper (%): 65%

Signature: [redacted] **Date:** 19/11/2019

Name of Principal Author: Dr. Andreas Beinlich

Contribution to the Paper (%): 10%

Signature: [redacted] **Date:** 14/11/2019

Name of Co-author: Michael Verrall

Contribution to the Paper (%): 10%

Signature: [redacted] **Date:** 15/11/2019

Name of Co-author: Dr. Laura Kuhar

Contribution to the Paper (%): 5%

Signature: [redacted] **Date:** 19/11/2019

Name of Principal Author: Dr. Andrew Putnis

Contribution to the Paper (%): 10%

Signature: [redacted] **Date:** 14.11.2019

Chapter 6

Publication title: Effect of multistage solution–mineral contact for low-grade natural copper samples: extraction, acid consumption, gangue-mineral changes and precipitation

Publication status: Submitted

Publication details: Under review at Minerals engineering

Authors contributions

To whom it may concern,

By signing the Statement of Authorship, each author certifies that their stated contribution to the publication is accurate and that permission is granted for the publication to be included in the candidate's thesis.

Name of Principal Author: Tania Marcela Hidalgo Rosero

Contribution to the Paper (%): 80%

Signature: [redacted] **Date:** 19/11/2019

Name of Co-author: Dr. Laura Kuhar

Contribution to the Paper (%): 10%

Signature: [redacted] **Date:** 19/11/19

Name of Principal Author: Dr. Andreas Beinlich

Contribution to the Paper (%): 5%

Signature: [redacted] **Date:** 14/11/2019

Name of Principal Author: Dr. Andrew Putnis

Contribution to the Paper (%): 5%

Signature: [redacted] **Date:** 14.11.19

Appendix A

Publication title: Comparative analysis of lixiviant/oxidant systems for chalcopyrite leaching from coarse samples at elevated temperature.

Publication status: Published.

Publication details: Hidalgo, T., McDonald, R., Kuhar, L., Beinlich, A. and Putnis, A., 2018b. Comparative analysis of lixiviant/oxidant systems for chalcopyrite leaching from coarse samples at elevated temperature, ALTA Nickel- cobalt - copper symposium, Perth, Western Australia. https://www.altamet.com.au/product/curtin-

university-csiro-comparative-analysis-of-lixiviant-oxidant-systems-for-chalcopyrite-leaching-from-coarse-samples-at-elevated-temperature/.

Authors contributions

To whom it may concern,

By signing the Statement of Authorship, each author certifies that their stated contribution to the publication is accurate and that permission is granted for the publication to be included in the candidate's thesis.

Name of Principal Author: Tania Marcela Hidalgo Rosero

Contribution to the Paper (%): 80%

Signature: [redacted] **Date:** 14/11/2019

Name of Co-author: Dr. Laura Kuhar

Contribution to the Paper (%): 10%

Signature: [redacted] **Date:** 19/11/19

Name of Principal Author: Dr. Andreas Beinlich

Contribution to the Paper (%): 7%

Signature: [redacted] **Date:** 14/11/2019

Name of Principal Author: Dr. Andrew Putnis

Contribution to the Paper (%): 3%

Signature: [redacted] **Date:** 14.11.2019

Appendix B

Publication title: Staged leaching of bornite with acidic solutions at moderate temperature in an in-situ recovery environment.

Publication status: Published.

Publication details: Hidalgo, T., McDonald, R., Kuhar, L., Beinlich, A. and Putnis, A., 2019b. Staged leaching of bornite with acidic solutions at moderate temperature in an in-situ recovery environment, ALTA ISR symposium, Perth, Western Australia. https://www.altamet.com.au/product/curtin-csiro-staged-leaching-of-bornite-with-acidic-solutions-at-moderate-temperature-in-an-in-situ-recovery-environment/.

Authors contributions

To whom it may concern,

By signing the Statement of Authorship, each author certifies that their stated contribution to the publication is accurate and that permission is granted for the publication to be included in the candidate's thesis.

Name of Principal Author: Tania Marcela Hidalgo Rosero

Contribution to the Paper (%): 70%

Signature: [redacted] **Date:** 19/11/2019

Name of Co-author: Dr. Robbie McDonald

Contribution to the Paper (%): 15%

Signature: [redacted] **Date:** 28/11/2019

Name of Co-author: Dr. Laura Kuhar

Contribution to the Paper (%): 10%

Signature: [redacted] **Date:** 19/11/19

Name of Principal Author: Dr. Andreas Beinlich

Contribution to the Paper (%): 2.5%

Signature: [redacted] **Date:** 19/11/2019

Name of Principal Author: Dr. Andrew Putnis

Contribution to the Paper (%): 2.5%

Signature: [redacted] **Date:** 14.11.2019